

A Data Fusion and Visualisation Platform for Multi-Phase Flow by Electrical Tomography



Qiang Wang

Submitted in accordance with the requirements for the degree of

Doctor of Philosophy

School of Chemical and Process Engineering

University of Leeds

July 2017

The candidate confirms that the work submitted is his/her/their own, except where work which has formed part of jointly authored publications has been included. The contribution of the candidate and the other authors to this work has been explicitly indicated below. The candidate confirms that appropriate credit has been given within the thesis where reference has been made to the work of others.

The publication of "Q Wang, M Wang, K Wei, and C Qiu. Visualisation of Gas-Oil-Water Flow in Horizontal pipeline using Dual-Modality Electrical Tomographic System. In *IEEE Sensors Journal*, 2017" contributes to Section 2.1.3 and Section 3.4. Dr K Wei and Mrs C Qiu provided descriptive information about the dual-modality ERT-ECT systems used for experiment, and the ECT results. Dr K Wei also helped on the operation of the ECT system during the experiment at TUV NEL. The rest of the work was done by Mr Q Wang. All authors provided valuable comments on the publication.

The publication of "Q Wang, J Polansky, M Wang, K Wei, C Qiu, A Kenbar, D Millington. Experimental Evaluation of Dual-Modality Electrical Tomographic Systems on Gas-Oil-Water Flow in Horizontal Pipeline. In: *8th World Congress on Industrial Process Tomography*, 2016" contributes to Section 3.2 and Section 3.6. Dr J Polansky, Dr K Wei, Dr A Kenbar, and Mrs D Millington conducted experimented at TUV NEL. Dr A Kenbar and Mrs D Millington provided the descriptive information regarding the flow test facility at TUV NEL. Dr K Wei processed the ECT data. The rest of the

work was done by Mr Q Wang. All authors provided valuable comments on the publication.

The publication of "Q Wang, Y Faraj, M Wang. Effects of Asymmetrical Sensing and Imaging on Scalar and Vector Tomograms. In: *5th International Workshop on Process Tomography, 2014*" contributes to Section 5.2. Mr Q Wang did the experiments and processed the data. Dr Y Faraj and Prof. M Wang provided valuable comments on the publication.

The publications of "Q Wang, B Karki, Y Faraj, M Wang. Improving Spatial and Temporal Resolution of Electrical Impedance Tomogram (EIT) by Partial Imaging with Limited Measurements (PILM). In *7th International Symposium on Process Tomography, 2015*" and "M Wang, Q Wang, and B Karki. Arts of electrical impedance tomographic sensing. In: *Phil. Trans. R. Soc. A, 2016*" contribute to Section 5.3. Mr B Karki generated the axially-stacked tomograms and produced the velocity profile. All authors provided valuable comments on the publication. Mr Q Wang did the static and flow experiments, and processed the data from the static experiments. He also generated the concentration profile for the flow experiment.

This copy has been supplied on the understanding that it is copyright material and that no quotation from the thesis may be published without proper acknowledgement.

To my beloved mother
For the many things she gave me
For the tears she often shed for me
For her heart as pure as gold
For her eyes that shone so brightly
How I wish you were here with me!

Acknowledgements

Undertaking this PhD has been a life-changing experience for me. I could not have achieved it without guidance and support from many people.

My first appreciation is to my parents, Ruiyu Wang and Wenjun Shao, for their understanding, encouragement, and love. All the love they have given me over the years was the greatest gift anyone has ever given me. Mum and Dad, you are wonderful parents and wonderful friends. I also appreciate my elder sister Qian Wang, my brother-in-law, Jun Liu, and my lovely niece Yuqi Liu, not only their unconditional support but also their help on taking good care of my parents when I am far away from them.

I owe my deepest gratitude to my supervisor Professor Mi Wang and Dr Xiaodong Jia, you have been tremendous mentors for me. I would like to thank both them for the continuous support during my PhD study and related research, for their patience, motivation, and immense knowledge. Their guidance has been invaluable to me throughout the whole period of my research and the writing up of this thesis. I could not have imagined having better advisers and mentors for my PhD study.

Also, my thanks go to my colleagues and friends in the OLIL group, University of Leeds, who have provided many kindly and useful suggestions for my research and life. They are Dr Jiabin Jia, Dr Yousef Faraj, Professor Jiri Polansky, Bishal Karki, Frian Hossein, Phillip Nwufoh, and Robert Harris. I also appreciate the assistance of Mrs Changhua Qiu and Dr. Kent Wei from Industrial Tomography Systems who have offered me unique opportunities to gain practical experience in process tomography. I would also like to thank Mrs Judith Sherrington for proof reading my thesis.

Finally, my indebtedness is to my wife Na Li and my son Jiangyue Wang. I found it is difficult to express my full appreciation because it is so boundless. She is my most enthusiastic cheerleader; she is my best friend; and she is an amazing wife and mother. She has given up so much to make my career a priority in our lives. Beyond this, I need to thank my little boy for being such a bundle of joy and laughter.

Abstract

Electrical tomography, e.g. electrical resistance tomography (ERT) and electrical capacitance tomography (ECT), has been successfully applied to many industries for measuring and visualising multiphase flow. This research aims to investigate the data fusion and visualisation technologies with electrical tomography as the key data processing tools of a platform for multiphase flow characterisation.

Gas-oil-water flow is a common flow in the gas and oil industries but still presents challenges in understanding its complex dynamics. This research systematically studied the data fusion and visualisation technologies using dual-modality electrical tomography (ERT-ECT). Based on a general framework, two data fusion methods, namely threshold and fuzzy logic with decision tree, were developed to quantify and qualify the flow. The experimental results illustrated the feasibility of the methods integrated with the framework to visualise and measure flows in six typical common flow regimes, including stratified, wavy stratified, slug, plug, annular, and bubble flow. In addition, the performance of ERT-ECT was also evaluated. A 3D visualisation approach, namely Bubble Mapping, was proposed to transform concentration distribution to individual bubbles. With a bubble-based lookup table and enhanced isosurface algorithms, the approach overcomes the limits of the conventional concentration tomograms in visualisation of bubbles with sharp boundaries between gas and liquid, providing sophisticated flow dynamic information. The experiments proved that Bubble Mapping is able to visualise typical flow regimes in different pipeline orientations. Two sensing methods were proposed, namely asymmetrical sensing and imaging (ASI) and regional imaging with limited measurement (RILM), to improve the precision of the velocity profile derived from the cross-correlation method by

enhancing ERT sensing speed, which is particularly helpful for industrial flows that their disperse phase velocity is very high, e.g. 20 m/s of the gas phase.

It is expected that the outcome of this study will significantly move electrical tomography for multiphase flow applications beyond its current challenges in both quantification and qualification.

Abbreviations

ERT:	Electrical Resistance Tomography
ECT:	Electrical Capacitance Tomography
LBP:	Linear Back-Projection
SBP:	Sensitivity Coefficient-based Back-Project
SCG:	Sensitivity Theorem-based Conjugate Gradient Reconstruction
DAS:	Data Acquisition System
FDM:	Finite Difference Method
DMTS:	Dual-modality tomographic systems
WMS:	Wire-mesh sensor
2-D/2D:	Two dimensions
3-D/3D:	Three dimensions
CFD:	Computational Fluid Dynamics
CG:	Computer Graphics
WLR:	Water-Liquid Ratio, i.e. the water volume flow rate, relative to the total liquid volume flow rate (oil and water) (Corneliussen et al. 2005)
GVF:	Gas Volume Fraction, i.e. the gas volume flow rate, relative to the multiphase volume flow rate (Corneliussen et al. 2005)
VF:	Void fraction, i.e. the ratio of the cross-sectional area in a conduit occupied by the gas phase and the cross-sectional area of the conduit (Corneliussen et al. 2005)
LCM:	least common multiple
IC:	Interrogation cell

Symbols and Definitions

R/r	Radius
D/d	Diameter
α	Concentration
σ	Conductivity
ϵ	Permittivity
∇	Gradient
$\Delta \cdot$	Divergence
Σ	Summation
ρ	Density
$X = \{x\}$	A set of elements
$ X $	The cardinality of the set $ X $ if X is a set, or otherwise the absolute value of the figure X
$\prod X$	The sum of elements in the set X
$C^{i,m} = \{c_x^{i,m}\}$	A cross-sectional concentration tomogram, where m represents different modalities, and $c_x^{i,m}$ is the x th pixel concentration of i th tomogram with a spatial resolution of $N \times N$
$T^m = \{F^{i,m}\}$	A set of cross-sectional concentration tomograms after data alignment, where $F^{i,m}$ represents i th cross-sectional tomogram (frame) by a modality m
$S^x = \{s_{i,j}^x\}$	Axially-stacked 2D concentration tomograms, where x represents different modalities, and $s_{i,j}^x$ is the pixel concentration at (i,j) on a $M = Q \times N$ regular square mesh, where Q is the number of the input tomograms
LCM	The operation of least common multiple
lcm	The result of LCM
DAS^m	Data acquisition speed of a modality m
$T : M \rightarrow N$	A conceptual function to transform the data in M to the data in N

Contents

Acknowledgement	i
Abstract	iii
Abbreviations	v
Symbols	vi
Contents	vii
List of Figures	xii
List of Tables	xxii
1 Introduction	1
1.1 Background	1
1.2 Aim and Objectives of the Research	3
1.3 Organization of the Thesis	3
2 Literature Review	5
2.1 Fundamentals	5

2.1.1	Multiphase flow	5
2.1.2	Electrical tomography	11
2.1.3	Dual-modality ERT-ECT systems	20
2.2	Multiphase flow visualisation	21
2.2.1	Advanced visualisation techniques in computer graphics	24
2.2.1.1	Edge detection	24
2.2.1.2	Image segmentation	25
2.2.1.3	Isosurface extraction	26
2.2.1.4	Volume rendering	29
2.2.2	Visualisation of gas-liquid flow	30
2.2.2.1	Computational Fluid Dynamics	30
2.2.2.2	Computer graphics	32
2.2.2.3	Tomographic systems	34
2.2.3	Visualisation of gas-oil-water three-phase flow	43
2.2.3.1	Tomographic systems	43
2.2.3.2	Image fusion approaches	48
2.3	Summary	54
3	Methods of Data Fusion for Visualisation of Gas-Oil-Water Flow	57
3.1	Introduction	57
3.2	TUV NEL multiphase flow facilities	58
3.3	A general framework for multi-dimensional data fusion	61
3.3.1	Introduction	61

3.3.2	The general framework	63
3.3.2.1	Data pre-processing	65
3.3.2.2	Data fusion	73
3.3.2.3	Data display	74
3.3.3	Conclusions	75
3.4	Thresholding method	77
3.4.1	Introduction	77
3.4.2	The approach	77
3.4.3	Evaluation	79
3.4.4	Conclusions	86
3.5	Fuzzy logic method	87
3.5.1	Introduction	87
3.5.2	Fuzzy logic-based data fusion	87
3.5.2.1	Fuzzification	89
3.5.2.2	Inference engine	90
3.5.2.3	Defuzzification	92
3.5.2.4	Phase decomposition	94
3.5.3	Evaluation	96
3.5.3.1	Feasibility	96
3.5.3.2	Stability	100
3.5.4	Conclusions	103
3.6	Experimental evaluation of dual-modality ERT-ECT systems	104

3.6.1	Introduction	104
3.6.2	Experimental results	106
3.6.2.1	WLR 0%	106
3.6.2.2	WLR 10%	111
3.6.2.3	WLR 25%	111
3.6.2.4	WLR 50%	113
3.6.2.5	WLR 75%	116
3.6.2.6	WLR 90%	118
3.6.2.7	WLR 100%	122
3.6.3	Discussion	123
3.6.3.1	ECT system	123
3.6.3.2	ERT system	124
3.6.3.3	Dual-modality electrical tomographic systems	124
3.6.4	Conclusions	126
3.7	Summary	128
4	Bubble Mapping Method for Visualising Gas-Liquid Flow	130
4.1	Introduction	130
4.2	Methodology	131
4.2.1	Data preprocessing	133
4.2.2	Construction of a new lookup table	135
4.2.3	Large bubble identification	137
4.3	Evaluation using ERT	139

4.3.1	Gas-water flow in a vertical pipeline	139
4.3.2	Gas-water flow in a horizontal pipeline	142
4.3.3	Impact of the parameters	144
4.4	Summary	147
5	Enhancement of Spatial and Temporal Resolution of ERT systems	150
5.1	Introduction	150
5.2	Asymmetrical Sensing and Imaging (ASI)	151
5.2.1	Determination of eligible distribution of ASI	151
5.2.2	Evaluation of selected ASI on gas-water upwards flow . . .	154
5.2.3	Conclusions	157
5.3	Regional Imaging with Limited Measurement (RILM)	159
5.3.1	Methodology	159
5.3.2	Evaluation	162
5.3.2.1	Imaging of statically-positioned objects	163
5.3.2.2	Evaluation of the gas-water pipeline flow	164
5.3.3	Conclusions	165
5.4	Summary	166
6	Conclusions and Suggestions for Future Work	168
6.1	Conclusions	168
6.2	Suggestions for Future Work	173
6.2.1	Dual-modality electrical tomography	173

6.2.2	Bubble mapping	175
6.2.3	ASI and RILM	176
6.2.4	GPU-accelerated on-line visualisation and measurement . .	176
6.2.5	An integrated platform for on-line visualisation and mea- surement	179
	References	180
	Publications	194
	Appendix A Visualisation of Three-Phase Horizontal Flow	198

List of Figures

2.1	Norwegian generic flow regime map (Corneliussen et al. 2005) for (a) horizontal pipeline flow, and (b) vertical pipeline flow.	7
2.2	6 typical flow regimes of gas-liquid flow in a horizontal pipeline, where the green is gas phase and the light blue is liquid phase. (a) stratified flow; (b) wavy stratified flow; (c) plug flow; (d) slug flow; (e) bubbly flow; and (f) annular flow.	8
2.3	4 typical flow regimes of gas-liquid upward flow in vertical pipeline, where the green is gas phase and the light blue is liquid phase. (a) bubbly flow; (b) slug flow; (c) churn flow; and (d) annular flow.	9
2.4	Three different sensing strategies. (a) adjacent sensing strategy, (b) PI/2 sensing strategy, and (c) opposite sensing strategy. (Wang et al. 2016a).	12
2.5	Reconstructed ERT images by (a) SBP on a regular 20*20 mesh, and (b) SCG on an irregular 248-element mesh, and ECT images (c) by LBP and Landweber on a 32*32 regular mesh.	13
2.6	Sensitivity distribution of (a) adjacent and (b) opposite sensing strategies (Wang et al. 2016a).	14
2.7	The incapability of ERT tomograms to identify (a) small bubbles in a horizontal bubbly flow, and (b) large bubble in a vertical slug flow.	15
2.8	The fundamental idea of best correlation between pixel $X_{(n,m)}$ and the neighbouring pixels of $Y_{(n,m)}$ (Mosorov et al. 2002).	18

2.9	A typical industrial application of dual-modality electrical tomography (Qiu et al. 2007).	20
2.10	ERT-ECT systems and integrated sensors used in the experiment.	21
2.11	Edge detection in LBP (a) and SCG (b) based electrical tomogram by Sober, LOG, and Canny operators.	25
2.12	Graph-cut based image segmentation on an electrical tomogram.	25
2.13	21 configurations for marching a cube using the Marching Cubes algorithm (Lorenson 2013).	28
2.14	Schematic diagram of the ray tracing algorithm (Wikipedia 2013a).	28
2.15	Four steps of ray casting: 1) ray casting; 2) sampling; 3) shading; and 4) compositing (Wikipedia 2013b)	29
2.16	Principle of Shear-Warp approach (Preim et al. 2007)	30
2.17	CFD-simulated gas-liquid (a) stratified flow and (b) annular flow.	31
2.18	Different approach for bubble simulation in CG. (a) a hybrid approach of SPH with grid-based simulation (Hong et al. 2008), (b) bubble rising in a tank using volume control method (Kim et al. 2007), (c) regional level set based multiphase fluid simulation (Kim 2010), and (d) reconstruction bubbles by direct mapping (Ren et al. 2015).	33
2.19	Gas-liquid vertical flow visualisation by (a) X-ray (Fischer et al. 2010), and (b) WMS (Manera et al. 2006).	35
2.20	ERT-based concentration tomograms of bubbly flow by (a) LBP and (b) SCG, and slug flow by (c) LBP and (d) SCG.	36
2.21	Mapping a scalar to a colour by a blue-to-red lookup table.	37
2.22	Same concentration distribution but different tomograms by (a) jet colour and normal scale; (b) jet colour but different scale [0, 1]; and (c) grey colour with normal scale.	38

2.23	Isosurface rendering of ERT tomograms by (a) Matlab, and (b) VTK.	40
2.24	Execution time of the rendering by Matlab and VTK.	40
2.25	Application of ray-tracing to two-phase flow visualisation (Manera et al. 2006).	41
2.26	The GUI for 3D realtime visualisation of ECT. (Ye et al. 2012) . .	42
2.27	Detection of gas-oil-water interface using ITS ERT-ECT systems (Qiu et al. 2007).	44
2.28	Detection of gas-oil-water interface in Sun’s approach (Sun et al. 2015).	45
2.29	Schematic diagram of fuzzy inference process.	50
2.30	Membership functions employed in Pusppanathan’s approach. (a) Z-shape function for UT, and (b) S-shape function for ECT (Pusppanathan et al. 2014).	51
2.31	Generic fusion scheme using wavelet (Pajares et al. 2004).	52
2.32	Examples of the incapability of electrical tomography to indicate small bubbles in bubbly flow by (a) LBP and (b) SCG, and sharp interface between phases in slug flow by (c) LBP and (d) SCG. . .	54
3.1	Schematic diagram of NEL multiphase flow facility (Wang et al. 2016b).	59
3.2	Target flow patterns (Wang et al. 2016b).	59
3.3	Arrangement of tomographic systems at test section line (Wang et al. 2016b).	61
3.4	A typical scheme of the data processing for dual-modality tomographic systems in multiphase flow.	62
3.5	Schematic diagram of the general framework.	64

3.6	Tomograms of a 316-pixel grid in a 20*20 square mesh and an 896-pixel grid in a 30*30 square mesh for pipeline flow (Wang et al. 2017).	65
3.7	Transformation of the original pixels (a) from 3mm*3mm pixel to 1mm*1mm pixel; and (b) from 2mm*2mm pixel to 1mm*1mm pixel.	66
3.8	A triangulated grid with 248 elements by SCG.	67
3.9	Overlapping a 248-element irregular grid with a 316-element regular grid and transforming from the old grid to the new grid.	67
3.10	Temporal alignment of two sets of tomograms by the modalities with the speed of DAS^1 and DAS^2 .	69
3.11	Temporal alignment of two sets of tomograms from $DAS^1 = 4$ and $DAS^2 = 2$ to $DAS^{lcm} = 4$ (Wang et al. 2017).	69
3.12	An example of extracting the central 4 columns of data from a 20 × 20 tomogram.	71
3.13	Data retrieval and average from a sequence of 2D cross-sectional concentration tomograms (Wang et al. 2017).	72
3.14	(a) a colour lookup table for two-phase flow, and (b) a triangular colour lookup table for three-phase flow.	75
3.15	Data flow for pixel-based thresholding fusion scheme.	78
3.16	Comparison of the fusion results with Qiu's and our approaches.	79
3.17	Visualisation result of stratified flow over 250 frames (Wang et al. 2017).	80
3.18	Visualisation result of wavy stratified flow over 500 frames (Wang et al. 2017).	80
3.19	Visualisation result of slug flow over 250 frames (Wang et al. 2017).	81
3.20	Visualisation result of plug flow over 125 frames (Wang et al. 2017).	81

3.21	Visualisation result of annular flow over 1000 frames (Wang et al. 2017).	81
3.22	Visualisation result of bubbly flow over 500 frames (Wang et al. 2017).	82
3.23	Visualisation results of different T^1 but same T^2 for the slug flow.	84
3.24	Visualisation results of the same T^1 but different T^2 for slug flow.	85
3.25	Possible phase combinations based on the concentration distributions by ERT and ECT.	88
3.26	The input membership functions for ECT (a) and ERT (b).	90
3.27	The output membership functions for (a) gas+oil and (b) oil+water.	91
3.28	Inference of given ECT (0.02) and ERT (0.25).	93
3.29	Decision tree for determining possible phases with given defuzzified values.	95
3.30	Images by high-speed video (first) and axial stacked images for stratified flow by ECT (second), ERT (third), threshold-based fusion (fourth), and fuzzy logic-based fusion (fifth).	97
3.31	Images by high-speed video (first) and axial stacked images for wavy stratified flow by ECT (second), ERT (third), threshold-based fusion (fourth), and fuzzy logic-based fusion (fifth).	98
3.32	Images by high-speed video (first) and axial stacked images for slug flow by ECT (second), ERT (third), threshold-based fusion (fourth), and fuzzy logic-based fusion (fifth).	98
3.33	Images by high-speed video (first) and axial stacked images for plug flow by ECT (second), ERT (third), threshold-based fusion (fourth), and fuzzy logic-based fusion (fifth).	99
3.34	Images by high-speed video (first) and axial stacked images for annular flow by ECT (second), ERT (third), threshold-based fusion (fourth), and fuzzy logic-based fusion (fifth).	99

3.35	Images by high-speed video (first) and axial stacked images for bubbly flow by ECT (second), ERT (third), threshold-based fusion (fourth), and fuzzy logic-based fusion (fifth).	100
3.36	Images with the same ECT threshold but different ERT thresholds by (a) conventional thresholding method; and (b) FIS-based approach.	102
3.37	Images with different ECT thresholds but same ERT threshold by (a) conventional thresholding method; and (b) FIS-based approach.	102
3.38	Visualisation results of WLR 0% for (a) stratified flow; (b) slug flow; (c) plug flow; (d) annular flow; and (e) bubbly flow.	108
3.39	Gas concentrations from different approaches at WLR 0%.	109
3.40	Visualisation results of WLR 10% for (a) slug flow; (b) plug flow; (c) annular flow; and (d) bubbly flow.	110
3.41	Gas concentrations from different approaches at WLR 10%.	110
3.42	Visualisation results of WLR 25% for (a) slug flow; (b) annular flow; and (c) bubbly flow.	112
3.43	Gas concentrations from different approaches at WLR 25%.	112
3.44	Visualisation results of WLR 50% for (a) stratified flow; (b) slug flow; (c) plug flow; (d) annular flow; and (e) bubbly flow.	114
3.45	Water and gas concentrations from different approaches at WLR 50%.	115
3.46	Visualisation results of WLR 75% for (a) stratified flow; (b) slug flow; (c) plug flow; (d) annular flow; and (e) bubbly flow.	117
3.47	Water and gas concentrations from different approaches at WLR 75%.	119
3.48	Visualisation results of WLR 90% for (a) slug flow; (b) plug flow; (c) annular flow; and (d) bubbly flow.	120

3.49	Water and gas concentrations from different approaches at WLR 90%.	121
3.50	Visualisation results of WLR 100% for (a) stratified flow; (b) slug flow; (c) plug flow; (d) annular flow; and (e) bubbly flow.	121
3.51	Gas concentrations from different approaches at WLR 100%.	123
3.52	Capability of the ERT-ECT system against WLR.	126
4.1	The pipeline of the new approach.	133
4.2	The new lookup table in 2D for bubble mapping.	136
4.3	2D stacked concentration tomograms by colour mapping and bubble mapping.	137
4.4	Opening contour by conventional Marching Cubes for a 2D concentration tomogram.	138
4.5	Closed contour by enhanced Marching Cubes for a 2D concentration tomogram.	138
4.6	Visualisation of upward gas-liquid flow in a vertical pipe by a high-speed camera, conventional colour mapping and proposed bubble mapping. (a) bubbly flow; (b) slug flow; and (c) annular flow.	141
4.7	Visualisation of a stratified flow in a horizontal pipe by a high-speed camera, conventional colour mapping, and bubble mapping.	142
4.8	Visualisation of a bubbly flow in a horizontal pipe by a high-speed camera, conventional colour mapping, and bubble mapping.	143
4.9	Visualisation of a slug flow in a horizontal pipe by a high-speed camera, conventional colour mapping, and bubble mapping.	143
4.10	Visualisation of a slug flow in a horizontal pipe by a high-speed camera, conventional colour mapping, and bubble mapping.	143

4.11	Visualisation of an annular flow in a horizontal pipe by a high-speed camera, conventional colour mapping, and bubble mapping.	144
4.12	Visualisation results by different T_l of 0.05, 0.02, and 0.08 (from top to bottom).	145
4.13	Visualisation results by different T_g of 0.4, 0.5, and 0.6 (from top to bottom).	146
4.14	Visualisation results by different IC of 4*4, 2*2, and 5*5 (from top to bottom).	146
5.1	Physical positions of cylindrical objects in a small phantom of x-axial mirror, central quadric mirror, and π -repetition.	151
5.2	Mesh structures and electrode arrangements as ASI-A, ASI-B, and ASI-C	152
5.3	SCG-generated tomograms for the first positioning of cylindrical objects in a small phantom by (a) the conventional 8-electrode ERT, (b)the conventional 16-electrode ERT , (c) ASI-A, (d) ASI-B, and (e) ASI-C	152
5.4	SCG-generated tomograms for the second positioning of cylindrical objects in a small phantom by (a) the conventional 8-electrode ERT, (b)the conventional 16-electrode ERT , (c) ASI-A, (d) ASI-B, and (e) ASI-C	153
5.5	SCG-generated tomograms for the first positioning of cylindrical objects in a small phantom by (a) the conventional 8-electrode ERT, (b)the conventional 16-electrode ERT , (c) ASI-A, (d) ASI-B, and (e) ASI-C	153
5.6	Physical position of 2 sets of sensor arrays in a vertical pipeline.	155
5.7	Two averaging strategies showing elements used to generate profiles.	155

5.8	Concentration and velocity profiles of bubbly flow by selected ASI, conventional 8 electrodes and 16 electrodes on (a) bubbly flow, and (b) slug flow.	157
5.9	Relative errors of selected ASI, conventional 8 electrodes against 16 electrodes on (a) bubbly flow, and (b) slug flow.	158
5.10	Arrangement of 316 tomogram elements by 20*20 grid.	159
5.11	Sensitivity map: (a) full sensitivity map for adjacent measurement, (b) central axial sensitivity map for adjacent measurement, and (c) sensitivity map for RILM.	160
5.12	PILM sensing strategy, (a) Rotary band, (b) Parallel band, (c) Complimentary band, and (d) Overall projections.	161
5.13	Distribution of non-conductive objects in a phantom.	163
5.14	Conventional tomogram and PILM-generated tomogram of 2 static objects in a phantom: (a) original tomogram, (b) centre-visible original tomogram, and (c) tomogram from PILM (Wang et al. 2016a).	163
5.15	Stacked images of gas-water flow: (a) from full measurement and (b) from RILM (Wang et al. 2016a).	164
5.16	Comparison of (a) concentration profiles and (b) velocity profiles.	165
6.1	Data processing procedure in a DMTS to multiphase flow.	177
A.1	Cross-sectional electrical tomograms for a stratified flow at WLR 50%. (See Figure 3.44a)	199
A.2	Cross-sectional electrical tomograms for a slug flow at WLR 50%. (See Figure 3.44b)	199
A.3	Cross-sectional electrical tomograms for a plug flow at WLR 50%. (See Figure 3.44c)	200

A.4	Cross-sectional electrical tomograms for an annular flow at WLR 50%. (See Figure 3.44d)	200
A.5	Cross-sectional electrical tomograms for a bubbly flow at WLR 50%. (See Figure 3.44e)	201
A.6	Cross-sectional electrical tomograms for a stratified flow at WLR 75%. (See Figure 3.46a)	201
A.7	Cross-sectional electrical tomograms for a slug flow at WLR 75%. (See Figure 3.46b)	202
A.8	Cross-sectional electrical tomograms for a plug flow at WLR 75%. (See Figure 3.46c)	202
A.9	Cross-sectional electrical tomograms for an annular flow at WLR 75%. (See Figure 3.46d)	203
A.10	Cross-sectional electrical tomograms for a bubbly flow at WLR 75%. (See Figure 3.46e)	203
A.11	Cross-sectional electrical tomograms for a slug flow at WLR 90%. (See Figure 3.48a)	204
A.12	Cross-sectional electrical tomograms for a plug flow at WLR 90%. (See Figure 3.48b)	204
A.13	Cross-sectional electrical tomograms for an annular flow at WLR 90%. (See Figure 3.48c)	205
A.14	Cross-sectional electrical tomograms for a bubbly flow at WLR 90%. (See Figure 3.48d)	205

List of Tables

2.1	Comparison of ERT and ECT.	16
2.2	Operating specification of ITS's ERT-ECT system.	20
3.1	Selected test conditions of liquid flowrate vs GVF.	60
3.2	Selected test conditions of liquid flowrate vs GVF.	60
3.3	Selected flow regimes with flow condition references for the evaluation of the proposed visualisation approach.	80
3.4	Phase concentration quantification results for different flow regimes (Wang et al. 2017).	83
3.5	Mean void fractions by different T^1 but same T^2 for the slug flow.	84
3.6	Mean void fractions by the same T^1 but different T^2 for slug flow.	85
3.7	Parameters for the input membership functions.	90
3.8	Fuzzy rules.	91
3.9	Parameters for the output membership functions.	92
3.10	Selected flow conditions for evaluating the proposed approach.	96
3.11	Mean concentrations of different flow regimes by a conventional threshold-based method and the proposed approach.	97
3.12	Definitions of membership functions for different threshold values.	101

3.13	Mean concentrations of each phase by different ERT thresholds for the conventional method and different definitions of ERT membership functions for the FIS-based approach.	101
3.14	Mean concentrations of each phase by different ECT thresholds for the conventional method and different definitions of ECT membership functions for the FIS-based approach.	101
3.15	All examined flow conditions at WLR 0%.	107
3.16	Selected flow conditions for visualisation at WLR 0%.	108
3.17	All examined flow conditions at WLR 10%.	109
3.18	Selected flow conditions for visualisation at WLR 10%.	109
3.19	All examined flow conditions at WLR 25%.	111
3.20	Selected flow conditions for visualisation at WLR 25%.	112
3.21	All examined flow conditions at WLR 50%.	113
3.22	Selected flow conditions for visualisation at WLR 50%.	115
3.23	All examined flow conditions at WLR 75%.	118
3.24	Selected flow conditions for visualisation at WLR 75%.	118
3.25	All examined flow conditions at WLR 90%.	119
3.26	Selected flow conditions for visualisation at WLR 90%.	120
3.27	All examined flow conditions at WLR 100%.	122
3.28	Selected flow conditions for visualisation at WLR 100%.	122
4.1	Selected conditions and corresponding IC dimensions for vertical flow.	140
4.2	Selected conditions and corresponding IC dimensions for horizontal flow.	142

5.1 Element indices used for averaging map to produce a profile. . . . 156

CHAPTER 1

INTRODUCTION

1.1 Background

Multiphase flow exists in many industrial sectors, e.g. chemical engineering, process engineering, medical engineering, and petroleum engineering. Measurement and visualisation of such phenomenon provide great insights into the physical and chemical process along with it. The flow is in the simplest case when it consists of two different components, i.e. two-phase flow, such as gas-water and oil-water. So far, a considerable amount of tomographic techniques have been investigated to measure and visualise two-phase flow, such as ERT (Wang et al. 1999), X-ray (Heindel 2011), and wire-mesh sensor (WMS) (Prasser et al. 2001) for gas-water flow, ECT (Marashdeh et al. 2008) and the capacitance wire-mesh sensor (Silva et al. 2010) for gas-oil flow. When an extra component is introduced, the flow becomes three-phase flow, e.g. gas-oil-water flow. In this case, the aforementioned tomographic systems are no longer suitable to distinguish each individual phase and, therefore, multi-modality tomographic systems, i.e. integration of multiple tomographic systems, were suggested for the measurement and visualisation of three-phase flow, such as ERT-ECT systems (Qiu et al. 2007), γ -ray and ECT systems (Hjertaker et al. 2011), dual-modality WMS (Santos et al. 2015).

Among these tomographic systems, electrical tomography devices, such as ERT and ECT, have proved to be robust, low-cost, non-intrusive, and non-invasive instruments, and been widely applied to many industries (Marashdeh et al. 2008; York et al. 2011; Wang 2015). In principle, electrical tomography differentiates phase distributions by electrical properties. For example, ERT utilises conductivity to reveal the gas phase in gas-water flow, since gas is non-conductive whereas water is conductive (Wang et al. 1999). Compared to other tomographic techniques, electrical tomography yields relatively low spatial resolution but high temporal resolution. The spatial resolution can be as low as 2% when an advanced reconstruction algorithm is applied (Wang et al. 1999), or 5% when single-step

LBP is utilised (Qiu et al. 2007), while for temporal resolution, contemporary electrical tomography is able to perform a full measurement, i.e. the amount of data for reconstructing one frame, at sub-millisecond (Wang et al. 2005; Jia et al. 2010; Cui et al. 2011), which makes the systems able to deal with industrial flow of high speed, with a reasonable margin for errors.

When multi-modality tomographic systems are engaged for multiphase flow, data processing becomes extremely challenging, since the results from different modalities represent different energy. For example, in the application of ERT-ECT for gas-oil-water flow, ERT is responsible for distinguishing gas and oil from water, whereas ECT is responsible for discriminating gas from oil and water. In addition, in order to reflect the flow dynamics under investigation, spatial and temporal information from both modalities also needs to be taken into account. As a result, multi-dimensional data fusion is required to differentiate each phase, and therefore achieve the objectives of three-phase flow characterisation (Hoyle et al. 2012). Moreover, the recent development and specific commonality of multi-modality tomographic imaging may provide an opportunity to develop a data analysis and visualisation platform, which can receive tomograms from multi-modality systems. After the data process with embedded data analysis and visualisation tools, the platform will output relevant process quantities and/or process images.

Visualisation and data fusion would play key roles in the platform. Visualisation of multiphase flow is used to display the spatial distribution of each phase, according to the derived concentration distribution of each phase by tomographic systems. With the advancement of modern visualisation techniques in computer science, more and more advanced techniques have been suggested, a few of which have been applied to the visualisation of multiphase flow. The simplest yet most widely applied visualisation method is colour mapping, i.e. converting scalar values to different colours according to a pre-defined look-up table, in which each value in the scalar field corresponds to an exclusive colour. Due to the relatively low spatial resolution of electrical tomography, the generated concentration distribution is incapable of reflecting sufficient information of investigated multiphase flow, such as size and distribution of small bubbles, when the colour mapping is utilised.

1.2 Aim and Objectives of the Research

The ultimate aim of this study is to develop an integrated platform for the quantification and qualification of multiphase flow using electrical tomography. In order to achieve the aim, there are two steps to be followed. The first step is to investigate the methods of data analysis, fusion, and visualisation, as principal components in the platform. The second step is to integrate the techniques into a platform, by which tomographic data input into the platform is analysed and visualised as the primary output of the platform, assisted by other parametrised conditions. This study will focus on the first step, which includes the following objectives need to be addressed in detail:

- To propose and implement novel approaches for electrical resistivity and capacitance tomography (ERT-ECT) systems to visualise gas-oil-water horizontal flow by multi-dimensional data fusion;
- To evaluate the performance of dual-modality ERT-ECT for imaging gas-oil-water flow;
- To develop a novel approach for three-dimensional visualisation of gas-liquid flow; and
- To improve the spatial and temporal resolution of conventional electrical resistivity tomography (ERT) with minimal or no modification of the hardware.

1.3 Organization of the Thesis

The thesis is organised as follows:

CHAPTER 1 The context of the research is briefly reviewed. Later, the objectives of the research are presented, and the originality of the study is listed.

CHAPTER 2 The context of the research is expanded in this chapter. The fundamental knowledge regarding electrical tomography and multiphase flow characteristics is reviewed firstly. Following this, existing approaches for visualising gas-liquid flow and gas-oil-water flow are reviewed in detail. The limitations of existing approaches are discussed and thus potential solutions are proposed.

CHAPTER 3 The engagement of multi-modality electrical tomographic systems in the domain of gas-oil-water three-phase flow characterisation increases the complexity in terms of data processing and visualisation, due to the relatively low spatial resolution of electrical tomograms and the data in multiple dimensions. In this chapter, systematic studies are carried out for dual-modality electrical tomography to visualise multiphase flow. In particular, a general framework for general data processing is explored. Based on the framework, two different proposals, i.e. threshold and fuzzy logic, are examined, and further evaluated on gas-oil-water flow in a horizontal pipeline layout.

CHAPTER 4 The drawbacks associated with the visualisation of gas-liquid flow by electrical tomography and conventional colour mapping are addressed. A novel approach, therefore, is investigated to overcome the problems, which is evaluated on gas-water flow in both horizontal and vertical pipelines by ERT.

CHAPTER 5 In order to combine the benefits of conventional 8- and 16-electrode ERT systems, i.e. high temporal resolution of an 8-electrode configuration and high spatial resolution of the 16-electrode configuration, with minimal or even without modification of the existing hardware, two novel approaches, called Asymmetrical Sensing and Imaging (ASI) and Regional Imaging with Limited Measurement (RILM), are proposed. The results are presented by experiments, while advantages and disadvantages are discussed.

CHAPTER 6 All the research is summarised and relevant conclusions are drawn in the final chapter. Finally, future work is suggested.

CHAPTER 2

LITERATURE REVIEW

Highlights: This chapter commences with the fundamentals of multiphase flow and electrical tomography. It then presents an in-depth review of the state of the art of multiphase flow characterisation by electrical tomography, particularly quantification and qualification of gas-liquid flow and gas-oil-water flow by ERT and/or ECT. Finally, motivations are raised in accordance with the research context.

2.1 Fundamentals

2.1.1 Multiphase flow

Multiphase flow refers to any fluid flow comprising two or more phases/components, which is extremely complex to understand, model, and measure (Corneliussen et al. 2005; Brennen 2005). However, it is so popular that it can be found in many industrial sectors, such as chemical engineering, processing engineering, and petroleum engineering, to name a few. Therefore, comprehensive insights into such phenomenon are in great demand for scientific and engineering research. In this study, gas-liquid and gas-oil-water flow are of particular interest.

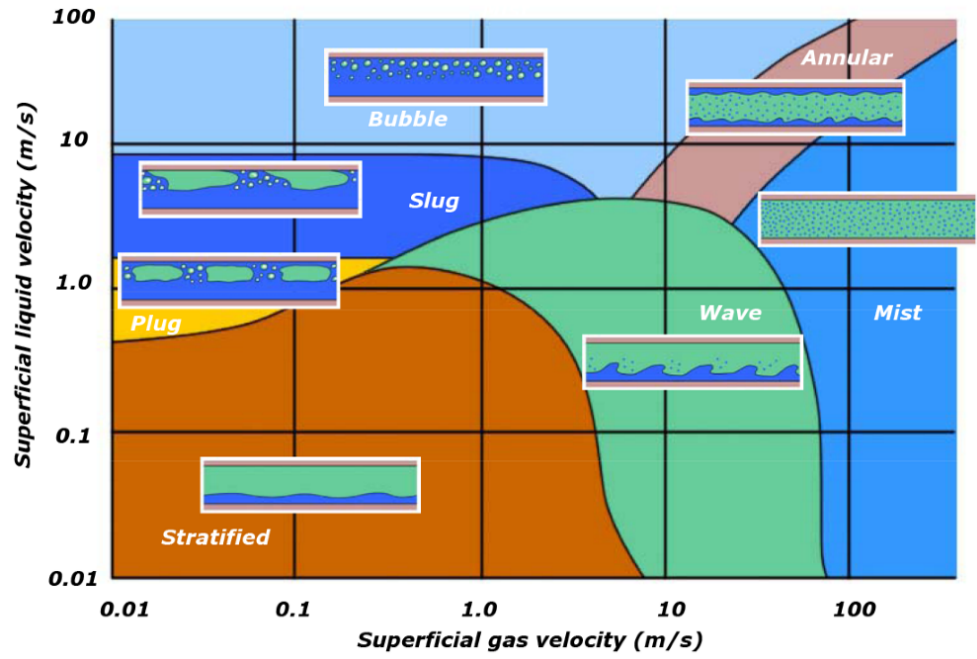
Many challenges exist from the understanding of complex flow behaviour in their transportation and production stages, among which flow pattern/regime is one of the critical features since many other parameters are dependent of it, e.g. pipe design, and hence it has attracted much attention from scientists and engineers (Corneliussen et al. 2005; Brennen 2005; Manera et al. 2006; Ramskill et al. 2011; Thorn et al. 2012; Kee 2014). Flow patterns/regimes are characterised by the geometrical distribution of each phase in a multiphase flow (Brennen 2005). Due to the complexity of the interaction between phases involved, as well as the impact of physical and fluid properties, such as channel inclination, surface tension, an

infinite number of flow structures could be inspected in a given channel. Fortunately, when a fully developed flow is in a steady state, i.e. the flow with certain superficial velocity of each phase, flow structures can be simply categorised into a few different forms reliant on pipe orientation. In this case, flow regimes can be estimated with the velocities of individual phases and therefore it can be characterised using a flow regime map. Figure 2.1 shows examples of flow regime maps for the flow in horizontal and vertical pipelines¹, which clearly demonstrates the difference between the two maps in terms of flow regimes.

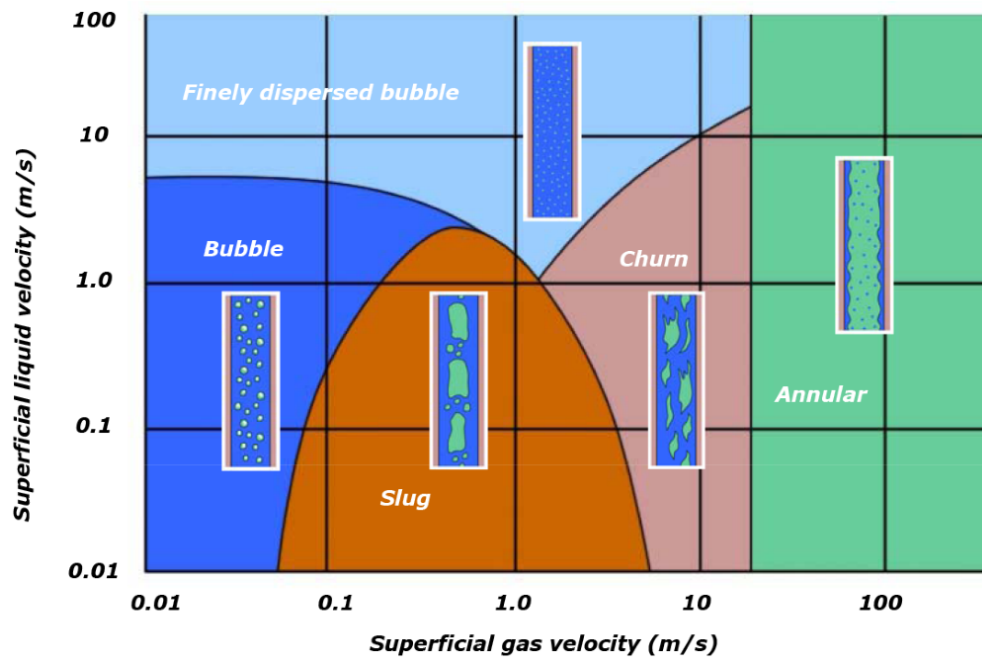
In the horizontal pipeline, there are 7 commonly-observed flow regimes according to the map in Figure 2.1a, but in this study, mist flow is excluded since it is beyond the scope of this research. Consequently, the other 6 flow regimes will be briefly discussed here, as presented in Figure 2.2, in which the green represents gas and the light blue represents liquid. The 6 commonly-investigated horizontal flow patterns include:

- **Stratified flow:** when gas and liquid velocities are low, the two phases are completely separated with a stable horizontal interface, and the liquid goes to the bottom of the pipe and gas to the top (Figure 2.2a).
- **Wavy stratified flow:** with the increase of mixture flowrate, instabilities appear on the gas-liquid interface due to the interfacial velocity differential (Wikipedia 2015). This is called wavy stratified flow and is characterised by the formation of small interfacial waves, as depicted in Figure 2.2b.
- **Slug flow:** at low liquid velocity and high gas velocity, some gas phase is trapped in the interfacial waves, and the interface becomes very unstable, which finally reaches the top wall of the pipe, resulting in a non-continuous gas phase. This is known as slug flow (Figure 2.2d). Slug length can vary depending on the velocity of the head and tail velocities of the slug. When the velocities are identical, a stable slug is established (Issa et al. 2003). Gas velocity plays an important role in slug length and frequency, but at stable state the frequency and the length becomes stable (Ahmed 2011).
- **Plug flow:** at lower gas velocity and relatively high liquid velocity, the separated gas phase is deformed into large bubbles with a diameter smaller than the pipe diameter, located at the top of the pipe wall, and a thin film

¹The term *liquid* can be either water, or oil, or a mixture of water and oil.



(a)



(b)

Figure 2.1: Norwegian generic flow regime map (Corneliussen et al. 2005) for (a) horizontal pipeline flow, and (b) vertical pipeline flow.

of liquid usually exists between the bubbles and the wall, which is called plug flow (Figure 2.2c). Plug flow is characterised by elongated bubbles,

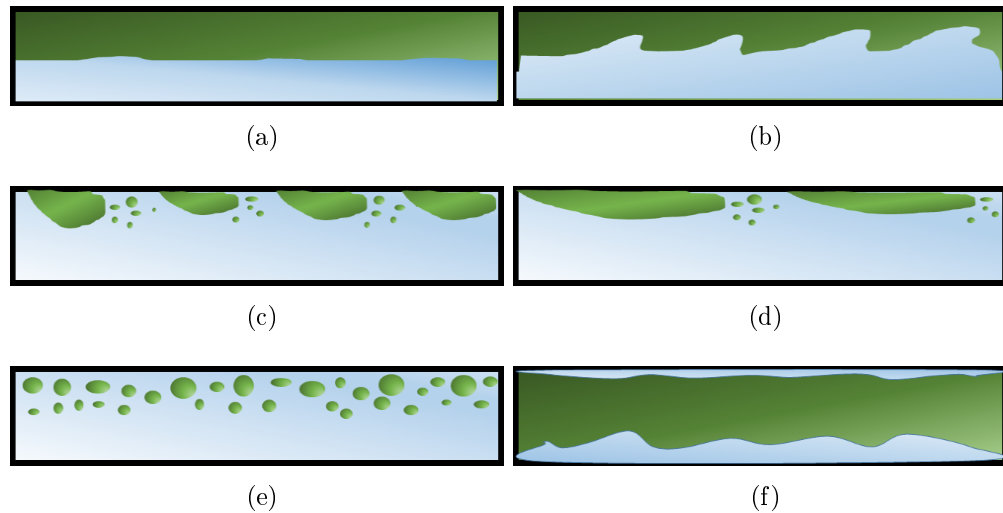


Figure 2.2: 6 typical flow regimes of gas-liquid flow in a horizontal pipeline, where the green is gas phase and the light blue is liquid phase. (a) stratified flow; (b) wavy stratified flow; (c) plug flow; (d) slug flow; (e) bubbly flow; and (f) annular flow.

which may be surrounded by smaller bubbles. High-frequency slug and plug flow is similar in terms of elongated bubbles, thereby being difficult to distinguish. The literature suggested using the criterion of whether a large bubble is enclosed by small bubbles (Kolev 2007; Y et al. 2010).

- **Bubbly flow:** when the gas flow is laminar, small bubbles are driven by buoyancy forces and flow primarily in the top half of the tube, known as bubble flow. As the Reynolds number of the gas increases while keeping other variables constant, the bubble size decreases and the bubbles begin to disperse across the entire tube cross section. This flow pattern is known as dispersed bubble flow. In general, due to the gravitational force, the closer the bubbles are to the bottom of the pipe, the smaller their diameters, as shown in Figure 2.2e.
- **Annular flow:** when gas flowrate is high enough, the gas phase becomes continuous at the centre of the pipe, pushing up the liquid phase around the pipe wall. The gas phase is now fully enclosed by the liquid phase and annular flow is established, depicted in Figure 2.2f. Due to gravity, the thickness of the liquid film in the horizontal pipe is inhomogeneous, i.e. the film becomes much thicker the closer it is to the bottom of the pipe, and

the top film is dependent on gas velocity (Y et al. 2010). In this flow, small droplets may entrain into the gas core.

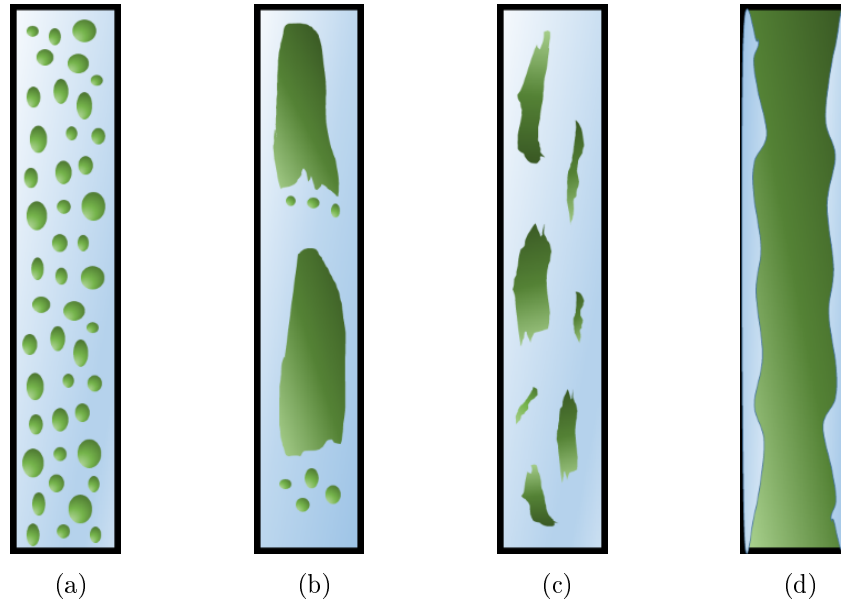


Figure 2.3: 4 typical flow regimes of gas-liquid upward flow in vertical pipeline, where the green is gas phase and the light blue is liquid phase. (a) bubbly flow; (b) slug flow; (c) churn flow; and (d) annular flow.

On the other hand, common flow regimes in vertical pipelines are different from the ones in horizontal pipelines, provided the flow conditions are the same, e.g. gas volume fractions, as depicted in Figure 2.1b. There are typically 4 flow regimes in vertical pipeline, namely bubbly, slug, churn, and annular flow, as depicted in Figure 2.3.

- **Bubbly flow:** when the gas phase is at low velocity it is introduced into the liquid, gas is distributed as small individual bubbles, as depicted in Figure 2.3a. When bubbles are very small, they are spherical and rise vertically. When beyond a certain size, e.g. 1.5mm, they start to deform and randomly move upwards in a zig-zag style, during which collision and coalescence occurs randomly. The interactions between bubbles result in a number of relatively large bubbles with a spherical cap.
- **Slug flow:** at a moderate flowrate of gas phase, bubbles collide and coalesce more frequently, which ultimately leads to bubbles with a large bullet-shaped gas pocket, and slug flow is established (Figure 2.3b). A Taylor

bubble is characterised by a spherical cap, a body surrounded by thin liquid film that moves downwards along the pipe wall, and eventually a tail followed by small bubbles (Anglart et al. 2002). It is reported that Taylor bubbles are generally symmetrical but will become asymmetrical when downward velocity of liquid is beyond some critical value (Fabre et al. 2014). In this flow, the liquid phase is continuous.

- **Churn flow:** as the gas flow rate is increased, Taylor bubbles are twisted and collapsed to form a highly disordered oscillation region, and churn flow appears as in Figure 2.3c. This flow pattern is a highly disturbed flow of gas and liquid, characterized by the presence of a very thick and unstable liquid film, with the liquid often oscillating up and down in an irregular manner. Churn flow used to be considered as a transition pattern due to its complex behaviour preventing it from being well defined, but Jayanti *et al.* proposed that it starts from the reverse movement of a thin liquid film (Jayanti et al. 1992).
- **Annular flow:** at very high gas velocities, an annular pattern is observed whereby the majority of the liquid flows along the pipe, which may contain some liquid droplets entrained in the gas flow as in Figure 2.3d. In the gas–liquid interface, especially for sufficiently high gas velocity, there may be large amplitude waves that break up during the flow process. The breakup of these waves is the continuous source of the deposition of droplets in the gas core.

In general, studies of multiphase flow can be classified into two categories: numerical analysis and experimental investigations. Numerical analysis focuses on using mathematical approaches to interpret physical problems, so that they can predict and model specific behaviour in multiphase flow (Brennen 2005; Prosperetti et al. 2009; Tryggvason et al. 2011; Banerjee 2013), which usually follows certain physical phenomena, such as conservation of mass, momentum, and/or energy. In contrast, experimental studies exploit complementary facilities to reveal multiphase flow.

The most straightforward experimental facility to inspect multiphase flow is high-speed cameras through a transparent observation chamber, but its applicability is highly dependent on the availability of experimental conditions, which is usually

unachievable in industrial situations. In addition, the opacity of observed flow also influences its capability. Previous research has reported the unsuitability of such optical methods for gas-liquid flow with gas concentrations over 10% (Prasser et al. 2001). Among other experimental approaches, tomography is a group of techniques which has aroused tremendous enthusiasm and interest. It usually functions in a non-intrusive/invasive manner to provide 2-D cross-section, 3-D, even 4-D reconstructed images to reveal informative contents of the flow under investigation, such as electromagnetic, radioactive, ultrasound, to name a few (Wang et al. 1999; Corneliussen et al. 2005; Soleimani et al. 2009; Heindel 2011; York et al. 2011; Wang 2015). A particular category of tomographic techniques is using electrical properties to reveal phase distribution, which is classified by the properties, e.g. electrical resistance tomography (ERT) or electrical capacitance tomography (ECT). In this research, these two types of electrical tomography are used through the entire research on the quantification and qualification of multiphase flow, and hence their sensing principles are reviewed in the next section.

2.1.2 Electrical tomography

Electrical tomography is a set of techniques that utilizes electromagnetic principles to sense the electrical property distribution within the sensors. Different tomography methods have different sensitive properties, depending on the operational principles. For example, ERT utilizes the variation of conduction current to detect process variation, hence the measurements are mainly dominated by electrical conductivity changes within the sensor. In contrast, ECT utilizes the variation of displacement current to sense the process variation. Its measurements are mainly affected by the electrical permittivity variation in the sensor. ERT and ECT have the same mathematical representation although they are physically different. Therefore, only ERT is discussed here, and comparisons between ERT and ECT are addressed later.

ERT provides the capability of revealing the conductivity distribution of a region of interest, e.g. a pipe, and consists of three logical parts: sensors, data acquisition system, and image reconstruction. Sensors are a number of evenly-mounted electrodes around a pipe where voltage/current is driven from a pair of electrodes and current is measured from another pair of electrodes. It is necessary

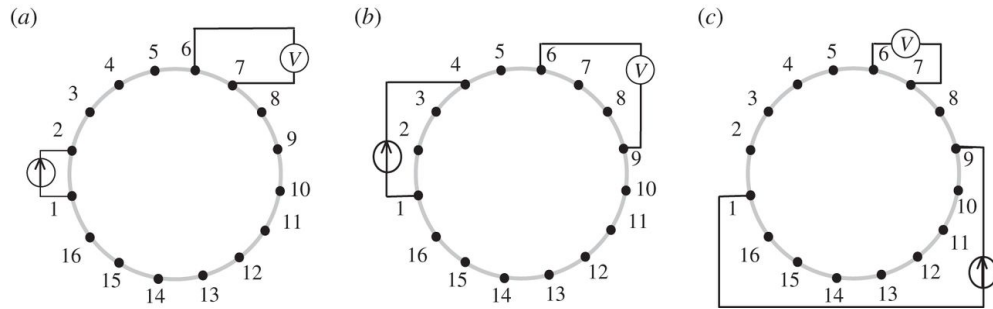


Figure 2.4: Three different sensing strategies. (a) adjacent sensing strategy, (b) $PI/2$ sensing strategy, and (c) opposite sensing strategy. (Wang et al. 2016a).

that ERT sensors need to have a direct contact with the material to be measured. A number of different sensing strategies have been reported based on the excitation/measurement differences. Figure 2.4. depicts three common sensing strategies, namely adjacent (Brown et al. 1985), $PI/2$ (Wang et al. 2002), and opposite sensing strategy (Hua 1987). A Data Acquisition System (DAS) is used to control the excitation/measurement sequence, de-modulation, and A/D conversion, etc. Image reconstruction processes the acquired values, e.g. impedance, to derive conductivity distribution.

The distribution electrical potential within a medium of ERT is governed by Poisson's equation:

$$\nabla \cdot (\sigma \nabla \phi) = 0 \quad (2.1)$$

where σ is the conductivity of the electrical property in ERT and ϕ is the electric potential. Since there is no analytical solution for conductivity, an inverse problem has to be considered. The forward problem is to predict boundary measurements given a known conductivity distribution. The inverse problem concerns the conductivity distribution from voltage measurements, which can be approximately described as a linear equation (Wang et al. 2016a):

$$\sigma = \mathbf{S}^{-1} \cdot \mathbf{U} \quad (2.2)$$

where \mathbf{U} is the known voltage measurements and \mathbf{S} is the so-called sensitivity matrix. The purpose of the image reconstruction is to derive the conductivity distribution σ . Unfortunately, Equation 2.2 is notorious for its non-linearity and ill-posedness, and existing solutions always seek the minimisation of the equation:

$$f(x) = \frac{1}{2} \|\mathbf{U} - \mathbf{S}\sigma\|^2 \quad (2.3)$$

Many approaches were proposed to solve Equation 2.3, including single-step back-projection algorithms and multi-step iterative algorithms. In this study, sensitivity coefficient back-projection method (SBP) (Kotre 1994) and modified SBP (MSBP) (Wang 2002) were applied as a single-step image reconstruction algorithm due to its computational simplicity, and multi-step iterative algorithm, sensitivity theorem based conjugate gradient method (SCG) (Wang 2002) is also used for the reconstructed images with better spatial resolution.

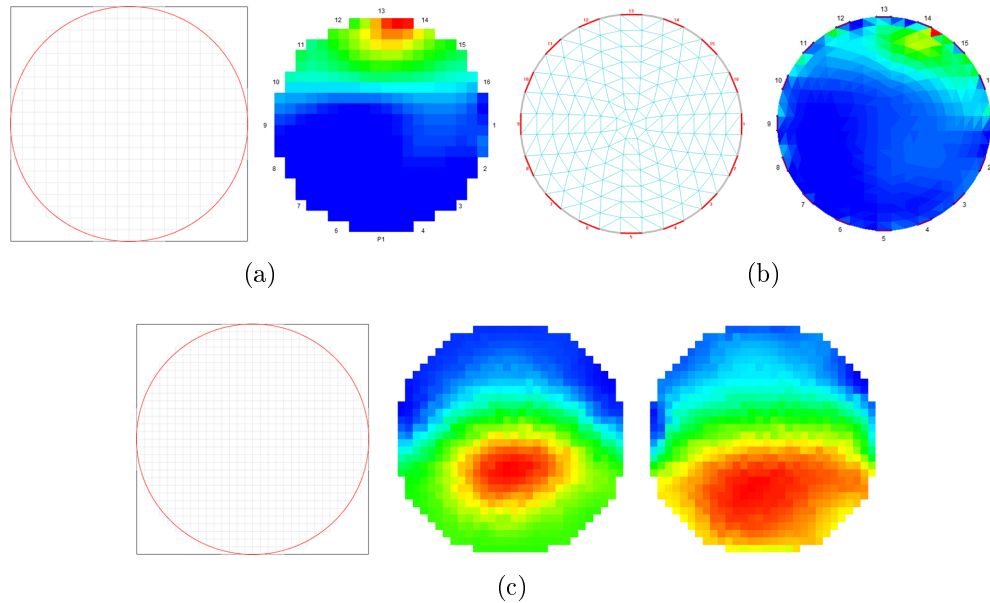


Figure 2.5: Reconstructed ERT images by (a) SBP on a regular 20×20 mesh, and (b) SCG on an irregular 248-element mesh, and ECT images (c) by LBP and Landweber on a 32×32 regular mesh.

Figure 2.5 depicts examples of image reconstruction results, in which Figure 2.5a is reconstructed using SBP on a 20×20 regular mesh, whereas Figure 2.5b is derived from an SCG algorithm on an irregular 248-element mesh, and Figure 2.5c is obtained by single-step LBP and iterative Landweber on a 32×32 regular mesh using ITS Reconstruction Toolsuite (Wei et al. 2015).

Due to the inhomogeneity of the electromagnetic field, sensitivity distribution of ERT is inhomogeneous despite the sensing strategy. Figure 2.6 demonstrates that in both cases, the sensitivity is higher when close to the boundary area than that in the central area. In other words, objects in the central area are more difficult to image than those in the boundary area. In addition, the number of independent

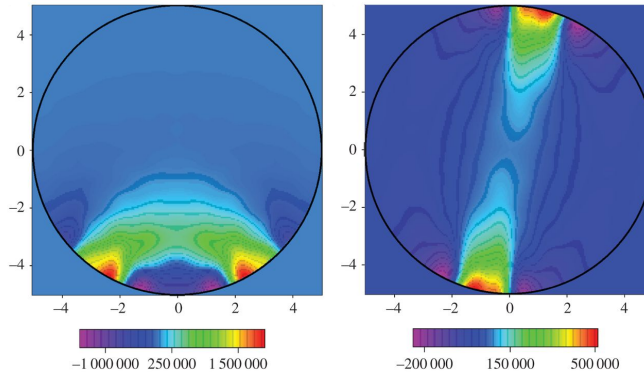


Figure 2.6: Sensitivity distribution of (a) adjacent and (b) opposite sensing strategies (Wang et al. 2016a).

measurements obtained by ERT, e.g. 104 independent measurements by a 16-electrode configuration is significantly less than the number of unknowns, e.g. 316 elements in Figure 2.5a to be solved in the inverse problem. The inhomogeneous sensitivity distribution and non-linear inverse problem result in the complex image reconstruction in ERT.

On the other hand, the quality of ERT tomograms is a prominent factor to evaluate the performance of ERT. Usually two measures can be used to represent the qualitative information of ERT imaging: the *spatial resolution* and the *conductivity resolution*. The spatial resolution refers to *the smallest pixel in which the conductivity can be independently determined*, and the conductivity resolution reflects *the smallest range into which the conductivity of a pixel can be isolated* (Seagar et al. 1987). Let r_a and σ_a be the radius and the conductivity of the smallest range, and r_b and σ_b be the radius and the conductivity of the whole imaged range, the spatial and conductivity resolution can be quantified by Equation 2.4 and Equation 2.5 respectively. Another important aspect that describes the capability of impedance imaging is the *distinguishability* with reference to the shortest distance between two objects that can be individually isolated (Wang et al. 1999).

$$\text{Spatial Resolution} = \frac{r_a}{r_b} \quad (2.4)$$

$$\text{Conductivity Resolution} = \frac{d\alpha}{\alpha} \quad \text{where} \quad \alpha = \frac{\sigma_a}{\sigma_b} \quad (2.5)$$

The inhomogeneous distribution of electromagnetic field in ERT has severely affected the quality of ERT tomograms, resulting in several limitations when vi-

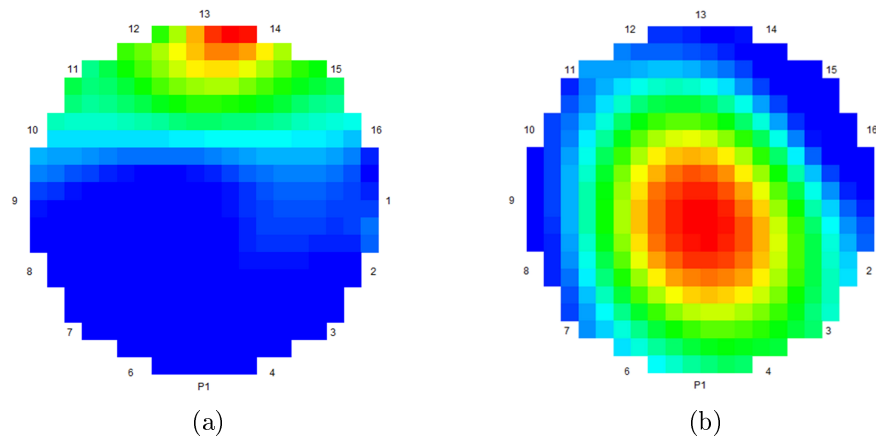


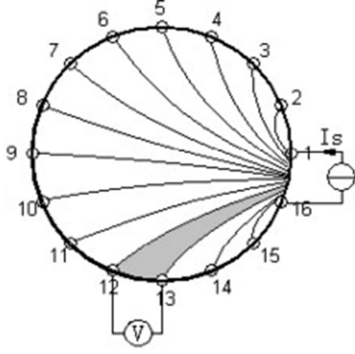
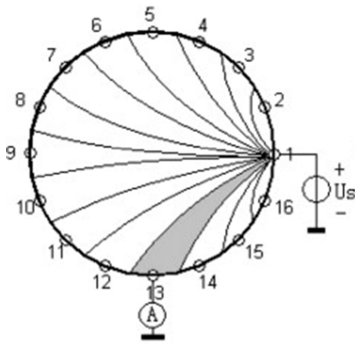
Figure 2.7: The incapability of ERT tomograms to identify (a) small bubbles in a horizontal bubbly flow, and (b) large bubble in a vertical slug flow.

visualising multiphase flow. It was reported that for an ERT with a 16-electrode configuration and adjacent sensing strategy, the spatial resolution is 5%, the conductivity resolution is 10%, and distinguishability is 20% (Wang et al. 1999). This indicates that for multiphase flow in a pipe with 100 mm diameter, bubbles with size below 5 mm are unidentifiable, and bubbles that have more than 20 mm geometrical interval are not isolatable. In addition, due to the non-linearity of image reconstruction, zero conductivity in sensing domain is impossible to reconstruct, which leads to continuous conductivity distribution of sudden conductivity change in tomograms, e.g. boundaries between bubbles and water are not sharp. Figure 2.7 demonstrates the incapability of ERT tomograms to separate small bubbles in a horizontal bubbly flow (Figure 2.7a) and identify large bubbles with sharp edges in a horizontal slug flow (Figure 2.7b), where an ERT was configured with 16 electrodes and an adjacent sensing strategy.

ERT and ECT are very similar in many aspects, such as the governing equation and image reconstruction, and so on. One exception is that ERT electrodes need to have a direct contact with the material to be measured, whereas ECT sensors do not require it, which are normally outside a non-conductive container. Therefore, ECT is known for its non-invasive and non-intrusive features. In contrast, ERT is invasive but non-intrusive. Table 2.1 lists the comparison between ERT and ECT from a few aspects.

For a cross-sectional conductivity tomogram, it can be converted to a cross-

Table 2.1: Comparison of ERT and ECT.

	ERT	ECT
Governing equation	$\nabla \cdot (\sigma \cdot \nabla \phi) = 0$ σ is conductivity	$\nabla \cdot (\epsilon \cdot \nabla \phi) = 0$ ϵ is permittivity
Inverse problem	$\sigma = \mathbf{S}^{-1} \cdot \mathbf{U}$	$\epsilon = \mathbf{S}^{-1} \cdot \mathbf{U}$
Inverse solutions	Single-step back-projections and iterative multi-step algorithms	
Example of sensing strategy		
Measurand	Resistance (impedance)	Capacitance

sectional concentration tomogram using Maxwell's equation (Maxwell 1982), as shown below:

$$\alpha = \frac{2\sigma_1 + \sigma_2 - 2\sigma_{mc} - \frac{\sigma_{mc}\sigma_2}{\sigma_1}}{\sigma_{mc} - \frac{\sigma_2}{\sigma_1}\sigma_{mc} + 2(\sigma_1 - \sigma_2)} \quad (2.6)$$

where α is the volume fraction of the dispersed component, σ_1 is the conductivity of the continuous component, σ_2 is the conductivity of the dispersed component, and σ_{mc} is the reconstructed conductivity. The unit of σ is mS/cm. When the conductivity of the dispersed component $\sigma_2 = 0$, Equation 2.6 becomes:

$$\alpha = \frac{2\sigma_1 - 2\sigma_{mc}}{\sigma_{mc} + 2\sigma_1} \quad (2.7)$$

The simplified Maxwell equation is commonly used in the calculation of concentration distribution for multiphase flow when the dispersed phase is non-conductive, e.g. gas concentration in gas-liquid flow.

In the domain of velocity extraction for multiphase flow by tomographic systems, the cross-correlation method is the predominant one introduced by Beck (Beck et al. 1987), which was originally designed for revealing the similarity between two

functions. Essentially, given two sets of cross-sectional concentration tomograms from two different planes of ERT sensors, the method is to evaluate whether the tomograms from both sets are cross-correlated with each other. Since the cross-correlation method is based on the statistical computation of the differences between two functions, the velocity derived is also named as structural velocity in order to distinguish the difference from real flow velocity. The least squares (LS) can be applied as the cross-correlation criterion, as proposed in (Wu et al. 2005), and the governing equation is:

$$\epsilon_k^2(n) = \sum_{m=1}^N [x_k(m) - y_k(m-n)]^2 \quad (2.8)$$

where N is sample length, n is the sample offset number and k is the number which indicates different pixels on the cross-section.

The quantification of cross-correlation was revised by Equation 2.9, where the 2^{nd} order terms of f_1 and f_2 were removed due to their contribution to R_{12} can be ignored:

$$R_{12}(n) = \sum_{m=n+1}^N f_1(m-n)f_2(m) \quad n = 0, 1, \dots, (N-1) \quad (2.9)$$

where N is the sample length, and $f_i(m)$ is the m th tomograms from i th planes of sensors. Equation 2.9 is the general form of cross-correlation method for process tomography to seek for the correlation (Lucas et al. 1999; Bolton et al. 2004; Dong et al. 2005; Wu et al. 2005; Li et al. 2005; Wang et al. 2015). The major difference between Equation 2.8 and Equation 2.9 is at the reduction of computation time.

Equation 2.9 is further adapted in (Ma et al. 2003) to become suitable for online calculation by updating $R_{12}(n)$ with the new k th tomograms, given by Equation 2.10:

$$R_{12}^{(k)}(n) = R_{12}^{(k-1)} + f_1(k-n)f_2(k) \quad n = 0, 1, \dots, (N-1) \quad (2.10)$$

where superscript (k) indicates that the related value is the k th sample.

The aforementioned cross-correlation methods were designed for the flows only axial velocity under the consideration, which applied the correlation between corresponding pixels, i.e. same pixel of different tomograms. In other words, dispersed phase, e.g. gas bubbles move in parallel to the pipeline. This, unfortunately, is not always true in reality, since the dispersed phase always floats in

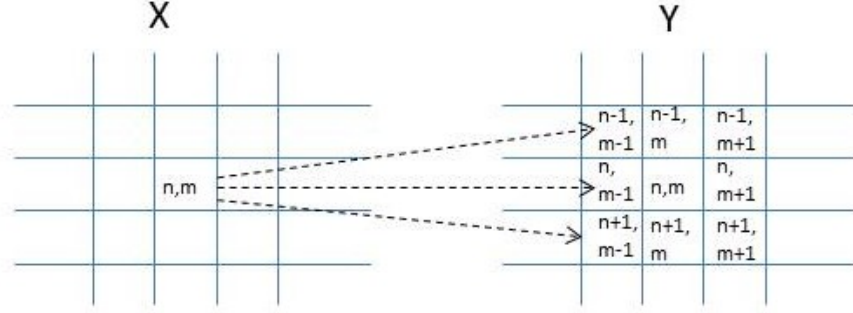


Figure 2.8: The fundamental idea of best correlation between pixel $X_{(n,m)}$ and the neighbouring pixels of $Y_{(n,m)}$ (Mosorov et al. 2002).

three dimensions. Consequently, the best-correlation was proposed by Mosorov (Mosorov et al. 2002), which not only correlates corresponding pixels, but also the neighbouring pixels around the corresponding pixel. The basic idea of best-correlation is depicted in Figure 2.8. Accordingly, Equation 2.9 is adjusted to Equation 2.11:

$$R_{X_{[n,m]}Y_{[n-i,m-j]}}[p] = \sum_{k=0}^{T-1} V_{X_{[n,m]}}[k]V_{Y_{[n-i,m-j]}}[k+p] \quad (i, j) \in B \quad (2.11)$$

where (n, m) are the coordinates of the pixel, V_X, V_Y are the values of the pixel (n, m) on planes X and Y , and B is the neighbourhood of the pixel (n, m) on plane Y , $B \subset Y$. The criterion for choosing the best-correlated pair of pixels $(n - i, m - j)$ is defined by the condition that:

$$\max_{(i,j) \in B} \{R_{X_{[n,m]}Y_{[n-i,m-j]}}\} \quad (2.12)$$

By experimenting for the best-correlation method, the authors concluded that the chosen pixel was best correlated with a non-corresponding pixel in about 17% of cases. Moreover, the average value of the maximum correlation function, calculated by Equation 2.12, for the best-correlated pixels was around 5% higher than the value calculated by the cross-correlation method. Accordingly, there was a significant difference between the time offset converted by cross-correlation and best-correlation, of which the maximum values of transit time of each correlation were 45 and 65 milliseconds, respectively, and in consequence the gap of calculated velocity between the two methods was significant too.

With the concentration distribution α and the cross-correlated velocity v , the flow rate Q^i of individual phase i can be derived by integrating the product of

the local concentration α^i and pixel velocity v^i :

$$Q^i = \int_A \alpha^i v^i dA \quad (2.13)$$

where A is the cross-sectional area.

When characterising gas-liquid flow by ERT, spatial and temporal resolutions of the system are of great importance for the characterisation accuracy of the flow. Spatial resolution of an ERT is the ratio of the size of minimal identifiable objects to a vessel containing the object (Wang 1999), and hence reveals the sensing capability of an ERT, which further determines concentration distribution of the gas phase. Temporal resolution reflects the sensing speed of an ERT, which is critical to derive the velocity of gas phase.

The accuracy of velocity measurement by ERT using the cross-correlation method is determined by discrimination error κ (Beck et al. 1987), which is expressed as:

$$\kappa = \frac{\delta}{2\tau} \quad (2.14)$$

where δ is the flow velocity, and τ is the time required for a flow passing the dual-plane sensor. For instance, if the distance between the two sensing planes of a dual-plane sensor is 0.05 m and flow velocity is 10 m/s, τ is 0.005 s. For a discriminatory precision of 5%, i.e. $\delta = 0.0005$ s, a speed of 2000 dual-frames per second is required. Consequently, ERT with higher DAS is required to achieve higher accuracy.

On the other hand, an important characteristic of steady-state multiphase flow is that its tomograms are symmetrical to the diameter of the pipeline in vertical flow, or the vertical diameter of the pipeline in horizontal flow. Since it is assumed that all multiphase flow under investigation is fully developed to reach a steady state, it is possible and reasonable to estimate a whole tomogram on the basis of special part of the original tomogram, e.g. obtain half of the original tomogram and mirroring/mapping to accomplish the whole tomogram. Alternatively, a central area along diameter of a tomogram can be utilised to approximate the whole one, when presenting concentration and velocity profiles.

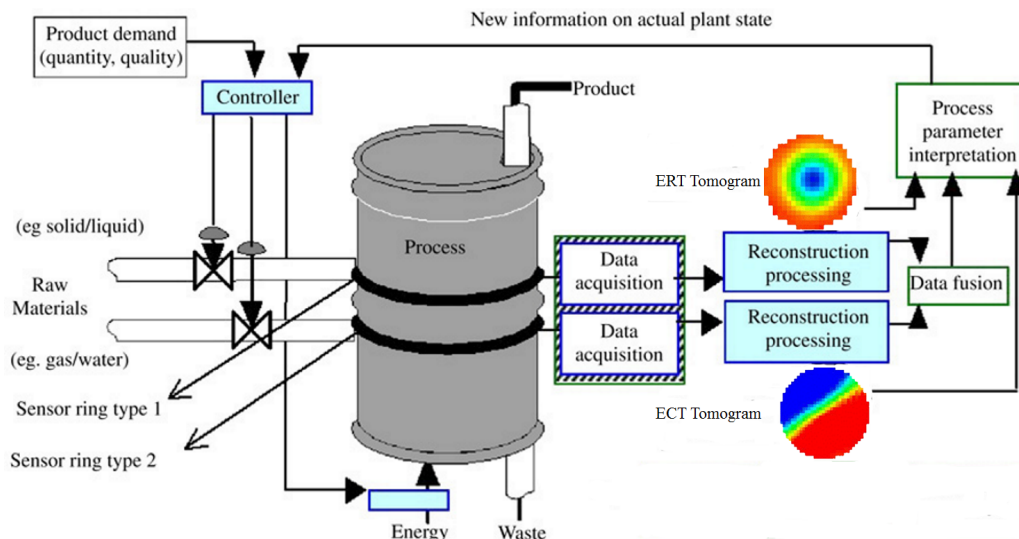


Figure 2.9: A typical industrial application of dual-modality electrical tomography (Qiu et al. 2007).

Table 2.2: Operating specification of ITS's ERT-ECT system.

	V5R	M3C
Sensor configuration	2 planes of 16 electrodes	1 plane of 12 electrodes
Sensing strategy	Voltage-driven adjacent	Voltage-driven sequential
Injection frequency	0.01 MHz	1 MHz
Reconstruction	Linear back projection (LBP)	Linear back projection (LBP)
Property of interest	Electrical conductivity	Electrical permittivity
Max acquisition speed	16 ms/Frame	100 ms/Frame
Image spatial resolution	5%	5%
Admittance sensitivity	1% ($5\mu\text{S}/\text{cm}$ in $500\mu\text{S}/\text{cm}$ water)	1% ($8.85\text{e-}14$ F/m in air)
Electrode dimensions	10 mm (w) \times 20 mm (l)	22 mm (w) \times 100 mm (l)

2.1.3 Dual-modality ERT-ECT systems

As mentioned earlier, because ERT and ECT have distinct sensing properties, they are often proposed to monitor multiphase processes as a dual-modality system. Figure 2.9 shows a typical concept of using an ERT-ECT system to monitor and control a multi-phase flow process (Qiu et al. 2007). By combining both images via an interpolation process, the composition of each phase within the sensor can be calculated. Figure 2.10 illustrates the set-up of the dual modality system

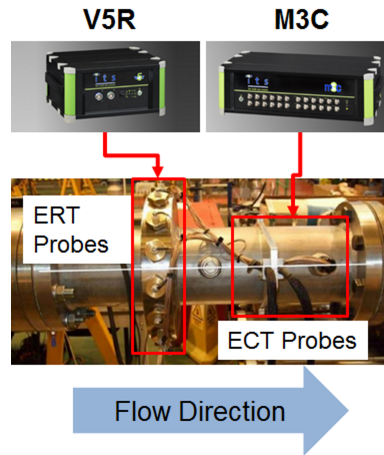


Figure 2.10: ERT-ECT systems and integrated sensors used in the experiment.

for visualization of gas-oil-water three phase flows and Table 2.2 lists the major specification of the ERT-ECT systems.

The ERT and ECT systems are used to measure the relative change instead of the absolute value of the electrical property distribution. Then, the phase concentration information in reconstructed tomograms is derived with effective medium approximations equations such as Maxwell Garnett theory (Levy et al. 1997), which reflect the non-linear behaviour of the mixtures electric property to phase concentration. For the three-phase flow under the investigation, a large permittivity difference between gas and oil/water or large conductivity difference between water and gas/oil exist. Therefore, the ECT permittivity image is reconstructed to report gas in liquid and ERT conductivity image to report gas and oil in water. With the sum of phase volume fractions equal to 1, the oil phase distribution can be derived approximately.

2.2 Multiphase flow visualisation

Multiphase flow exists in many industries. In gas-oil production, extraction and transportation of the production is a multiphase flow, consisting of time-varying ratios of gas, oil, and water. In chemical reaction engineering, *“the heart of chemical transformations in all process and energy industries is multiphase reactor technology, as over 99% of reactor systems require the presence of more than one phase for proper operation.”* (Dudukovic 2007). This has necessitated the

qualification and quantification of multiphase flow, where multiphase flow visualisation is a prominent approach for comprehensive understanding of the flow, both qualitatively and quantitatively.

Conventional multiphase flow visualisation technologies can be broadly classified into two categories: numerical simulations and experimental techniques. The former rely on mathematical solutions of physical equations, such as Navier-Stokes, to predict the geometrical distribution of individual phases, e.g. void fraction and velocity field, whereas the latter utilises external facilities to reveal the actual presence of multiphase flow. Simulations are able to provide detailed information of the flow at fine-grain level and hence are essential at the design and engineering stages. The major disadvantage of numerical simulation is that they are computation and resource expensive. Experimental techniques, in contrast, are capable of presenting real flow information at relatively coarse-grain level, and hence are extremely helpful for the validation and improvement of numerical simulations. In addition, they are also able to deliver off-line or real-time information for analysing, monitoring, and tuning the processes involved, but requiring much less time and resources for the computation. Among the experimental techniques, there is a particular category: tomographic systems.

After a few decades development, tomography has proved to be an influential group of multiphase flow visualisation techniques and been applied in many industrial sectors. Most tomographic systems work in a non-intrusive/invasive way to provide 2D cross-section, 3D, or even 4D (space and time) presentation of multiphase flow by means of off-line analysis or on-line monitoring. According to the number of deployed modalities, tomographic systems can be roughly categorised into two groups: single- or multi-modality tomography. Single-modality tomography is the first generation and hence the most common existence of tomographic systems, which utilises single modal to measure and visualise multiphase flow (Hoyle 2016). However, due to the inherent limitation using single modal, individual phases can not be effectively isolated when the flow containing more than two components are investigated. The second generation of tomography is multi-modality or multi-energy systems (Hoyle 2016). Multi-modality tomography is characterised by integrating different modalities together to interpret the flow under investigation, where each modality is material-specific. By combining the results from all modalities, a mixture can be decomposed and hence individual components can be isolated. Multi-modality examples include

dual-modality ERT-ECT systems for gas-liquid flow (Yue et al. 2013) and gas-oil-water flow (Qiu et al. 2007; Marashdeh et al. 2007; Sun et al. 2015; Ji et al. 2016), Gammay-ray and ECT for a gas-oil-water mixture (Hjertaker et al. 2011), and a three-modality system of ERT, ECT, and Ultra-sound tomography (Hoyle et al. 2001), etc.. Multi-energy tomography is usually utilised for distinguishing multiple components having similar properties, which are unable to be effectively isolated by multiple modalities. This type of tomographic systems includes dual-energy Gamma-ray system (Froystein et al. 2005), dual-energy X-ray system (Gehrke et al. 2005), multi-frequency EIT (Nahvi et al. 2008; Wu et al. 2016), ect.

Among available tomography, electrical tomography stands out among existing tomographic techniques due to its unique features, including being non-radioactive, low-cost, and having a high temporal resolution, to name a few. Despite its successful reports, the application of electrical tomography to multiphase flow visualisation still needs enormous effort, because of the inherent limitations associated with the electromagnetic field and an ill-posed inverse problem. These limitations prevent electrical tomography from conveying detailed information of multiphase flow dynamics, such as invisible small bubbles below a certain size. In addition, the incapability of single-modality tomography on the decomposition of individual phases in three-phase flow demands the expansion of single modality to multiple modalities, which inherently involves multi-dimensional data fusion.

The primary objective of this study is to use electrical tomography to visualise multiphase flow. Unlike other visualisation technologies, electrical tomography has unique characteristics for multiphase flow visualisation. As discussed earlier, electrical tomograms in this study are 2D cross-sectional images of pipeline flow, and they are low-spatial resolution but high-temporal resolution, of which the spatial resolution is not high enough to reveal certain flow information, e.g. bubble distribution. In addition, the data to be processed is a sequence of electrical tomograms, i.e. a 3D scalar field containing both spatial and temporal information, accompanied by no other information, e.g. velocity field. Therefore, direct visualisation of multiphase flow by electrical tomography has some difficulties in delivering sufficient flow dynamics and thus an advanced approach is demanded.

In this section, advanced visualisation techniques in computer graphics is firstly reviewed to seek for potential candidates for our study. Later, contemporary

techniques from both simulation and experimental investigations of gas-liquid flow visualisation are addressed. Finally, major methodologies in DMTS-based gas-oil-water flow visualisation are examined, along with several advanced approaches from general data/image fusion which could potentially fulfil our requirements in the data fusion and visualisation of gas-oil-water flow by dual-modality electrical tomography in this study.

2.2.1 Advanced visualisation techniques in computer graphics

In order to visualise multiphase flow based on volume data collected by electrical tomography, individual components in multiphase flow have to be distinguished. Ideally, each component should be presented in its original form, i.e. bubbles. Unfortunately, this is extremely challenging in both simulation and experimental methods. All existing approaches seek to approximate the flow with some assumptions. Nevertheless, there are various advanced techniques in modern computer graphics which target to identify and isolate objects from images and volumetric scalar data, which are potential helpful to our study.

2.2.1.1 Edge detection

A well-developed technique in CG that may relate to our study is edge detection, which locates and extracts sharp discontinuities in an image (Bhardwaj et al. 2012; Ohtake et al. 2013; Birchfield 2017). Edge detection is a fundamental approach that identifies object boundaries in an image, which can be further used for many purposes, such as object recognition and reconstruction. In general, edge detection operators can be classified into two groups: first-order derivative (gradient) and second-order derivative (Laplacian) (Juneja et al. 2009). The former indicates that the operators seek for edges by identifying maximum/minimum of the approximated gradient of an image, such as the Sobel operator (Sobel et al. 1968), whereas the latter locate edges by positioning zero points of second-order derivative of an image, such as the Laplacian of a Gaussian (LOG) (Marr et al. 1980), i.e. a Gaussian filter is applied to smooth/de-noise the image before using Laplacian for edge detection, and Canny operator (Canny 1986). Edge detection is a powerful technology to isolate edges in 2D images, but unfortunately, it is unsuitable for our study since sharp edges are unable to be reconstructed

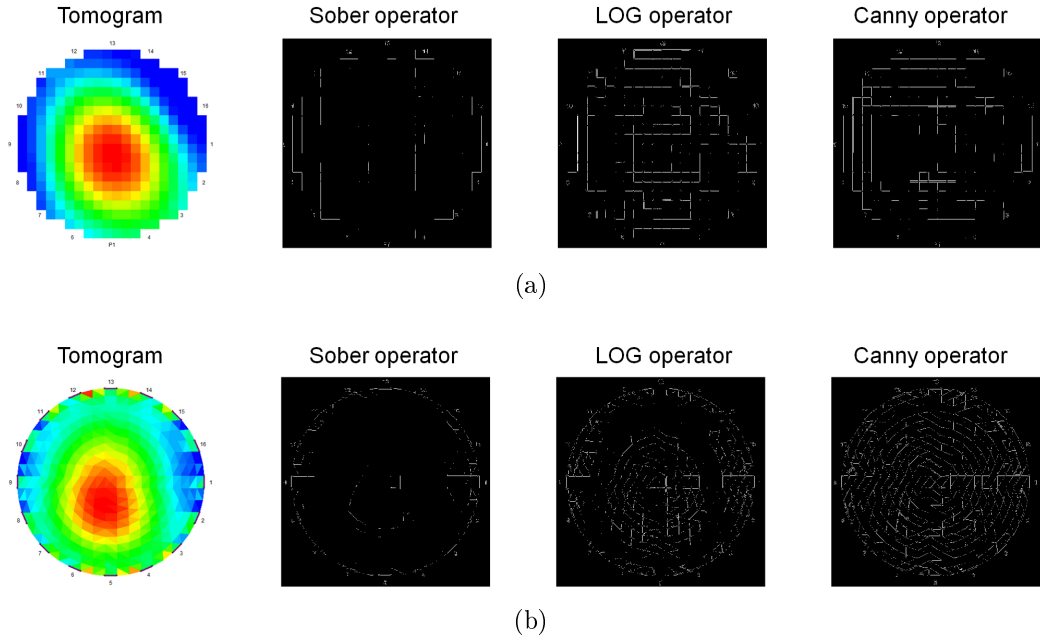


Figure 2.11: Edge detection in LBP (a) and SCG (b) based electrical tomogram by Sober, LOG, and Canny operators.

by electrical tomography. Figure 2.11 demonstrates the infeasibility of popular edge detection algorithms of Sober, LOG, and Canny on electrical tomograms to locate boundaries between gas and water, for both the LBP-based tomogram (Figure 2.11a) and SCG-based tomogram (Figure 2.11b).

2.2.1.2 Image segmentation

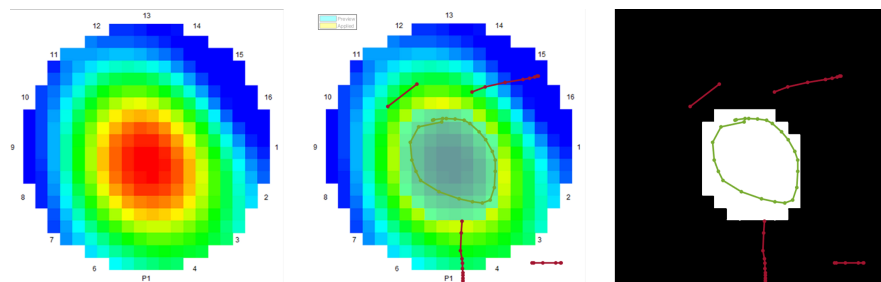


Figure 2.12: Graph-cut based image segmentation on an electrical tomogram.

There are also other advanced algorithms in CG relating to boundary/surface identification and extraction. One of the well-known approaches is image segmentation, i.e. partitioning a digital image into several segments which reflect

certain characteristics of the image in order for the image to be more meaningful and more easily analysed (Bankman 2008; Birchfield 2017). Edge detection is also helpful for image segmentation since interfaces always relate to regions, although interfaces are not always continuous. Image segmentation has been studied intensively over many areas, e.g. medical imaging, and a wide variety of algorithms have been proposed, from a threshold-based simple method (Al-amri et al. 2010), to mathematics-based partition, e.g. statistics and graph theory (Felzenszwalb et al. 2004; Senthilkumaran et al. 2009), to name a few. Figure 2.12 demonstrates an example of using a graph-cut algorithm (Boykov et al. 2001) to segment an electrical tomogram for the purpose of identifying a slug bubble in water. Essentially, graph-cut is an interactive semi-automatic algorithm for image segmentation. In Figure 2.12, the left image is an electrical concentration tomogram, the middle one is the intermediate result, in which the circle line points out the objective segment to be isolated and the rest of the lines indicate the background, and the right one is the result in which the white area is the resultant region, i.e. a bubble, and the black area represents water and other auxiliary areas. It seems that a graph-cut algorithm is suitable for identifying sharp boundaries between gas and liquid in our study but actually it was not. Unlike high-resolution images, e.g. CT, electrical tomograms are unable to provide sufficient features for segmentation unless users have a solid background in electrical tomograms. Although it could help isolate large bubbles from liquid, it is still infeasible to locate small bubbles since they are hardly possible to reconstruct.

2.2.1.3 Isosurface extraction

Surface visualisation is another group of popular algorithms in CG used to extract object surface from volumetric data (Hansen et al. 2011; Wenger 2013). Basically, surface rendering approaches firstly extract geometric primitives, and then render the surface based on the primitives. The extraction of the primitives is usually based on a given isovalue, resulting in the isosurface, i.e. the surface on which all values are equal to the give isovalue. In a typical application, e.g. CT, the isosurface represents a connected surface, such as a skin or brain boundary. With the support of modern graphics hardware, indirect methods are often chosen due to their speed advantages (Bankman 2008).

Various isosurface-extraction approaches can generally be classified into three categories based on the space on which the different approaches operate, i.e. geometric, value and image decomposition, of which different methods are suitable for a variety of datasets (structured or unstructured grid) (Hansen et al. 2011; Wenger 2013). *Geometric space decomposition* techniques decompose the space by taking advantages of the coherence between neighbouring cells, based on the (explicit or implicit) geometry of the cells on a structured grid. Rather than decomposing the space in geometric terms, the *value space decomposition* approach divides the space by values, which is suitable for unstructured grid since the geometric structure is not important. The *image space decomposition* approach is to either handle the whole image space separately or only cope with part of the space, such as view-dependent isosurface extraction (Livnat et al. 1998), resulting in the reduction of polygons and isosurface to be processed.

Marching Cubes, proposed by Lorensen and Cline (Lorensen et al. 1987), uses a divide-and-conquer approach to generate the isosurface in an imaginary cube from the adjacent 8 pixels which come from two neighbouring slices. For each logical cube, the algorithm calculates how the surface intersects this cube by checking whether the values of each cube vertex are below or above the given isovalue. If above, the vertex is inside (or on if equal) the surface, otherwise it is outside the surface. Figure 2.13 demonstrates all possible configurations for marching a cube. A thorough investigation had been made by Newman and Li (Newman et al. 2006) with respect to the extensions of MC algorithm, which contribute to the MC family to allow the MC algorithm to work for different datasets, improve performance by avoiding useless computation, apply parallel and distributed computation and represent the output of a triangular-assembled surface in different terms, such as points, mesh or polyhedra. In our case, a threshold value as an isovalue could be used to march concentration tomograms to derive isosurface. However, Marching Cubes alone are not sufficient to achieve our goal because only large bubbles could be identified but small bubbles will be left due to the inadequate spatial resolution of electrical tomograms, and therefore extra consideration besides isosurface extraction is required in our research.

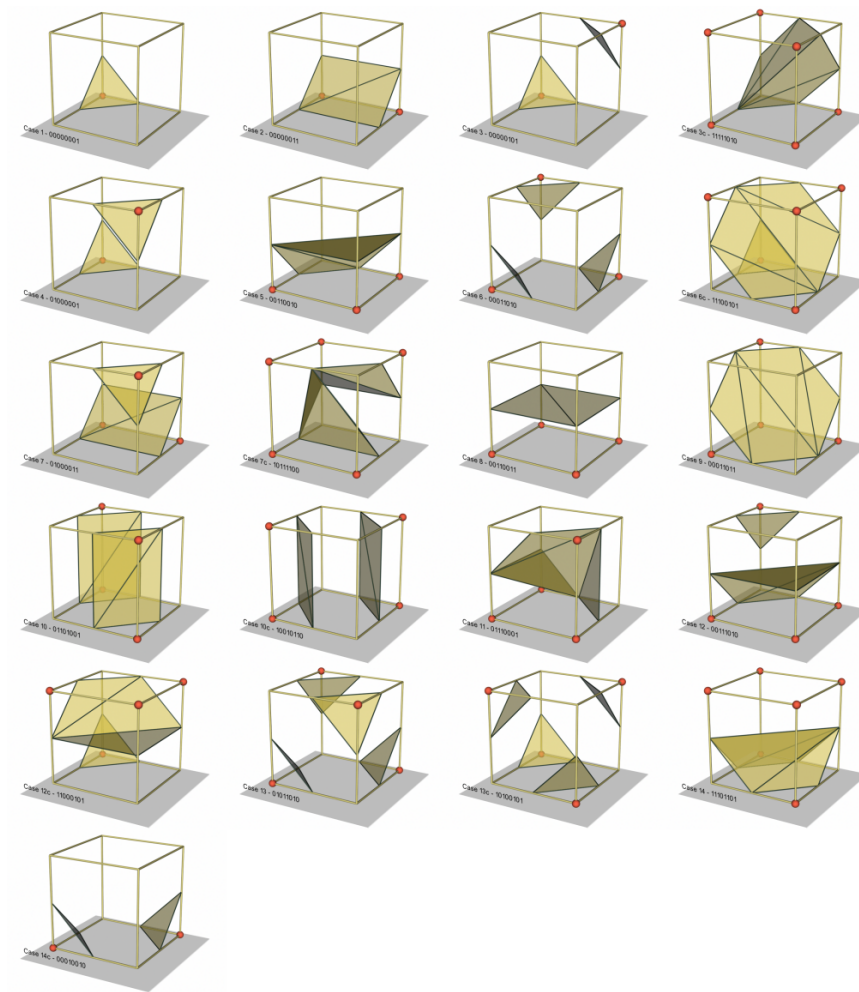


Figure 2.13: 21 configurations for marching a cube using the Marching Cubes algorithm (Lorenson 2013).

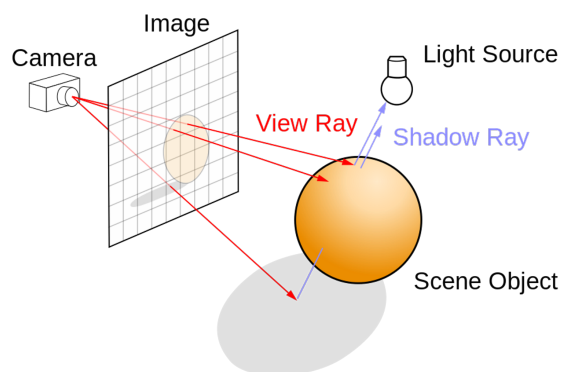


Figure 2.14: Schematic diagram of the ray tracing algorithm (Wikipedia 2013a).

2.2.1.4 Volume rendering

A major disadvantage of isosurface rendering algorithms is that there is an intermediate result from which the isosurface is extracted, which is obviously a time and resource-consuming process. In contrast to isosurface extraction methods, the volume rendering process does not generate intermediate objects, i.e. isosurface. Instead, it projects a 3D dataset to 2D images directly. Volume rendering can be achieved using an object-order, image-order or hybrid techniques, and the principle of volume rendering is depicted in Figure 2.14.

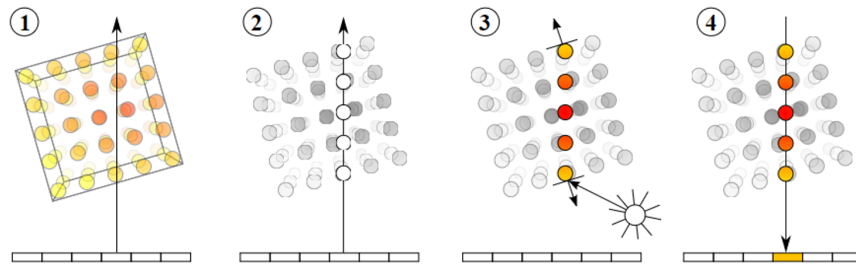


Figure 2.15: Four steps of ray casting: 1) ray casting; 2) sampling; 3) shading; and 4) compositing (Wikipedia 2013b)

Ray Casting, proposed by Roth (Roth 1982), is an image-order direct volume rendering algorithm. In this method, rays are cast from the eye or viewpoint through the image plane and through the dataset. As depicted in Figure 2.15, this approach first casts a ray through the volume for each pixel of the final image and then samples the volumetric dataset along the path of each cast ray by selecting the equi-distant sampling points along the ray within the volume. Further, shading is computed in terms of colour and light according to the orientation and location of the ray for each sampling point. Finally, after all samples have been shaded, they are composited along the ray, of which the compositing result is the final colour value for the pixel being processed. The compositing is in back-to-front style, i.e. the furthest sample is computed first and the nearest sample is computed last.

Shear Warp, originally proposed by Lacroute (Lacroute et al. 1994), is a highly optimized variation of a ray casting algorithm, incorporating the advantages of object-order rendering algorithms, e.g. they simply address arithmetic to achieve good performance from spatial data structures by traversing the volume in storage

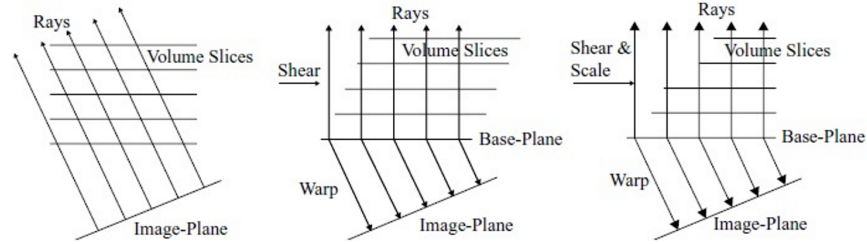


Figure 2.16: Principle of Shear-Warp approach (Preim et al. 2007)

order. Therefore, it is no longer a pure image-based approach, instead, a hybrid-order approach. The basic idea of shear-warp factorization is to simplify the volume sampling to reduce memory access cost, depicted as Figure 2.16. Instead of sampling volume in an arbitrary direction in ray casting, shear warp casts the rays from a base-plane which is always parallel to the side of the data volume that faces the viewpoint most. The resulting ray direction is now perpendicular to the respective volume face, enabling a very regular data access pattern. Later, the volume slices are sheared to get the same sampling pattern as for the original image-plane. Finally, the intermediate image is warped to the original image-plane to correct for the different viewing position and direction.

From previous discussion, it can be concluded that volume rendering essentially simulates the interactions between objects and their surrounding environment, e.g. light and shadow, thereby being able to deliver realistic images of objects. Unfortunately, it is not directly applicable to our research, since objects, i.e. bubbles, are unidentifiable in the original tomograms, but could be an post-processing after individual bubbles have been isolated.

2.2.2 Visualisation of gas-liquid flow

2.2.2.1 Computational Fluid Dynamics

Computational Fluid Dynamics (CFD) is perhaps the most common but influential approach to study gas-liquid flow. It applies numerical solutions to governing equations that model physical problems in regard to fluid flow, with the assistance of the powerful computational capabilities of modern computers (Brennen 2005; Prosperetti et al. 2009; Y et al. 2010). By doing so, it is able to deliver qualitative and even quantitative information of various properties for describing multiphase

flow, e.g. concentration distribution and velocity field, at both coarse- and fine-grain levels. Those valuable results are able to provide insights into multiphase flow.

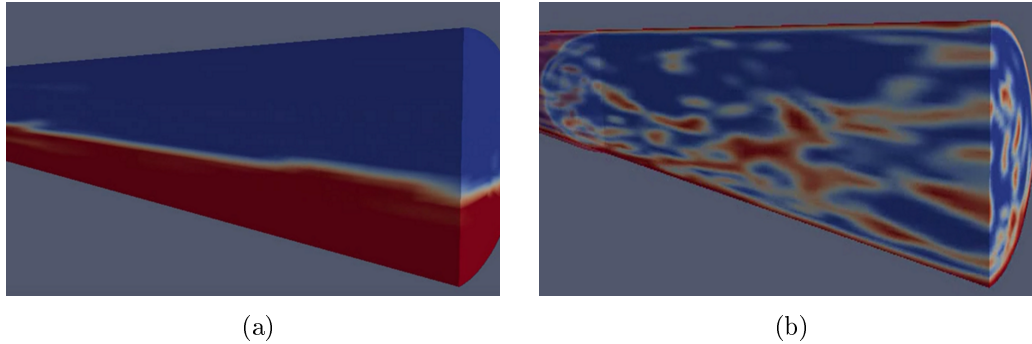


Figure 2.17: CFD-simulated gas-liquid (a) stratified flow and (b) annular flow.

So far there is numerous commercial/open-source software dedicated to fluid flow simulation, such as free open-source software OpenFOAM ¹, and commercial software ANSYS FLUENT ². Although they are different in some aspects, the overall processing in CFD is very similar. In general, the CFD process contains three steps. A geometrical domain to be investigated is firstly discretised, and a physical model is determined, along with initial and boundary conditions. Then, the simulation is started by iteratively solving the model. Finally, the results are analysed and visualised for human/machine perception. Figure 2.17 presents concentration results of gas-liquid stratified flow (Figure 2.17a) and annular flow (Figure 2.17b) in a horizontal pipe simulated by OpenFOAM³.

CFD simulation has some advantages over experimental methods. It provides comprehensive information regarding flow dynamics, which has more properties than experimental studies, such as velocity field and pressure distribution. It can also simulate the conditions that experiments struggle with, e.g. bending pipe. On the other hand, it has some disadvantages. The primary concern is the time and resources consumed by CFD simulation, which could take days of computation. Another influential aspect is that CFD models may not be universal. That is, different flow may require a different model. For example, laminar flow, e.g. stratified flow in Figure 2.17a, simulation is quite straightforward, whereas

¹<http://www.openfoam.com/>

²<http://www.ansys.com/Products/Fluids/ANSYS-Fluent>

³The results were produced by Dr. Jiri Polansky at University of Leeds.

turbulent flow, e.g. annular flow in Figure 2.17b, simulation needs special considerations. Nevertheless, CFD is a powerful tool for multiphase flow analysis and visualisation.

2.2.2.2 Computer graphics

In computer graphics (CG), there is a special branch that concerns physically-based visualisation of multiphase flow. In this area, multiphase flow is simulated by the approximation of the Navier-Stokes equation (Hong et al. 2008; Tan et al. 2009; Kim et al. 2010; Chen et al. 2011). In CG, three different approaches are utilised to approximate governing equations: particle-based Lagrangian method, fluid quantity based Eulerian method, and Lattice Boltzmann equation based method (LBM) (Chen et al. 2011). Admittedly, the ideas behind the multiphase flow animation in CG are based on CFD, although their primary aim is to provide *a realistic appearance and plausible visual effect* by detecting and presenting sharp boundaries/interfaces between different materials (Tan et al. 2009; Chen et al. 2011). In order to extract implicit interfaces, special algorithms are required. Existing algorithms can be roughly grouped into three different categories: front tracking method (FT), level set method (LSM), and volume of fluid method (VOF) (Chen et al. 2011). Studies in this area are beyond the scope of this research, and thus a few examples are presented here for demonstration purposes only.

Monaghan (Monaghan 2005) introduced the smoothed particle hydrodynamics (SPH) method to solve the equation under irregular discretization of the continuum for incompressible Navier-Stokes equations, which is further coupled with advanced algorithms, such as grid-based simulation (Hong et al. 2008) to achieve both coarse- and fine-level bubbles (Figure 2.18a). the LSM-based volume control method is another approach to simulate bubbles rising and foaming (Figure 2.18b), which preserves volume over time by applying divergence of the velocity field to fluid regions in order to compensate their volume error (Kim et al. 2007). Another example is applying a regional level set to simulate multiple immiscible material interaction Figure 2.18c, which is supported by a regional level set graph (RLSG) that tracks the evolution and interaction of every volume region (Kim 2010). Another example is a volume control method based on the simulation of bubble rising and foaming in a water tank (Kim et al. 2007).

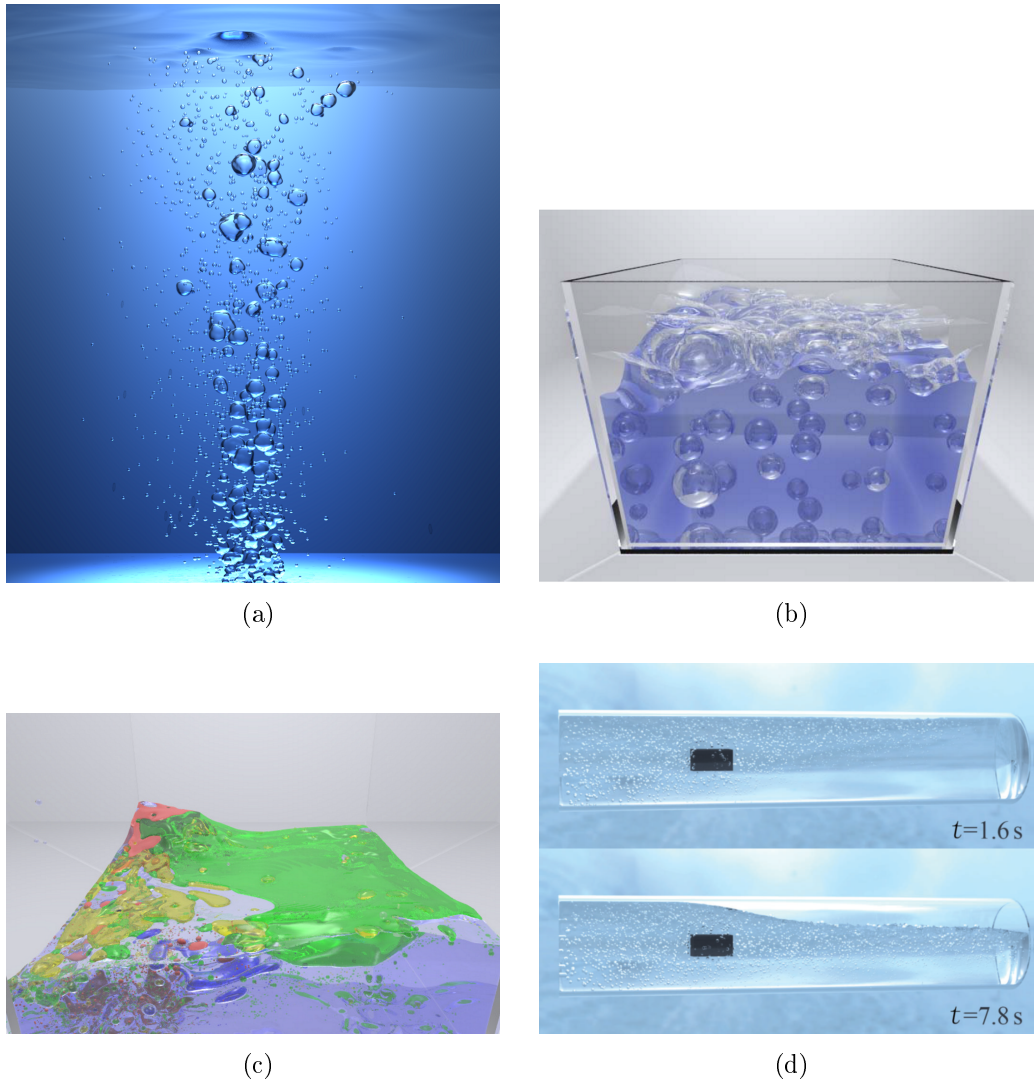


Figure 2.18: Different approach for bubble simulation in CG. (a) a hybrid approach of SPH with grid-based simulation (Hong et al. 2008), (b) bubble rising in a tank using volume control method (Kim et al. 2007), (c) regional level set based multiphase fluid simulation (Kim 2010), and (d) reconstruction bubbles by direct mapping (Ren et al. 2015).

Despite the aforementioned algorithms are different, they share similar features: advanced algorithms are integrated into physical modelling used in CFD. Ren et al. (Ren et al. 2015) presented a bubble modelling method to post-process simulation results, by representing a local volume fraction as bubbles using different thresholds, as depicted in Figure 2.18d. In their work, bubbles were grouped into small, medium, and large bubbles, of which the last form was shaped directly by isosurface algorithm, while the first two forms were represented by spheres.

Although simulations in CG deploy advanced algorithms to deliver realistic and plausible visualisation of multi-material fluid, they are hardly directly applicable to our study, since they always require extra information that is not available in our study, such as surface tension and velocity field.

2.2.2.3 Tomographic systems

The most straightforward visualisation method of multiphase flow is a high-speed camera, i.e. taking pictures/videos of the flow via a transparent inspection chamber. This method, nevertheless, relies on the availability of the chamber and the opaqueness of the fluid, which is not always achievable in an industrial environment, e.g. in subsea gas and oil engineering. In addition, the reliability of the observation is also affected by the concentration of dispersed phase. For example, it was reported that in gas-water flow, this method is out of function when gas concentration is beyond a certain threshold, e.g. 10% (Prasser et al. 2001). Process tomography as the alternative has been successfully applied to many industrial sectors for quantitative and qualitative purposes.

Tomographic systems and simulations have very different but complementary abilities when visualising multiphase flow. They can answer the questions that simulations cannot, i.e. "*what is happening or has happened in multiphase flow?*" This capability enables tomography to evaluate the accuracy of simulations, as well as providing on-line/off-line understanding of real-world situations regarding multiphase flow.

Tomographic systems can be broadly categorised into two groups according to their sensing principles: hard-field and soft-field tomography. In hard-field tomography, energy waves from the power source travel through the medium constantly, whereas in soft-field tomography, the travel is not constant. In consequences, hard-field tomography provides tomograms with high spatial but low temporal resolution, but soft-field tomography offers tomograms of low spatial but high temporal resolution. Typical examples of hard-field tomography include X-ray, CT, and Gamma-ray. Electrical tomography, such as ERT and ECT, is classic soft-field tomography.

As far as tomographic techniques are concerned, primary attention has been paid to instrumentation and reconstruction algorithms, so as to improve the spatial and

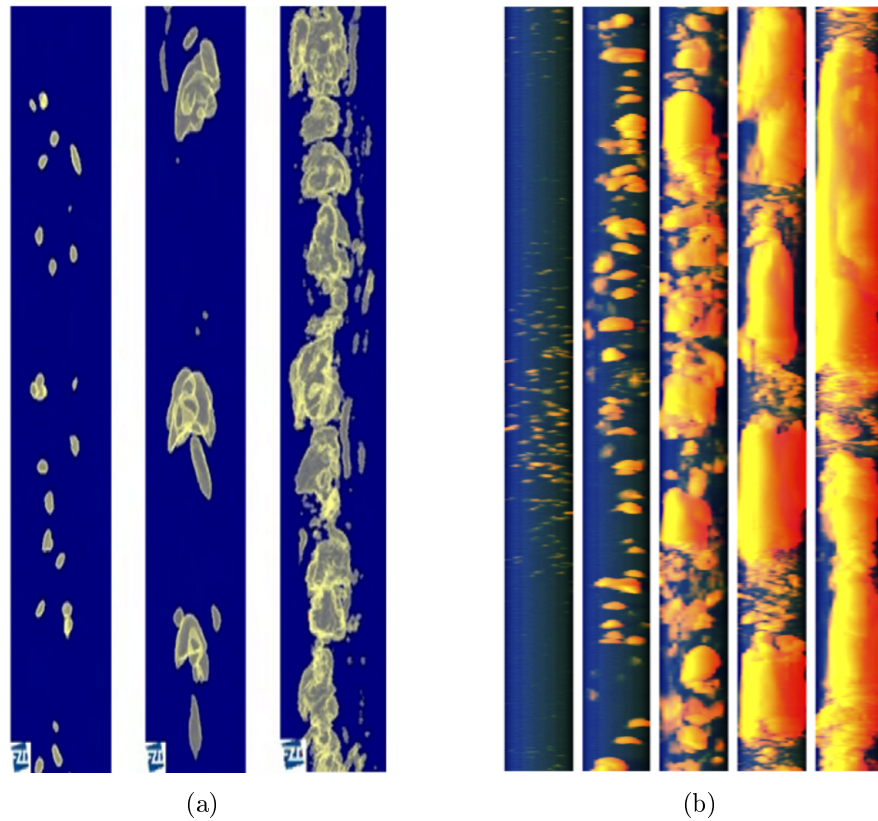


Figure 2.19: Gas-liquid vertical flow visualisation by (a) X-ray (Fischer et al. 2010), and (b) WMS (Manera et al. 2006).

temporal resolution of reconstructed images, but some efforts have already been made to improve the visual limitation resulting from colour mapping. Advanced X-ray computed tomography is capable of detecting small particles at 1 mm level within a 60 mm bubble column (Fischer et al. 2010), and thus generating high-quality reconstructed images, as depicted in Figure 2.19a. The primary weakness of X-ray, however, is its low temporal resolution, resulting in the incapability of visualizing high-speed gas-liquid flow, e.g. gas superficial velocity over 10 m/s, which is common in the gas and oil industries. Although an ultra-fast X-ray system was implemented, which enabled a few thousands frames per second (fps) cross-sectional reconstructed images (Fischer et al. 2008), its application was limited to the flows in small-diameter pipes, e.g. laboratory-scale pipeline. On the other hand, wire-mesh sensor (WMS)-based visualization is able to identify dispersed bubbles and large bubbles of gas-liquid flow in both upward vertical pipeline and horizontal pipeline, with comparable results to x-ray tomography (Prasser et al. 2001; Prasser et al. 2005; Manera et al. 2006). Figure 2.19b

shows an example of using WMS to visualise gas-water upward flow. However, the intrusiveness caused by WMS has been criticized in terms of fragmentation of bubbles, which may affect the original structure of multiphase flow. Further evaluation also demonstrated the large discrepancy in bubble size which can be above 20% (Ito et al. 2011; Nuryadin et al. 2015).

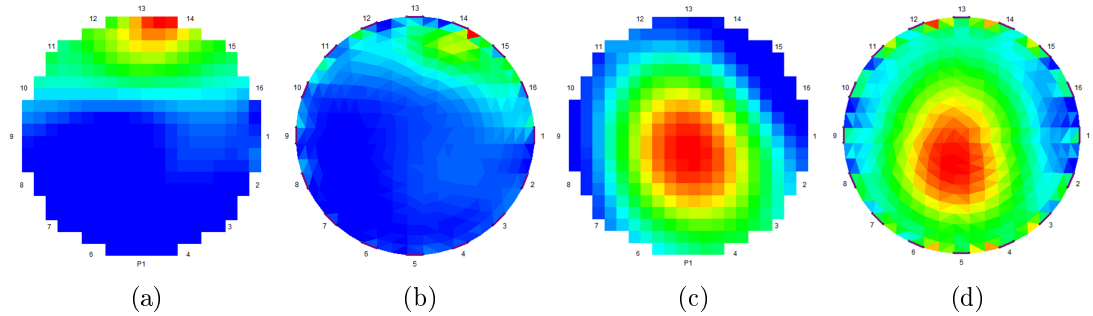


Figure 2.20: ERT-based concentration tomograms of bubbly flow by (a) LBP and (b) SCG, and slug flow by (c) LBP and (d) SCG.

Electrical tomography utilises electrical properties to differentiate different phases in multiphase flow, such as resistance and capacitance. Comparing with other tomographic systems, electrical tomography is capable of producing cross-sectional or 3D images with a relatively high temporal resolution (at the sub-millisecond level (Wang et al. 2005; Jia et al. 2010; Cui et al. 2011)) but relatively low spatial resolution (up to 5%¹ (Wang et al. 1999; Yang et al. 2003)). Due to the nature of the electrical field, electrical tomography is incapable of generating homogeneous sensitivity distribution over its sensing domain (Wang et al. 2016a), which results in the inhomogeneity of sensing outcome, e.g. the same object at different positions within the sensing area of electrical tomography may produce different tomograms. In addition, ill-conditioned problems in association with inverse solution and limited number of measurement also cause problems for electrical tomography. All these limitations cause electrical tomography to fail to deliver tomograms with high resolution comparable to other systems, e.g. computerised tomography (CT). A direct consequence is that its tomograms are unable to indicate small bubbles below a certain size. In addition, it cannot provide sharp interfaces between large bubbles and the liquid phase. Figure 2.20 depicts the incapability of ERT tomograms, in which small bubbles in a bubbly flow disappear (Figure 2.20a), even though an iterative reconstruction algorithm is

¹The ratio of the smallest size of identifiable objects to a container's diameter.

applied (Figure 2.20b). In Figure 2.20c and Figure 2.20d, the tomograms show only the rough existence of a large bubble in a slug flow, but the boundary is too blurred to be identified. Nonetheless, electrical tomography is still able to measure gas-liquid flow with up to 100% gas concentration (Jia et al. 2015).

In visualisation of multiphase flow, a common practice is that the investigated flow is presented by scalar and/or vector identities. More specifically, scalar values usually include concentration, pressure, density, etc., and the velocity field is normally representative of the vector. Simulation-based approaches reveal flow characteristics of one or more identities. For instance, the concentration and velocity field are integrated together to reconstruct bubbles in computer visualisation and animation (Tan et al. 2009). In experimental approaches, there is only scalar data available for presenting flow dynamics. Although velocity information can be extracted, for example using a cross-correlation method, the values are always statistical, rather than instantaneous. Particularly, tomography normally produces scalar field, and hence tomography-based visualisation of multiphase flow is built upon scalar information, e.g. concentration distribution.

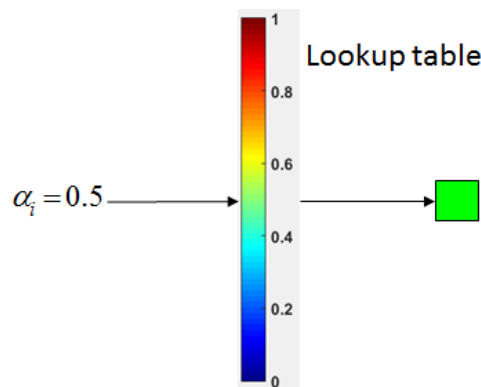


Figure 2.21: Mapping a scalar to a colour by a blue-to-red lookup table.

From the visualisation point of view, a common practice of visualisation upon scalar data is transferring scalar data to colour schemes with the assistance of lookup tables, namely colour mapping (Hansen et al. 2011). Figure 2.21 demonstrates an example of colour mapping, where a scalar 0.5 is transferred to a colour *green* according to the lookup table. Because of its computational and conceptual simplicity, colour mapping is one of the most widely utilised visualisation algorithms for scalar values. It is generally anticipated that the application of colour mapping should emphasise significant features but minimise trivial or

irrelevant information. However, colour mapping based visualisation by electrical tomography struggles to reveal sufficient flow dynamics, e.g. bubble size and distribution, due to the aforementioned limitations of the systems. In addition, concentration distribution from tomography is discrete, and thus the transferred colour is non-linear. Although, in most cases, this causes little misunderstanding for human or machine perception, it is still not difficult to imagine that in some cases this simple design is inadequate. For example, when scalar values in a data set are clustered in a narrow band but maximum and minimum values have a considerable difference, e.g. a few orders, a limited number of colours are dedicated to a large number of values in a narrow range. In this case, subtle changes in magnitude are very difficult to be reflected by mapped colours. Figure 2.20a shows that in the middle area of the figure, trivial quantitative changes in concentration from a visibility point of view are barely perceptible therefore the details are lost.

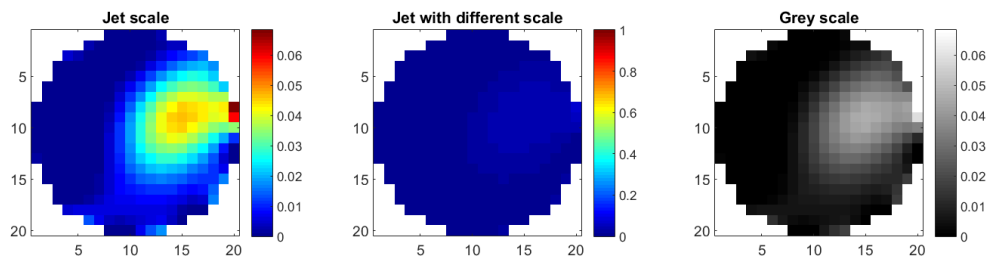


Figure 2.22: Same concentration distribution but different tomograms by (a) jet colour and normal scale; (b) jet colour but different scale $[0, 1]$; and (c) grey colour with normal scale.

From the human perspective, it is not difficult for experienced users to obtain sufficient information regarding flow regimes from electrical tomograms. Unfortunately, this is not always true for the users with little tomographic knowledge, since there are no identifiable objects in the tomograms. In addition, the conventional tomograms by colour mapping are strongly affected by the lookup table, i.e. same concentration distribution may have different tomograms because of different lookup tables. Figure 2.22 demonstrates an example of the impact of lookup table, including colour range and transferring scale, on concentration tomograms. With insufficient background of electrical tomograms, the first tomogram shows an ambiguous impression that there is a large bubble in the right section. However, this actually is not true if the scale is changed to the full range $[0, 1]$, as

depicted in the middle tomogram. If only colour range is changed to grey, the resultant tomogram (the right one) still delivers suspicious information.

Isosurface, or contour in 2D, is another common visualisation technique. Essentially, for volume representing a set of input scalar values, an isosurface is the connection of all points that have the same value, i.e. isovalue (Hansen et al. 2011). In other words, the value of all connected points is identical. As far as gas-liquid flow visualisation goes, an isosurface is the boundary between gas and liquid phase. In Figure 2.19a, bubbles are extracted using an isosurface algorithm with a given concentration volume. Because of the high spatial resolution of the X-ray, bubbles above 1mm can be visualised. For instance, the authors in (Wei et al. 2015) extracted the edge between conductive and non-conductive phases by identifying the isosurface using isovalue 0.5. Unfortunately, isosurface extraction is only applicable to locate the edges between large bubbles and liquid with a given dataset, i.e. a stack of sequence concentration tomograms. It is unable to position the edges between small bubbles and liquid, due to the relatively low spatial resolution of electrical tomograms, even when multiple isovalues are applied.

As a prominent rendering method, isosurface has been extensively applied to many scientific and engineering areas, and has been inherently implemented in many visualisation softwares and libraries, such as Matlab ¹ and Visualisation Toolkit (VTK) (Schroeder et al. 2006b). Both isosurface rendering functions are tested using several cross-sectional ERT tomograms collected from gas-liquid flow by the V5R system using a threshold value of 0.5, as depicted in Figure 2.23, and the performance regarding execution time against a different number of tomograms is also presented in Figure 2.24. It is clearly indicated that in Figure 2.23, neither approach is able to deliver apparent and reasonable multiphase flow information, such as flow regimes. This is because the isosurface approach does not take account of implicit information residing in the tomograms, e.g. temporal resolution. In addition, the inherent limitations of electrical tomograms add extra challenge onto the visualisation of gas-liquid flow. Direct application of the isosurface to electrical concentration tomograms is inadequate to visualise the flow, and thus it has to be extended and/or integrated with another approach so that it becomes suitable for the purpose of visualising the flow and further reflecting sufficient flow dynamics.

¹<http://www.mathworks.co.uk/>

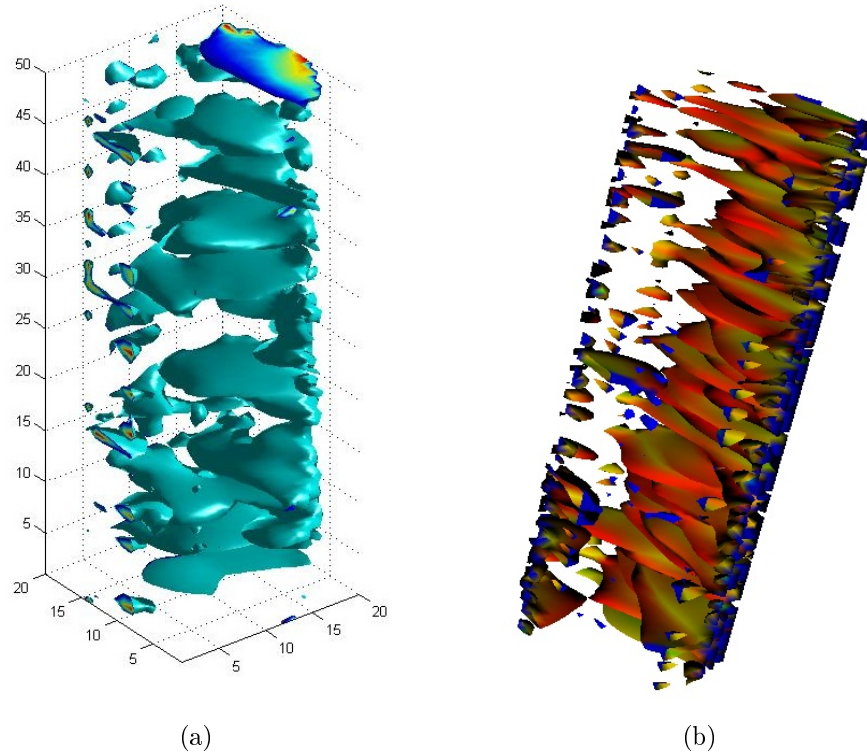


Figure 2.23: Isosurface rendering of ERT tomograms by (a) Matlab, and (b) VTK.

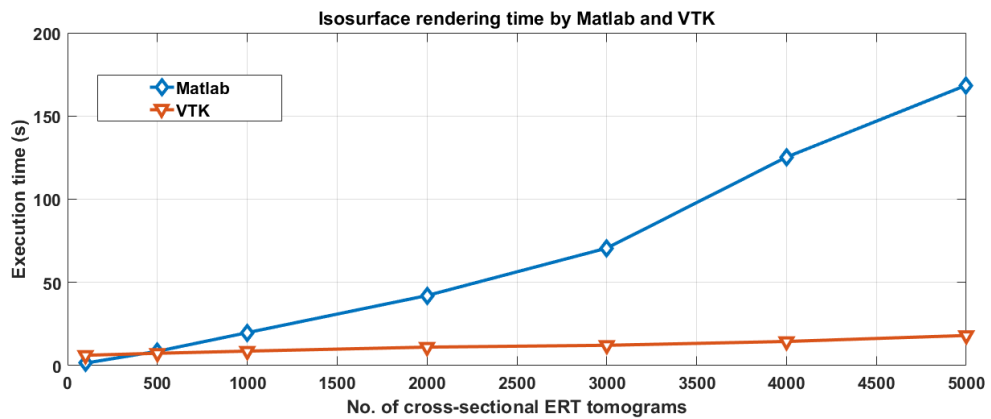


Figure 2.24: Execution time of the rendering by Matlab and VTK.

There are also some other advanced visualisation algorithms devoted to multiphase flow imaging using tomographic systems, besides the aforementioned common approaches. Manera *et al.* utilised an advanced technology in computer graphics, namely ray tracing, to visualise flashing flow in a vertical pipe using WMS (Manera *et al.* 2006). Essentially, it traces a path of light from an imagi-

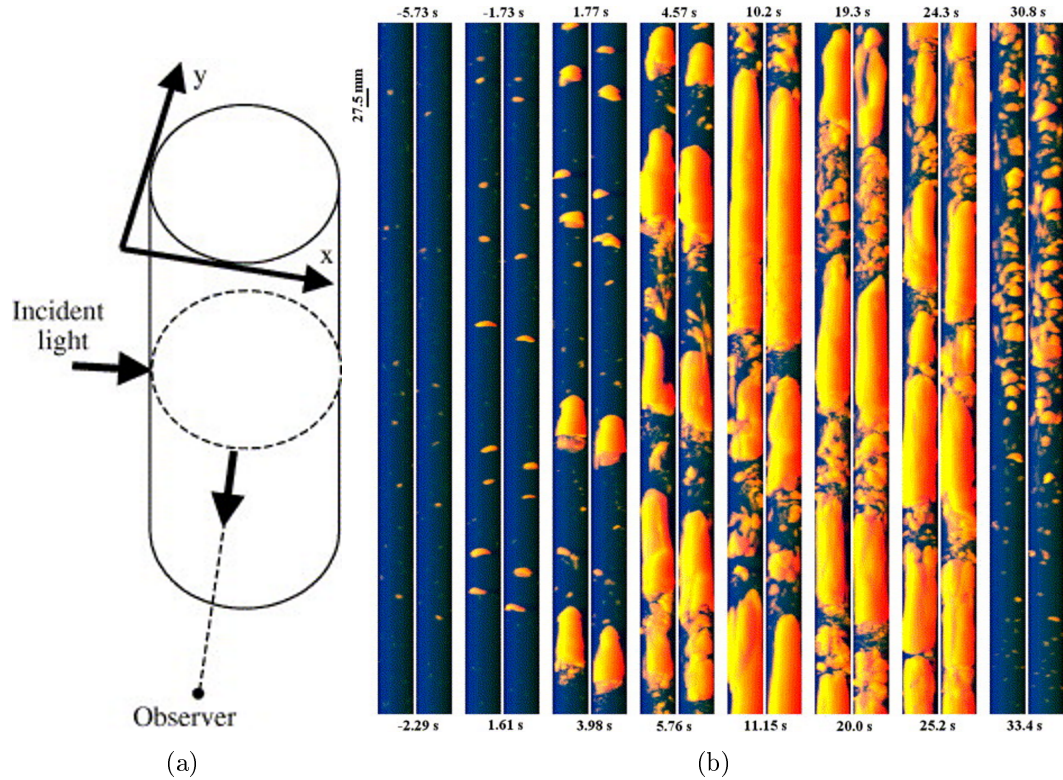


Figure 2.25: Application of ray-tracing to two-phase flow visualisation (Manera et al. 2006).

nary eye through each pixel in a virtual image plane and simulates the physics involved in light and object interaction, such as reflection refraction (Hansen et al. 2011). The principle of ray-tracing is depicted in Figure 2.25a. This algorithm is easy to understand and implement, and the flow investigated in the article was visualised to a certain extent which provides sufficient information regarding flow patterns. It however requires that objects to be visualised exist physically or conceptually. Unfortunately, this is not applicable to electrical tomograms due to their relatively low spatial resolution.

Another example is the real-time 3D visualisation of multiphase flow by ECT (Ye et al. 2012). In their approach, conventional approaches to computer graphics were utilised, namely volume rendering and texture. Volume rendering technology is a prominent approach to display 3D discrete data in a 2D projection, and thus widely applied in many areas, e.g. medical imaging, whereas texture is a mapping approach that applies an image (texture) to a 3D surface so that resultant images are able to deliver more surface characteristics and appearance (Hansen et al.

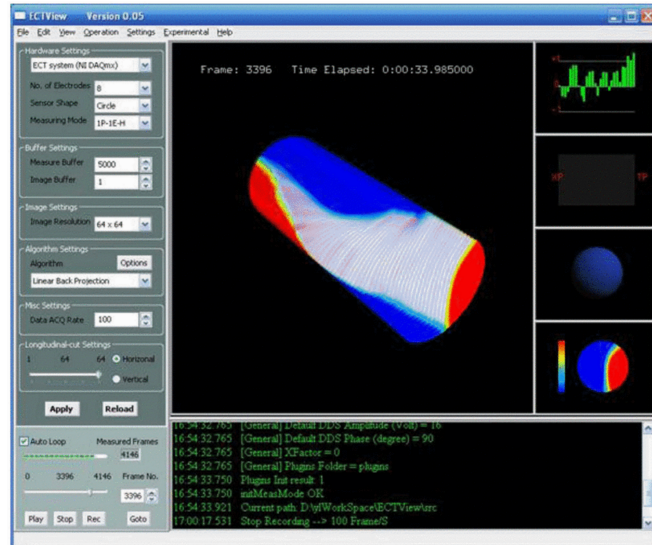


Figure 2.26: The GUI for 3D realtime visualisation of ECT. (Ye et al. 2012)

2011). Their exemplary result is depicted in Figure 2.26. Unfortunately, like ERT tomograms, they are unable to provide sufficient and detailed information of multiphase flow, such as small bubbles size and distribution.

In this research, a novel approach is proposed to overcome the problems when using electrical tomography to visualise gas-liquid flow, which essentially 'reconstructs' bubbles based on concentration tomograms. For simplicity, it is assumed that gas bubbles are randomly distributed with a homogeneous volume fraction inside a small region, and the growth and collapse of the bubbles are trivial and can be ignored (Brennen 2005). According to the assumptions and the definition of the gas volume fraction (Brennen 2005; Corneliussen et al. 2005), a new bubble-based lookup table can be defined to replace the lookup table in conventional colour mapping in which bubble size relates to the average concentration of a unit, namely an interrogation cell (IC), while its location is random inside the volume. With a carefully selected threshold, adjacent volumes are merged to form large bubbles. Those large bubbles are further processed using an enhanced isosurface algorithm to identify the boundaries between the large bubbles and the liquid. In this procedure, small bubbles are assumed to be spherical, whereas the shape of large bubbles is determined from input tomograms. In this attempt, gas distribution is reflected by bubbles of different sizes and distribution, and hence the limitations are overcome so that the resulting tomograms convey sufficient and unambiguous gas-liquid flow dynamics, e.g. flow regimes.

2.2.3 Visualisation of gas-oil-water three-phase flow

2.2.3.1 Tomographic systems

Gas-oil-water flow is a common phenomenon in many industrial sectors, e.g. petroleum engineering, but measuring and visualising such flow is extremely challenging due to the unpredictable and complex interactions between each phase, despite a few decades of intensive research and development from all over the world (Thorn et al. 2013). Conventional optical methods, e.g. high-speed videos, are the most straightforward solutions, but their applicability is restricted by the availability of certain conditions, e.g. a transparent optical inspection chamber. Moreover, its success is heavily dependent on the opacity of the flow. For instance, it is reported that optical methods are ineffective when air concentration is higher than 10% in air-water flow, because of a large amount of opaque bubbles (Prasser et al. 2001). As a result, alternatives have to be sought for the measurement and visualisation of such flow when optical methods are inapplicable.

Multi-modality tomographic systems (MMTS) have attracted much attention in the past a few decades, particularly dual-modality systems (DMTS) which simultaneously employ two different tomographic techniques to one physical phenomenon, such as in medical engineering and process engineering (York et al. 2011; James et al. 2014). The primary purpose of introducing an extra modality is to provide complementary information so that the outcomes reveal more information than the individuals for human and/or machine perception. For example, computed tomography (CT) is able to reveal the anatomical structure of bone tissues, whereas nuclear magnetic resonance imaging (MRI) is able to image the anatomical structure of soft tissues. When CT and MRI are combined together, the fused images can reflect the anatomical structure of both bone and soft tissues (Teng et al. 2010; James et al. 2014).

In multiphase flow measurement and visualisation, DMTS has been proposed to either enhance the spatial resolution of reconstructed tomograms for two-phase flow, or derive the spatial resolution of the phases in three-phase flow. Examples of the former case include the integration of Gamma-ray computerised tomography (GCT) with ECT to gain higher-resolution images for visualising gas-oil two-phase flow (Zhang et al. 2014), the combination of ERT and ECT to visualise

gas-liquid flow (Li et al. 2009b), or ERT with an Electro-magnetic flow meter (EMF) on oil-water flow (Faraj et al. 2015). All applications are to improve the precision of the measurements by incorporating extra information from the second modality. In the case of three-phase flow, a number of studies have been carried out, including dual-modality WMS for gas-oil-water flow (Santos et al. 2015), GCT with ECT for three-phase flow (Hjertaker et al. 2011), Magnetic inductance tomography (MIT) with ECT for the flow (Zhang et al. 2015), and so on.

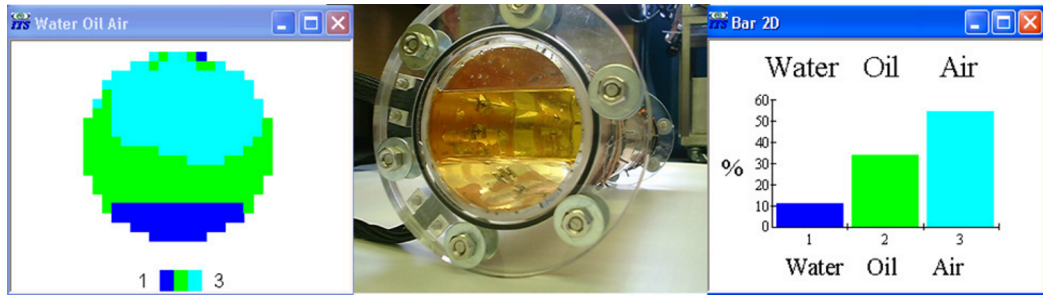


Figure 2.27: Detection of gas-oil-water interface using ITS ERT-ECT systems (Qiu et al. 2007).

A particular group of DMTS is ERT-ECT systems, which are characterized by low-cost, non-intrusive/invasive and non-radioactive electrical tomography. They usually offer tomograms with high temporal resolution, at sub-millisecond (Wang et al. 2005; Cui et al. 2011) but relatively low spatial resolution up to 5% (Wang et al. 1999; Yang et al. 2003; Qiu et al. 2007). A number of efforts have been made to explore the application of dual-modality ERT-ECT systems for multiphase flow imaging, such as gas-liquid flow or gas-oil-water three-phase flow. (Qiu et al. 2007; Li et al. 2009b; Yue et al. 2013; Sun et al. 2015; Wang et al. 2017). In (Qiu et al. 2007), the authors used the commercial ERT-ECT systems to visualise a stationary stratified gas-oil-water flow in a horizontal vessel, and the fused result is depicted in Figure 2.27. Another example is the one by Sun (Sun et al. 2015), which utilised an electrical impedance analyser based system to image four different stratified gas-oil-water horizontal flow, and their results are depicted in Figure 2.28.

The engagement of an extra modality inherently requires the integration of the information derived from different sources, such as different excitation frequency in the ERT-ECT system, or different energy in the GCT-ECT system. In addition, one characteristic when studying multiphase flow is that the study should

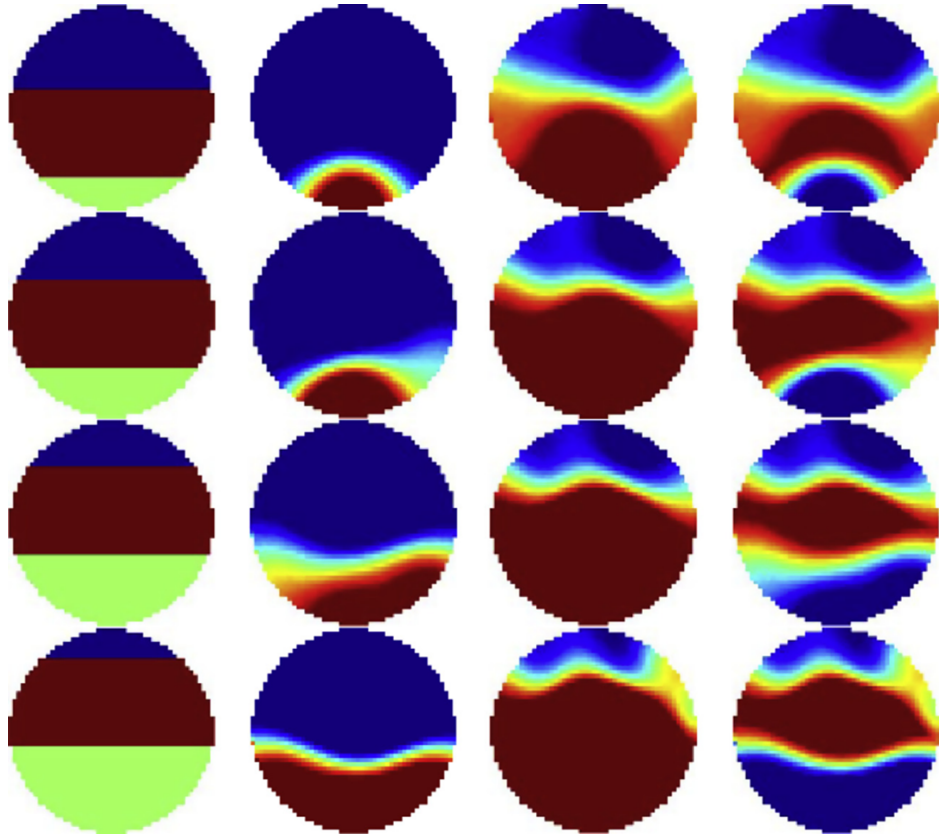


Figure 2.28: Detection of gas-oil-water interface in Sun's approach (Sun et al. 2015).

be continuous in order to reflect the full features of the flow investigated, such as flow regimes. Therefore, the information in temporal dimension has to be taken into account as well. As a result, data processing for DMTS always requires the fusion of the data from multiple dimensions, including, but not limited to space, time, and energy (Hoyle et al. 2012).

In general, data fusion is a broad topic discussed in many fields where multiple sensors are involved, such as remote sensing systems, medical imaging, sensor networks, to name a few. The primary purpose of data fusion is to automatically or semi-automatically integrate the data from multiple sources and different points in time into one representation that provides effective support for human and machine perception (Blum et al. 2005; Mitchell 2012). According to (Piella 2003; Mitchell 2012; Khaleghi et al. 2013), it generally requires data fusion techniques should (i) be reliable to introduce as little noise as possible; (ii) retain as much relevant information contained in the source data as possible; and (iii) be robust

to deal with imperfect sources. In addition to those generic requirements for multisensors, data fusion for DMTS also has its own domain-specific features.

Due to the involvement of the image reconstruction process in tomographic systems, data fusion could be performed at different stages, i.e. before, during, and after image reconstruction. Fusion before reconstruction needs to combine raw signal data, as the input for image reconstruction, and no further fusion is required. Signal-level fusion, unfortunately, does not exist so far (Hjertaker et al. 2011). Fusion during reconstruction is that the information from one modality is used as input for the image reconstruction process of the other modality. After the reconstruction, the images already reflect the information concerned and no further fusion is needed. To the best of our knowledge, pure reconstruction-level data fusion for DMTS is so far non-existent. In (Zhang et al. 2015), they partially applied reconstruction-level fusion in their approach by using MIT produced images to update the forward model in ECT reconstruction, but further image-based fusion still required after the reconstruction. Fusion after reconstruction, i.e. data are integrated based on the individually reconstructed tomograms by each modality, refers to image-level fusion, or image fusion, and it is the predominant approach in DMTS-based multiphase flow measurement and visualisation.

Despite a number of DMTS having been proposed for imaging multiphase flow, the research in this domain is still at an early stage. As far as data fusion is concerned, there are only a limited number of algorithms. Using thresholds to determine geometrical distributions of gas-oil-water flow is the predominant method for DMTS to visualise gas-oil-water flow (Qiu et al. 2007; Li et al. 2009b; Hjertaker et al. 2011; Santos et al. 2015; Zhang et al. 2015; Wang et al. 2017). In this method, priori threshold values, usually two and each of them is specific for the images by one modality, are applied to binarise the original images, which are further fused to produce the distributions. Thresholding is conceptually and implementationally simple, as well as computationally inexpensive. In general, the utilised thresholding methods can be roughly grouped into two categories: one is based on pixel concentration, e.g. (Qiu et al. 2007), and the other is on reconstructed images, e.g. (Hjertaker et al. 2011).

In the first category, two threshold values are implicitly applied for the concentration tomograms of each modality respectively. For ECT concentration tomograms, if a pixel concentration is larger than the corresponding threshold, it

assumes that this pixel is full of gas, or otherwise oil-water mixture. As for ERT tomograms, a pixel is filled with pure water if the concentration is smaller than the designated threshold, or otherwise gas-oil mixture. The thresholded tomograms are further fused to extract the oil phase and thus individual phases are derived. The fusion can be described by the following equation:

$$f_{i,j} = \begin{cases} gas & s_{i,j}^{ECT} \geq T^{ECT} \\ water & s_{i,j}^{ECT} < T^{ECT} \text{ and } s_{i,j}^{ERT} \leq T^{ERT} \\ oil & \text{otherwise} \end{cases} \quad (2.15)$$

As far as image-based fusion is concerned, there are also two threshold values that apply to individual tomograms by each modality. Similar to the values in the first category, central values of the grey level of tomograms are chosen for the fusion. For example, in (Hjertaker et al. 2011), two different thresholds are applied to ECT and GT respectively to binarise the tomograms firstly, and then perform fusion based on the binarised tomograms. The fusion can be described as:

$$f_{i,j} = \begin{cases} gl[127] & g_{i,j}^{ECT} = 0 \\ gl[255] & g_{i,j}^{GT} = 255 \\ gl[0] & \text{otherwise} \end{cases} \quad (2.16)$$

Threshold values, however, have a significant impact on the determination of phase concentration, of which a little deviation may result in considerable error. Moreover, the pinpointing of the values is theoretically and practically challenging, since they are influenced by many factors, such as the hardware, phase properties of the flow under investigation, and so on. In essence, the thresholding method can be treated as a special case of weighted average, where weights are set to either 1 or 0 according to the threshold values.

In addition, a few advanced algorithms have been proposed without threshold values. Yue *et al.* (Yue et al. 2013) utilised fuzzy clustering algorithms to fuse the data from different sensing strategies, as well as ERT and ECT, and the results yielded comparable phase concentration to the thresholding method. Their investigation, however, is more suitable for the images reconstructed by advanced iterative algorithms since it is sensitive to tomograms' resolution, and their evaluation was on laboratory-scale flow but not on real-world industrial cases. What's more, their approach was designed for two-phase flow imaging thereby the feasibility of three-phase flow being in doubt.

Pusppanathan *et al.* (Pusppanathan et al. 2014) proposed fuzzy logic for ultrasonic tomography (UT) and ECT to integrate separately reconstructed images. In their approach, two sets of tomograms were firstly obtained by UR and ECT respectively, and then the fusion was performed on a pixel basis. However, the applicability of their method is unknown when the original images have different resolutions due to hardware changing from UT to ECT. Besides, because their method was only evaluated by simulation, whether it is eligible for the case of fluid flow still needs further investigation. In addition, the employed membership functions in their proposal as reported do not have the best performance, in comparison to other membership functions (Zhao et al. 2002).

Despite much effort has been made for the multiphase flow visualisation by dual-modality tomographic systems, they still lack sophisticated studies in several aspects to enable them deliver more informative content.

2.2.3.2 Image fusion approaches

In the field of image fusion, the actual fusion process could happen at different levels, including pixel, feature, and decision (Zhang et al. 1999). Pixel-level fusion combines several raw images into one image on a pixel-by-pixel basis, and hence can retain more detailed information in the original images (Li et al. 2017). Feature-level fusion integrates input images based on the features in the images, such as edges and regions. Decision-level fusion consists of integrating information at a higher level of abstraction, i.e. combines the results from multiple techniques to derive a final fused decision. There are also hybrid algorithms that apply different levels of fusions to yield more reliable and meaningful representations. For example, Piella (Piella 2003) proposed the combination of pixel- and feature-level fusions together. In his method, source images were segmented first and pixel-by-pixel fusion was performed based on the segmentations.

Among the existing image fusion techniques, one of the most straightforward algorithms is weighted average, which exhausts and fuses corresponding pixels in input images to generate a single output image (Stathaki 2008). Let $X^i = \{x_1^i, x_2^i, \dots, x_n^i\}$ be the i th source image, and $W^i = \{w_1^i, w_2^i, \dots, w_n^i\}$ be the associated weight of each pixel in the i th source image. Given M number of input

images, the resultant image X^f is then defined as:

$$X^f = \{x_k^f | x_k^f = \frac{\sum_{i=1}^M w_k^i x_k^i}{\sum_{i=1}^M w_k^i}, i \in [1, M], k \in [1, N]\} \quad (2.17)$$

Weighted average-based algorithms are fast and easy to implement, but determining optimal weights is very challenging, and the precision of the fused results rely heavily on the weights. Unless the optimal weights can be obtained, this type of approach has limited application.

Another widely applied image fusion is fuzzy logic. classical logic, or two-valued logic, deals with combinations of input variables, and infers conclusions according to a set of predefined rules. The conclusions are either true or false with no exceptions. However, there are some phenomena that can not simply be described as either true or false. For example, different people could have different answers to the weight of an object. Some people feel it heavy, some others believe it is neutral, whereas others think it light. In this case, classical logic is unable to fully describe the phenomenon. Accordingly, fuzzy logic is introduced to solve this problem. Fuzzy logic, introduced by Zadeh in 1960s (Zadeh 1965), is *a precise logic of imprecision and approximate reasoning* (Zadeh 2008) which transfers input space to output space, of which the former contains a set of variables, and the latter is a set of crisp values within the range $[0.0, 1.0]$ that represent the degrees of truth (Chen et al. 2000; MathWorks 2016). Due to its tolerance to imprecise data, and its capability to model non-linear functions with arbitrary complexity, it has been successfully applied to many scientific and engineering areas where data fusion is required, such as medical image fusion, remote sensing, and multi-sensor data fusion, to name a few (Teng et al. 2010; James et al. 2014; Khaleghi et al. 2013; Li et al. 2017; Puspanathan et al. 2014).

In general, fuzzy logic contains a few fundamental elements:

- Fuzzy sets or universal of discourse (UOD): a number of variables that describe existing phenomena, which are usually linguistic rather than numerical;
- Membership functions: a set of pre-defined functions that map input variables to the degrees of truth;

- Fuzzy logic operators: the amount of logic operators used to connect input variables, which usually contain three basic ones: intersection/conjunction, union/disjunction, and complement; and
- Fuzzy rules: a few of *if-then* rules for the formulation of conditional statements.

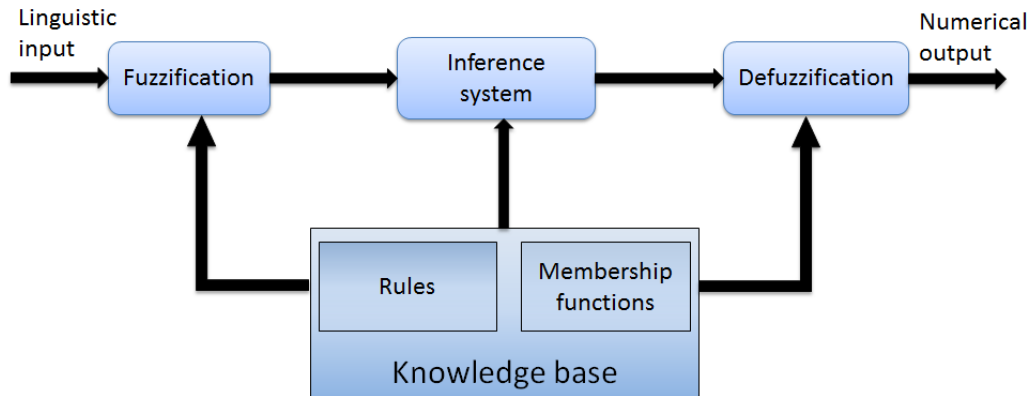


Figure 2.29: Schematic diagram of fuzzy inference process.

Based on these four elements, the general process of the fuzzy inference system can be split into 3 steps, as shown in Figure 2.29:

1. Transfer input values in a fuzzy set to membership degrees (numbers) between 0 and 1 using membership functions;
2. Interpret all the rules with the numbers in parallel to calculate the fuzzy output functions by aggregating all results from the interpretation; and
3. Defuzzify the aggregated output to a single number as the outcome of the process.

$$\mu_A(u) = \begin{cases} 1 & u \leq a \\ 1 - 2\frac{(u-a)^2}{(a-b)^2} & a < u \leq \frac{a+b}{2} \\ 2\frac{(b-u)^2}{(a-b)^2} & \frac{a+b}{2} < u \leq b \\ 0 & u > b \end{cases} \quad (2.18)$$

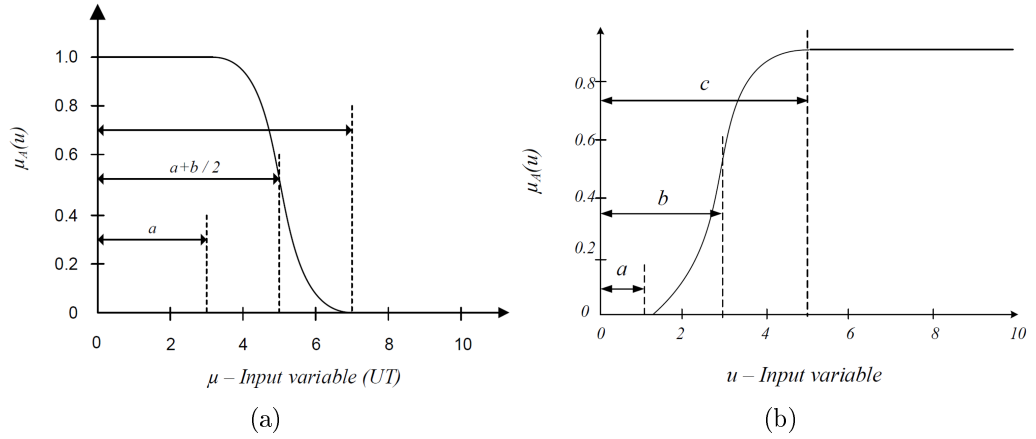


Figure 2.30: Membership functions employed in Pusppanathan's approach. (a) Z-shape function for UT, and (b) S-shape function for ECT (Pusppanathan et al. 2014).

$$\mu_A(u) = \begin{cases} 1 & u \leq a \\ 2 \frac{(b-u)^2}{(a-b)^2} & a < u \leq b \\ 1 - 2 \frac{(u-b)^2}{(c-b)^2} & b < u \leq c \\ 0 & u \geq c \end{cases} \quad (2.19)$$

In Pusppanathan's article, Z-shape and S-shape membership functions were utilised to fuzzify the input tomograms, the definition of the functions are defined in Equation 2.18 and Equation 2.19, and depicted in Figure 2.30 (Pusppanathan et al. 2014).

Modern image fusion techniques always transform original images to different scales, and perform actual fusion in the transformed scales. A widely applied example is the intensity-hue-saturation (IHS) transform, in which intensity refers to the brightness of a colour, hue refers to the most predominant wavelength of the colour, and saturation refers to the purity of the colour. IHS-based fusion is usually applied to the integration of high-spectral-resolution (multispectral) images and high-spatial-resolution panchromatic images. In general, multi-spectral images are first converted to IHS-formatted images, and then the intensity component is replaced by panchromatic images, and IHS inverse conversion is eventually performed to obtain a fused image (Tu et al. 2001; Li et al. 2010; Al-Wassai et al. 2011). The main issue associated with IHS-based methods is that colour information is distorted during the process since only spatial information is injected to the multispectral images.

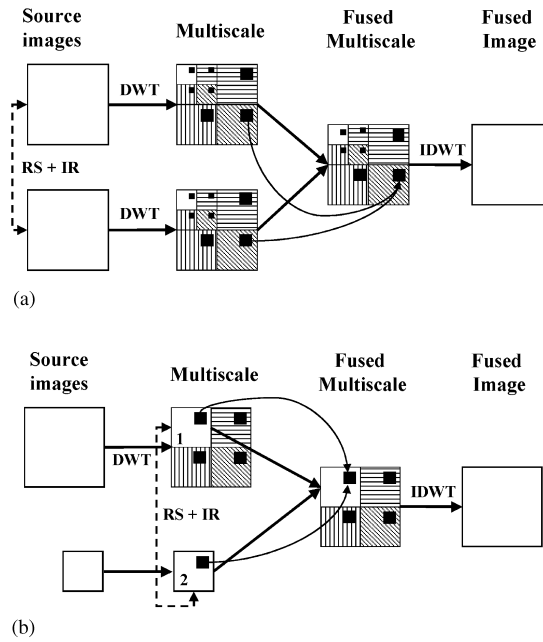


Figure 2.31: Generic fusion scheme using wavelet (Pajares et al. 2004).

Another important group of image fusion is wavelet-based image fusion techniques (Stathaki 2008; Li et al. 2017), along with the development of wavelet theory. Wavelet transforms are essentially multiresolution decompositions in image fusion, by means of using the idea that spatial details are reflected by high frequencies. In principle, detailed information is extracted from input panchromatic and/or multispectral images using wavelet transforms, and the decomposed information is either partially or entirely injected into the multispectral image. Finally, a fused image is generated after inverse wavelet transforms. A generic fusion scheme by wavelet is illustrated in Figure 2.31. Compared to IHS transform, wavelet-based fusion, in general, yields better results, particularly colour distortion problem, especially when advanced wavelet schemes are applied (Amolins et al. 2007).

At first glance, it seems trivial to directly apply those fusion algorithms to multiphase flow visualisation. This, nonetheless, actually introduces several technical challenges, rising from the fact that the spatial-resolution of electrical tomograms is too low to distinguish small bubbles below a certain size, as well as sharp edges between the dispersed phase and continuous phase. Comparing the modalities in medical imaging to electrical tomography, a significant difference is that electrical tomography is a 'soft field' tomographic technique, whereas the techniques for medical imaging are usually based on 'hard field', such as CT and X-ray (Wang 2015), which results in a noticeable difference on the spatial resolution of the

imaging. That is, hard field based tomographic systems produce tomographic images of higher spatial resolution than that by electrical tomographic systems. For example, advanced X-ray computed tomography is capable of detecting small particles at 1 mm level within a 60 mm bubble column, and thus generating high-quality reconstructed images (Fischer et al. 2010). Another example is that in (Manera et al. 2006), 16×16 WMS was applied to visualise gas-water flow in a pipe of diameter 47mm, thereby the minimal bubble that can be visualised is 2.9mm (47mm/16). In this case, the derived tomograms are able to deliver certain features of the investigated flow, such as bubble size and distribution. In contrast, electrical tomography normally has a spatial resolution of 5%, i.e. the ratio of the largest detectable object to the size of the container (Wang et al. 1999). This situation becomes worse when single-step LBP is involved for the reconstruction process. In addition to the limitations by the modalities, the nature of multiphase flow also introduces extra challenges, such as flow dynamics, which demands the involved fusion has to take account of temporal information.

Another prominent challenge for the data fusion in DMTS is that the resultant tomograms not only concern qualitative images to deliver informative content regarding flow dynamics, e.g. flow regimes, but also the quantitative outcome to reveal time-varying ratio of individual phases, which is usually secondary in other fields. From this perspective, conventional evaluation criteria in other data fusion are no longer predominant. Instead, the gap between the mean concentration from fused results and reference concentration is the primary criterion. Therefore, there are two criteria which should be utilised for the results of data fusion in DMTS: one is the fused tomograms to reference images, such as high-speed video logger, and the other is the fused mean concentration against reference concentration.

Given the electrical tomograms in Figure 2.32, it is rarely feasible to extract useful features regarding the exact spatial distribution of the gas phase, such as the edges between large bubbles and water. In consequence, feature-level image fusion is inapplicable to the tomograms directly. This inapplicability further makes the higher level image fusion, i.e. decision-level, unsuitable for electrical tomograms. Therefore, it seems only pixel-level fusion is eligible for image fusion by dual-modality ERT-ECT systems. It is worth noting that electrical tomograms are constructed by colour mapping based on reconstruction results, i.e. a set of scalar data that represent pixel concentration. In consequence, image fusion could

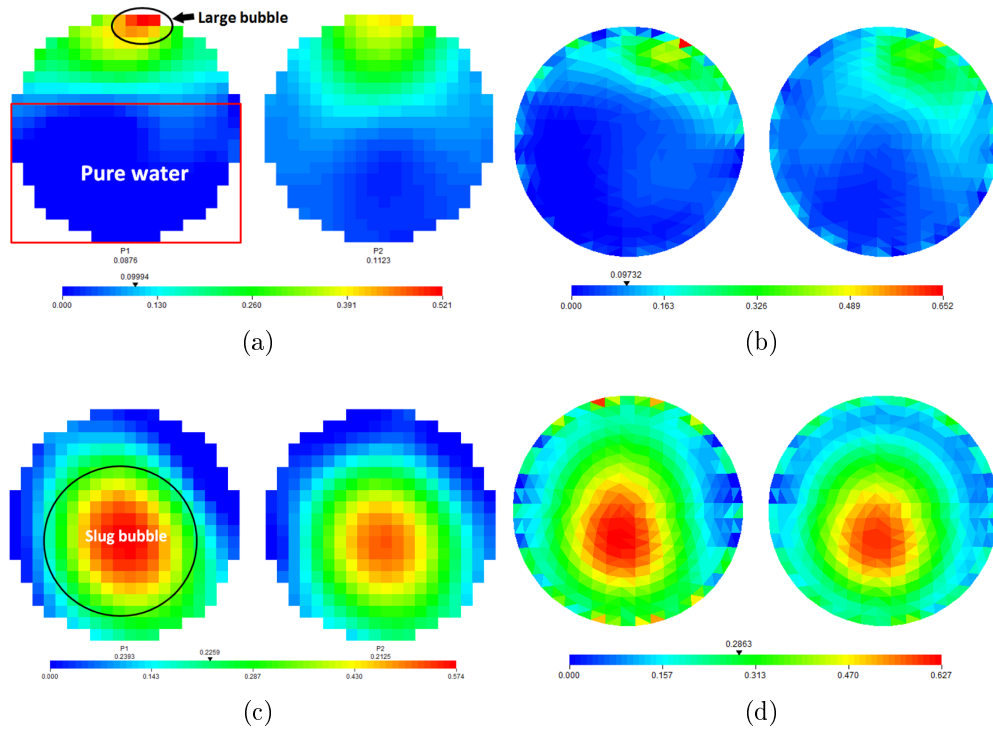


Figure 2.32: Examples of the incapability of electrical tomography to indicate small bubbles in bubbly flow by (a) LBP and (b) SCG, and sharp interface between phases in slug flow by (c) LBP and (d) SCG.

be performed either on scalar data or on the transformed images, i.e. tomograms. So far, the majority of research on data fusion in DMTS has been on the basis of the reconstructed scalar data, e.g. pixel concentration, but a few studies deal with the fusion directly on reconstructed images (Zhang et al. 2014).

2.3 Summary

Multiphase flow, such as gas-liquid and gas-oil-water three-phase flow, is a complicated and challenging area. Visualisation of such flow is a prominent way to provide an insight into such phenomenon. Electrical tomography is a type of non-intrusive/-invasive tomography which is able to provide spatial and temporal information regarding the flow. Existing methodologies of multiphase flow visualisation are reviewed, and the advantages/disadvantages of electrical tomography in gas-liquid and gas-oil-water flow are discussed. As far as electrical tomography

in multiphase flow visualisation is concerned, there are primarily two aspects needing more effort. One is the low spatial resolution of electrical tomograms that is unable to deliver sufficient flow dynamic information of gas-liquid flow, and the other is the data fusion when using dual-modality electrical tomography on gas-oil-water three-phase flow.

When using dual-modality electrical tomography to qualify and quantify gas-oil-water flow, there are several aspects which need careful consideration: the registration of the data from multiple dimensions, the fusion technologies working on the low spatial resolution of electrical tomograms, the decomposition of the involved phases, and the criteria for the quality of the fused images. Unfortunately, all these aspects have not been comprehensively examined so far. In this research, the above problems will be addressed, and the primary objectives are twofold: one is to sort out eligible fusion algorithms for dual-modality electrical tomography to visualise gas-oil-water flow, and the other is to evaluate the performance of the systems by the proposed algorithms.

Due to the limited spatial resolution and distinguishability, electrical tomograms hardly deliver the detailed information on gas-liquid flow, such as the boundaries between the gas and liquid phase. Although advanced visualisation algorithms in computer graphics may be helpful to reconstruct the large bubbles, they are hardly applicable to extract the small bubbles. Consequently, this study is going to explore the approach to extract small bubbles and reconstruct large bubbles based on electrical concentration tomograms so that the limitations could be overcome and hence unambiguous information could be presented.

Although modern electrical tomography is capable of producing tomograms of a high temporal resolution, it still generates unacceptable errors when characterising industrial flows at very fast speeds. This research will study the possible solutions to improve the temporal resolution of the electrical tomograms with minimum or with no modification of the existing hardware from two angles, including using fewer sensing electrodes or sensing a sub-area in the domain of interest.

In summary, this research is motivated by the desire to overcome the limitations of electrical tomography as single- and dual-modality tomographic system(s) on the visualisation of multiphase flow. In particular, it comprehensively discusses the data fusion for dual-modality electrical tomography on gas-oil-water horizontal

flow and thus proposes systematic methods to solve the problems. Later, it addresses the limitations of electrical tomograms on visualisation gas-liquid flow by a novel proposal. Finally, it investigates the improvement of the temporal resolution of an ERT system.

CHAPTER 3

METHODS OF DATA FUSION FOR VISUALISATION OF GAS-OIL-WATER FLOW

Highlights: This chapter explores the methods of data fusion for quantitative and qualitative visualisation of gas-oil-water pipeline flows in the use of dual-modality electrical tomography. First of all, a general framework is proposed, which reflects the general procedure engaged in the data processing of such systems, but independent of employed modalities and particular fusion techniques. Based on the framework, two data fusion techniques are proposed: one is thresholding assumptions using a priori knowledge, and the other is fuzzy logic. Both approaches are applied to experimental data obtained with ERT-ECT systems from an industrial flow facility. The capability and performance of the methods were evaluated with fast photography and the commonly recognised flow conditions to generate specific flow regimes. The experimental results demonstrate the feasibility of proposed approaches to visualise gas-oil-water flow, and further reflect the capability of ERT-ECT systems in the domain of multiphase flow measurement and visualisation.

3.1 Introduction

As discussed in CHAPTER 2, single-modality tomography is no longer feasible to retrieve individual phases in gas-oil-water three-phase flow and multi-modality tomography is needed for the decomposition of the phases. Despite that various combinations have been proposed to investigate such physical phenomenon, the research is still at an early stage, and the majority focused on the hardware itself, but only a little attention on data fusion. The engagement of DMTS inherently requires the processing of data from multiple dimensions, including space, time, and energy. Therefore, data fusion is unavoidable for DMTS. Moreover, compared with the fusion in other fields, DMTS has its unique characteristics, because it demands not only qualitative images but also quantitative results to reflect

time-varying flow dynamics, particularly when electrical tomography is employed. Therefore, a systematic study regarding the data fusion for DMTS is essential for the systems to deliver more informative content of gas-oil-water flow.

In this chapter, a general framework for multi-dimensional data fusion involved in multiphase flow imaging by DMTS is first proposed, so that the domain-specific data fusion process can be standardised to maximise the reflection of multiphase flow characteristics, while different fusion schemes can be incorporated into the framework seamlessly. In the meantime, the framework is designed to be independent of engaged modalities, and therefore can be used for any tomographic systems that produce cross-sectional concentration tomograms. Later, a thresholding approach is proposed for the visualisation of gas-oil-water flow by ERT-ECT systems and the relationship between the thresholding approach and weighted average scheme is discussed. The results are presented based on the experimental data from real-world industry-scale multiphase flow facilities. In addition, an advanced fusion scheme, i.e. fuzzy logic, is proposed, which is proven to be feasible and stable by using the same experimental data for the thresholding approach. Finally, the performance of dual-modality ERT-ECT systems in gas-oil-water flow visualisation is thoroughly evaluated using the thresholds-based approach.

3.2 TUV NEL multiphase flow facilities

The data used later on in this chapter was collected using TUV NEL¹ multiphase flow testing facilities. The NEL multiphase flow loop is a three component flow facility featuring oil, water and gas. Each component is measured individually using reference turbine flow meters prior to being combined into a multiphase mixture. After passing through the test section, the multiphase flow is then separated via a gravity separation vessel whereby the oil and water is re-circulated and gas is expelled to the atmosphere. A graphical representation of the flow facility is shown in Figure 3.1. The facility can achieve gas volume fraction (GVF) and water-liquid ratio (WLR) ranges from 0 to 100%. The target flow patterns are shown in Figure 3.2, and selected flow conditions are listed in Table 3.1, in terms of GVF against liquid flowrate. The testing objective was to evaluate the functional

¹<http://www.tuvnel.com>

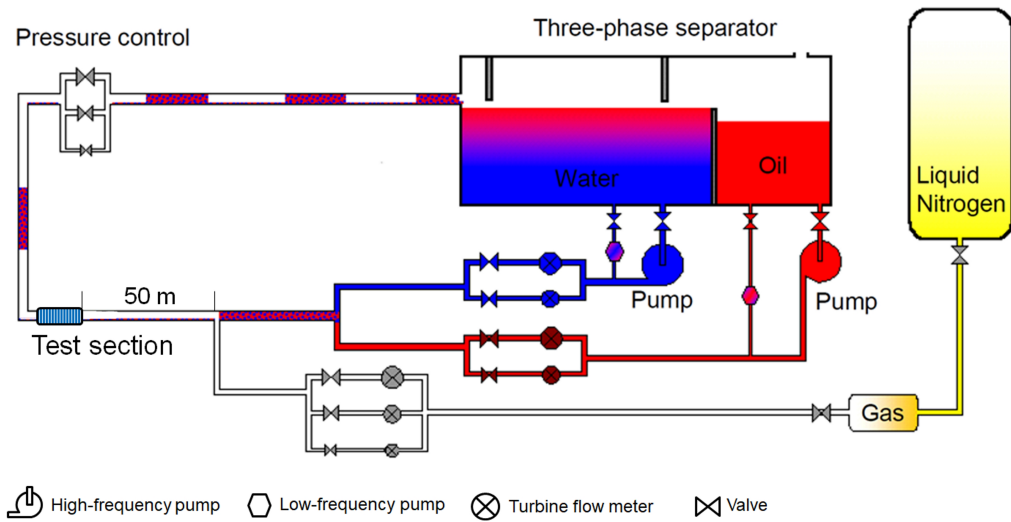


Figure 3.1: Schematic diagram of NEL multiphase flow facility (Wang et al. 2016b).

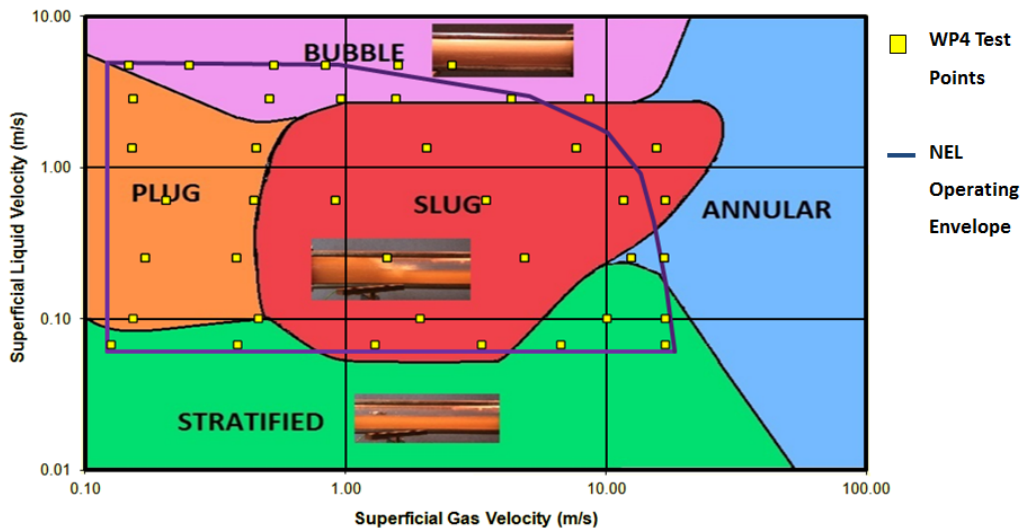


Figure 3.2: Target flow patterns (Wang et al. 2016b).

Table 3.1: Selected test conditions of liquid flowrate vs GVF.

GVF (%)	Liquid flowrate (m ³ /h)						
	2	3	7.5	18	40	85	140
3							x
5						x	x
10							x
15						x	x
25				x	x	x	x
35						x	x
40			x				
42			x				
60							
75						x	
82		x				x	
85	x		x	x	x		
92					x		
95	x	x	x	x			
96.5				x			
98	x		98.5				
99	99.6	99.4	x				

performance of dual-modality ERT-ECT systems in terms of multiphase flow visualisation. Several reference devices were installed in the test section, and the arrangement of the reference equipment is illustrated in Figure 3.2.

Table 3.2: Selected test conditions of liquid flowrate vs GVF.

	Gas	Oil	Water
Fluid	Nitrogen	Paraflex (HT9)	Salty water
Conductivity (<i>mS/cm</i>)	0	0	33.5
Dielectric constant (ϵ)	1	2.2	80
Dynamic viscosity (<i>cP</i>)	0.0174	16.18	1.35
Density (<i>kg/m³</i>)	12	830	1049.1

A 4-inch pipe was deployed for the experiments. On the test section, ITS ERT-ECT systems were mounted, after an inspection chamber for a high-speed camera to log flow structures as reference. The test section was positioned approximately

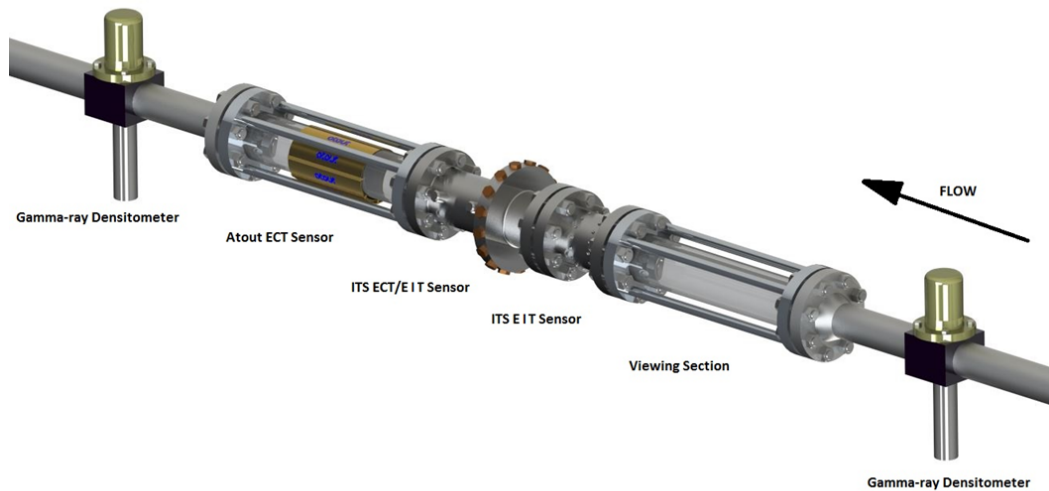


Figure 3.3: Arrangement of tomographic systems at test section line (Wang et al. 2016b).

50 metres away from component injection points, in order to let flow fully develop in the test section. In the experiments, Paraflex (HT9) oil was used alongside substitute salt water Magnesium Sulphate (MgSO_4) and a dry gas (Nitrogen) was injected externally via a pressurised storage tank, with pressure at 10 bars and temperature at 20 degree. The physical properties of each component are listed in Table 3.2. The combination of a full range of GVF and WLR enabled all common flow regimes observed for gas-liquid flow in horizontal pipe, including (wavy) stratified flow, slug flow, plug flow, annular flow, and bubbly flow.

3.3 A general framework for multi-dimensional data fusion

3.3.1 Introduction

An exemplary application of DMTS in multiphase flow measurement and visualisation is depicted in Figure 3.4. Signals are first collected by individual modality through equally-distributed sensors mounted on the surface of a pipe. Then, they are reconstructed to a certain number of scalars that represent the distribution

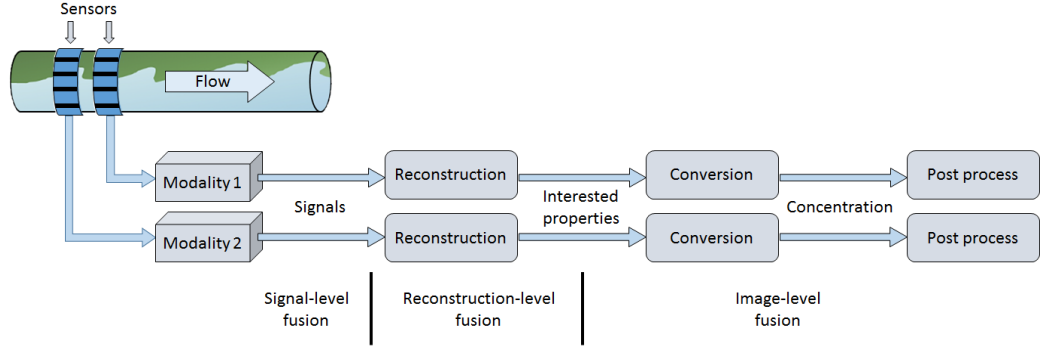


Figure 3.4: A typical scheme of the data processing for dual-modality tomographic systems in multiphase flow.

of interested properties, e.g. conductivity for ERT. Those numbers are further converted by Maxwell equation (Maxwell 1982) to concentration distribution of certain phase(s) in multiphase flow. For example, in the case of ERT, reconstructed results are conductivity distribution, which is further converted to the concentration distribution of disperse phase, e.g. gas and oil in gas-oil-water flow. Before being displayed, there may be some other post process, e.g. filtering abnormal data.

As previously discussed, data fusion for such applications is conducted after the reconstruction process. That is, the signal collection and reconstruction process are individually performed by each modality. As a result, data fusion in DMTS for multiphase flow visualisation is at image level, as depicted in Figure 3.4. On one hand, since the reconstructed images/tomograms are transformed from the scalar data representing different properties by colour mapping, the fusion could be carried out on the scalar data or on the transformed images/tomograms, i.e. data fusion or image fusion. Due to the low spatial resolution, along with the impact from the limitations of electrical tomography, the fusion directly on the images seems barely feasible. In consequence, the fusion in this study will be based on the data. On the other hand, the fusion could occur after the reconstruction but before the conversion, i.e. reconstructed tomograms, or after the conversion, i.e. concentration tomograms, as shown in Figure 3.4. Although reconstructed tomograms reveal certain phase distribution of multiphase flow, they are tomography specific thereby reflecting different energy information, e.g. conductivity for ERT, or permittivity for ECT. Therefore, it is extremely challenging to integrate the reconstructed tomograms directly. In this study, the fusion is based on concen-

tration distributions. Combining the aforementioned considerations, the rest of this study is carried out on pixel-level data fusion of concentration distributions¹.

3.3.2 The general framework

Considering the characteristics in multiphase flow visualisation by dual-modality tomographic systems, the framework should: (i) be general so that it is independent of employed tomographic systems; (ii) seamlessly incorporate any possible fusion algorithms into it, so that it does not rely on any specific fusion techniques; (iii) be able to take account of the data from space, temporal, and energy dimensions, in order to reveal more flow dynamics, e.g. flow regimes; and (iv) be potentially suitable for visualising two-phase and three-phase flows.

In order for the framework to be independent of tomographic systems, it needs to be fed into the data without tomography-specific information, e.g. conductivity or permittivity. Concentration distributions, on the other hand, are the eligible option since they reflect the geometrical distributions of certain phase(s), instead of particular properties. Therefore, the input for the framework is concentration distributions.

Generally, pixel-level data fusion requires the input data to represent the same physical phenomenon and be spatially and temporally registered, so that during the integration, all pixels are involved, and no subtle information is missed. When a dual-modality tomographic system is deployed on a pipeline flow, each modality certainly monitors exactly the same flow phenomenon. If concentration distributions derived by each modality are spatially and temporally different, they have to be aligned before a particular fusion algorithm is applied. Concentration distributions by tomographic systems for pipeline flow are usually presented in 2D cross-sectional disk-shaped mesh of a certain size, e.g. 20×20 for the ERT system, and 30×30 for the ECT system used in this study, in which case, spatial alignment is in demand. In addition, temporal alignment has to be considered when deployed modalities work at different speeds. Afterwards, any feasible fusion algorithms could be applied for the actual integration.

¹The term *concentration distributions* means the data representing 2D cross-sectional concentration tomograms. *Distribution* and *tomogram* are used interchangeably in the rest of this chapter, unless otherwise stated.

The engagement of DMTS always requires methods that allow the data from multiple dimensions to be fused effectively, including, but not limited to, space, time, and energy (Hoyle et al. 2012). Spatial fusion involves the geometrical combination of the images at different times and/or from different modes and thus is critical for resolving the phase distributions. Temporal fusion engages the transformation of local times by each mode to a common time axis, so that the images to be fused reflect the interesting objects occurring at the same time. Since temporal contents are linked to the properties under investigation, temporal fusion is critical for reflecting property dynamics. Data fusion concerns the integration of the data, i.e. properties of interest, from two or more modes, or from one mode with a different frequency, of which the properties are responsible for the decomposition of different phases. As a result, all dimensional information has to be integrated to reveal as much flow dynamics as possible.

When DMTS is deployed for two-phase flow, the major objective is to enhance the spatial resolution of individual modality, whereas for three-phase flow, it is to decompose the phase distribution of each phase in the flow, which is impossible to derive by individual modality. No matter what the purpose is, both applications need to follow the same procedure before and after fusion, except the actual fusion algorithm may be different. Consequently, the framework could be easily utilised for both cases.

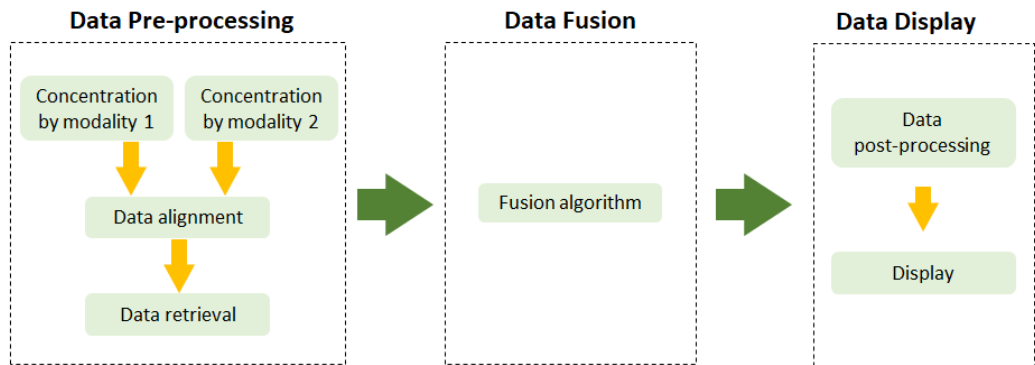


Figure 3.5: Schematic diagram of the general framework.

The general framework is depicted in Figure 3.5, which contains three steps, namely data pre-processing, data fusion, and data display. In data pre-processing, input tomograms are spatially and temporally aligned firstly if the modalities work at different frequencies and generate different sized tomograms, and then

useful information is retrieved from input concentration distributions. Afterwards, actual fusion occurs, where a particular fusion technique is applied, which could be any one that deals with pixel-level data fusion. After the actual fusion, the fused data may need further process, e.g. to remove abnormal data, before it is presented for human and/or machine perception. A common approach for the display is colour mapping, i.e. transforms data into colours according to a lookup table (Hansen et al. 2011).

3.3.2.1 Data pre-processing

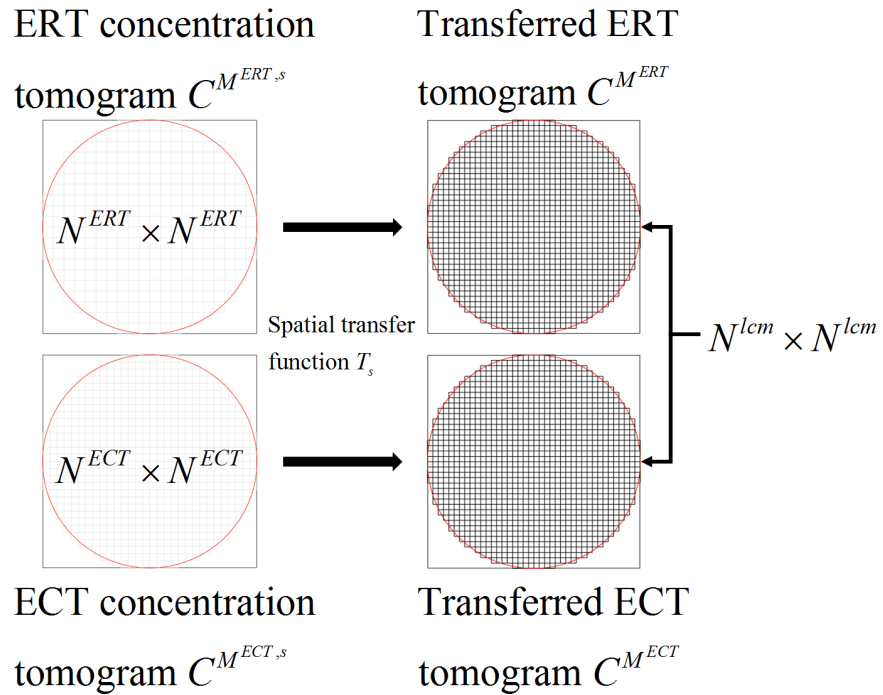


Figure 3.6: Tomograms of a 316-pixel grid in a 20×20 square mesh and an 896-pixel grid in a 30×30 square mesh for pipeline flow (Wang et al. 2017).

The overall objective of data alignment/registration is to transfer the data from the original coordinate systems to a new common coordinate system, so that the transferred data represents the same information with the same coordinate system (Mitchell 2012). In the case of multiphase flow imaging by DMTS, the grid definitions of the tomograms are determined when the working modes of the modalities are selected, and the grids are usually disk-shaped which represents the cross-sectional area of a pipe, which are subtracted from a regular $N^m \times N^m$

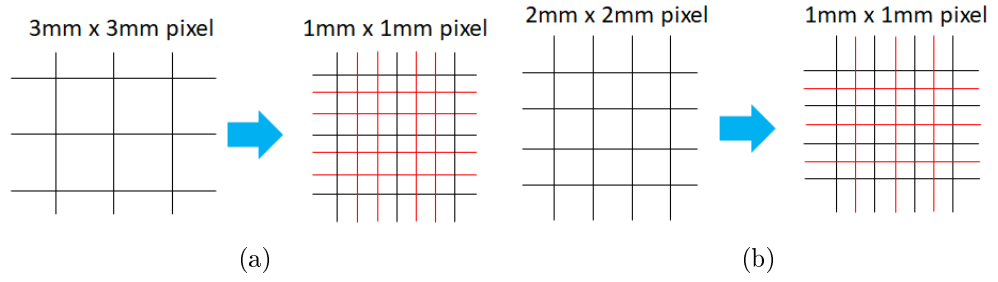


Figure 3.7: Transformation of the original pixels (a) from $3mm \times 3mm$ pixel to $1mm \times 1mm$ pixel; and (b) from $2mm \times 2mm$ pixel to $1mm \times 1mm$ pixel.

square mesh, where m is the modality. Figure 3.6 illustrates an example, in which the left tomographic system produces a grid with 316 elements in 20×20 mesh, and the right one generates an 896-element grid in a 30×30 mesh. Consequently, the spatial alignment is to resample the grids into a new grid in a new square mesh so that the original pixels to the resampled still physically correlate with each other after transformation, i.e. representing a corresponding physical location in cross-section.

Let the diameter of the monitored pipe be D , and the mesh definition of each tomogram is $N^m \times N^m$, where m is either 1 or 2 to represent the first and second tomographic systems. The actual pixel size in each tomogram is then determined by D/N^m . When $N^1 = N^2$, i.e. the tomograms from each modality have the same grid definition, spatial alignment is not needed. Otherwise resampling is required. A simple way to find an appropriate mesh is to obtain the least common multiple of N^1 and N^2 , by which the original pixels can be evenly split into smaller pixels. After the split, the resampled pixels now have the same size and are physically aligned.

Following the example in Figure 3.6, for a given pipe with diameter a 60 of mm, the pixel size in the first tomogram is $60/20 = 3mm$, and the second one is $60/30 = 2mm$. Accordingly, the pixel in the first tomogram is split into 3×3 finer pixels, while the second one is split into 2×2 finer pixels. As a result, the original tomograms are resampled from 20×20 mesh and 30×30 mesh to 60×60 mesh, and the resultant pixel is now $1mm \times 1mm$. Figure 3.7 illustrates the transformation.

When finite element method (FEM) is utilised for image reconstruction, the grid

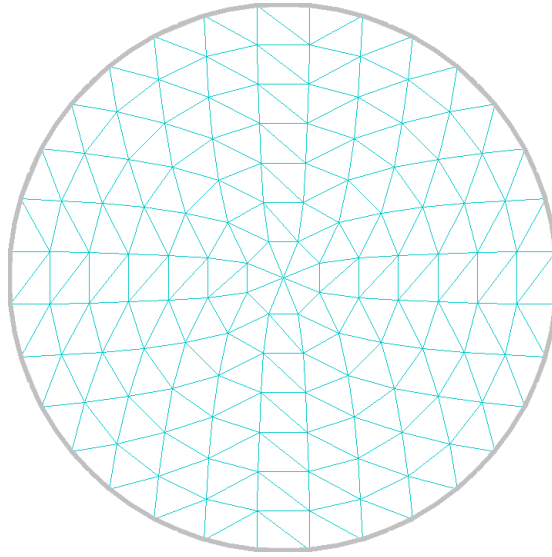


Figure 3.8: A triangulated grid with 248 elements by SCG.

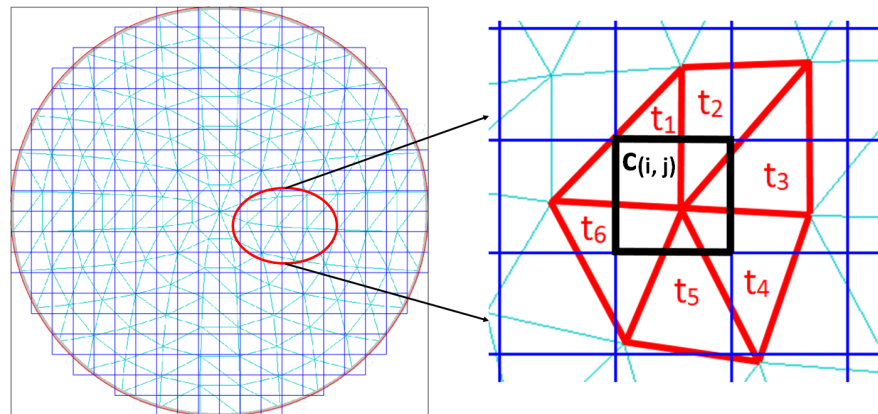


Figure 3.9: Overlapping a 248-element irregular grid with a 316-element regular grid and transforming from the old grid to the new grid.

is usually unstructured because of the triangulation. Figure 3.8 illustrates an example of irregular grid with 248 elements, generated by SCG software (Wang 2002). Spatial registration, therefore, is required to regularise the unstructured grid. A simple approach for the regularisation is overlapping the original unstructured grid and a resampled regular grid, and averaging a number of triangular pixels in the original grid that correspond to a square pixel in the targeting grid. Figure 3.9 shows an example of the overlapping and transformation from a 248-element irregular grid to a 316-element grid in a 20×20 regular mesh. By zooming in a certain area, as depicted in the right side of Figure 3.9, it shows that for a square pixel at (i,j) , there are 6 triangular pixels, i.e. t_1, t_2, t_3, t_4, t_5 , and t_6 , in the original mesh. Accordingly, the pixel concentration at (i,j) is derived by $c_{i,j} = \frac{1}{6}(t_1 + t_2 + t_3 + t_4 + t_5 + t_6)$. After exhausting all pixels in the targeting mesh, the original irregular grid is then transformed to a structured square mesh. If there is only one irregular mesh in the two tomograms input from different modalities, the structured mesh of one tomogram can be used as a targeting mesh, to which the irregular one can be transformed into. If both tomograms are reconstructed on irregular mesh, a common regular square mesh has to be defined so that all original meshes can be converted to the same representational coordinate system.

Taking account of both situations, a spatial transform function T_s can be conceptually defined as $T_s : (C^{M^{1,s}}, C^{M^{2,s}}) \rightarrow C^M$, which means the original tomograms with $M^{m,s}$ mesh are transformed to the target with a $M = N \times N$ structured square mesh, where m is either 1 or 2 to represent different modalities. If both tomograms are built on regular mesh, i.e. $M^{m,s} = N^m \times N^m$, a resampled mesh can be defined as $M = N^{lcm} \times N^{lcm}$, where N^{lcm} is determined by the least common multiple of N^1 and N^2 , i.e. $N^{lcm} = LCM(N^1, N^2)$. When one mesh is irregular, e.g. $M^{1,s}$ is an irregular mesh, and the other mesh is a regular mesh, i.e. $M^{2,s} = N^2 \times N^2$, $M^{1,s}$ can be transformed to the second mesh $M^{2,s}$. That is, the transform function T_s is $T_s : (C^{M^{1,s}}, C^{N^2 \times N^2}) \rightarrow C^{N^2 \times N^2}$. In the case where both meshes are unstructured, a common regular square mesh $M = N \times N$ can be defined, so that the original meshes are converted to the regular mesh by $T_s : (C^{M^{1,s}}, C^{M^{2,s}}) \rightarrow C^{N \times N}$.

As far as temporal information is concerned, the sampling frequency is fixed at a given tomography. That is, the time interval between any two consecutive tomograms by a tomographic system is constant. Let the data acquisition speed of

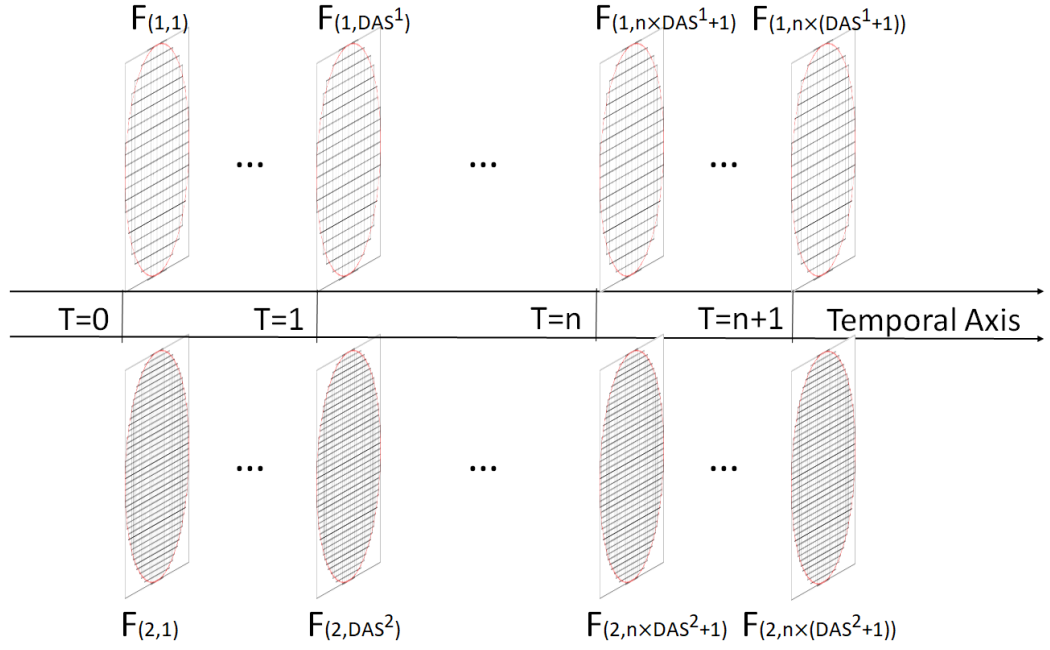


Figure 3.10: Temporal alignment of two sets of tomograms by the modalities with the speed of DAS^1 and DAS^2 .

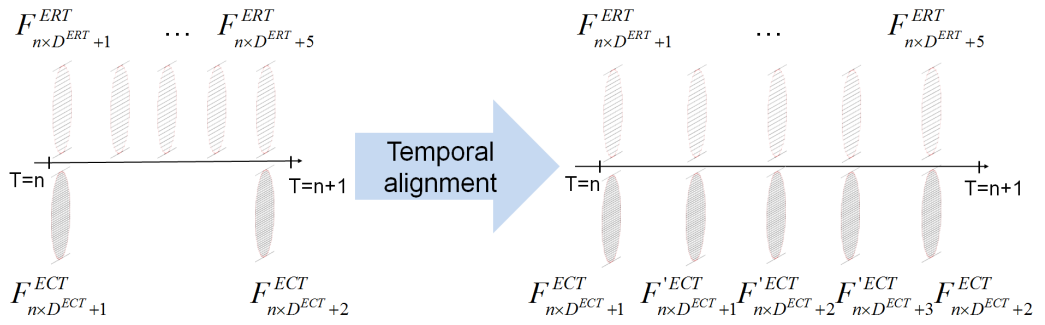


Figure 3.11: Temporal alignment of two sets of tomograms from $DAS^1 = 4$ and $DAS^2 = 2$ to $DAS^{lcm} = 4$ (Wang et al. 2017).

a tomograph be DAS^m frame/second (fps), i.e. DAS^1 and DAS^2 is the number of frames collected by each modality for every second, as shown in Figure 3.10. If $DAS^1 = DAS^2$, temporal alignment is unnecessary, or otherwise is demanded. Since the interval is constant, a similar strategy for the spatial alignment can be applied for temporal alignment. In other words, let DAS^{lcm} is the least common multiple of the DAS^1 and DAS^2 , i.e. $DAS^{lcm} = LCM(DAS^1, DAS^2)$, and T_t is the temporal transform function, which is conceptually defined as $T_t : F^{DAS^m} \rightarrow F^{DAS^{lcm}}$. By the transformation, the original DAS^m number of frames in a second is resampled into the DAS^{lcm} number of frames, and thus the frames from each tomography are temporally aligned. Figure 3.11 depicts an example of temporal alignment, in which $DAS^1 = 4$ and $DAS^2 = 2$, and hence $DAS^{lcm} = 4$. As a result, two frames $F'_{(2,DAS^2+1)}$ and $F'_{(2,DAS^2+2)}$ are inserted into the second tomogram sequence between $F_{(2,DAS^2+1)}$ and $F_{(2,DAS^2+2)}$, which can be approximated by interpolation.

At this point, the original two sets of tomograms are transformed into another two sets of tomograms which are spatially and temporally aligned. Each tomogram has the same spatial resolution of $M = N * N$. In addition, the numbers of the tomograms by each modality is identical and distributed homogeneously along the temporal axis, where there are $DAS^{lcm} = LCM(DAS^1, DAS^2)$ number of tomograms per second. The aligned tomograms are used as the input for the data retrieval sub-process.

In order to incorporate temporal information into fusion results, the input 2D cross-sectional concentration tomograms need to be stacked sequentially. When the investigated flow in horizontal pipeline is fully developed, it is reasonable to assume that the tomograms are symmetrical to its vertical diameter. Thus, a few columns at the central area of a tomogram can be utilised to represent the original tomogram. By averaging the columns and stacking the averaged results of the input tomograms, spatial and temporal information is integrated together, and hence flow regimes can be revealed. In the meantime, it is also helpful to dramatically reduce computation time, which can be used for online investigation purpose. Therefore, the next step is to retrieve axially-stacked concentration tomograms from the aligned dataset.

Let $T^m = \{F^{i,m} \mid i \in \{1, 2, \dots, Q\}\}$ denote two sets of aligned concentration tomograms, where m is 1 or 2 to represent the first and the second tomographic

systems. Let $C^{i,m} = \{c_x^{i,m} | x \in \{1, 2, \dots, N * N\}\}$ denote the i th two-dimensional cross-sectional concentration tomogram with a spatial resolution of $N \times N$. The resultant axially-stacked tomograms can be written as:

$$S^m = \{s_{x,y}^m | s_{x,y}^m = \frac{1}{A} \sum_{a=1}^A c_{idx+(a-1)*m}^{y,m}, \quad (3.1)$$

$$x \in \{1, \dots, N\}, y \in \{1, \dots, Q\}\}$$

where idx is the starting index of the selected central area in a tomogram, and A

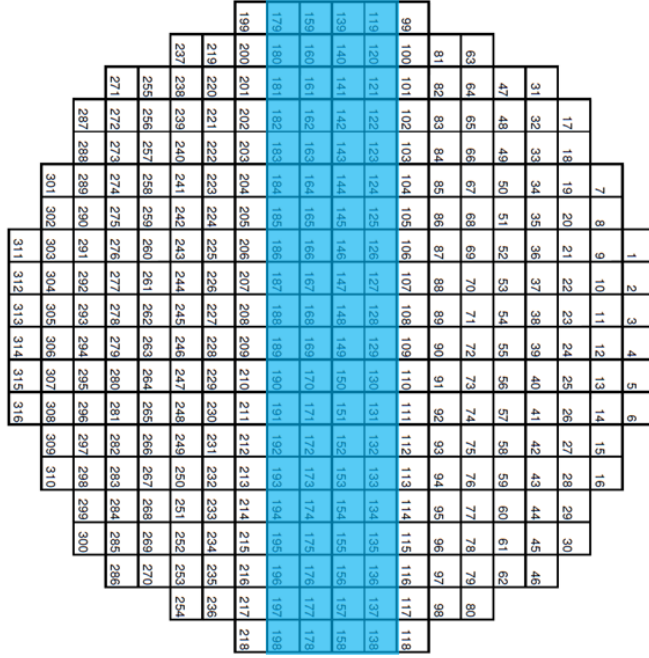


Figure 3.12: An example of extracting the central 4 columns of data from a 20×20 tomogram.

is the number of columns to be averaged in the central area. Taking the tomogram with the mesh of $20 * 20$ in Figure 3.12 as an example, suppose 4 central columns are selected for the average (as the colour-masked area in Figure 3.12), the idx in Equation 3.1 is then 119, A is 4, and N is 20. As a result, Equation 3.1 can be written as:

$$S^m = \{s_{x,y}^m | s_{x,y}^m = \frac{1}{4}(c_{119}^{y,m} + c_{139}^{y,m} + c_{159}^{y,m} + c_{179}^{y,m}), x \in \{1, \dots, 20\}, y \in \{1, \dots, Q\}\}$$

Accordingly, for a given sequence of tomograms, a stacked tomogram of axial cross-section can be obtained, and Figure 3.13 illustrates the generation of an

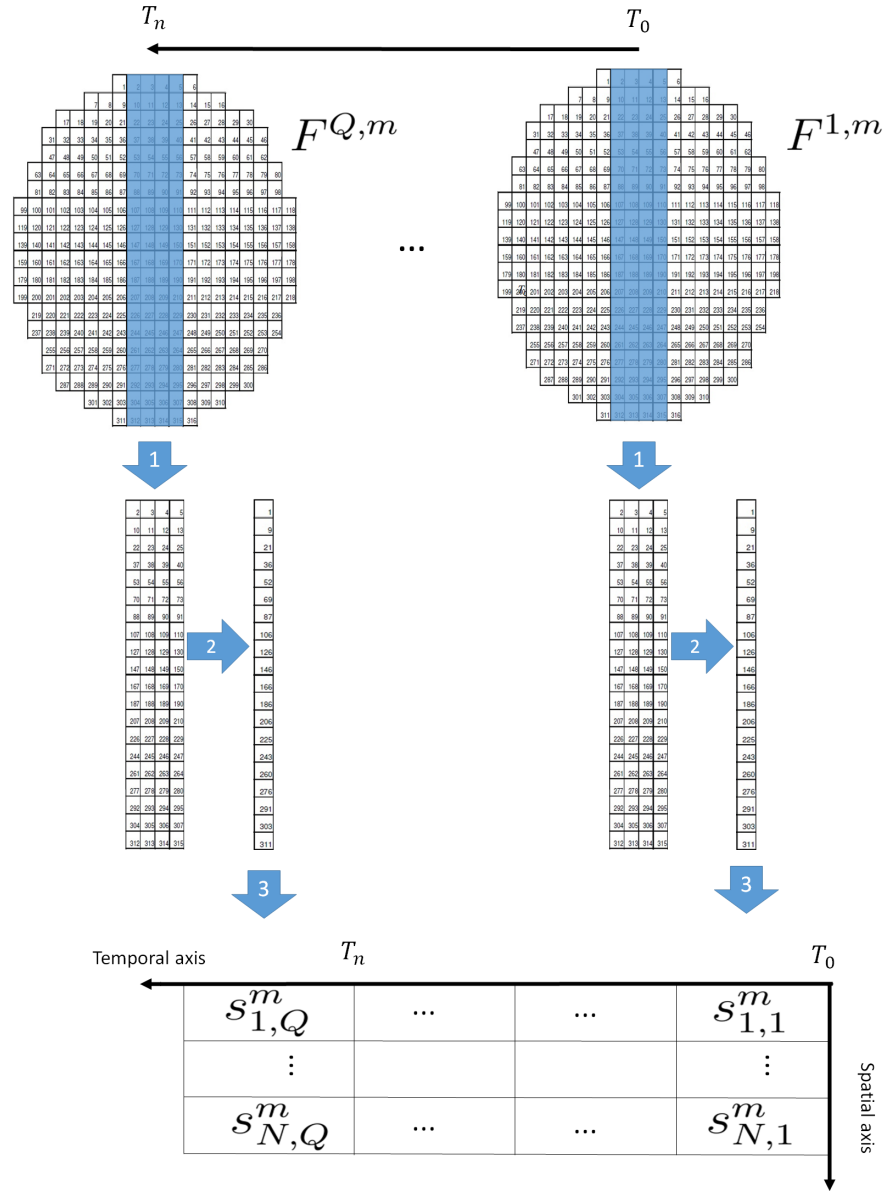


Figure 3.13: Data retrieval and average from a sequence of 2D cross-sectional concentration tomograms (Wang et al. 2017).

axially stacked concentration tomogram from a sequence of concentration tomograms in Figure 3.13,. The spatial information in the original tomogram is approximated by averaging a few columns in the central area, while the temporal information is reflected by stacking the sequential tomograms by a modality.

After data pre-processing, two axially stacked tomograms are generated with the same resolution. That is, both tomograms contain $Q \times N$ number of pixels, where Q is the length of the input tomograms, and N is the mesh dimension of the input tomograms. In addition, the tomograms are able to reflect the distributions of certain phase(s) in an investigated flow, as well as the flow regime information of the flow. Now, a particular data fusion algorithm can be applied to integrate both tomograms so that individual phase can be decomposed and thereby the flow can be visualised.

3.3.2.2 Data fusion

The purpose of the fusion for imaging multiphase flow by DMTS is to decompose an individual phase in the flow based on input tomograms and, therefore, obtain phase distributions for visualisation, and phase mean concentrations for measurement. From a visualisation point of view, the investigated flow should be visualised in a way that each component should be distinguished with clear boundaries between the components, without any ambiguity for human perception. From a measurement perspective, the results should be as precise as possible by comparing with reference values. Because actual fusion is directly on scalar data, i.e. concentration distributions, the outcome by data fusion therefore is 2D geometrical distributions of involved phases.

Due to the characteristics of multiphase flow imaging by DMTS, data fusion has to be carried out after image reconstruction. Since tomograms are produced using colour mapping, on the basis of the reconstruction result, the actual integration could be on reconstructed data directly, or on tomograms, i.e. the images that represent the distribution of interested properties. Due to the particularities of tomograms, such as blurred interfaces among phases and invisibility of small bubbles below a certain size, it is rarely feasible to extract meaningful and useful features, and thus fusion at the levels other than pixel-level is extremely challenging. So far, existing fusion techniques for imaging multiphase flow by

DMTS are all on a pixel-by-pixel basis. Later on in this chapter, two specific fusion algorithms will be discussed, which can be seamlessly incorporated into this framework.

3.3.2.3 Data display

Prior to the displaying of fused images, some post-processing may be required. For example, systematic errors or random errors during measurement are inevitable, and usually propagate till the end of the whole procedure. Meanwhile, artificial uncertainties could also be introduced during data processing. In consequence, fused results may contain unreasonable values, such as concentrations larger than 100%, which severely affect the final display. In this case, the data needs to be further dealt with, e.g. by filtering or normalisation.

After post-processing, the data is ready for visualisation. A predominant visualisation approach for scalar data is colour mapping, i.e. transferring scalar data to different colours according to a lookup table (Hansen et al. 2011). Let $P = \{p_i | i \in \{1, 2, \dots, N * Q\}\}$ denote fused results. Every p_i comprises two or three components for two-phase or three-phase flow respectively. The relationship between each phase for pixel p_i is governed by:

$$p_i = \{(\alpha_i^1, \alpha_i^2, \alpha_i^3) | \alpha_i^1 + \alpha_i^2 + \alpha_i^3 = 1, \alpha_i^x \in [0, 1]\} \quad (3.2)$$

where α_i^x is the concentration value of the phase x . A colour space $C = \{c_i | i \in \{1, 2, \dots, N \times Q\}\}$ can be defined as:

$$c_i = (r_i, g_i, b_i), i \in \{1, 2, \dots, N \times Q\}, \text{ and } r_i, g_i, b_i \in [0, 255] \quad (3.3)$$

where r , g , and b are the fundamental colours in RGB space, i.e. red, green, and blue. A generic transfer function is then defined as $T : P \rightarrow C$.

When the flow investigated contains two components, e.g. gas-water flow, a colour lookup table with a linearly-distributed scale can be defined, as shown in Figure 3.14a. The colour lookup table is one of the dominant approaches in tomography-based two-phase flow visualisation. When three-phase flow is involved, the lookup table is no longer suitable, due to the number of components in the flow. Alternatively, a triangular colour space is required, as depicted in

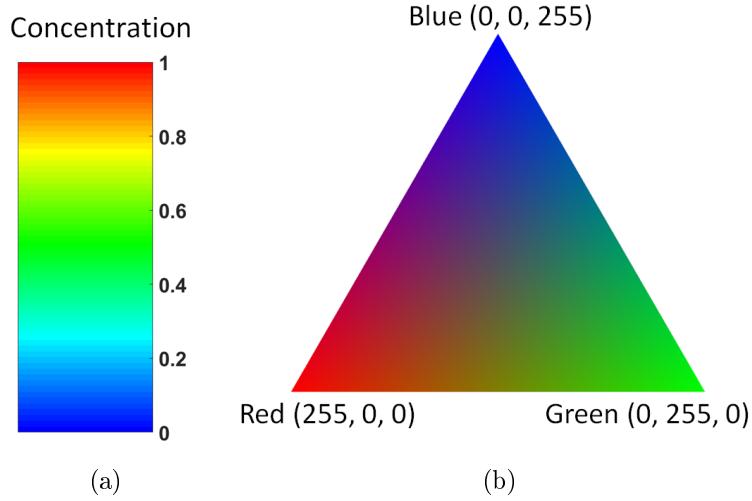


Figure 3.14: (a) a colour lookup table for two-phase flow, and (b) a triangular colour lookup table for three-phase flow.

Figure 3.14b, in which the vertices are blue, red, and green, and colours continuously distribute within the triangle. Based on Equation 3.2 and Equation 3.3, the transfer function T can be defined using matrix multiplication:

$$[r_i \ g_i \ b_i] = [\alpha_i^1 \ \alpha_i^2 \ \alpha_i^3] \begin{bmatrix} 255 & 0 & 0 \\ 0 & 255 & 0 \\ 0 & 0 & 255 \end{bmatrix} \quad (3.4)$$

3.3.3 Conclusions

A general framework is proposed for multiphase flow visualisation by DMTS, based on the characteristics in this field, due to the involvement of DMTS, as well as the nature of multiphase flow. The proposed framework is fed by two sequences of concentration tomograms, instead of the tomography-specific tomograms, and hence is independent of employed modalities. Multi-dimensional information implied in the tomograms is retrieved after they are aligned spatially and temporally, and therefore capable of revealing flow dynamics, such as flow regimes. Afterwards, any fusion algorithms could be applied to the pre-processed 2D axially-stacked concentration tomograms to perform actual integration, providing they focus on pixel-by-pixel data fusion. Finally, the fused data is displayed using conventional colour mapping.

Various frameworks have been proposed for data/image fusion, such as those for multi-sensor data fusion (Carvalho et al. 2003; Blum et al. 2005), the one for multiresolution image fusion (Piella 2003), and for functional medical image fusion (Barra et al. 2001). Compared with these frameworks, the one presented shares some common features. For example, the overall procedure can be generally separated into three sub-processes: data pre-process, actual fusion process, and data post-process.

Our framework, on the other hand, is fundamentally different from others, due to the nature of multiphase flow as continuous yet time-varying physical phenomena, as well as the unique characteristics of the data fusion and visualisation involved in the characterisation of gas-oil-water three-phase flow by DMTS, e.g. relatively low spatial resolution of the images, and evaluation metric for the fused results, the processing for DMTS introduces some additional challenges, and hence conventional frameworks in general data/image fusion have to be modified/enhanced to be suitable for DMTS.

It is expected that the proposed general framework could be a universal guideline for fusing and visualising multi-dimensional data from DMTS. In addition, the framework could enable researchers to pay more attention to the data fusion algorithm more suitable for their particular case. It is also anticipated that through the framework, the impact of the modality-special tomograms on the fused results, and the advantages and disadvantages of the deployed fusion algorithm could be estimated in advanced in order for the users to approximate the uncertainty of the procedure. Although the framework is proposed for dual-modality ERT-ECT systems, it is potentially applicable to other modalities since it is based on concentration tomograms/images regardless of modalities.

In the following chapters, two specific fusion algorithms will be addressed, based on the proposed framework. The application of the algorithms will prove the feasibility of the proposed framework for visualising three-phase flow by dual-modality electrical tomographic systems, while the utilisation of the framework also evaluates the capabilities of the proposed aggregation schemes.

3.4 Thresholding method

3.4.1 Introduction

In this section, a novel approach is proposed, by integrating threshold-based fusion method with the aforementioned framework, to visualise the common flow regimes in industry-scale pipeline flow by dual-modality ERT-ECT systems. This approach makes full use of the advantages which implicitly reside in the framework and the simplicity of the threshold-based fusion algorithm to aggregate tomographic data from ERT and ECT systems, so that the results are able to convey multi-dimensional information in spatial, temporal and frequency terms. The evaluation of the approach, in terms of both aggregated images and averaging concentrations of individual phases, by industry-scale testing facilities proves the eligibility of the proposal to deal with common flow regimes in horizontal pipe, including stratified flow, slug flow, plug flow, annular flow, and bubbly flow.

3.4.2 The approach

The principle behind the threshold-based fusion is on the basis that one modality is able to distinguish one phase from gas-oil-water flow, while the other modality is suitable for differentiating another phase from the flow. The tomograms by each modality are binarised to extract individual phase. By combining the binarised information together, the third phase can be extracted. In the case of ERT-ECT systems, ECT is able to separate gas from the liquid (oil and water) phase, while ERT can retrieve water from the flow. After integrating both tomograms by ERT and ECT, the oil phase can be derived, thereby the concentration distribution of each phase can be obtained.

Let $S^m = \{s_{x,y}^m | x \in \{1, \dots, N\} \text{ and } y \in \{1, \dots, Q\}\}$ be the aligned data of the modality m , T^m be the threshold value to binarise the aligned data S^m , and p_x , where $x = 1, 2, \text{ or } 3$, be the components in the gas-oil-water flow. Let $F = \{f_{x,y}, x \in \{1, \dots, N\} \text{ and } y \in \{1, \dots, Q\}\}$ be the fused data. In general, suppose p_1 in S^1 can be distinguished by modality 1 using a threshold value T^1 , and p_2 in S^2 can be distinguished by modality 2 using a threshold value T^2 , $f_{i,j}$

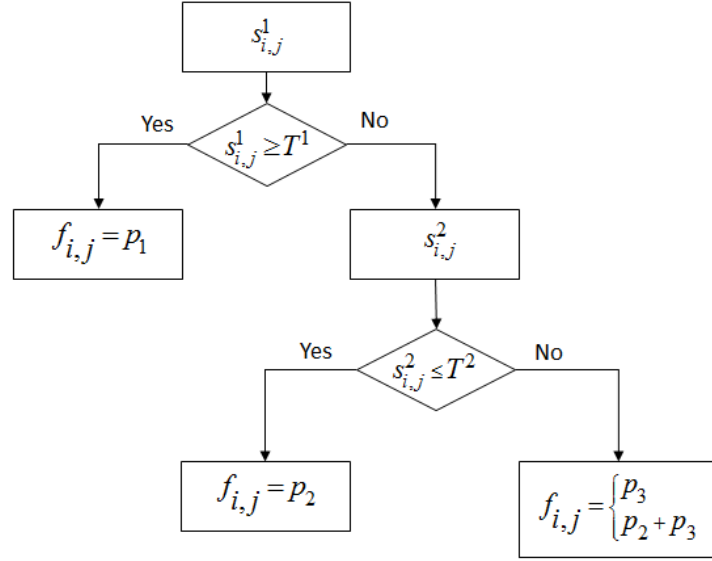


Figure 3.15: Data flow for pixel-based thresholding fusion scheme.

is then calculated by:

$$f_{i,j} = \begin{cases} p_1 & s_{i,j}^1 \geq T^1 \\ p_2 & s_{i,j}^2 \leq T^2 \\ p_3 \text{ or } p_2 + p_3 & \text{otherwise} \end{cases} \quad (3.5)$$

The corresponding data flow of the fusion process is shown in Figure 3.15. A pixel concentration $s_{i,j}^1$ is first compared to the threshold T^1 . If it is beyond the threshold, the fused pixel $f_{i,j}$ is phase p_1 . Otherwise, a corresponding pixel concentration $s_{i,j}^2$ from the second aligned tomograms is examined to check whether it is less or equal than the other threshold T^2 . If so, the relevant pixel in the result is occupied by phase p_2 , or otherwise it is either phase p_3 or a mixture of p_2 and p_3 , depending on the selection of the threshold T^2 . In the latter case, the relevant pixel value is determined by $s_{i,j}^2$, i.e. $f_{i,j} = s_{i,j}^2$.

Taking an example of the method in (Qiu et al. 2007), suppose S^1 are the tomograms by ECT, S^2 are the tomograms by ERT, and p_1 , p_2 , and p_3 are gas, oil, and water components, T^2 in the method is to distinguish water from the components and, therefore, the related result is oil phase when the pixel value is larger than the threshold. That is, the ERT tomograms are binarised as either water or oil, in which case a pixel in the fused tomograms hosts one and only one phase, instead of a mixture. The situation becomes different in (Wang et al. 2017), where a different threshold value is chosen to differentiate pure water or

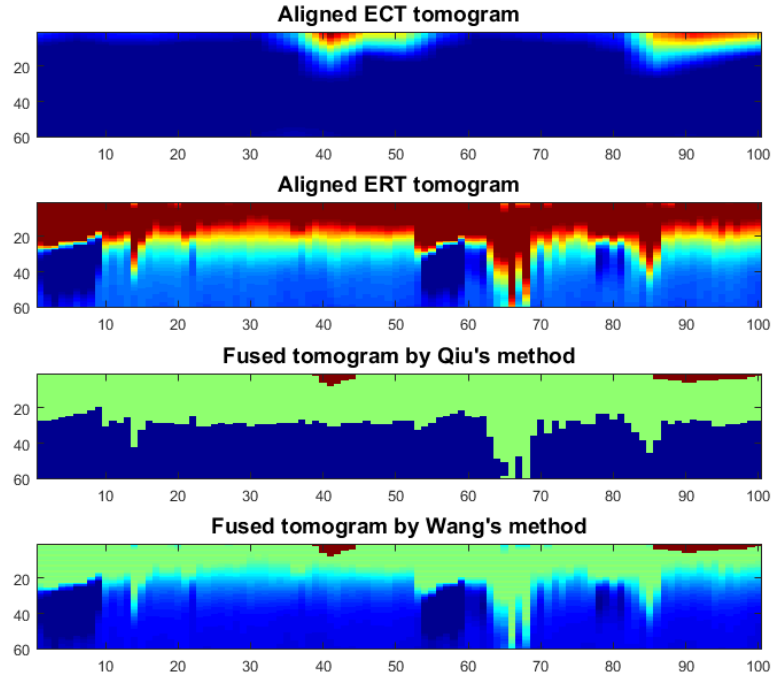


Figure 3.16: Comparison of the fusion results with Qiu's and our approaches.

a mixture of water and oil. In other words, the ERT tomograms are binarised to either water or a water-oil combination. As a consequence, the corresponding pixel value in the fusion result is water plus oil. In this study, the latter case will be utilised for the fusion. Figure 3.16 demonstrates an example of the fusion results by Qiu's and Wang's methods, where $T^1 = 0.5$ and $T^2 = 0.5$ are used as the thresholds in Qiu's method, whereas $T^1 = 0.5$ and $T^2 = 0.05$ are used as the thresholds in Wang's method. The figure clearly shows the difference between the two methods.

3.4.3 Evaluation

In order to evaluate the proposed fusion scheme, 6 common flow regimes are selected, and the detailed information regarding the selected flow conditions is listed in Table 3.3. The listed conditions cover 6 common flow patterns observable for gas-liquid flow in a horizontal pipe. It should be noted that the measured mean concentrations are on the basis of local tomograms. Since phase velocities and local pressure at the sensing location were not measured during the experiments, the local volume fraction, hence, is unable to be obtained. Nonetheless,

Table 3.3: Selected flow regimes with flow condition references for the evaluation of the proposed visualisation approach.

Observed flow regime	Water-cuts (%)	GVF (%)	Q_{gas} (l/s)	Q_{oil} (l/s)	Q_{water} (l/s)
Stratified flow	50	60	3.13	1.04	1.04
Wavy stratified flow	75	40	1.39	0.52	1.56
Slug flow	75	42	3.62	1.25	3.75
Plug flow	75	5	1.24	5.90	17.71
Annular flow	90	92	127.78	1.11	10.00
Bubbly flow	90	35	20.94	3.89	35.00

the comparison between the measured mean concentrations and volume fractions from WLR and GVF would still provide useful information because of their obvious correlation. To avoid any confusion, hereafter, the terms *void fraction* and *volume fraction* are used to correspond the local the mean concentration at sensing location and reference volume fraction at feed-in point, respectively.

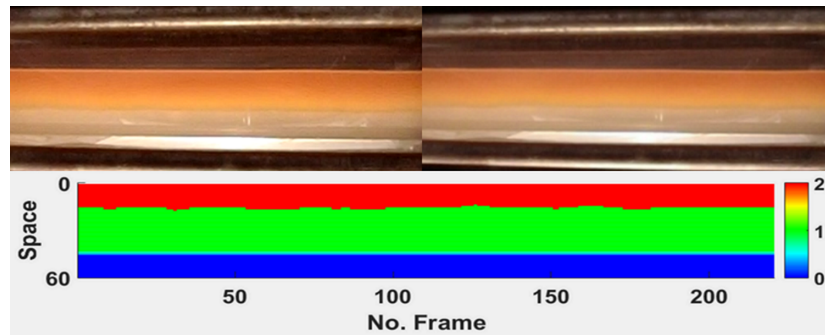


Figure 3.17: Visualisation result of stratified flow over 250 frames (Wang et al. 2017).

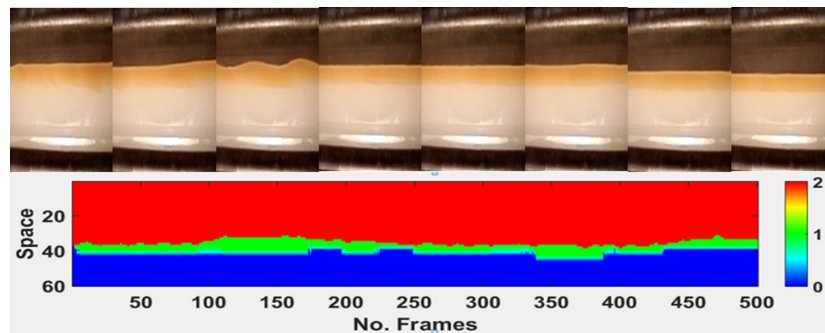


Figure 3.18: Visualisation result of wavy stratified flow over 500 frames (Wang et al. 2017).

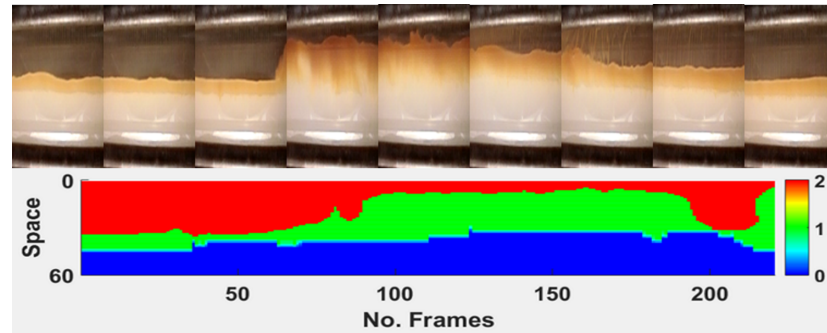


Figure 3.19: Visualisation result of slug flow over 250 frames (Wang et al. 2017).

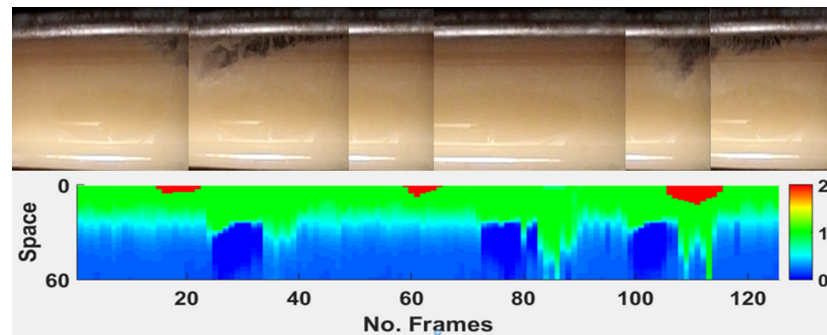


Figure 3.20: Visualisation result of plug flow over 125 frames (Wang et al. 2017).

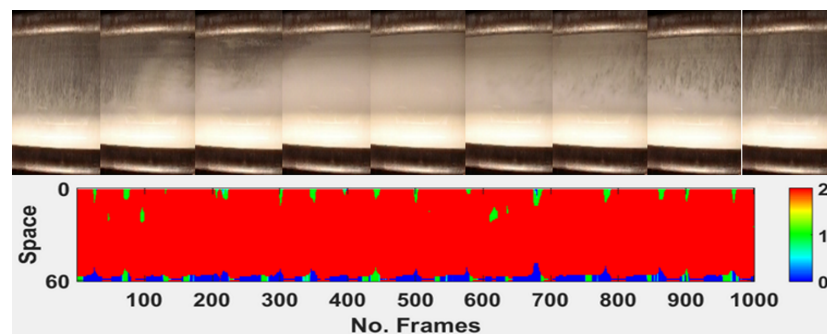


Figure 3.21: Visualisation result of annular flow over 1000 frames (Wang et al. 2017).

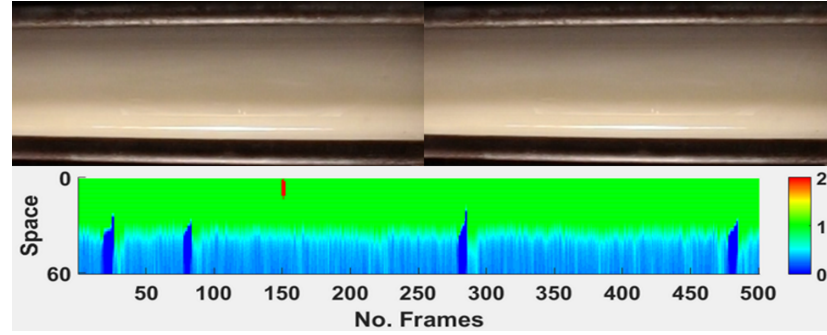


Figure 3.22: Visualisation result of bubbly flow over 500 frames (Wang et al. 2017).

According to the observation during the experiments and the experience from previous testing, T^1 is set to 0.5 which is identical to the one in other literature, such as (Qiu et al. 2007). On the other hand, it is usually believed that the uncertainty caused by systematic errors of ERT systems is 5% (Wang et al. 1999). In other words, it presumes that the measured phase is non-conductive, i.e. pure water in our case, when the corresponding concentration is less than 5%. Consequently, T^2 is assigned to 0.05. p_1 , p_2 , and p_3 in Figure 3.15 are the gas, the water, and the oil. The $f_{i,j}$ therefore is set by:

$$f_{i,j} = \begin{cases} 2 & s_{i,j}^1 \geq 0.5 \\ 0 & s_{i,j}^2 \leq 0.05 \\ s_{i,j}^2 & \text{otherwise} \end{cases} \quad (3.6)$$

From Equation 3.6, it can be concluded that $f_{i,j} \in \{0, 2\} \cup \{x|x \in (0.05, 1.0]\}$. Based on the discussion in Section 3.3.2.3, the pixel values can be transferred to different colours for visualisation purposes. In this section, the value 2 is presented in red as the gas phase, the value 0 in blue as the water phase, and the range (0.05, 1.0] in colours from blue to green. The visualisation results are depicted in Figure 3.17 to Figure 3.22.

From a visualisation point of view, the results in Figure 3.17, Figure 3.18, Figure 3.19, and Figure 3.20 clearly demonstrate the geometrical distributions of the components, and show good agreement with the corresponding video loggers. When it comes to annular flow, the image becomes worse, in terms of the disappearance of the thin liquid film at the top of the pipe. This is mainly because the film is too thin to be identifiable by either system (Figure 3.21). As far as bubbly flow is concerned, since the gas phase is determined by an ECT system,

but it is unable to indicate individual bubbles, the visualisation, hence, is unable to present the existence of dispersed bubbles, as depicted in Figure 3.22.

Table 3.4: Phase concentration quantification results for different flow regimes (Wang et al. 2017).

		Gas	Oil	Water
Stratified Flow	Reference volume fraction (%)	40.00	30.00	30.00
	Fused void fraction (%)	44.21	23.56	32.24
Wavy stratified flow	Reference volume fraction (%)	60.00	10.00	30.00
	Fused void fraction (%)	59.73	4.21	36.06
Slug flow	Reference volume fraction (%)	42.00	14.50	43.50
	Fused void fraction (%)	60.11	5.60	34.29
Plug flow	Reference volume fraction (%)	5.00	24.00	71.00
	Fused void fraction (%)	6.23	23.76	70.01
Annular flow	Reference volume fraction (%)	92.00	2.00	7.00
	Fused void fraction (%)	95.12	1.03	3.85
Bubbly flow	Reference volume fraction (%)	35.00	6.50	58.50
	Fused void fraction (%)	16.87	26.91	56.22

Phase composition information is also quantified from the fused tomograms in Figure 3.17 to Figure 3.22, by the following equations:

$$\alpha_g = \frac{1}{N * Q} |\{f_{i,j} | f_{i,j} = 2\}| \quad (3.7)$$

$$\alpha_w = \frac{1}{N * Q} (|\{f_{i,j} | f_{i,j} = 0\}| + \prod \{(1 - f_{i,j}) | f_{i,j} \in (0.05, 1]\}) \quad (3.8)$$

$$\alpha_o = \frac{1}{N * Q} \prod \{f_{i,j} | f_{i,j} \in (0.05, 1]\} \quad (3.9)$$

where N and Q are the grid definitions of the fused image, $|\{f_{i,j}\}|$ is the cardinality of the set $\{f_{i,j}\}$, and $\prod \{f_{i,j}\}$ is the sum of the set $\{f_{i,j}\}$. The measured void fractions for all flows examined are listed in Table 3.4, together with reference volume fractions calculated by the GVF and WLR. The percentages also correspond well with the images. That is, when the images are qualitatively comparable with the correlating video, the mean void fractions are quantitatively comparable with the reference volume fractions, except for bubbly flow. The small bubbles are not visible in the image, whereas the gas void fraction is not zero, primarily because ECT can measure the existence of the gas phase, even though it is unable to visually indicate the size and distribution of small bubbles.

On the other hand, since both thresholds are crucial for the qualification and quantification of the flow, the combinations of different threshold values are examined, where T^1 is 0.4, 0.45, 0.5, 0.55, 0.6, and T^2 is 0.03, 0.04, 0.05, 0.06, 0.07. The selected flow regime to be examined is the slug flow. The first examination is by fixing T^1 at 0.5, but changing T^2 for the aforementioned five values, whereas the second one is by fixing T^2 at 0.05, but alternating T^1 for the aforementioned five values.

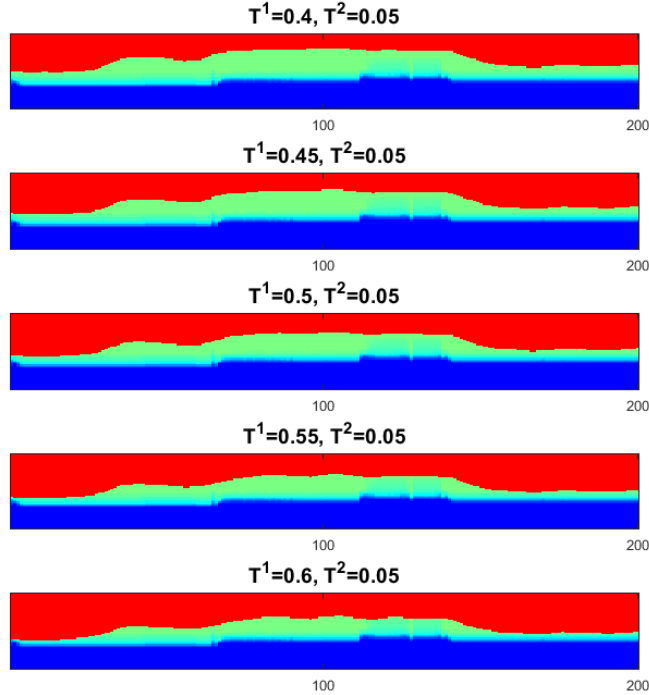


Figure 3.23: Visualisation results of different T^1 but same T^2 for the slug flow.

Table 3.5: Mean void fractions by different T^1 but same T^2 for the slug flow.

T^2	α_{gas} (%)	α_{oil} (%)	α_{water} (%)
0.4	33.87	25.29	40.85
0.45	36.45	22.72	40.83
0.5	39.13	20.08	40.79
0.55	41.76	17.51	40.73
0.6	44.56	14.83	40.61

The fused images for the first evaluation are shown in Figure 3.23, and mean void fractions are listed in Table 3.5. From the visualisation perspective, different T^1 influences the gas phase, i.e. the higher the value is, the more the gas is, and

consequently there is more red area in the images. Since T^2 is unchanged, the water phase therefore remains unchanged, i.e. the blue area is unchanged in the images. As a consequence, the variation in the green area is inversely relevant to T^1 . That is, the higher the T^1 , the more the green area there is, i.e. the more the oil phase is. Table 3.5 also proves the tendency with different T^1 . With the increase of T^1 , gas void fraction decreases dramatically from 33.87% to 44.56%, whereas the void fraction of the oil phase declines significantly from 25.29% to 14.83%. In contrast, the void fraction of the water phase almost remains the same.

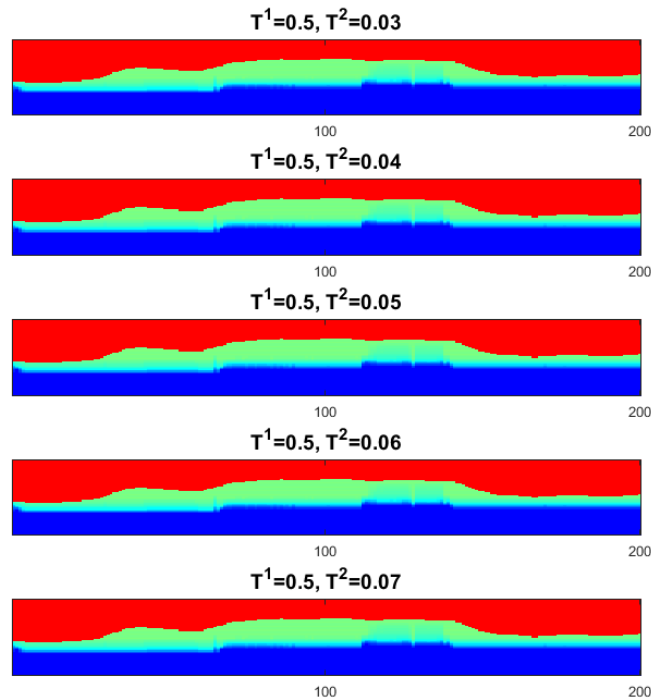


Figure 3.24: Visualisation results of the same T^1 but different T^2 for slug flow.

Table 3.6: Mean void fractions by the same T^1 but different T^2 for slug flow.

T^1	α_{gas} (%)	α_{oil} (%)	α_{water} (%)
0.03	39.13	20.08	40.79
0.04	39.13	20.08	40.79
0.05	39.13	20.08	40.79
0.06	39.13	20.08	40.79
0.07	39.13	20.08	40.79

The fusion results for the second assessment are shown in Figure 3.24, and mean void fractions are itemised in Table 3.6. Unlike the impact of T^1 on the final re-

sults, there is hardly any impact of T^2 on the results. The images in Figure 3.24 and the figures in Table 3.6 prove the impact, where there is no perceivable difference between 5 images, while the mean void fractions are identical for different T^2 . This phenomenon probably results from the interface between the conductive phase (the water phase) and non-conductive phase (the gas-oil phase) by the ERT is relatively sharp when SBP is used for the reconstruction process, in the case of horizontal flow.

3.4.4 Conclusions

A novel data fusion approach with threshold assumptions has been proposed for gas-oil-water flow imaging by dual-modality ERT-ECT systems. By integrating the approach into the aforementioned general framework, the flow in horizontal pipe is qualified and quantified, with the incorporation of multi-dimensional information and results based on the data acquired by ERT-ECT systems at an industry-scale flow facility demonstrate the feasibility of the approach.

The threshold-based fusion algorithm is simple to implement and requires reasonable time and resources, and therefore potentially suitable for on-line purpose. It also proved to be effective to reflect qualitative and quantitative information of the flow patterns in a horizontal pipe. However, the comparison of different threshold assumptions clearly shows the influence of threshold values on both quantitative and qualitative results. The determination of the thresholds, on the other hand, is extremely challenging, since they are affected by many factors, such as the hardware itself, and the physical properties of the experiments involved, e.g. pipe diameter. Therefore, the related fusion approaches usually determine the values empirically.

In the next section, an advanced fusion scheme will be proposed, which requires no *priori* knowledge about threshold values, and therefore is able to minimise the influence associated with thresholding assumptions.

3.5 Fuzzy logic method

3.5.1 Introduction

The earlier-mentioned threshold-based data fusion algorithm has proved to be effective for the imaging of gas-oil-water horizontal flow, and the results have demonstrated the feasibility of the approach. However, the major problem associated with the algorithm is that the determination of the threshold values relies on users' experience of both the systems employed and the investigated conditions of the flow. In this section, a novel approach is proposed, which utilises fuzzy logic to image gas-oil-water flow by dual-modality electrical tomography (ERT-ECT). Based on the framework introduced in Section 3.3, a fuzzy inference system (FIS) is designed to determine possible phase combinations and corresponding truth degree. The FIS is implemented by Matlab's Fuzzy Logic Toolbox (MathWorks 2016), with two input membership functions and two output membership functions. The defuzzified outputs, i.e. the combinations and the degrees of truth, are further decomposed with the assistance of a decision tree to obtain an individual phase and its concentration. The approach is finally evaluated using the data by ERT-ECT systems on industry-scale flow testing facilities at TUV NEL.

3.5.2 Fuzzy logic-based data fusion

In the case of gas-oil-water flow, ERT is able to distinguish water as the conductive phase from gas and oil as the non-conductive phase, whereas ECT is able to differentiate gas and liquid (water and oil) based on relative permittivity (Qiu et al. 2007; Li et al. 2009b). As far as the concentration by ERT is concerned, 5% is considered as system error due to noise (Wang et al. 1999), below which the flow contains only water. There is also a threshold for ERT, above which the flow is fully occupied by gas and oil. When the concentration is between 5% and the threshold, the flow is considered to be a mixture of water, oil, and gas. A similar criteria can also be applied to the concentration by ECT, and the only difference is the phase composition. That is, when the concentration is below 5%, the flow is full of liquid (water and oil), whereas when the concentration is above

the threshold, the flow is only gas. Based on the 5% and the not-easy-to-be-identified threshold, the full concentration range [0%, 100%] can be divided into four sub-ranges, namely low, low-mid, mid-high, and high concentration sections. In the low concentration section, i.e. concentration is less than 5%, only the water or liquid phases exists for ERT or ECT. In the mid-low concentration section, the flow is a mixture of gas, oil, and water for both ERT and ECT systems. In the high concentration section, the flow is considered full of gas-oil mixture for ERT, but only gas for ECT. In the mid-high section where the threshold falls in, the flow could be those in low-mid and high sections. Figure 3.25 depicts the possible flow component combinations by the concentration values from ERT and ECT.

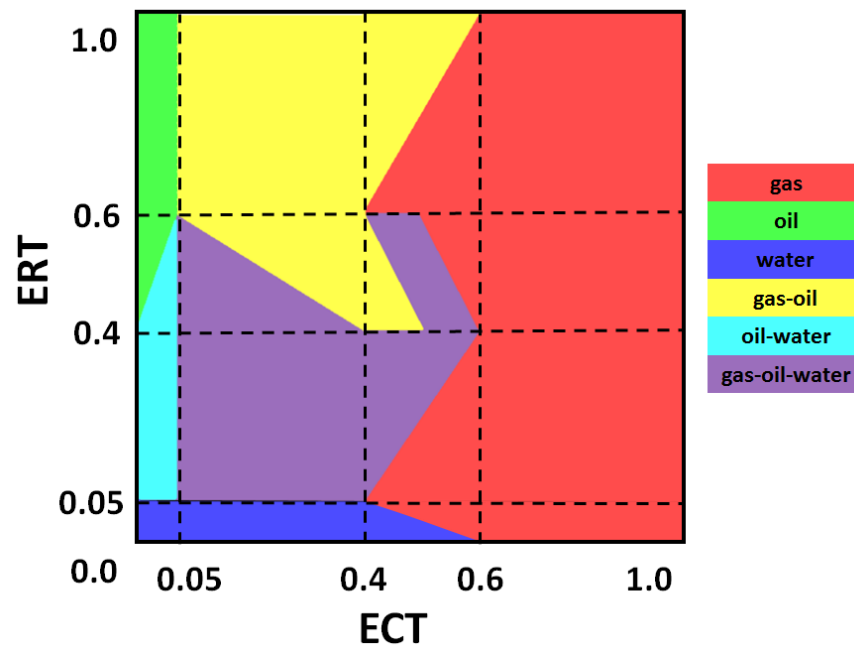


Figure 3.25: Possible phase combinations based on the concentration distributions by ERT and ECT.

Following this fundamental principle, a fuzzy inference system (FIS) can be constructed and further utilised to determine possible combinations of gas, oil, and water phases, as well as the probability of each combination if there is more than one combination. With the combinations and the probability, mixture can be decomposed into individual phase and concentration values of each phase can be estimated. Overall, the FIS for our purpose has two inputs from ECT and ERT images and two outputs for gas+oil and oil+water. The inputs are fuzzified

firstly using membership functions to obtain corresponding membership degrees. Afterwards, 16 pre-defined rules are all evaluated according to the membership degrees, of which the results are aggregated for later processing. Finally, the aggregation is defuzzified to a crisp value as a basis for the decomposition and estimation.

3.5.2.1 Fuzzification

The purpose of fuzzification, as mentioned previously, is to transfer input values to membership degrees in $[0, 1]$. In our case, the input values are concentration values by ERT and ECT. Let a universe of discourse (UOD) $U = (S^m)$, i.e. the registered images from pre-processing. Then, a fuzzy set F^E , based on the images can be defined as:

$$F^E = \int \{\mu_F(p^E)/p^E\} \forall p^E \in U \quad (3.10)$$

where p^E is the pixel concentration in the input images, and $\mu_F(p^E)$ is a fuzzy membership function (MF) of p^E in the set F^E which maps the p^E into the closed interval $[0, 1]$, i.e. $\mu_F(p^E) : F^E \rightarrow [0, 1]$. In this study, triangle-shaped MF is chosen for *low-mid* and *mid-high* segments, due to its simple implementation and stability to errors (Zhao et al. 2002; Monicka et al. 2011), whereas trapezoidal-shaped MF is utilised for the *low* and *high* segments, because of the complete and full membership to satisfy $\mu_F(p^E) = 1$ (Ross 2009). Triangle-shaped MF and trapezoidal-shaped MF are given by Equation 3.11 and Equation 3.12 respectively.

$$\mu_F(p^E) = \begin{cases} 0 & p^E < a \\ \frac{p^E - a}{b - a} & a \leq p^E \leq b \\ \frac{c - p^E}{c - b} & b \leq p^E \leq c \\ 0 & p^E \geq c. \end{cases} \quad (3.11)$$

$$\mu_F(p^E) = \begin{cases} 0 & p < x \\ \frac{p^E - x}{y - x} & x \leq p^E \leq y \\ 1 & y \leq p^E \leq z \\ \frac{w - p^E}{w - z} & z \leq p^E \leq w \\ 0 & p^E \geq w. \end{cases} \quad (3.12)$$

The a and c are so-called *bases*, and b is the so-called *peak* for triangle-shaped MF. Similarly, the x and w are the so-called *bases*, and y and z are so-called

shoulders for trapezoidal-shaped MF. Integrating the principle in Figure 3.25 with Equation 3.11 and Equation 3.12, the MFs can be defined for the two fuzzy sets by ECT and ERT, as depicted in Figure 3.26, and the values for a , b , c , x , y , z , and w are defined in Table 3.7.

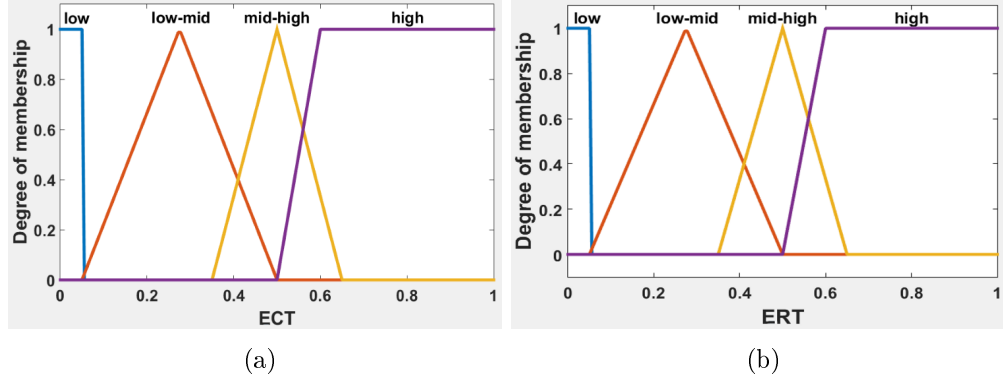


Figure 3.26: The input membership functions for ECT (a) and ERT (b).

Table 3.7: Parameters for the input membership functions.

	ECT	ERT
low	-0.3, -0.0333, 0.05, 0.05	-0.3, -0.0333, 0.05, 0.05
low-mid	0.05, 0.275, 0.5	0.05, 0.275, 0.5
mid-high	0.35, 0.5, 0.65	0.35, 0.5, 0.65
high	0.5, 0.6, 1.033, 1.3	0.4, 0.5, 1.033, 1.3

For example, suppose 0.02 and 0.25 are two input values from ECT and ERT respectively. The 0.02 falls in the low section for ECT, which is mapped to 1.0 according to Figure 3.26a. In contrast, the 0.25 falls in the low-mid section for ERT, which is mapped to 0.86 based on Figure 3.26b.

3.5.2.2 Inference engine

The inference engine performs the implications using pre-defined "if-then" rules and fuzzy logic operators (Ross 2009; Raol 2015). According to Figure 3.25, the fuzzy rules are defined in Table 3.8. When there is more than one possible combination in a case, it assumes that the possibility for every combination is the same, thereby the weight for each combination is evenly divided by the number. In addition, if the mixture includes *water+oil+gas*, the consequence is set in two

Table 3.8: Fuzzy rules.

$ECT \backslash ERT$	Low	Low-Mid	Mid-High	High
Low	water	water+oil	water+oil or oil	oil
Low-Mid	water	water+oil+gas	water+oil+gas or oil+gas	oil+gas
Mid-High	water or gas	water+oil+gas or gas	water+oil+gas or oil+gas or gas	oil+gas or gas
High	gas	gas	gas	gas

parts: one is $gas+oil$, and the other is $oil+water$. That is, the implication engages both output MFs.

As far as fuzzy logic operators are concerned, the intersection (AND), union (OR), and complement (NOT) are defined using *min*, *max*, and *complement* as:

$$\mu_{F^{ERT} \cap F^{ECT}}(p) = \min\{\mu_F(p^{ERT}), \mu_F(p^{ECT})\} \quad (3.13)$$

$$\mu_{F^{ERT} \cup F^{ECT}}(p) = \max\{\mu_F(p^{ERT}), \mu_F(p^{ECT})\} \quad (3.14)$$

$$\mu_{\bar{F}}(p^E) = 1 - \mu_F(p^E) \quad (3.15)$$

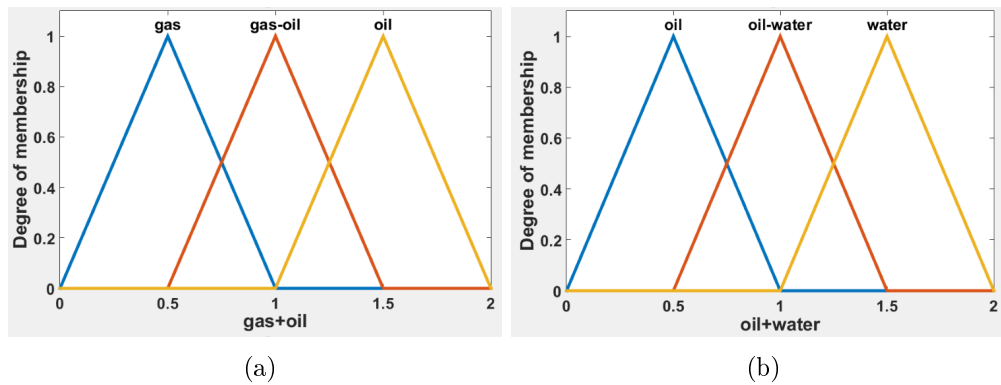


Figure 3.27: The output membership functions for (a) $gas+oil$ and (b) $oil+water$.

With Equation 3.13, Equation 3.14, and Equation 3.15, the antecedent in a rule is evaluated to obtain one number that represents the degree of that antecedent.

Table 3.9: Parameters for the output membership functions.

gas+oil		oil+water	
gas	0, 0.5, 1	oil	0, 0.5, 1
gas-oil	0.5, 1, 1.5	oil-water	0.5, 1, 1.5
oil	1, 1.5, 2	water	1, 1.5, 2

The number is then applied to an output MF to infer a subset of the fuzzy set represented by the consequence. In our case, the output MF utilises triangle-shaped MF as well, including all possible phase combinations, as illustrated in Figure 3.27, and related a , b , and c are defined in Table 3.9. After all rules are evaluated with given input, and thus all consequences are inferred, the results, i.e. fuzzy subsets, are aggregated as one fuzzy set for defuzzification.

Following the example in Section 3.5.2.1, i.e. ECT is 0.02 and ERT is 0.25, there is only one rule that produces a non-zero degree of antecedent, i.e. *if (ECT is low) and (ERT is low-mid) then (phases is oil-water)*, and thus there is only one consequence, as depicted in Figure 3.28.

3.5.2.3 Defuzzification

Defuzzification is to convert the aggregated result to a crisp value. The *centre of gravity (COG)* determination is utilised here to defuzzify the input fuzzy set from inference engine. *COG* is defined as:

$$q^* = \begin{cases} -1 & \int \mu_{F_o}(q) dq = 0 \\ \frac{\int q \mu_{F_o}(q) dq}{\int \mu_{F_o}(q) dq} & \text{otherwise} \end{cases} \quad (3.16)$$

Where q^* is the output value, F_o is the aggregated fuzzy set, $\mu_{F_o}(q)$ is the aggregated output MF, and q is the output variable of the output MF. Further with the previous example, the defuzzified values using COG are -1 and 1 for *gas+oil* and *oil+water*, respectively.

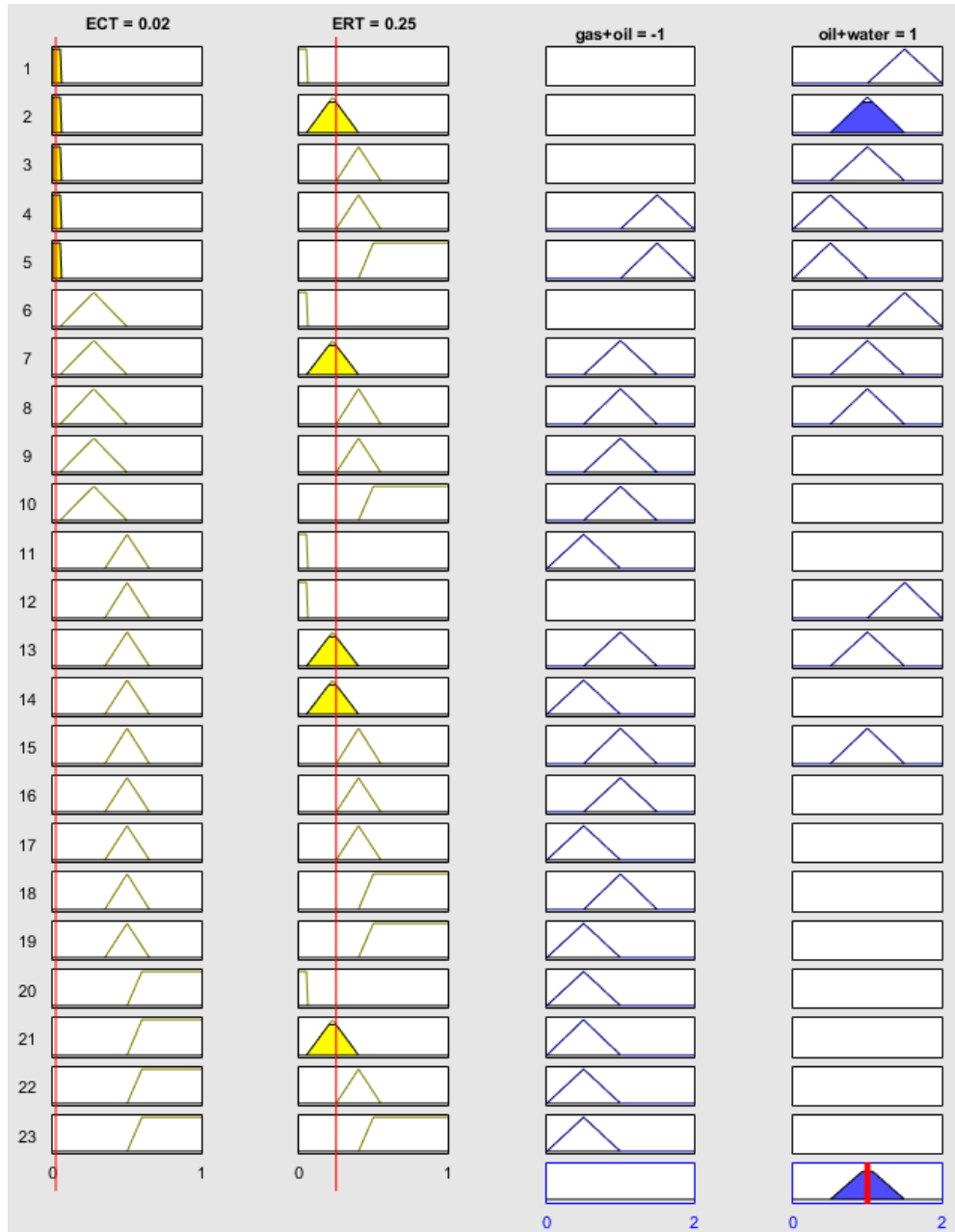


Figure 3.28: Inference of given ECT (0.02) and ERT (0.25).

3.5.2.4 Phase decomposition

The output from the FIS contains two important pieces of information: one is the possible combination of gas, oil, and/or water, and the other is the degree of each component, i.e. the concentration of each phase. Let $D_x = \{d_i^x | i \in \{1, 2, \dots\}\}$ represent defuzzified values, where x is either *gas + oil* or *oil + water*, and $d_i^x \in \{-1\} \cup [0, 2]$. According to the definition of the output MF (Figure 3.27) and COG defuzzification definition Equation 3.16, d_i^x can be categorised into 4 sub-spaces, within which the mixture contains different components:

$$mixture_{p,q} = \begin{cases} N/A & d_i^x = -1 \\ p & d_i^x \in [0, 0.5] \\ p + q & d_i^x \in (0.5, 1.5) \\ q & d_i^x \in [1.5, 2] \end{cases} \quad (3.17)$$

where p and q are gas and oil for *gas + oil* output, or oil and water for *oil + water*, and N/A means the $mixture_{p,q}$ contributes nothing to final result. By combining both $mixture_{gas,oil}$ and $mixture_{oil,water}$, a decision tree can be built up to determine possible phases and their ratios, i.e. local concentration of each phase. The decision tree is depicted in Figure 3.29, in which *NULL* means negative decisions, i.e. impossible combinations by given conditions. Furthermore, local concentrations for the decision nodes can be calculated. When the result is single phase, the concentration is 1 for that phase. The concentrations for the phases, i.e. gas-oil, oil-water, and gas-oil-water, can be calculated by Equation 3.18, Equation 3.19, and Equation 3.20, respectively.

$$\alpha_i = \begin{cases} \alpha_g & = d_i^{gas+oil} - 0.5 \\ \alpha_o & = 1.5 - \alpha_w = 1.5 - d_i^{gas+oil} \\ \alpha_w & = 0 \end{cases} \quad (3.18)$$

$$\alpha_i = \begin{cases} \alpha_g & = 0 \\ \alpha_o & = d_i^{oil+water} - 0.5 \\ \alpha_w & = 1 - \alpha_o = 1.5 - d_i^{oil+water} \end{cases} \quad (3.19)$$

$$\alpha_i = \begin{cases} \alpha_g & = d_i^{gas+oil} - 0.5 \\ \alpha_o & = (1 - \alpha_g) \times (d_i^{oil+water} - 0.5) \\ \alpha_w & = 1 - \alpha_g - \alpha_o \end{cases} \quad (3.20)$$

where α_g , α_o , and α_w are local concentrations at i for gas, oil, and water, respectively. After the mixture has been decomposed and the concentration of each phase

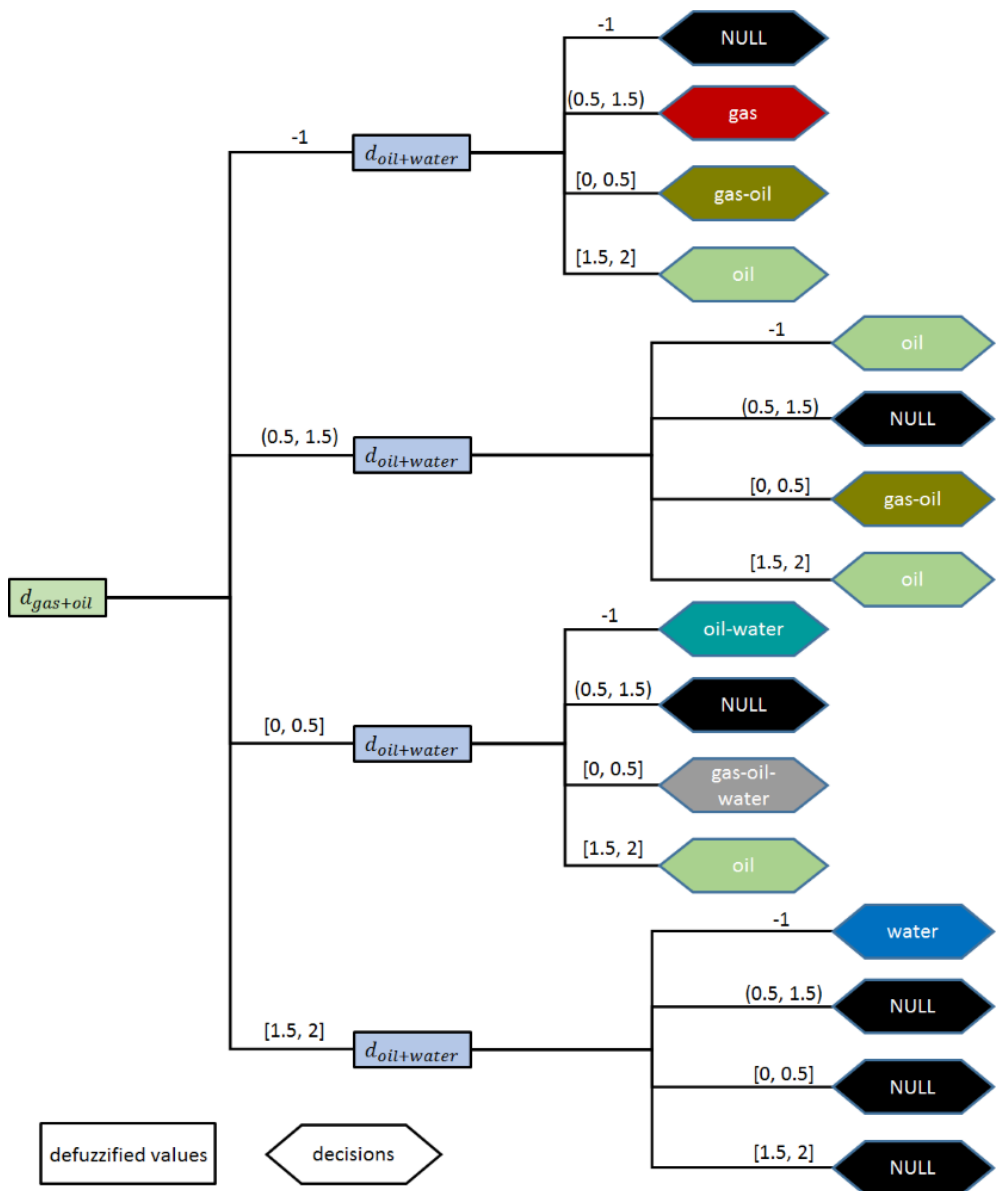


Figure 3.29: Decision tree for determining possible phases with given defuzzified values.

has been computed, the image is going to be displayed using colour mapping as discussed in Section 3.3.2.3.

3.5.3 Evaluation

Experiments were carried out on gas-oil-water flow at industry-scale flow facilities in TUV NEL as discussed in Section 3.2. Different Water-in-Liquid Ratio (WLR) and Gas Volume Fraction (GVF) were combined in order to produce common flow regimes in horizontal pipe. The selected testing matrix for the evaluation of the proposed imaging approach is shown as Table 3.10. The evaluation is separated into two parts: one is to appraise the feasibility of the proposed approach for different flow regimes with the same thresholds and membership functions; and the other is to check the stability with different threshold values and different definitions of input MFs using one flow regime.

Table 3.10: Selected flow conditions for evaluating the proposed approach.

	WLR (%)	GVF (%)
Stratified flow	50	60
Wavy stratified flow	75	40
Slug flow	75	42
Plug flow	75	5
Annular flow	90	92
Bubbly flow	90	35

3.5.3.1 Feasibility

The results are depicted in Figure 3.30 to Figure 3.35. For each flow regime, stacked images from a high-speed camera and four axial cross-sectional images extracted from 500 consecutive frames are displayed by ECT, ERT, threshold-based fusion, and fuzzy logic-based fusion. In this chapter, 0.5 is used as the threshold for ERT images to determine the conductive phase (water) and the non-conductive phase (oil and gas), and 0.5 is used as another threshold for ECT images to determine the gas phase and liquid phase (oil and water).

Table 3.11: Mean concentrations of different flow regimes by a conventional threshold-based method and the proposed approach.

	Stratified flow		Wavy stratified flow		Slug flow	
	Threshold	FIS	Threshold	FIS	Threshold	FIS
gas (%)	48.6322	48.1491	51.5587	51.8408	49.6188	47.5766
oil (%)	19.5742	21.0873	11.6207	14.1891	12.6008	17.5036
water (%)	31.7937	30.7636	36.8207	33.9702	37.7803	34.9198
	Plug flow		Annular flow		Bubbly flow	
	Threshold	FIS	Threshold	FIS	Threshold	FIS
gas (%)	2.8478	5.9287	91.5432	93.7222	10.9888	0.9727
oil (%)	30.0507	58.3846	1.9015	4.06299	35.6685	74.2768
water (%)	67.1015	35.5844	6.5533	2.21478	53.3427	24.7506

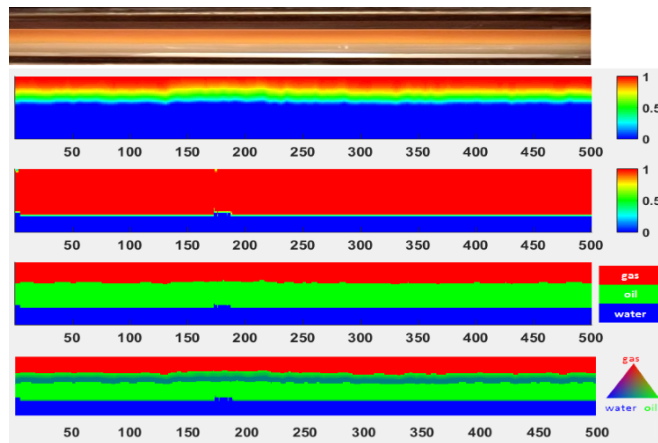


Figure 3.30: Images by high-speed video (first) and axial stacked images for stratified flow by ECT (second), ERT (third), threshold-based fusion (fourth), and fuzzy logic-based fusion (fifth).

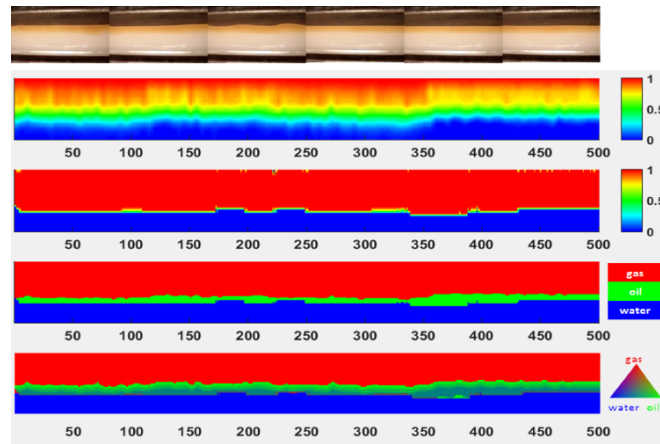


Figure 3.31: Images by high-speed video (first) and axial stacked images for wavy stratified flow by ECT (second), ERT (third), threshold-based fusion (fourth), and fuzzy logic-based fusion (fifth).

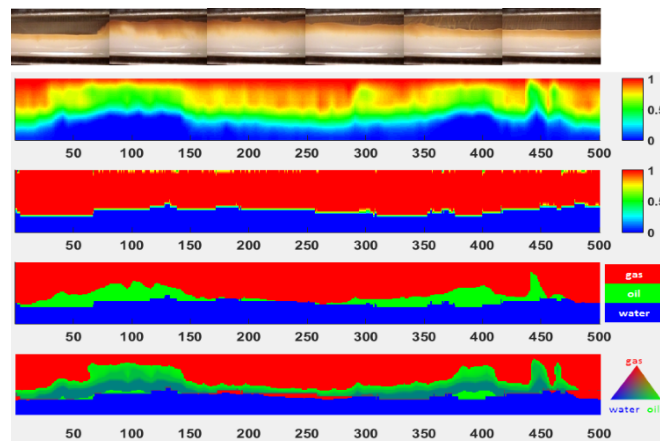


Figure 3.32: Images by high-speed video (first) and axial stacked images for slug flow by ECT (second), ERT (third), threshold-based fusion (fourth), and fuzzy logic-based fusion (fifth).

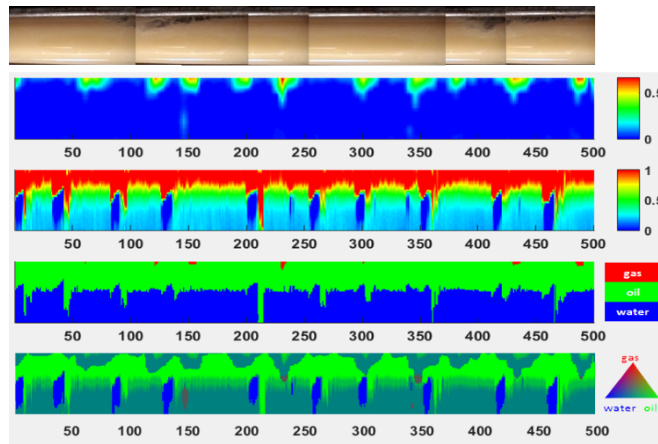


Figure 3.33: Images by high-speed video (first) and axial stacked images for plug flow by ECT (second), ERT (third), threshold-based fusion (fourth), and fuzzy logic-based fusion (fifth).

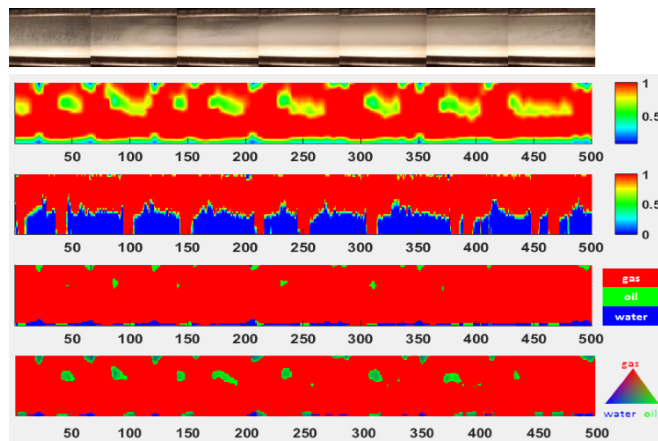


Figure 3.34: Images by high-speed video (first) and axial stacked images for annular flow by ECT (second), ERT (third), threshold-based fusion (fourth), and fuzzy logic-based fusion (fifth).

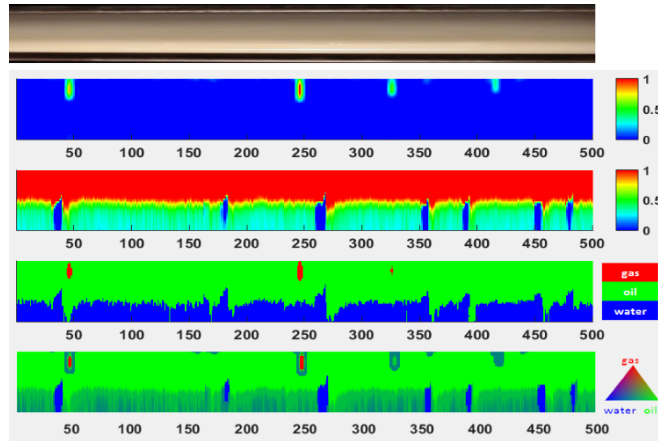


Figure 3.35: Images by high-speed video (first) and axial stacked images for bubbly flow by ECT (second), ERT (third), threshold-based fusion (fourth), and fuzzy logic-based fusion (fifth).

From a visual perspective, the proposed approach, overall, is able to produce fused images competitive with the ones achieved using the conventional threshold-based method. When ECT and ERT are able to identify, although approximately, the interface between each phase, e.g. in Figure 3.31, the FIS-based approach generates qualitative images very close to the ones using the conventional method, despite some distortion close to the interface. This, however, reflects the limitations of the electrical tomographic system when imaging multiphase flow, e.g. blurred boundaries between gas and liquid. However, when either of them is incapable of presenting good-quality tomograms, the FIS-based results are not as good as the ones obtained using the thresholding method, e.g. the bubbly flow in Figure 3.35. Table 3.11 lists the mean concentrations for all tested flow conditions by the threshold-based method and the proposed approach, which reveals similar situations to those by observation.

3.5.3.2 Stability

In the stability evaluation, different input MFs are examined, along with different threshold values for the purpose of comparison. For each threshold, particular low-mid, mid-high, and high MFs are defined for both ECT and ERT input MFs, as specified in Table 3.12. The selected flow regime is stratified flow. The first set of experiments is conducted by fixing the ECT threshold at 0.5, but changing the ERT threshold with different values, including 0.4, 0.45, 0.5, and 0.55. The

Table 3.12: Definitions of membership functions for different threshold values.

	low-mid MF			mid-high MF			high MF			
Threshold=0.4	0.05	0.225	0.4	0.25	0.4	0.55	0.4	0.5	1.033	1.3
Threshold=0.45	0.05	0.25	0.45	0.3	0.45	0.6	0.45	0.55	1.033	1.3
Threshold=0.5	0.05	0.275	0.5	0.35	0.5	0.65	0.5	0.6	1.033,	1.3
Threshold=0.55	0.05	0.3	0.55	0.4	0.55	0.7	0.55	0.65	1.033	1.3

Table 3.13: Mean concentrations of each phase by different ERT thresholds for the conventional method and different definitions of ERT membership functions for the FIS-based approach.

	Threshold-based method			FIS-based method		
	α_{gas} (%)	α_{oil} (%)	α_{water} (%)	α_{gas} (%)	α_{oil} (%)	α_{water} (%)
$T_{ERT} = 0.4$	48.6322	19.6178	31.75	48.155	21.2745	30.5705
$T_{ERT} = 0.45$	48.6322	19.602	31.7658	48.1510	21.1629	30.6861
$T_{ERT} = 0.5$	48.6322	19.5742	31.7937	48.1491	21.0873	30.7636
$T_{ERT} = 0.55$	48.6322	19.5607	31.8072	47.9889	20.8739	31.1372

Table 3.14: Mean concentrations of each phase by different ECT thresholds for the conventional method and different definitions of ECT membership functions for the FIS-based approach.

	Threshold-based method			FIS-based method		
	α_{gas} (%)	α_{oil} (%)	α_{water} (%)	α_{gas} (%)	α_{oil} (%)	α_{water} (%)
$T_{ECT} = 0.4$	36.8543	31.352	31.7937	50.0819	19.1545	30.7636
$T_{ECT} = 0.45$	38.579	29.6273	31.7937	49.2050	20.0314	30.7636
$T_{ECT} = 0.5$	48.6322	19.5742	31.7937	48.1491	21.0873	30.7636
$T_{ECT} = 0.55$	66.1822	2.02417	31.7937	46.6224	22.614	30.7636

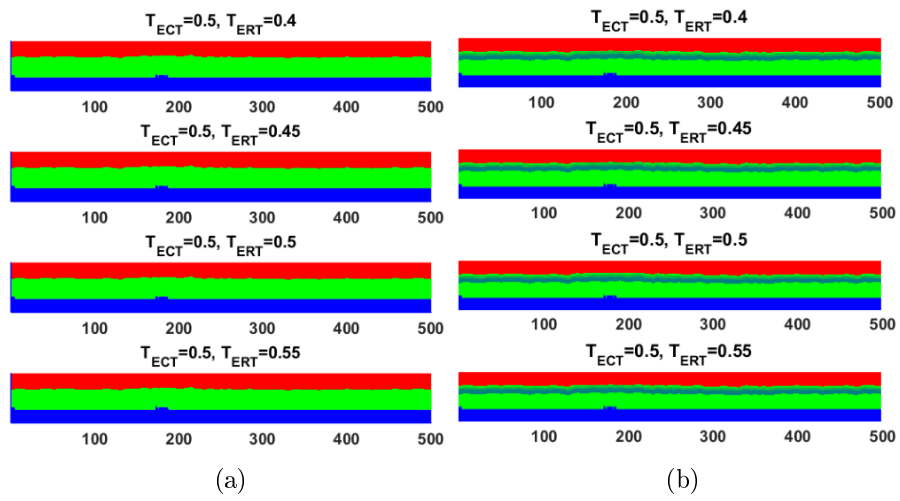


Figure 3.36: Images with the same ECT threshold but different ERT thresholds by (a) conventional thresholding method; and (b) FIS-based approach.

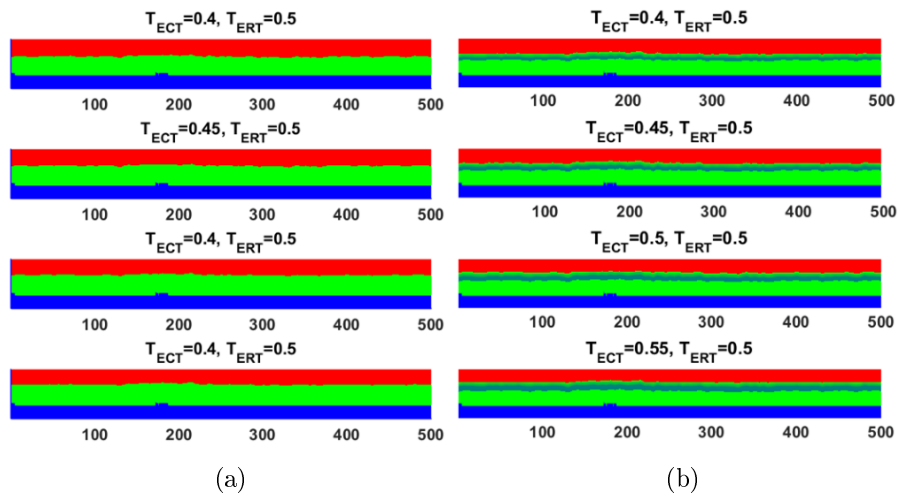


Figure 3.37: Images with different ECT thresholds but same ERT threshold by (a) conventional thresholding method; and (b) FIS-based approach.

images are depicted in Figure 3.36 and the mean concentrations are listed in Table 3.13. From a visualisation point of view, the images by both methods are hardly distinguishable, except the blurred interface between gas and oil by the new approach, as illustrated in Figure 3.36b, because of the blurred boundary between gas and liquid by ECT. The figures in Table 3.13 also present similar results, which also shows that when ECT threshold is unchanged, the modification of ERT threshold rarely influences the results.

The second set of experiments is carried out using the same ERT threshold 0.5 but different ECT threshold values of 0.4, 0.45, 0.5, and 0.55. The images are shown in Figure 3.37 and the mean concentrations are listed in Table 3.14. From the viewpoint of visualisation, the results are very similar to the ones in the first set of evaluations. In contrast, the numerics in Table 3.14 demonstrate the impact of the ECT threshold on the conventional method, whereas the fuzzy logic-based approach is still able to produce stable results.

3.5.4 Conclusions

A novel approach has been proposed to resolve the problems associated with multi-dimensional image fusion by multi-modality electrical tomography for imaging gas-oil-water flow in real-world industrial sectors. Through the approach, images from different electrical tomographic systems are integrated along spatial, temporal, and energy dimensions, and hence gas-oil-water flow in real industries is visualised. The approach does not require a *priori* knowledge to threshold values, which are critical for identifying the geometrical distribution of the phases in the flow, but are usually domain-specific and empirically determined. Unlike the conventional threshold-based method, the proposed approach is insensitive to the changes in different membership functions, resulting in stable outcomes in both qualitative and quantitative terms.

The fusion algorithm based on fuzzy logic with decision tree is independent of threshold values, but due to the complexity of the algorithm, it requires more time and resources to perform the fusion and decomposition, comparing with the threshold-based fusion approach. Therefore, it may not be eligible for the purpose of on-line visualisation and measurement. The results also indicate that

the performance of the proposal is prone to the quality of input images, i.e. spatial resolution.

In spite of its feasibility and stability in multiphase flow imaging, there are still a few aspects which need to be addressed in the future. The interpolation utilised in the image pre-processing is simple but less precise for image registration. As a result, advanced algorithms should be applied to improve the performance. Another aspect is the application of different membership functions. Although the applied ones prove to be superior to others (Zhao et al. 2002) in other areas, it is still unclear whether they are also applicable in multiphase flow-involved image fusion. Higher-resolution images by advanced reconstruction algorithms, e.g. SCG (Wang 2002) or others in (Wei et al. 2015) should be incorporated to make improvements to the outcomes, and meanwhile address the possible error sources in the process.

3.6 Experimental evaluation of dual-modality ERT-ECT systems

3.6.1 Introduction

Despite that a variety of DMTS have been attracted much attention, they are still at an early stage with regard to research and development. The majority of studies were performed on hardware, i.e. from the systems with standalone modalities (such as ERT-ECT systems) to integrated modalities (such as the one by Ji (Ji et al. 2016)), yet a few instruments have not yet been evaluated thoroughly, where simulations and experiments on simple flow regimes, e.g. stratified flow, predominates the effort. Gas-oil-water flow is particularly concerned with this study.

In addition, it was reported that ERT is functional with water-continuous flow, i.e. WLR above 40%, whereas ECT is able to measure oil-continuous flow, i.e. WLR below 40% (Li et al. 2009b). This conclusion, unfortunately, has insufficient experimental support. Besides, the function range for ECT is also underestimated based on the experiments carried out in this study.

The purposes of experimental evaluation of the methods are twofold: one is to experimentally evaluate the performance of dual-modality ERT-ECT systems to provide complementary evidence based on the data gauged on an industrial-scale flow loop, and the other is for the assessment of proposed fusion techniques. This section reports the theoretical and experimental analysis of dual-modality ERT-ECT systems based on the experiments conducted at the industrial-scale multiphase flow facility at TUV NEL (Section 3.2). The flow conditions tested include WLR from 0% to 100% in parallel with GVF from 0% to 100%, which produces common horizontal flow regimes, including stratified flow, slug flow, plug flow, bubbly flow, and annular flow. The evaluation embraces both qualitative and quantitative outcomes, by means of images and mean concentrations, respectively, where the fused images are obtained using the aforementioned threshold-based data fusion (Section 3.4). It is worth noting that the quantitative comparison is directly performed between volume fractions by reference values and void fractions by the systems, since the objective of the project was visualisation but not metering.

The results are presented in the format of axially-stacked tomograms by ECT, ERT, and the fusion approach, along with the images by high-speed video logger as a visual reference and also mean concentrations of gas and/or water. At each WLR, five common flow conditions, representing different flow regimes, namely stratified flow, slug flow, plug flow, annular flow, and bubbly flow, are chosen for visualisation evaluation. In addition, quantitative outcomes at each WLR are also derived and compared in regard to water and/or gas mean concentrations. Because the primary objective of the project is visualisation, instead of measurement of gas-oil-water flow using ERT-ECT systems, volumetric fraction values, i.e. WLR and GVF, are utilised directly as references for mean concentration. For water mean concentrations, 3 values are obtained by WLR+GVF (Equation 3.21), ERT (Equation 3.22), and the data fusion (Equation 3.5).

$$\alpha_w^{ref} = (100 - GVF) \times WLR/100 \quad (3.21)$$

$$\alpha_w^{ERT} = 1 - \alpha^{ERT} \quad (3.22)$$

As far as gas is concerned, the mean concentrations come from GVF (Equation 3.23), ECT (Equation 3.24), the data fusion (Equation 3.5), and γ -ray.

$$\alpha_g^{ref} = GVF \quad (3.23)$$

$$\alpha_g^{ECT} = \alpha^{ECT} \quad (3.24)$$

The mixture density by gamma-ray is as below:

$$\rho_m = \rho_g \times \alpha_g + \rho_w \times \alpha_w + \rho_o \times \alpha_o \quad (3.25)$$

where ρ_x is the density for each phase or the mixture, and α_x is the volume fraction of each phase. Compared to ρ_w and ρ_o , the ρ_g is so small that it can be ignored. In addition, ρ_w and ρ_o are approximated using density of liquid ρ_l , of which the value is replaced by water density ρ_w . Consequently, Equation 3.25 is changed to:

$$\rho_m \approx \alpha_l * \rho_w \Rightarrow \alpha_l \approx \frac{\rho_m}{\rho_w} \quad (3.26)$$

Further, the gas volume fraction can be calculated using Equation 3.27:

$$\alpha_g \approx 1 - \alpha_l \approx 1 - \frac{\rho_m}{\rho_w} \quad (3.27)$$

According to Equation 3.27, another fraction of gas can be approximated for the comparison.

3.6.2 Experimental results

3.6.2.1 WLR 0%

At WLR 0%, in total 42 different flow conditions were examined (as listed in Table 3.15), covering most common flow regimes in a horizontal pipeline (Corneliusson et al. 2005). Since WLR is 0%, i.e. gas-oil two-phase flow, which is beyond the ERT's measurable range, only stacked ECT tomograms are presented, along with the images taken using high-speed video, as depicted in Figure 3.38. The flow conditions selected for demonstrating the capability of ECT are listed in Table 3.16. From a visualisation point of view, the ECT tomograms agree well with the videos, except the ones for bubbly flow as shown in Figure 3.38e. This is because the ECT utilised is unable to identify small bubbles of a size very much smaller than pipe diameter. On the other hand, Figure 3.39 presents the quantitative comparison of ECT result with the results by GVF and gamma-ray. Since the ERT part in the dual-modality system is not functional, the quantitative result only compares gas concentrations by GVF, gamma-ray, and ECT.

Table 3.15: All examined flow conditions at WLR 0%.

Test No.	GVF %	ERT %	ECT %	Data gas	fusion oil	(%) water	Gammy %	Flow Regimes
1	65	x	56.78	x	x	x	72.11	stratified
2	85	x	60.51	x	x	x	87.89	stratified
3	95	x	60.82	x	x	x	94.75	stratified
4	98	x	70.69	x	x	x	97.24	stratified
5	99	x	72.74	x	x	x	98.10	stratified
6	99.6	x	72.69	x	x	x	99.37	transition
7	60	x	55.44	x	x	x	68.65	stratified
8	82	x	58.38	x	x	x	85.45	stratified
9	95	x	62.76	x	x	x	94.89	stratified
10	97	x	69.50	x	x	x	96.44	stratified
11	99	x	73.46	x	x	x	96.44	stratified
12	99.4	x	72.07	x	x	x	99.21	transition
13	40	x	44.03	x	x	x	51.50	stratified
14	60	x	43.46	x	x	x	68.39	transition
15	85	x	55.73	x	x	x	87.27	slug
16	95	x	65.32	x	x	x	94.97	transition
17	98	x	75.72	x	x	x	98.00	annular
18	98.5	x	75.72	x	x	x	98.50	annular
19	25	x	28.87	x	x	x	39.55	slug
20	42	x	35.78	x	x	x	53.73	slug
21	60	x	41.57	x	x	x	67.54	slug
22	85	x	71.61	x	x	x	86.98	annular
23	95	x	71.35	x	x	x	95.55	annular
24	96.5	x	68.10	x	x	x	96.87	annular
25	10	x	17.68	x	x	x	28.93	plug
26	25	x	26.50	x	x	x	40.62	plug
27	40	x	35.49	x	x	x	52.40	transition
28	60	x	44.38	x	x	x	67.91	slug
29	85	x	64.38	x	x	x	87.46	slug
30	92	x	68.19	x	x	x	93.57	transition
31	5	x	16.53	x	x	x	25.16	bubbly
32	15	x	19.91	x	x	x	33.06	slug
33	25	x	24.28	x	x	x	40.51	slug
34	35	x	29.79	x	x	x	48.40	slug
35	60	x	46.57	x	x	x	68.19	transition
36	75	x	54.95	x	x	x	79.26	annular
37	3	x	17.52	x	x	x	23.57	bubbly
38	5	x	18.93	x	x	x	25.05	bubbly
39	10	x	24.02	x	x	x	30.16	bubbly
40	15	x	27.63	x	x	x	33.13	bubbly
41	25	x	34.31	x	x	x	40.81	bubbly
42	35	x	39.90	x	x	x	49.13	bubbly

Table 3.16: Selected flow conditions for visualisation at WLR 0%.

	GVF (%)	Q_{oil} (m^3/hr)	Q_{gas} (m^3/hr)
Stratified flow	97	2.948	94.640
Slug flow	42	17.890	13.009
Plug flow	25	39.334	13.298
Annular flow	95	18.023	340.655
Bubbly flow	25	139.360	47.466

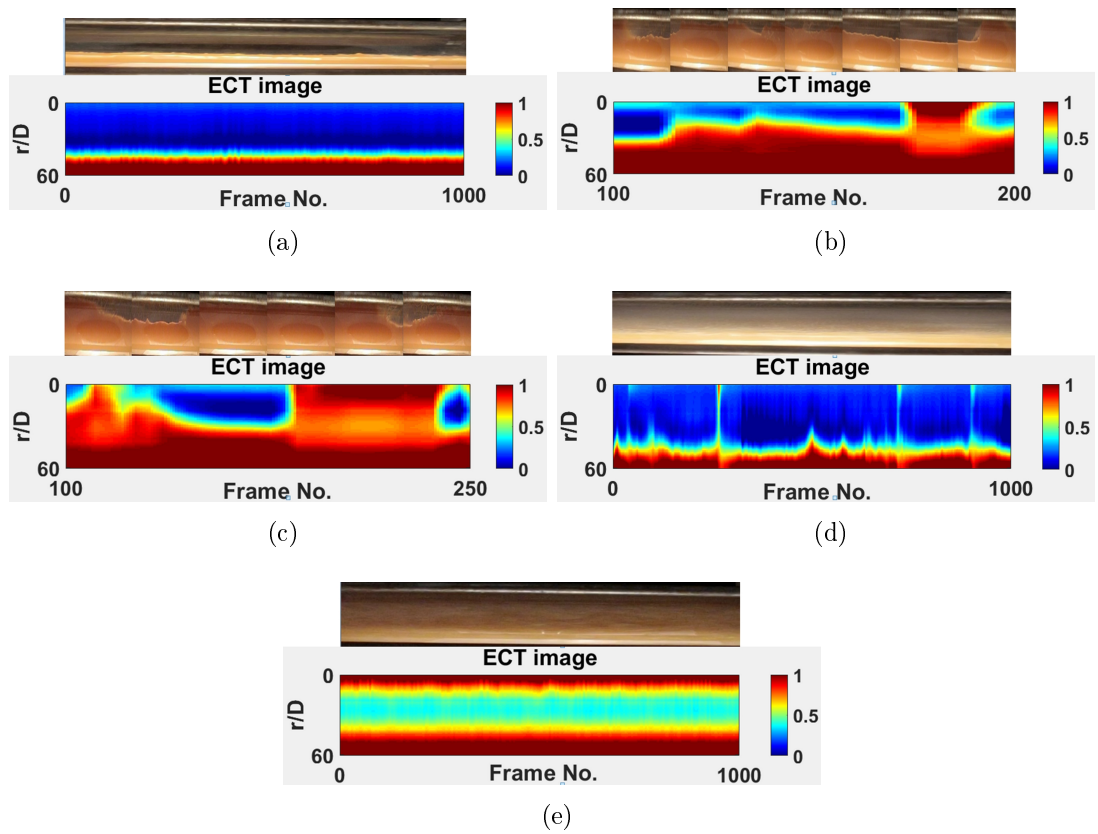


Figure 3.38: Visualisation results of WLR 0% for (a) stratified flow; (b) slug flow; (c) plug flow; (d) annular flow; and (e) bubbly flow.

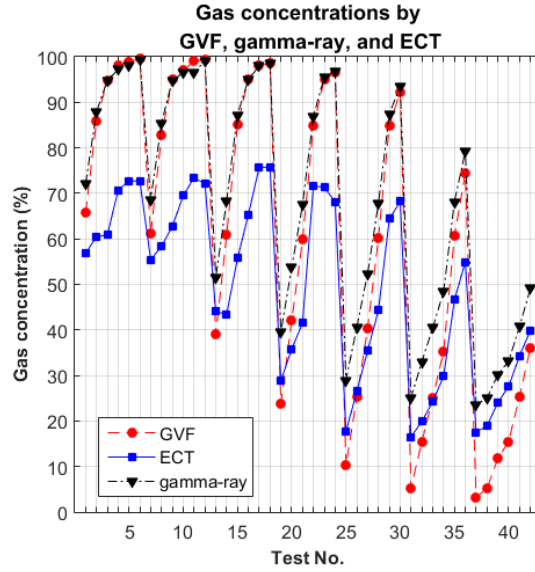


Figure 3.39: Gas concentrations from different approaches at WLR 0%.

Table 3.17: All examined flow conditions at WLR 10%.

Test No.	GVF %	ERT %	ECT %	Data fusion (%)			Gammy %	Flow Regimes
				gas	oil	water		
1	60	x	47.13	x	x	x	63.71	slug
2	85	x	63.07	x	x	x	85.52	slug
3	95	x	71.06	x	x	x	94.33	transition
4	96.5	x	74.16	x	x	x	96.46	annular
5	5	x	11.01	x	x	x	23.31	bubbly
6	15	x	18.21	x	x	x	30.62	plug
7	25	x	25.26	x	x	x	39.21	transition
8	35	x	32.22	x	x	x	46.64	transition
9	60	x	50.71	x	x	x	66.46	slug
10	75	x	59.49	x	x	x	77.52	transition
11	3	x	9.29	x	x	x	21.00	bubbly
12	5	x	12.92	x	x	x	22.79	bubbly
13	10	x	17.43	x	x	x	27.25	bubbly
14	15	x	21.33	x	x	x	30.40	bubbly
15	25	x	31.18	x	x	x	38.68	bubbly
16	35	x	38.31	x	x	x	45.53	bubbly

Table 3.18: Selected flow conditions for visualisation at WLR 10%.

	GVF (%)	Q_{water} (m^3/hr)	Q_{oil} (m^3/hr)	Q_{gas} (m^3/hr)
Slug flow	85	2.178	18.451	103.398
Plug flow	15	8.877	76.756	14.759
Annular flow	75	2.211	18.214	495.811
Bubbly flow	5	14.544	124.980	7.161

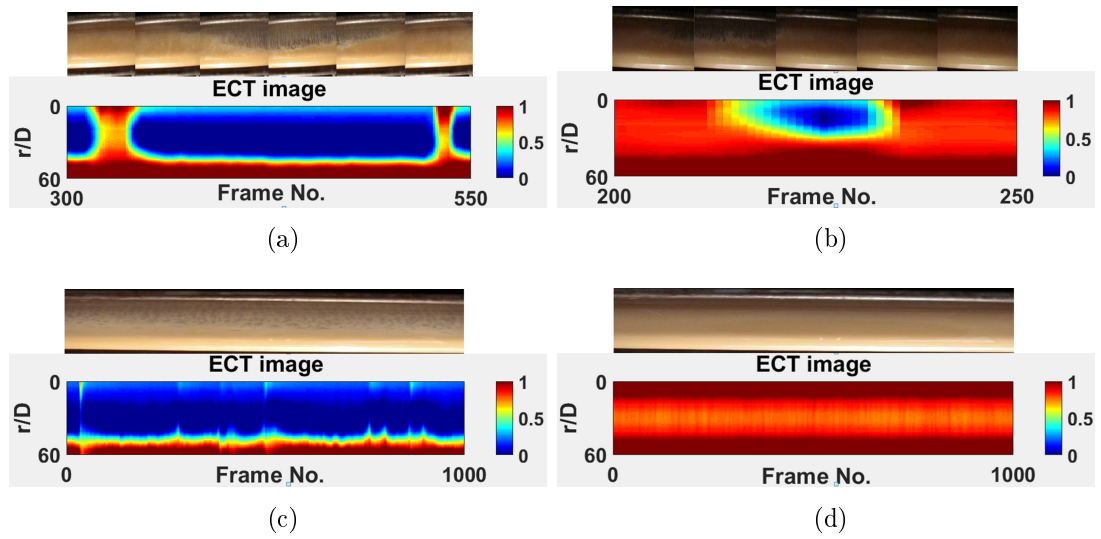


Figure 3.40: Visualisation results of WLR 10% for (a) slug flow; (b) plug flow; (c) annular flow; and (d) bubbly flow.

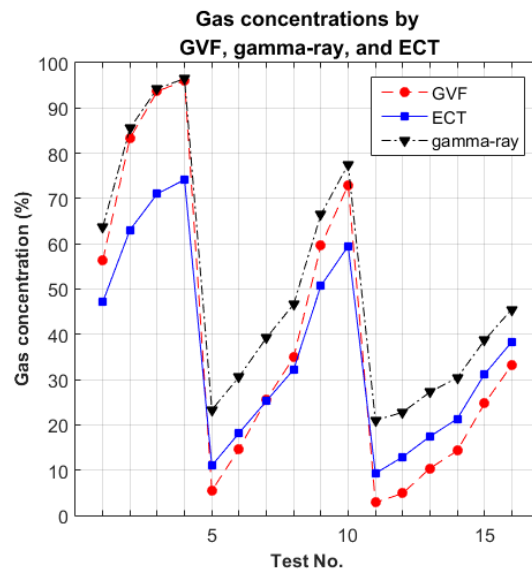


Figure 3.41: Gas concentrations from different approaches at WLR 10%.

3.6.2.2 WLR 10%

With WLR at 10%, 18 different flow conditions were tested, which are listed in Table 3.17. Due to the limited number of flow conditions, the facility did not manage to produce all common flow regimes. The visualisation results illustrated in Figure 3.40 involve only four flow regimes, i.e. slug, plug, annular, and bubbly flow, of which the flow conditions are itemised in Table 3.18. Similar to the situation at WLR 0%, ERT is still incapable of generating acceptable images. As far as imaging is concerned, ECT is generally able to provide reasonable results, as presented in Figure 3.40. It is, however, also noticed that in Figure 3.40c, ECT struggled to identify the liquid film at the top of the pipe wall. This is primarily because the film is too thin to be identifiable, which suggests the thinness is below the resolution of the ECT (Qiu et al. 2007). Figure 3.41 presents the comparison of gas concentrations by GVF, gamma-ray, and ECT.

3.6.2.3 WLR 25%

Table 3.19: All examined flow conditions at WLR 25%.

Test No.	GVF %	ERT %	ECT %	Data fusion (%)			Gammy %	Flow Regimes
				gas	oil	water		
1	95	x	80.14	x	x	x	94.40	transition
2	98	x	79.31	x	x	x	97.31	transition
3	98.5	x	81.52	x	x	x	98.16	annular
4	85	x	69.38	x	x	x	85.43	slug
5	95	x	75.04	x	x	x	95.34	transition
6	96.5	x	75.04	x	x	x	96.73	annular
7	25	x	44.89	x	x	x	36.83	slug
8	40	x	37.93	x	x	x	47.83	slug
9	60	x	47.62	x	x	x	64.45	transition
10	85	x	67.72	x	x	x	85.71	annular
11	92	x	74.59	x	x	x	93.03	annular
12	5	x	10.03	x	x	x	20.09	bubbly
13	15	x	19.37	x	x	x	28.87	transition
14	25	x	31.47	x	x	x	37.36	transition
15	35	x	36.59	x	x	x	44.42	transition
16	60	x	54.53	x	x	x	65.45	transition
17	75	x	62.09	x	x	x	77.61	annular
18	3	x	15.08	x	x	x	18.39	bubbly
19	5	x	16.16	x	x	x	19.94	bubbly
20	10	x	21.34	x	x	x	24.70	bubbly
21	15	x	27.21	x	x	x	28.63	bubbly

Given WLR at 25 %, 16 flow conditions were involved in the experiment which,

Table 3.20: Selected flow conditions for visualisation at WLR 25%.

	GVF (%)	Q_{water} (m^3/hr)	Q_{oil} (m^3/hr)	Q_{gas} (m^3/hr)
Slug flow	40	10.635	31.481	26.505
Annular flow	92	10.213	28.840	458.146
Bubbly flow	10	35.406	105.336	16.833

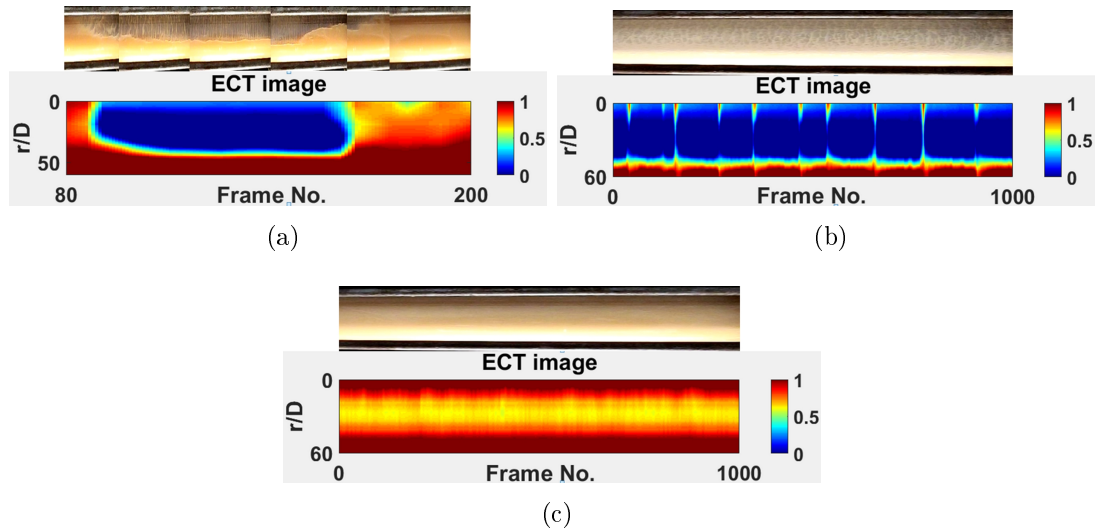


Figure 3.42: Visualisation results of WLR 25% for (a) slug flow; (b) annular flow; and (c) bubbly flow.

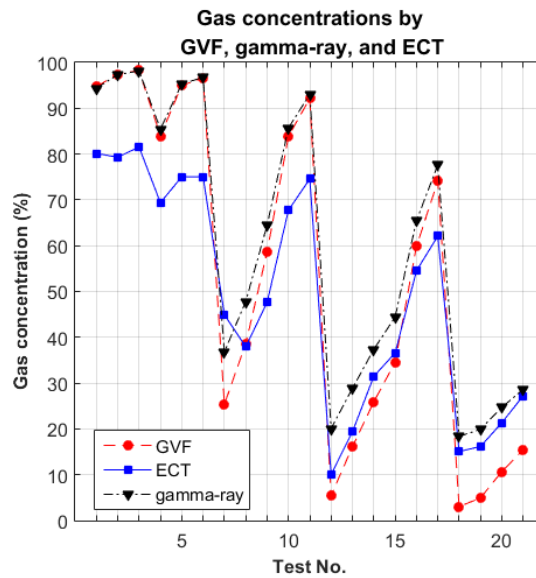


Figure 3.43: Gas concentrations from different approaches at WLR 25%.

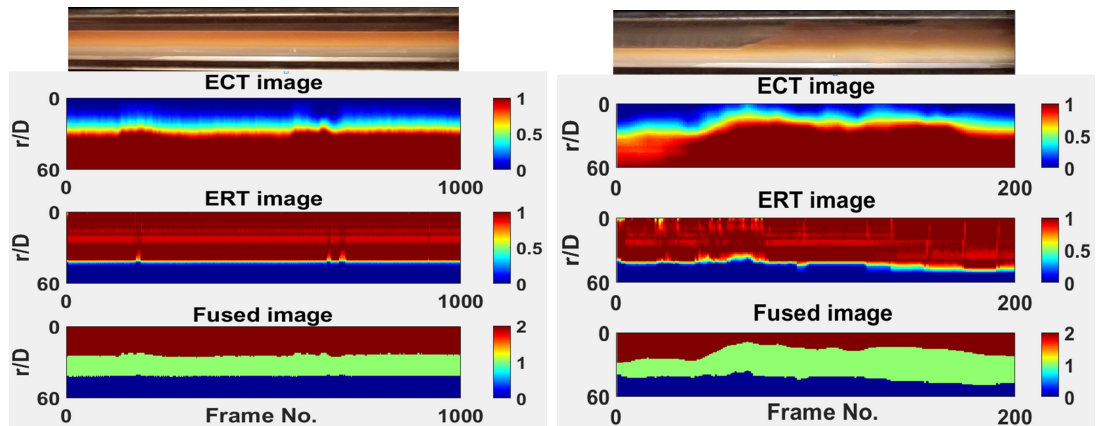
however, only reflect three flow regimes, including slug, annular, and bubbly flow. A complete list of the tested flow conditions is in Table 3.19. Figure 3.42 depicts the selected visualisation results in line with the conditions in Table 3.20. Similar to the results for WLR 0% and 10%, ECT tomograms are generally consistent with video footage, except for bubbly flow. Figure 3.42b shows an interesting phenomenon, i.e. the thickness of the liquid film at the top of the pipe changes almost periodically, implying that the flow was fully developed, and hence at steady state. The gas concentrations calculated by GVF, gamma-ray, and ECT, are demonstrated in Figure 3.43.

3.6.2.4 WLR 50%

Table 3.21: All examined flow conditions at WLR 50%.

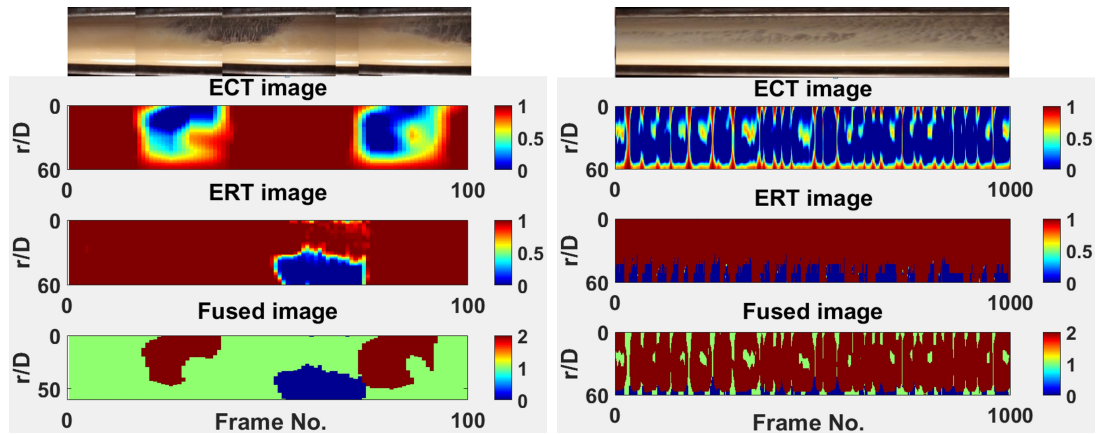
Test No.	GVF %	ERT %	ECT %	Data fusion (%)			Gammy %	Flow Regimes
				gas	oil	water		
1	40	74.37	41.20	40.75	27.59	31.66	47.74	stratified
2	60	74.37	40.42	39.90	28.47	31.63	62.58	stratified
3	85	87.03	48.04	42.51	38.08	19.41	85.70	stratified
4	95	93.83	74.34	84.23	8.75	7.02	94.21	stratified
5	98	97.94	91.88	98.47	1.53	0.00	97.79	transition
6	98.5	95.25	92.84	99.83	0.18	0.00	98.25	annular
7	25	74.05	36.37	36.23	31.20	32.57	33.39	slug
8	42	74.83	37.20	36.12	31.95	31.94	46.58	slug
9	60	87.66	46.43	40.73	36.54	22.73	64.53	slug
10	85	84.49	64.05	67.81	20.70	11.49	85.04	slug
11	95	84.34	75.99	84.36	10.61	5.03	95.02	transition
12	96.5	86.39	76.37	82.38	15.20	2.43	96.83	bubbly
13	10	74.53	29.56	28.54	38.21	33.25	19.98	transition
14	25	76.11	28.53	26.46	41.13	32.41	31.93	slug
15	40	74.68	23.72	19.83	57.91	22.27	47.47	slug
16	60	76.74	37.50	31.40	45.67	22.93	63.11	slug
17	85	79.27	43.75	31.57	41.91	26.53	86.28	transition
18	92	78.96	76.31	83.79	11.11	5.10	91.89	annular
19	15	58.55	11.95	9.78	82.53	7.70	23.16	plug
20	25	67.71	18.38	16.85	69.38	13.78	32.64	plug
21	35	72.63	72.68	26.81	57.70	15.49	42.28	plug
22	60	70.57	51.00	57.69	29.44	12.87	63.16	transition
23	75	70.25	70.81	81.36	13.12	5.52	77.33	annular
24	3	58.19	0.01	0.00	5.00	95.00	13.31	bubbly
25	5	59.27	0.01	0.00	100.00	0.00	14.97	bubbly
26	10	97.27	2.69	0.39	96.89	2.72	19.88	transition
27	15	95.26	7.68	2.57	92.73	4.70	24.23	transition
28	25	98.91	20.44	15.74	79.50	4.76	32.63	annular
29	35	69.78	35.96	42.60	50.97	6.42	41.83	annular

At WLR 50%, in total 28 flow conditions were involved, as shown in Table 3.21.



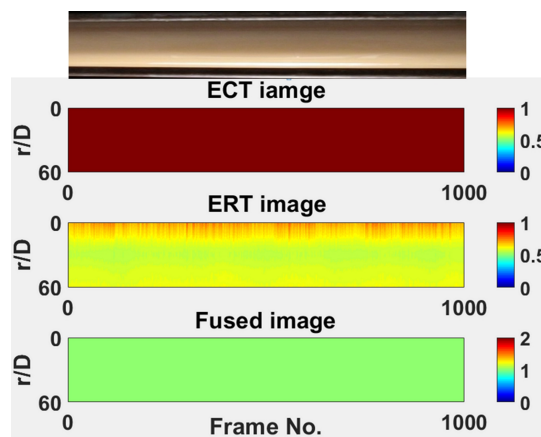
(a)

(b)



(c)

(d)



(e)

Figure 3.44: Visualisation results of WLR 50% for (a) stratified flow; (b) slug flow; (c) plug flow; (d) annular flow; and (e) bubbly flow.

Table 3.22: Selected flow conditions for visualisation at WLR 50%.

	GVF (%)	Q_{water} (m^3/hr)	Q_{oil} (m^3/hr)	Q_{gas} (m^3/hr)
Stratified flow	60	3.790	3.860	10.978
Slug flow	60	9.031	9.030	27.896
Plug flow	25	42.520	40.626	27.841
Annular flow	75	42.451	40.974	254.034
Bubbly flow	5	70.327	69.061	7.606

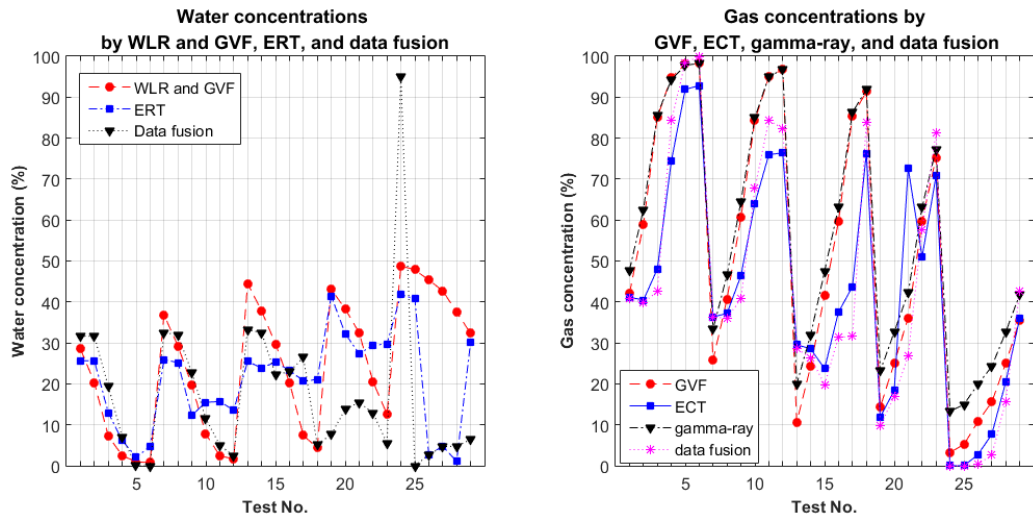


Figure 3.45: Water and gas concentrations from different approaches at WLR 50%.

The selected flow conditions are listed in Table 3.22, and the images are presented in Figure 3.44. Since ERT is functional at the WLR, the visualisation results are presented using the tomograms by ECT, ERT, and the data fusion approach (Wang et al. 2017), along with the images by high-speed camera as a reference. Figure 3.44 shows the results. From the visualisation perspective, the figures demonstrate the overall capability of the systems for imaging gas-oil-water flow at WLR 50%. In Figure 3.44d, however, when the top liquid film is very thin, ECT fails to detect it, whereas ERT is completely unable to extract the top film regardless of its thickness for the annular flow. The system also fails to manage bubbly flow in Figure 3.44e, due to the incapability of both ERT and ECT systems to identify small bubbles.

Figure 3.45 explains the quantitative results in terms of water and gas concentrations by different approaches. Generally, the results from ERT-ECT systems have a good agreement with the ones using reference values based on WLR and GVF. It is noticeable that the quantities are also in accordance with the visualisation. That is, the deviation of gas concentration from the references becomes significant for bubbly flow which, in turn, affects the accuracy of the water concentration.

3.6.2.5 WLR 75%

Similar to the results at WLR 50%, the ones at WLR 75 % reveal the general capability of the dual-modality system to qualify and quantify gas-oil-water flow. The demonstration with regard to visualisation is in Figure 3.46. The full set of the conditions is in Table 3.23, and the selected conditions are in Table 3.24. The results have comparable patterns with the ones of WLR 50%. That is, the visualisation of stratified flow (Figure 3.46a), slug flow (Figure 3.46b), plug flow (Figure 3.46c), and annular flow (Figure 3.46d) is in good agreement with the references, but not for bubbly flow (Figure 3.46e). As far as water and gas concentrations are concerned, the data fusion approach outperforms individual tomographic system, as illustrated in Figure 3.47.

In contrast to the reported performance of ECT in (Li et al. 2009b), i.e. ECT cannot manage the flow with WLR beyond 40%, both images and figures prove that ECT is still functioning at WLR 75%.

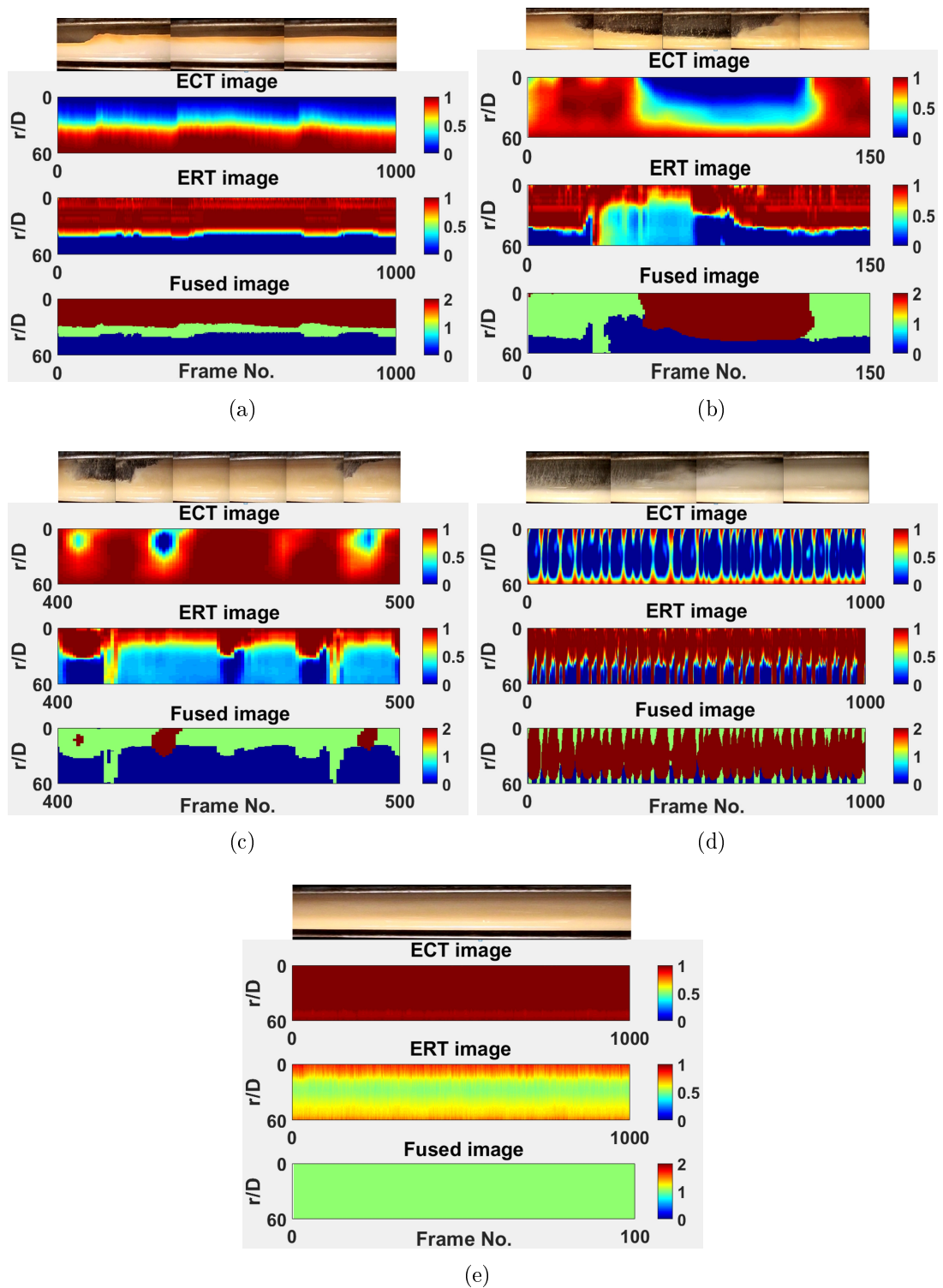


Figure 3.46: Visualisation results of WLR 75% for (a) stratified flow; (b) slug flow; (c) plug flow; (d) annular flow; and (e) bubbly flow.

Table 3.23: All examined flow conditions at WLR 75%.

Test No.	GVF %	ERT %	ECT %	Data fusion (%)			Gammy %	Flow Regimes
				gas	oil	water		
1	40	71.25	48.21	48.43	15.93	35.64	40.34	stratified
2	60	73.26	49.31	49.68	16.61	33.71	61.77	stratified
3	85	87.34	64.65	63.42	14.84	21.74	87.68	slug
4	95	86.08	73.79	77.95	1.84	20.21	93.73	transition
5	98	85.76	80.18	88.13	0.10	11.78	97.31	transition
6	98.5	85.76	82.01	90.22	0.01	9.77	98.23	annular
7	25	63.31	38.41	39.24	20.16	40.60	29.17	slug
8	42	73.42	44.56	43.74	19.70	36.56	44.77	slug
9	60	84.18	55.71	53.20	20.34	26.45	66.04	slug
10	85	83.23	67.50	70.95	6.78	22.28	84.79	slug
11	95	84.49	79.32	86.82	1.61	11.58	94.58	transition
12	96.5	83.86	81.85	90.43	0.96	8.61	96.28	annular
13	10	53.55	18.84	9.64	46.24	44.12	14.86	slug
14	25	64.34	24.28	18.44	38.56	43.00	27.72	slug
15	40	74.68	31.59	27.01	29.54	43.45	43.50	slug
16	60	79.77	43.82	40.45	28.76	30.79	61.04	slug
17	85	82.91	74.42	82.19	5.31	12.49	86.08	annular
18	92	80.70	80.50	90.09	2.69	7.23	92.36	transition
19	5	54.24	1.62	0.06	36.47	63.47	10.33	plug
20	15	52.31	8.31	3.41	36.48	60.11	18.95	plug
21	25	70.47	17.27	14.60	32.92	52.49	28.37	transition
22	60	70.73	51.38	54.43	29.14	16.44	61.32	annular
23	75	70.57	68.52	78.96	12.11	8.93	75.31	annular
24	5	60.40	0.76	0.00	99.52	0.48	10.11	bubbly
25	15	74.00	3.95	0.67	94.61	4.71	19.54	plug
26	35	71.70	18.11	5.41	81.39	13.20	38.58	plug

Table 3.24: Selected flow conditions for visualisation at WLR 75%.

	GVF (%)	Q_{water} (m^3/hr)	Q_{oil} (m^3/hr)	Q_{gas} (m^3/hr)
Stratified flow	40	5.533	2.063	4.508
Slug flow	60	29.697	9.834	58.471
Plug flow	15	63.898	21.654	14.568
Annular flow	75	63.937	20.462	247.125
Bubbly flow	5	105.102	35.264	7.654

3.6.2.6 WLR 90%

Due to the unavailability of stratified flow, the visualisation for WLR 90% contains the other four flow regimes for the given conditions in Table 3.25, and the conditions presented in Table 3.26. The flow is visualised by ECT, ERT, and the data fusion approach, as depicted in Figure 3.48, and similar results occur with the given conditions. Figure 3.49 compares water and gas concentrations by

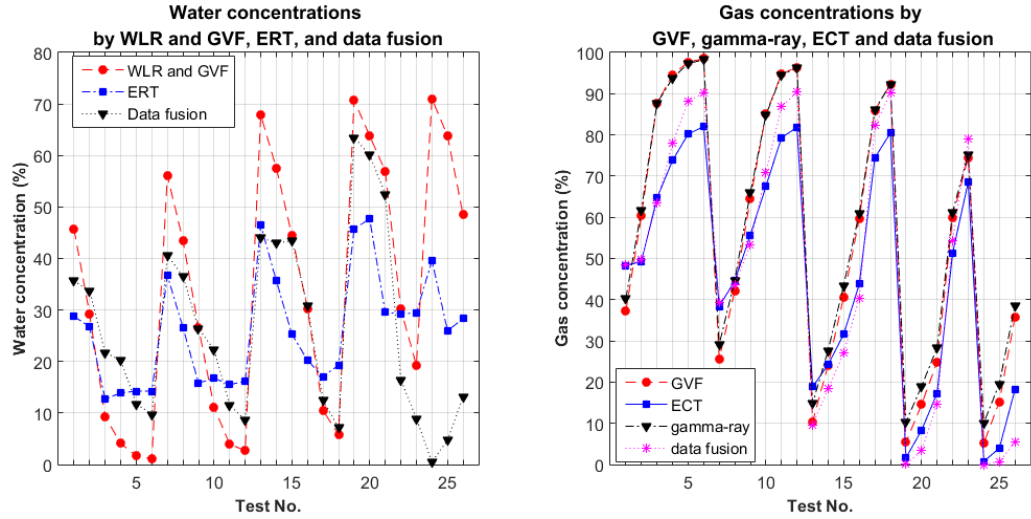


Figure 3.47: Water and gas concentrations from different approaches at WLR 75%.

Table 3.25: All examined flow conditions at WLR 90%.

Test No.	GVF %	ERT %	ECT %	Data fusion (%)			Gammy %	Flow Regimes
				gas	oil	water		
1	25	58.23	31.71	31.68	21.12	47.20	26.22	transition
2	42	66.30	39.28	37.87	19.78	42.35	42.39	transition
3	60	74.68	50.05	46.90	16.78	36.33	61.86	transition
4	85	71.52	65.35	65.09	22.06	12.85	84.56	slug
5	95	84.18	81.17	88.33	1.44	10.23	94.77	annular
6	96.5	84.18	83.68	91.59	0.85	7.55	7.16	annular
7	10	47.42	14.07	9.25	48.15	42.59	12.29	slug
8	25	62.35	19.93	17.38	28.82	53.81	26.82	slug
9	40	73.73	28.52	25.43	22.77	51.80	42.02	slug
10	60	78.55	41.75	40.23	22.98	36.79	58.88	slug
11	85	83.23	69.82	75.40	9.82	14.79	85.29	annular
12	92	78.96	79.43	89.02	3.33	7.65	91.61	annular
13	5	41.67	2.74	0.23	14.03	85.75	7.16	transition
14	15	52.74	9.71	4.86	19.46	75.68	17.62	plug
15	25	67.57	17.77	14.01	21.85	64.14	27.05	slug
16	35	68.99	20.15	16.89	25.76	57.35	35.86	slug
17	60	68.51	44.05	45.25	29.37	25.38	61.80	slug
18	75	68.31	65.61	76.23	15.52	8.25	76.28	annular
19	3	12.70	0.05	0.00	0.00	100.00	5.23	bubbly
20	15	64.05	0.45	0.00	26.55	73.45	16.70	bubbly
21	35	67.66	17.40	0.73	57.51	41.77	37.10	bubbly

different approaches. It is noted that ECT is still operational at WLR 90%.

Table 3.26: Selected flow conditions for visualisation at WLR 90%.

	GVF (%)	Q_{water} (m^3/hr)	Q_{oil} (m^3/hr)	Q_{gas} (m^3/hr)
Slug flow	35	76.601	8.438	45.577
Plug flow	15	76.329	8.485	16.158
Annular flow	92	36.563	4.130	455.277
Bubbly flow	3	126.374	13.932	4.716

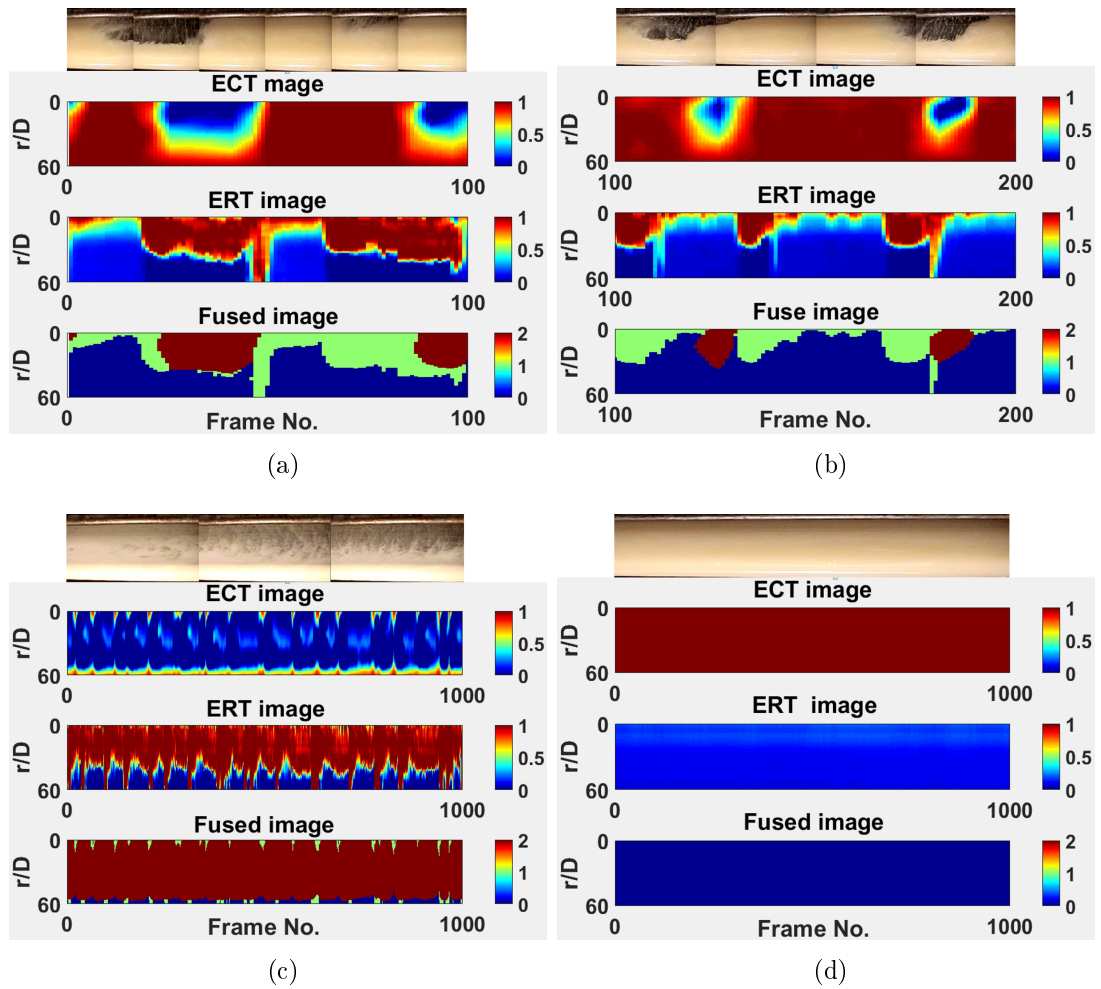


Figure 3.48: Visualisation results of WLR 90% for (a) slug flow; (b) plug flow; (c) annular flow; and (d) bubbly flow.

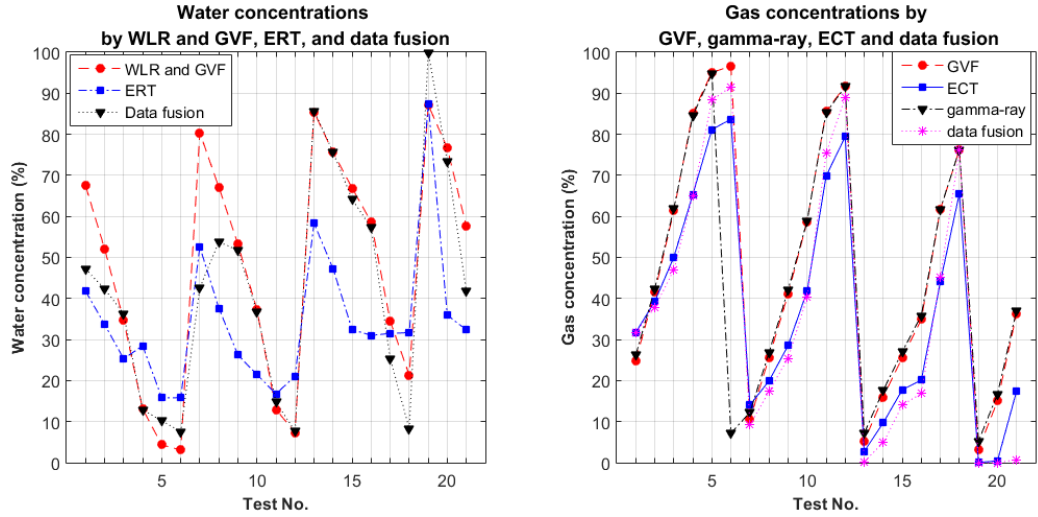


Figure 3.49: Water and gas concentrations from different approaches at WLR 90%.

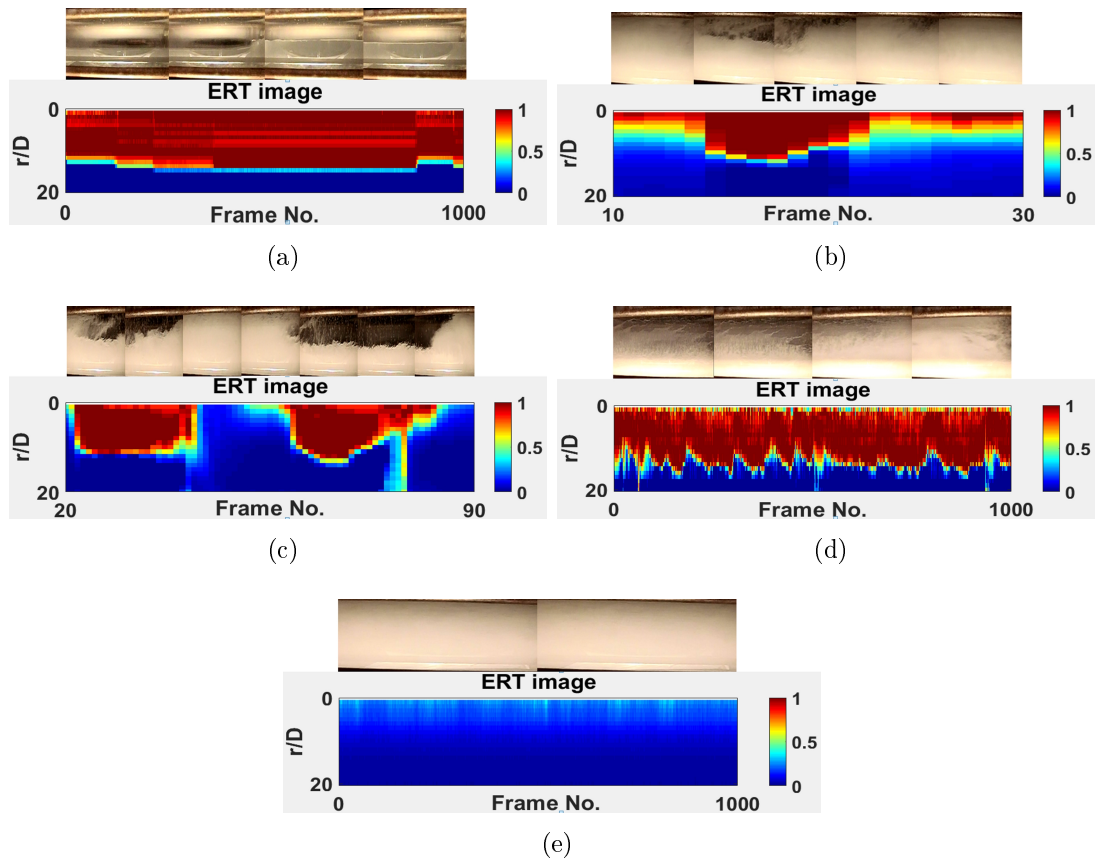


Figure 3.50: Visualisation results of WLR 100% for (a) stratified flow; (b) slug flow; (c) plug flow; (d) annular flow; and (e) bubbly flow.

Table 3.27: All examined flow conditions at WLR 100%.

Test No.	GVF %	ERT %	ECT %	Data fusion (%)			Gammy %	Flow Regimes
				gas	oil	water		
1	82	75.29	x	x	x	x	80.78	stratified
2	97	84.81	x	x	x	x	96.01	stratified
3	99.4	81.33	x	x	x	x	99.20	annular
4	60	60.67	x	x	x	x	59.90	stratified
5	95	83.70	x	x	x	x	94.11	stratified
6	98.5	78.32	x	x	x	x	98.20	annular
7	42	55.77	x	x	x	x	41.97	slug
8	85	76.58	x	x	x	x	85.11	slug
9	95	81.79	x	x	x	x	94.64	annular
10	96.5	73.29	x	x	x	x	96.34	annular
11	25	52.85	x	x	x	x	24.73	slug
12	60	70.41	x	x	x	x	59.80	slug
13	92	68.31	x	x	x	x	91.90	annular
14	15	50.82	x	x	x	x	15.17	plug
15	35	57.16	x	x	x	x	34.66	plug
16	60	61.03	x	x	x	x	58.97	stratified
17	75	71.87	x	x	x	x	74.82	stratified
18	3	6.21	x	x	x	x	3.50	bubbly
19	5	8.50	x	x	x	x	4.91	bubbly
20	10	21.31	x	x	x	x	9.48	bubbly
21	15	35.94	x	x	x	x	14.23	slug
22	25	52.30	x	x	x	x	25.06	slug
23	35	56.57	x	x	x	x	33.87	slug

Table 3.28: Selected flow conditions for visualisation at WLR 100%.

	GVF (%)	Q_{water} (m^3/hr)	Q_{gas} (m^3/hr)
Stratified flow	82	2.891	12.883
Slug flow	25	138.896	47.193
Plug flow	35	85.272	46.084
Annular flow	98.5	7.501	507.037
Bubbly flow	5	139.348	7.250

3.6.2.7 WLR 100%

When WLR is 100%, flow becomes a gas-water two-phase flow. It was observed that ECT was still able to produce some tomograms, although they were distorted. Consequently, the images are only generated by ERT, as demonstrated in Figure 3.50. For all engaged flow conditions shown in Table 3.27, there were five conditions selected for the evaluation (Table 3.28). ERT tomograms are reasonable, which is also proven by the gas concentration in Figure 3.51.

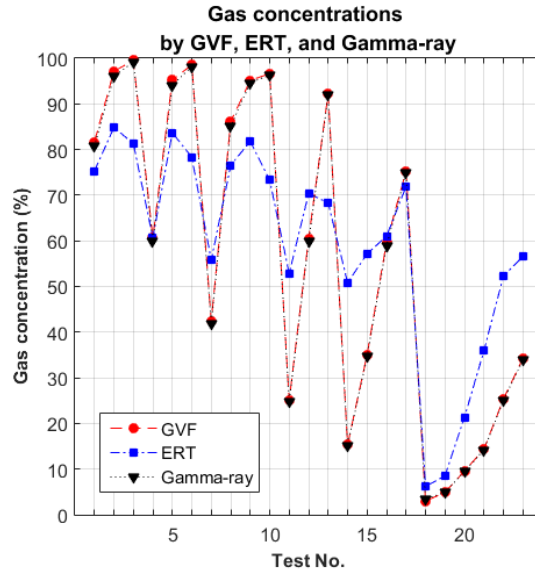


Figure 3.51: Gas concentrations from different approaches at WLR 100%.

3.6.3 Discussion

3.6.3.1 ECT system

The results in the previous section demonstrate the capability of the applied ECT system to visualise multiphase flow in a horizontal pipeline. Compared to the reported suitability of the ECT system for the flow with WLR less than 40%, i.e. oil-continuous flow (Li et al. 2009b), the results clearly prove the capability of the ECT system can be extended to 90% WLR, with appropriate taking of reference.

When flow structure is relatively simple, i.e. stratified flow and slug flow, and flow is with relatively low or moderate flowrate, i.e. water and oil are not fully mixed, the ECT can detect the interface between gas and liquid, with great accuracy, such as the ones in Figure 3.38a and Figure 3.44b, etc. As for annular flow, the ECT is still able to image it with certain accuracy, e.g. in Figure 3.38d and Figure 3.42b. It is also able to detect the change in thickness of the top liquid film, as in Figure 3.42b. Nevertheless, it has to be pointed out that when the thickness is below the resolution of the ECT system, the film is undetectable, as in Figure 3.40c. Moreover, there are some ECT tomograms, e.g. Figure 3.46d, that depict a strange phenomenon, i.e. some liquid is at the centre of the pipe,

which might be caused by the liquid droplets at the centre. As far as bubbly flow is concerned, when gas is fully dispersed in liquid, the ECT fails to extract tiny bubbles due to their size being below the ECT's resolution, whereas the quantitative results present that gas concentration can be extracted by the ECT.

3.6.3.2 ERT system

For the examined WLR values, the deployed ERT system has good agreement with the report (Li et al. 2009b). That is, it is capable of handling gas-oil-water flow with WLR above 40%, i.e. water-continuous flow. Nonetheless, it was seen that the applied ERT system managed to image stratified and slug flow when WLR was at 25%, although the measured quantities had a large discrepancy to the reference values.

Within the effective WLR range, the ERT produces similar results compared with the ones using the ECT. When flow structure is simple and total flowrate is relatively low, the interface between conductive (water) and non-conductive (gas and oil) is clearly addressed. For stratified, slug, and plug flow, the boundaries are quite sharp and reasonable, compared with related video log; whereas when water and oil are mixed together, the performance of the ERT deteriorates. The ERT was unable to image the top liquid film for engaged annular flow, due to the limitation of the ERT with respect to resolution. It is also noticed that there is an overestimate of the thickness of the bottom liquid film, which may result from the disturbance of the oil phase since the oil phase is supposed to be fully dispersed in the water phase for annular flow. Similar to the ECT, the ERT has no ability to identify dispersed tiny bubbles in bubbly flow, and hence no bubbles are seen in the ERT tomograms for bubbly flow. But it still presents water concentration even though tiny bubbles disappear in the images.

3.6.3.3 Dual-modality electrical tomographic systems

On the basis of the performance of the ERT and the ECT, a general conclusion can be drawn in regard to the ERT-ECT systems: the dual-modality ERT-ECT systems are an effective method when characterising gas-oil-water horizontal flow of WLR between 40% and 90%, in accordance with the capabilities of the ERT

and the ECT as single modality. Within this range, single-modality electrical tomography struggles to provide sufficient and accurate information to decompose the phases in the flow, whereas the integrated systems complement the limitations of either system by fusing the data from both modalities. In contrast, when WLR is out of the range, the systems cannot provide complementary information by fusing the data from each modality.

By applying the threshold-based data fusion approach, individual phases are distinguished, and therefore visualised using different colours. In principle, the gas concentration by the fusion is determined by the CT result, whereas the water concentration by fusion depends on the ERT results. In consequence, the accuracy of the data fusion relies on the resolution of the ECT and the ERT. When total flowrate is relatively low, i.e. stratified flow and slug flow, both qualification and quantification are in great agreement with references. In contrast, the performance of data fusion deteriorates when either modality cannot perform well, especially in terms of visualisation. A typical example is bubbly flow, in which both ERT and ECT are incapable of locating tiny bubbles, and hence the fused images provide little clues about tiny bubbles, although concentration information is still presented.

Overall, the application of the dual-modality electrical tomography results in more accurate quantities of phase concentrations within its functional range, compared to that of each single modality. However, it is also noted that under some extreme conditions, e.g. bubbly flow, data fusion results are not as good as those by individual modality. As for gas concentration, the one by data fusion is better than the one by those ECT alone, except on bubbly flow. This is essentially because of the limit of the ECT in this flow. On the other hand, the comparisons of water concentrations by different approaches indicate that the ERT results are not always as good as expected, especially at lower WLR, which reflects the negative effect of the oil phase as an additional non-conductive phase on the ERT. The quantities, however, become better after data fusion, despite there being extreme cases where the ERT outperforms data fusion, such as bubbly flow.

Despite the error caused by the above data fusion, however, it is worth noting that measurement uncertainty does play an important role. The measurement uncertainty mainly comes from two sources: one is systematic error, and the other is random noise. It is usually believed that about the 5% of systematic

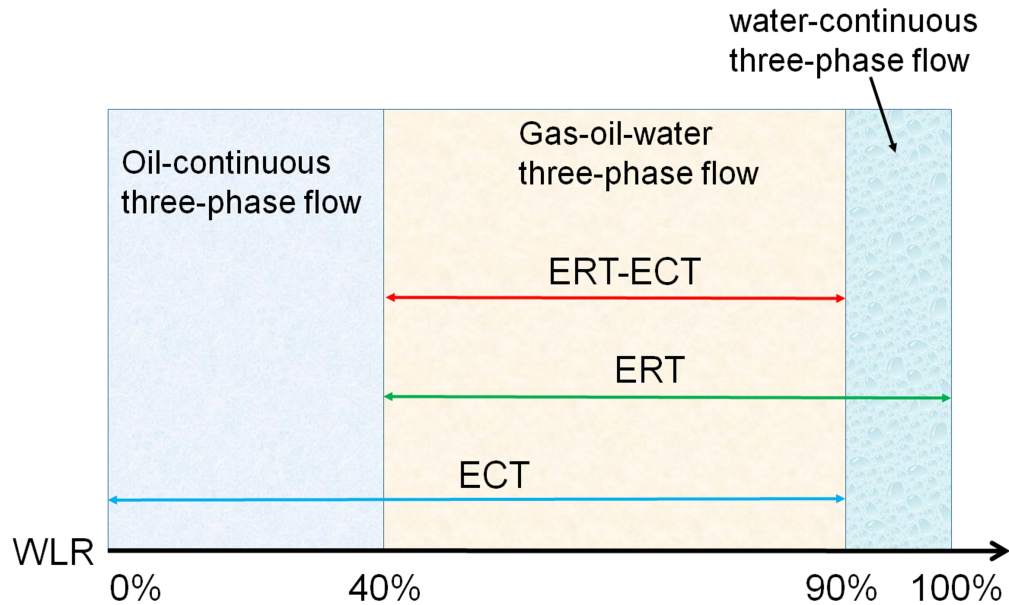


Figure 3.52: Capability of the ERT-ECT system against WLR.

error comes from hardware (Wang et al. 1999), which could be introduced by the imprecision of sensing electronics and A/D conversion, improper compensation to temperature and/or ionic concentration changes etc. and also the artificial error from imaging reconstruction. Consequently, the ERT-ECT systems could introduce up to 10% systematic error. Random noise, on the other hand, is generally as a consequence of uncontrollable and unrepeatable factors, such as the flow instability, electricity crosstalk, and so on. The uncertainty due to random noise could be 5% but can be reduced with the cost of increasing sampling number. Together the potential systematic error with the random noise, the final uncertainty of the mean concentration measurements could be up to 10-15%.

3.6.4 Conclusions

The experimental results demonstrate the overall capability of the dual-modality ERT-ECT systems in the domain of gas-oil-water flow characterisation. From the hardware perspective, the systems have proved to be effective, robust, and reliable for the purpose of multiphase flow visualisation and measurement. Likewise, the images and numbers further substantiate the conclusions from the viewpoint of data processing. In WLR 0%-90%, the ECT is able to produce acceptable

tomograms to reflect the distribution of gas phase and liquid phase, whereas the ERT is able to deal with the flow of WLR [40%, 100%] to distinguish gas and oil as conductive phase from water as a non-conductive phase. As a dual-modality system, the ERT-ECT can quantify and qualify the flow of WLR within [40%, 90%]. The capabilities of the ERT-ECT systems as single- and dual-modality are depicted in Figure 3.52.

Despite the advantages, there are still some aspects to be addressed in the future. First of all, further experiments should be carried out to make the evaluation more thorough. For example, WLR between 30% and 50% should be covered to determine the lower bound of the effective range for the systems. Moreover, a cross-correlation method should be applied to quantify the flowrate of each phase, so that the comparisons with GVF and WLR are more meaningful and accurate. The quantification of velocity would also contribute to study slip characteristics between each phase. Since the performance of ERT-ECT systems totally depend on the tomograms by each individual modality. The systems utilised in this study have low resolution due to the application of single-step LBP (Kotre 1994), advanced iterative reconstruction algorithms could be applied to improve the resolution of the tomograms, which in turn improves the final results, especially as the data-processing speeds develop over time. Last but not least is the improvement of the data fusion methodology, although a threshold-based approach is effective, few efforts have made on a comprehensive evaluation of the impact of the selected threshold values on the final fused results. In addition, advanced fusion algorithms requires more computational power. Data fusion may mature into a process that can support the development, operation and optimisation of multiphase flow measurement technology.

An essential impact on the performance of the systems is the spatial resolution of the input concentration tomograms. The systems utilised in this study have relatively low resolution due to the application of single-step linear back-projection (LBP) (Kotre 1994), advanced reconstruction algorithms, e.g. sensitivity theorem based conjugate gradients (SCG) (Wang 2002) and the iterative Landweber method (Yang et al. 2003), could be applied to improve the resolution of the tomograms, which in turn improves the final results, especially as the data-processing speeds develop over time.

The improvement of data fusion methodology is also worthy of more effort. Although a threshold-based approach is effective, little effort has been made on a comprehensive evaluation of the impact of the selected threshold values on the final fused results. In addition, advanced fusion algorithms, e.g. fuzzy clustering (Yue et al. 2013), requires more computational power. Data fusion may mature into a process that can support the development, operation, and optimisation of multiphase flow measurement technology.

Last but not least is artificial errors during data fusion due to the registration process on spatial and temporal dimensions could be removed by the advanced design of hardware. For instance, the systems in (Marashdeh et al. 2007; Ji et al. 2016) are able to obtain both conductivity and permittivity information simultaneously, and thus the temporal registration in the fusion process is no longer necessary thereby reducing partial errors caused by the temporal interpolation during the registration.

3.7 Summary

In regard to tomography-based measurement and visualisation of gas-oil-water flow, various modalities have been combined together to reveal flow dynamics. However, there are still challenges with regard to data fusion techniques and comprehensive evaluation involved in the applications of such systems. This chapter, therefore, aimed to overcome the limitations. First of all, a generic framework was proposed to formally and explicitly describe the overall procedure of data processing for DMTS in imaging multiphase flow. In particular, it discussed in detail the issues with regard to the registration of multi-dimensional data, i.e. transferring the data acquired at different speeds, with different grid definitions, and by different modalities to a common coordination system so that the processed data are spatially and temporally registered to be fused.

In addition, it also explored the problems of how to properly display fused data using conventional colour mapping. Based on the framework, two different fusion algorithms were reported, including threshold-based and fuzzy logic-based approaches, both of which have been applied to experimental data obtained from

ERT-ECT systems from an industrial flow facility. The capability and performance of the methods were evaluated with fast photography and the commonly recognised flow conditions to generate specific flow regimes, as well as references of flow quantities provided from the facilities. The feasibility of the fusion techniques was seamlessly integrated into the framework, which in turn proved the generality of the framework.

Finally, gas-oil-water flow in a horizontal pipe with the combination of WLR 0-100% with GVF 0-100% was quantified and qualified using the proposed framework and threshold-based fusion scheme by ERT-ECT systems on the industry-scale gas-oil-water flow testing facilities at TUV NEL. The quantification and qualification not only proved the feasibility of the proposed approaches, but also evaluated the performance of the systems.

CHAPTER 4

BUBBLE MAPPING METHOD FOR VISUALISING GAS-LIQUID FLOW

Highlights: In this chapter, a novel approach, known as bubble mapping, is proposed to overcome the limitations associated with the visualisation of gas-liquid flow by electrical tomography, i.e. incapability of identifying small bubbles and the sharp interfaces between large bubbles and liquid. By replacing conventional colour-based representation with proposed bubble-based representation, along with an enhanced isosurface algorithm, bubbles are reconstructed based on a stack of electrical tomograms. The experimental results on both vertical and horizontal pipe using ERT demonstrate the feasibility of the proposal. Compared with the results from conventional colour mapping, the proposed approach yields more realistic flow visualisation and visual recognition of flow regimes. It is also worth noting that the approach is designed to be generic and hence could be easily adapted to other techniques that produce concentration distributions of gas-liquid flow.

4.1 Introduction

Due to the limitations of electrical tomography when visualising multiphase flow and the shortcomings of visualisation methods employed for electrical tomography, electrical tomograms are unable to provide sufficient information regarding flow dynamics, e.g. bubble size and distribution. In this chapter, a novel approach, known as *bubble mapping*, is proposed for the 3D visualisation of gas-liquid flow by electrical tomography. It essentially reconstructs bubbles from a stack of cross-sectional concentration tomograms derived from electrical tomography, with the assumptions that gas bubbles are randomly distributed within a small volume, called the *interrogation cell* (IC), and the growth and collapse of the bubbles is trivial and so can be ignored (Brennen 2005). According to

the assumption and the definition of the gas volumetric fraction (Brennen 2005; Corneliussen et al. 2005), a new lookup table can be constructed to replace the conventional colour-based lookup table. The new lookup table transfers averaged volume fraction of an IC to a bubble, of which the size is fractional to the averaged volume fraction and the position is randomly inside the IC. In order to build the bubbles larger than an IC, a number of neighbouring ICs are swarmed together, whose averaged concentrations are larger than a carefully chosen threshold. By applying an enhanced isosurface algorithm, the boundaries between large bubbles and the liquid phase are extracted. It is assumed that small bubbles are spherical, whereas the shape of large bubbles is random and determined by input tomograms.

Compared to conventional visualisation methods for multiphase flow by tomographic techniques, our approach yields a few advantages. First of all, it is independent of flow direction and pipe orientation, and hence can manage a number of common flow regimes existing in vertical and horizontal pipe, including bubbly flow, slug flow, and annular flow in a vertical pipeline, as well as (wavy) stratified flow, slug flow, plug flow, bubbly flow, and annular flow in horizontal pipeline. In addition, presenting gas-liquid flow by bubbles instead of colours is able to convey more useful and vivid information to reflect the spatial distribution of gas and liquid phases, such as visual recognition of flow patterns. Moreover, the approach is designed to be generic since concentration distribution is utilised as input, it can be easily adopted to suit other tomographic techniques, as long as their output is stacked in cross-sectional concentration tomograms.

The rest of the chapter is arranged as follows. Section 4.2 explains the technical aspects of the approach in detail. The approach is evaluated in Section 4.3 using commercialised ERT (V5R and FICA), and the discussion and conclusions are presented in Section 4.4.

4.2 Methodology

Pixel colours in electrical tomograms are derived from a lookup table, in which an input pixel concentration is mapped to a colour. Concentration of pixels varies from 0.0 to 1.0, corresponding to a pixel which is fully occupied by liquid and

gas, respectively. If the value is within the range (0.0, 1.0), it means that the relating pixel is partially filled with gas. According to the definition of a gas void fraction (Corneliussen et al. 2005), a void fraction is the ratio of the flow area occupied by gas and the total flow area. Therefore, a new lookup table can be built, in which a concentration value of one pixel can be transferred to a circular bubble instead of a colour, and the value is maintained by the ratio of the areas of the circle and the pixel. Following this fundamental concept, bubbles can be reconstructed, and therefore gas-liquid flow can be visualised using bubbles, and it is easy to extend this 2D concept to a 3D case.

In a 3D case, the input is a stack of cross-sectional electrical concentration tomograms. In order for 3D bubbles to be built up correctly, both spatial and temporal information from electrical tomograms have to be integrated together. In spatial terms, 2D cross-sectional tomograms represent the concentration distribution of the dispersed phase of gas-liquid flow in a pipe, i.e. gas. Whereas in temporal terms, with the assumption that the local velocity of the gas phase at the point of measurement is equal to the superficial velocity of the gas phase by reference, bubbles flow forward a certain distance dependent on the data acquisition speed of tomography employed and the local velocity of the gas phase. On the other hand, real-case bubble diameter in a fully-developed gas-liquid flow is within the range of 5mm to 20 mm regardless of the vessel diameter (Guet et al. 2002; Sean et al. 2004; Jin et al. 2007; Qi et al. 2012). By assuming that all small bubbles are below 20 mm, a number of neighbouring pixels along spatial and temporal dimensions can be clustered together to form an interrogation cell (IC) to ensure that no small bubble is larger than an IC. As for large bubbles beyond an IC, an isosurface algorithm can be used to isolate the bubbles and liquid phase.

The overall procedure of the approach is depicted in Figure 4.1. A stack of electrical concentration tomograms are firstly split into a number of properly-defined ICs. Later, a new bubble-based lookup table is applied to map IC concentration to bubbles so that small bubbles and the approximated location of large bubbles are identified. At this stage, clear boundaries between large bubbles and liquid are not located. Therefore, an enhanced isosurface algorithm is applied to locate the boundaries and meanwhile to overcome the limitation of a conventional iso-surface algorithm. After all the bubbles are reconstructed, the results are rendered and displayed using an inherent method in modern computer graphics.

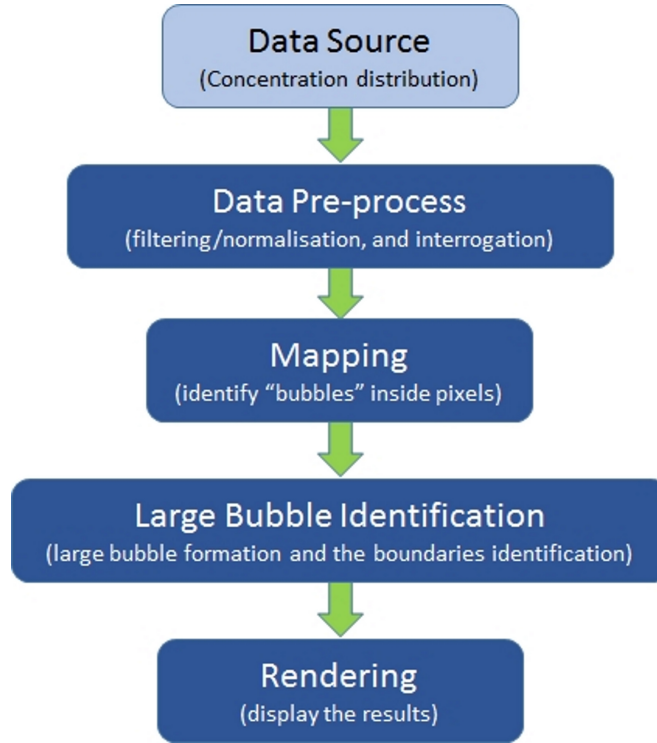


Figure 4.1: The pipeline of the new approach.

4.2.1 Data preprocessing

Because of the uncertainty relating to electrical tomography, the converted concentration tomograms may unavoidably contain some abnormal data, e.g. negative values. Hence, the data has to be pre-processed first. The in-the-range concentration distribution is then separated into ICs by considering both spatial and temporal dimensions. In particular, the spatial dimension needs to take account of the size of small bubbles, as well as the resolution of the tomography employed, while the temporal dimension needs to incorporate the local velocity of the gas phase and DAS of the tomography.

Given a scalar field $\phi : R^d \rightarrow R$ and a concentration set C over ϕ , i.e. sequentially stacked cross-sectional concentration tomograms, concentration values can be defined as

$$C = \{c_i\} \quad c_i \in R \quad (4.1)$$

When abnormal data exists, filter/normalisation may be required to make the data fit into a reasonable range, i.e. $[0.0, 1.0]$. In this report, the input tomograms are generated by commercialised software (ITS 2009), and are always in non-

shifted terms, due to the internal restrictions provided by the software. Therefore, no extra pre-processing is needed here. Otherwise, a simple filter could be applied by:

$$F(c_i) = \begin{cases} 0.0 & c_i < 0 \\ c_i & 0 \leq c_i \leq 1.0 \\ 1.0 & c_i > 1.0. \end{cases} \quad (4.2)$$

It is noted that when filtering is utilised for the removal of abnormal data, a shift of averaged concentration with and without it may be introduced. Fortunately, the discrepancy is too trivial to negatively affect the quality of visualisation, and hence the shift is considered to be ignorable.

The minimal size of identifiable objects by electrical tomography is reported to be 5% (Wang et al. 1999), meaning that for a given pipe with diameter D_p , the minimal D_m is $D_m = 0.05D_p$. The spatial resolution of electrical tomography is influenced by many factors, such as the number of electrodes and reconstruction algorithms. Given an electrical tomography and a reconstruction algorithm, the lower bound primarily relies on pipe diameter. Due to the inhomogeneity of the sensitivity distribution, an area closer to the boundary of the pipe has higher sensitivity (Wang et al. 2016a). In addition, because of the inverse relationship between distance and the strength of the electrical field, further distance from the citation source has a lower field. In consequence, electrical tomography on larger pipe usually has weaker sensitivity. However, it is extremely challenging to discover the quantitative relationship between the minimum distinguish-ability and the influencing factors, particularly when LBP is applied, in which case bubbles which are much smaller than pipe diameter are all indistinguishable.

It is, however, reported that small bubbles are usually less than 20 mm regardless of pipe diameter (Guet et al. 2002; Sean et al. 2004; Jin et al. 2007; Qi et al. 2012). Therefore, it is acceptable to assume that the size of all small bubbles is below 20 mm, i.e. $D_s = 20mm$. With the assumption that small bubbles are spherical and there is only one small bubble inside an IC, an IC is thus expected to host one small bubble, and hence the physical size reflected by an IC is 20 mm, i.e. both spatial and temporal dimensions are 20 mm. Accordingly, the spatial dimension of an IC can be defined as:

$$Dim_s^{IC} = \frac{D_s}{D_p} * \frac{D_s}{D_p} \quad (4.3)$$

where D_p is the diameter of a pipe containing a gas-liquid flow, m and n are the spatial grid definition of the original concentration set.

As far as temporal dimension is concerned, it relates to temporal information, i.e. imaging speed, rather than spatial information. It is thus necessary to transfer it to spatial information by taking account of the local velocity of the gas phase and the DAS of the applied tomography, of which the local velocity is assumed to be equal to the superficial velocity of the gas phase at injection point. For example, suppose the superficial velocity of the gas phase is 1 m/s and the tomography works at 1000 frames per second (fps), if measurement is performed for 1 second, the 1000 frames collected reflect that bubbles move forward for one metre. That is, when two consecutive frames are collected, bubbles move forward $1m/s * 1ms = 1mm$. Therefore, the temporal dimension of an IC can be derived by:

$$Dim_s^{IC} = \frac{D_s}{v * \Delta t} \quad (4.4)$$

where v is the superficial velocity of the gas phase, and Δt is the temporal resolution of the deployed tomography.

According to Equation 4.3 and Equation 4.4, IC is defined, and consequently the original input tomograms can be split into a number of IC that will be further processed.

4.2.2 Construction of a new lookup table

A new lookup table that maps a scalar value to a bubble is going to be built up in this section, so that after this step the averaged concentration of the IC is represented by bubbles, i.e. small bubbles or the core of large bubbles. For gas-liquid flow, an IC's mean concentration can be calculated by:

$$c_i^{IC} = \frac{\sum_{i=1}^m v_i^b}{v_i^{IC}} \quad (4.5)$$

where c_i^{IC} is the mean concentration of the cell, v_i^b is the volume of the i th bubble inside the given volume v_i^{IC} , and m is the number of bubbles inside the volume. In fully developed gas-liquid flow, it is reasonable to approximate that there is one and only one spherical bubble inside an IC, i.e. $m=1$, thereby Equation 4.5 is rewritten to:

$$c_i^{IC} = \frac{v_i^b}{v_i^{IC}} \quad (4.6)$$

where v_i^b is the volume of the bubble in i th cell. Equation 4.6 can be further rearranged to:

$$v_i^b = v_i^{IC} * c_i^{IC} \quad (4.7)$$

According to the dimension definition of an IC (Equation 4.3 and Equation 4.4), c_i^{IC} can be derived by:

$$c_i^{IC} = \frac{1}{Dim_x^{IC} * Dim_y^{IC} * Dim_s^{IC}} \sum_{k=1}^{Dim_s^{IC}} \sum_{y=1}^{Dim_y^{IC}} \sum_{x=1}^{Dim_x^{IC}} c_{x,y}^k \quad (4.8)$$

By considering Equation 4.3, Equation 4.4, Equation 4.7, and Equation 4.8 altogether, the radius of the bubble with the volume v_i^b can be derived:

$$\begin{aligned} R_b &= \left(\frac{3}{4\pi} * c_i^{IC} * v_i^{IC} \right)^{\frac{1}{3}} \\ &= \left(\frac{3(D_s)^3 * \left(\sum_{k=1}^{Dim_s^{IC}} \sum_{y=1}^{Dim_y^{IC}} \sum_{x=1}^{Dim_x^{IC}} c_{x,y}^k \right)}{4\pi * Dim_x^{IC} * Dim_y^{IC} * Dim_s^{IC}} \right)^{\frac{1}{3}} \end{aligned} \quad (4.9)$$

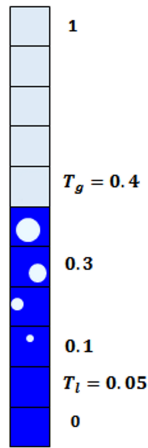


Figure 4.2: The new lookup table in 2D for bubble mapping.

It is usually believed that electrical tomography has 5% uncertainty due to systematic errors and random noise, such as imprecision of sensing electronics and approximation of image reconstruction (Wang et al. 1999; Qiu et al. 2007). Consequently, when the mean concentration c_i^{IC} is below 5%, it is assumed that the IC is fully occupied by liquid phase. It was also reported that in a static bubble column with a diameter of 5 cm, bubbly flow was observed when air concentration was below 40%, whereas slug flow appeared when the concentration was above 40% (Deckwer 1992; Wang et al. 2001). Accordingly, it is approximated that

40% is an important threshold, below which there are only small bubbles, whereas beyond which large bubbles emerge. That is, when mean concentration c_i^{IC} is higher than 40%, the IC is assumed to be fully occupied by gas phase. When mean concentration c_i^{IC} is between 5% and 40%, there is one and only one small spherical bubble inside the IC, of which the diameter is determined by c_i^{IC} and calculated by Equation 4.9. Following these principles along with the assumptions, a new lookup table can be constructed, by which c_i^{IC} is transferred to bubbles of a certain size and at a random location within the IC. A demonstration of the lookup table in 2D is depicted in Figure 4.2.

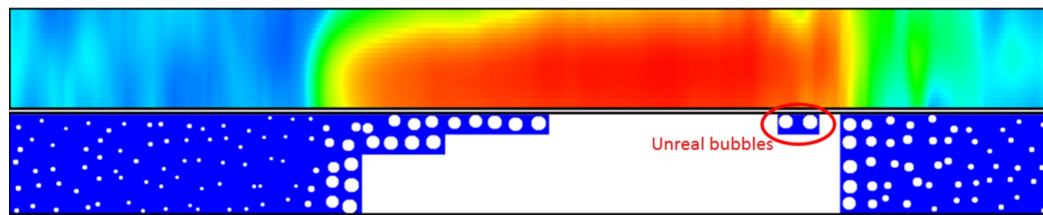


Figure 4.3: 2D stacked concentration tomograms by colour mapping and bubble mapping.

Once the lookup table is built up, it is time to apply it to the whole IC-based dataset so that all bubbles are reconstructed. Figure 4.3 shows an example of the mapping from a 2D axially-stacked tomogram by ERT to a bubble-based image. In comparison to conventional presentation of gas-liquid flow (upper image in Figure 4.3), the proposed one (lower image in Figure 4.3) is able to show bubbles up, which were invisible in the conventional one. It is, however, noted that the large bubble in the figure is not consistent with real-world examples, in terms of its shape. In addition, there are also some unreal small bubbles in the red ellipse in the lower image. The reason is because merging adjacent bubbles beyond a particular size is not taken into consideration. Therefore, the next step is to identify a reasonable shape of large bubbles by clustering neighbouring bubbles.

4.2.3 Large bubble identification

Due to the averaging during the construction of IC and the mapping to bubbles, boundary segments may be eliminated. Instead, small bubbles are derived since averaged values are below the threshold 40%. Fortunately, this undesirable situation only occurs at the boundaries between large bubbles and the liquid phase.

As a result, those IC adjacent to the body of large bubbles (the large white area in Figure 4.3) have to be counted during identification of large bubbles.

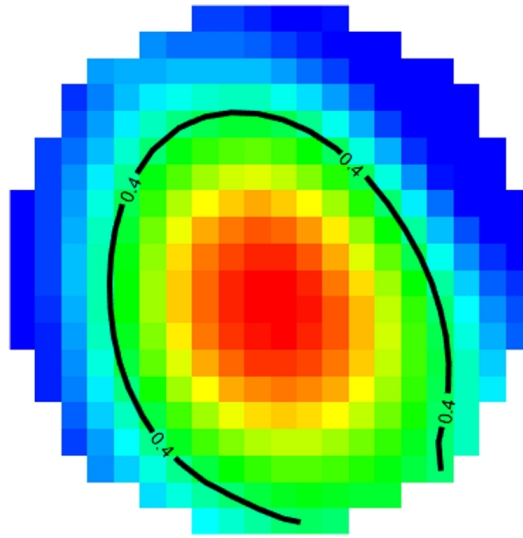


Figure 4.4: Opening contour by conventional Marching Cubes for a 2D concentration tomogram.

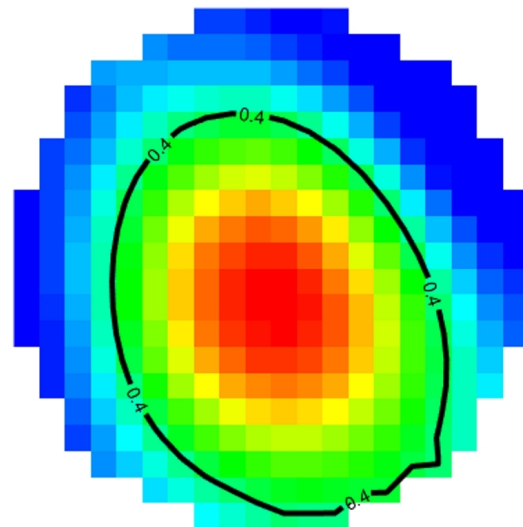


Figure 4.5: Closed contour by enhanced Marching Cubes for a 2D concentration tomogram.

After those pure-water IC and their adjoining IC are located, an isosurface algorithm can be applied to extract the interfaces between large bubbles and liquid phase. In particular, Marching Cubes (Lorensen et al. 1987) are utilised in this

research. Figure 4.4 shows an example of an isosurface extraction in 2D, i.e. contour, in which a threshold value of 0.4 is used as the isovalue and the black line is the retrieved contour. Unfortunately, the large bubble represented by the contour is not sensible since it is not a closed line. This is because the physical boundary, i.e. pipe wall, is not taken into account. In other words, when the averaged concentration of an IC at a pipe wall is over the threshold, Marching Cubes does not respect the existence of the physical boundary by forming an open contour. In consequence, it has to be enhanced to overcome this limitation. Figure 4.5 illustrates a closed contour using enhanced Marching Cubes by integrating the physical boundary with the contour.

4.3 Evaluation using ERT

In order to evaluate the proposed approach, two sets of experiments were conducted using a commercial ERT system, namely FICA (Wang et al. 2005) and V5R (Jia et al. 2010), on vertical and horizontal pipe, respectively. All concentration tomograms were reconstructed using ITS P2+ software (ITS 2009). The experiments covered typical flow regimes in both orientations, including bubbly, slug, and annular flow in a vertical pipe¹, and (wavy) stratified, slug, plug, bubbly, and annular flow in a horizontal pipe. The results are presented, along with the consecutively-stacked images by a high-speed camera and conventional colour mapping. The colour mapping based images are all produced using the same colour lookup table (blue to red) and same scale [0.0, 1.0]. Since local velocity was not measured, the superficial velocity of the gas phase is applied to derive the temporal dimension of the IC.

4.3.1 Gas-water flow in a vertical pipeline

Firstly, the approach was evaluated for upward gas-liquid flow in a 100 m vertical section of the flow loop located at the University of Leeds. Air was used as the gas phase and tap water as the liquid phase. The data was gauged by the FICA system at a sampling speed of 1000 frames per second, and reconstructed using

¹The results exclude churn flow, not for lack of applicability of the approach, but for lack of corresponding image/video.

Table 4.1: Selected conditions and corresponding IC dimensions for vertical flow.

Gas superficial velocity (m/s)	Flow regimes	Spatial dimension of IC	Temporal dimension of IC	IC dimension
0.085	Bubbly flow	4*4	0.0085	4*4*118
0.51	Slug flow	4*4	0.051	4*4*20
18.424	Annular flow	4*4	1.8424	4*4*0.55

P2+ software with the grid of concentration tomograms at 20×20 . The gauged frames are later stacked to form a 3D concentration dataset. The selected flow conditions to issue bubbly, slug, and annular flow are listed in Table 4.1. Spatial and temporal dimensions of the IC for each condition are also presented along with the relative conditions, which are calculated using the threshold $T_g = 40\%$ and $T_l = 5\%$. It is worthwhile noticing that in Table 4.1, the temporal dimension of the IC for annular flow is less than 1, meaning the data has to be interpolated along the temporal axis.

The visualisation results are presented in Figure 4.6, with given threshold values, together with the images by video logger (the left one) and colour mapping (the middle one). As far as bubbly flow is concerned (Figure 4.6a), a video logged image confirms the flow pattern and shows the small bubbles and their distribution, whereas the images by conventional colour mapping failed to demonstrate the existence of small bubbles and therefore is unable to convey more informative content regarding flow dynamics. Similar to the video logger, the results from the proposed approach are capable of reflecting the actual flow regime. For a slug flow (Figure 4.6b), the overall flow regime can be recognised by colour-based visualisation, but detailed information, e.g. large bubble shape and position, is blurred. In contrast, bubble mapping not only reveals the size and location of large bubbles but also delivers other information, such as large bubbles are surrounded by small bubbles. When it comes to annular flow (Figure 4.6c), both colour mapping and bubble mapping are unable to provide sufficient information regarding the thin water film between the gas phase and the pipe wall. This is because the film is too thin to be measured by the ERT system.

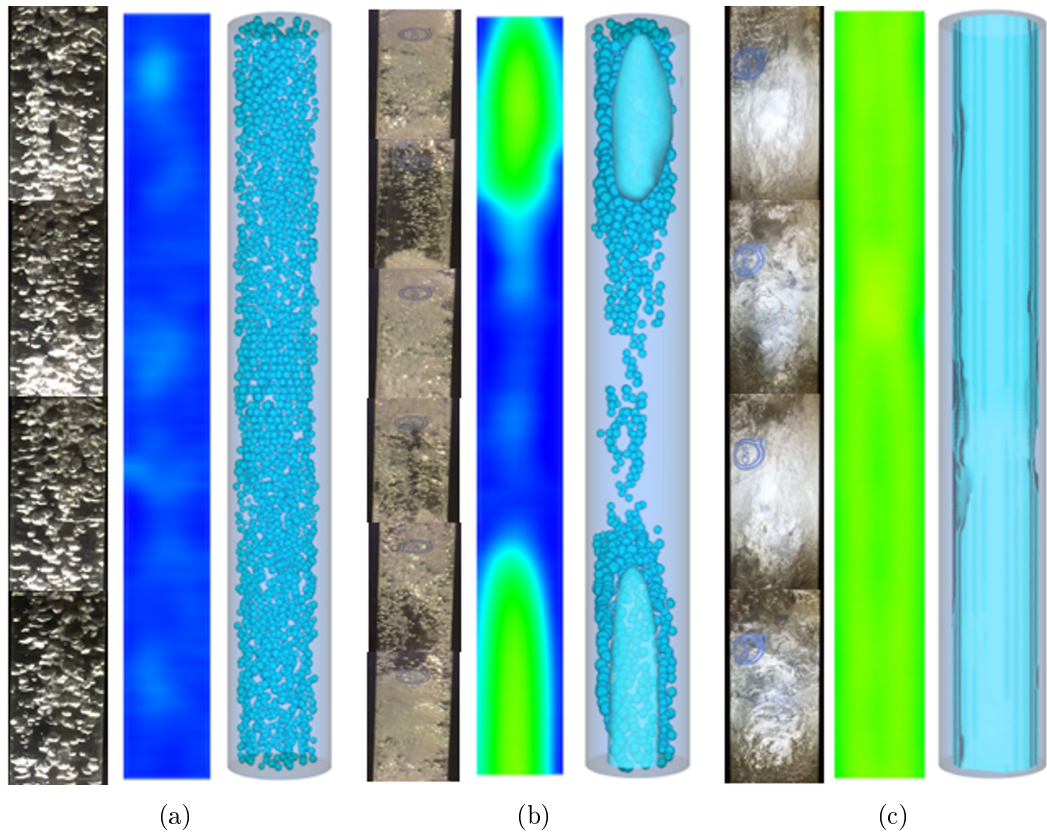


Figure 4.6: Visualisation of upward gas-liquid flow in a vertical pipe by a high-speed camera, conventional colour mapping and proposed bubble mapping. (a) bubbly flow; (b) slug flow; and (c) annular flow.

4.3.2 Gas-water flow in a horizontal pipeline

Table 4.2: Selected conditions and corresponding IC dimensions for horizontal flow.

Gas superficial velocity (m/s)	Flow regimes	Spatial dimension of IC	Temporal dimension of IC	IC dimension
0.47	Stratified flow	4*4	0.0752	4*4*14
0.15	Bubbly flow	4*4	0.024	4*4*42
0.51	Plug flow	4*4	0.0816	4*4*13
2.06	Slug flow	4*4	0.3296	4*4*3
17.00	Annular flow	4*4	2.72	4*4*0.37

In order to further check the suitability of the approach for horizontal flow, another set of experiments was carried out in a horizontal pipe of 200 mm diameter on the flow testing facilities at TUV NEL. In the experiment, nitrogen was used as gas phase and salty water as liquid phase. The data was collected by another commercialised ERT system, called V5R, with the sampling speed at 312.5 fps. The grid definition of the resultant tomograms is 20*20. The chosen flow conditions are itemised in Table 4.2, along with the related superficial velocity of the gas phase. Accordingly, IC dimensions are derived aligned with Equation 4.3 and Equation 4.4, and the outcome is presented along with each relevant condition. During the experiment, it was observed that the error of measuring pure liquid was less than 3%, and thus T_l is set to 3%, instead of 5% as used for the vertical experiment.

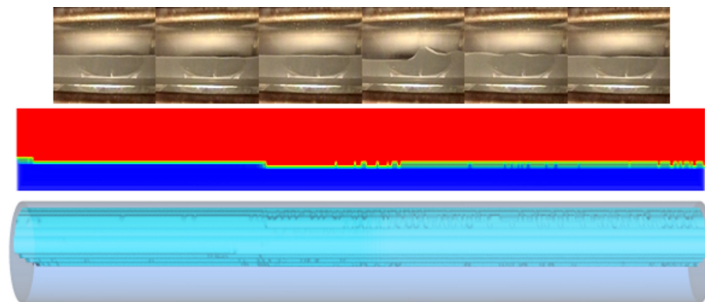


Figure 4.7: Visualisation of a stratified flow in a horizontal pipe by a high-speed camera, conventional colour mapping, and bubble mapping.

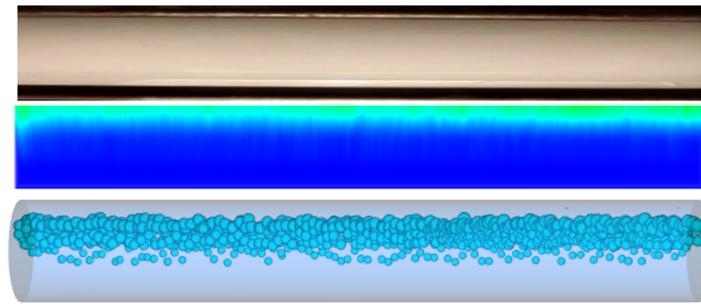


Figure 4.8: Visualisation of a bubbly flow in a horizontal pipe by a high-speed camera, conventional colour mapping, and bubble mapping.

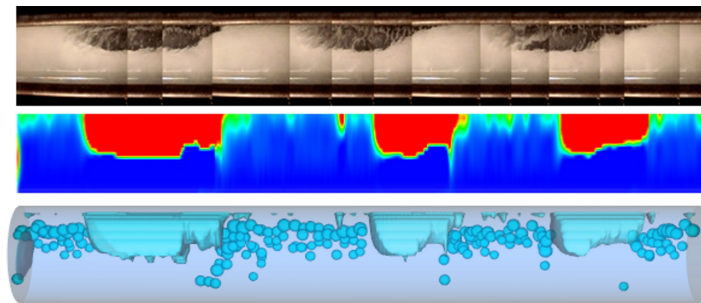


Figure 4.9: Visualisation of a slug flow in a horizontal pipe by a high-speed camera, conventional colour mapping, and bubble mapping.

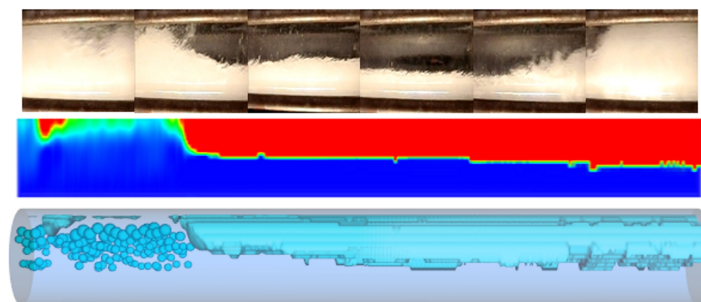


Figure 4.10: Visualisation of a slug flow in a horizontal pipe by a high-speed camera, conventional colour mapping, and bubble mapping.

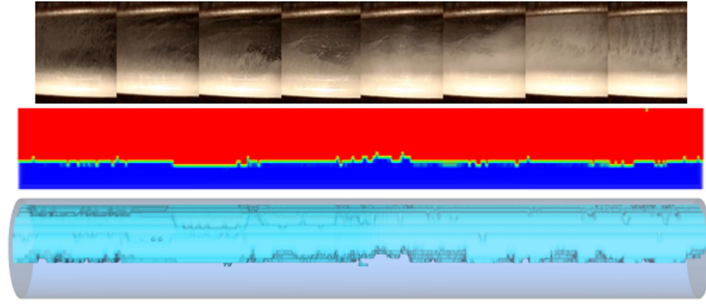


Figure 4.11: Visualisation of an annular flow in a horizontal pipe by a high-speed camera, conventional colour mapping, and bubble mapping.

With the aforementioned parameters, all targeting flow is visualised, and the results are depicted in Figure 4.7, Figure 4.8, Figure 4.9, Figure 4.10, and Figure 4.11 for stratified flow, bubbly flow, plug flow, slug flow, and annular flow, respectively. In Figure 4.7, all of the the imaging methods can visualise stratified flow with little uncertainty. As for bubbly flow (Figure 4.8), the situation changes completely, where both high-speed camera and colour mapping fail in the attempt to image bubbly flow, since no bubble was visible by either method. Fortunately, bubble mapping fills in the blanks by showing the existence of small bubbles. It also demonstrates that due to the gravitational force, bubbles tend to be moving at the top of the pipe. As far as slug and plug flow is concerned (Figure 4.9 and Figure 4.10), the results are similar to those for slug flow in a vertical pipe. That is, large bubbles can be addressed by all methods without much effort, but small bubbles are only identified by bubble mapping but not camera logger and the stacked tomograms. For annular flow (Figure 4.11), both approaches have similar performance. That is, the top water film is undetectable by either approach, whereas the film at the bottom of the pipe is thick enough to be detected by the ERT system.

4.3.3 Impact of the parameters

During the "reconstruction" of bubbles, there are a few critical parameters that influence the visualisation results, including IC dimensions, T_g , and T_l . Therefore, it is necessary to quantify and qualify the influence. For each parameter, three different values are chosen, and related results are provided by leaving the other two parameters unchanged. Since small bubbles and large bubbles are generated

differently, the plug flow in a horizontal pipe (Figure 4.9) is picked up for the investigation.

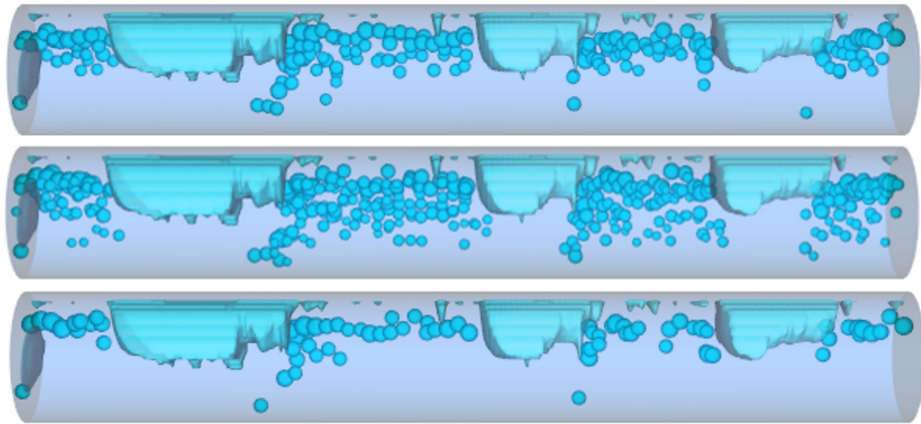


Figure 4.12: Visualisation results by different T_l of 0.05, 0.02, and 0.08 (from top to bottom).

Figure 4.12 presents the impact of pure liquid T_l on the visualisation. With fixed values of $T_g = 0.4$ and the spatial dimension of IC 4*4, three different values are investigated, including 0.02, 0.05, and 0.08. In Figure 4.12, the upper image is the original result, i.e. $T_l = 0.05$, the middle and the bottom are with $T_l = 0.02$ and $T_l = 0.08$, respectively. In the renderings, there are 174, 245, and 79 small bubbles for each case, but the number of large bubbles stayed the same. As a result, T_l contributes to the determination of the number of small bubbles but not large bubbles. This is owing to the fact that T_l connects to the proportion of the liquid phase. In other words, the higher the T_l is, the more the liquid is, and in turn the less the gas is. However, from the perspective of flow regime visualisation, T_l has little impact on the visual recognition.

The effect of T_g is illustrated in Figure 4.13, in which different T_g 0.4, 0.5, and 0.6 are applied to the procedure, and the images are the upper, the middle, and bottom ones, respectively. In each image, 174, 175, and 183 small bubbles are acknowledged, respectively. In the meantime, there are still three large bubbles but with a subtle difference in size and shape, which is hardly recognisable by visual observation. Since T_g is responsible for the formation of large bubbles, and thus the change has a major effect on the volume and shape of large bubbles. That is, the lower the value is, the larger the bubbles are, which further negatively impacts on the volume fraction of the liquid phase.

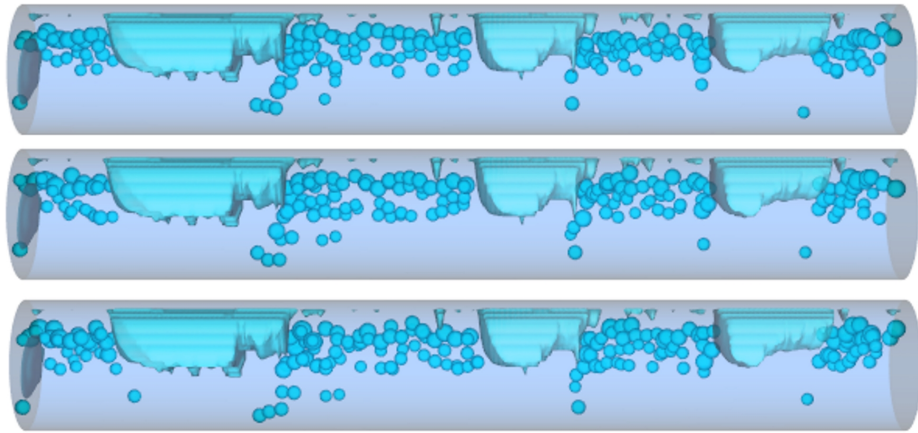


Figure 4.13: Visualisation results by different T_g of 0.4, 0.5, and 0.6 (from top to bottom).

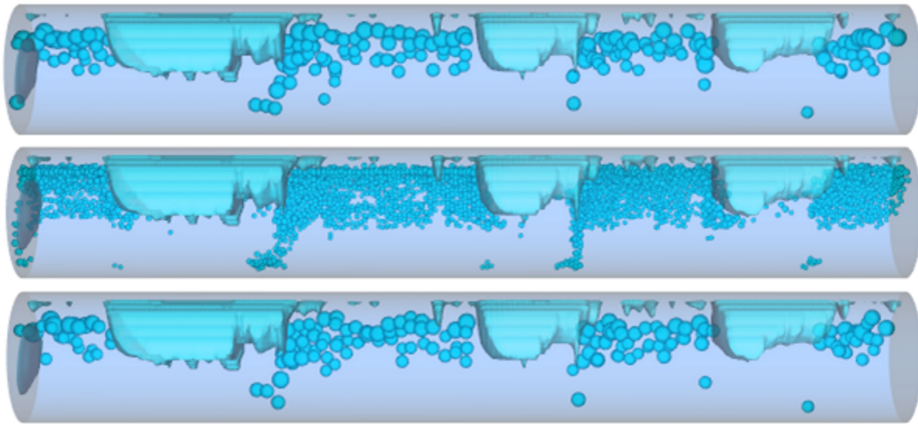


Figure 4.14: Visualisation results by different IC of 4×4 , 2×2 , and 5×5 (from top to bottom).

As another crucial parameter, the dimension definition of the IC has to take account of a number of factors, such as the DAS speed of the employed tomography and local velocity of the gas phase. Essentially, since the IC is assumed to host one small bubble, it is critical for the size of small bubbles. In addition, with a given input dataset, the volume of the data is therefore confirmed, and hence smaller IC results in more bubbles, which in consequence increases the number of small bubbles. That is, the smaller the IC is, the smaller the small bubbles are, and the higher the number is. This is also reflected by the visualisation results depicted in Figure 4.14. In the figure, different spatial dimensions of IC at 4×4 , 2×2 , and 5×5 are allocated to the images from top to bottom, associated with the number of small bubbles 174, 3251, and 158, respectively. In contrast, the size and the shape of large bubbles does not change.

4.4 Summary

In this chapter, a novel approach is reported for electrical tomography to visualise gas-liquid flow in 3D. With the assumption that in a fully-developed gas-liquid flow, a small bubble is spherical and randomly positioned inside a properly-designed interrogation cell, while large bubbles are random in shape and location, a stack of electrical concentration tomograms using colour mapping are transferred into bubbles, and the results for horizontal and vertical pipeline flow have demonstrated the feasibility of the algorithm. With this new approach, conventionally colour-based presentation of the spatial distribution of the gas phase is superseded by bubbles. The supersession overcomes the limitations of electrical tomography in multiphase flow visualisation and, therefore, provides a visually more straightforward manner than colour mapping of concentration distribution can.

In contrast to the visualisation by colour mapping, bubble mapping provides more enlightening insights into flow dynamics, since the visibility of those bubbles enhances human and machine perception, e.g. visual recognition of flow regimes. For example, in Figure 4.8, it is challenging for humans to recognise the real flow regimes from both high-speed camera and colour mapping, whereas the one by bubble mapping clearly reveals the bubble sizes and distribution, and hence

provides sufficient flow pattern information. In addition, the figure also demonstrates that the bubbles in the horizontal pipe tend to accumulate at the top of the pipe due to buoyancy, and moreover they become larger when closer to the top, whereas in a vertical pipe they distribute more homogeneously, as shown in Figure 4.6a. Moreover, this presentation, along with the binary format of the pixels in the results, i.e. a pixel is either filled with gas or liquid, paves the way for computer-aided online flow regime recognition using Boolean logic (Ramskill et al. 2011), of which 2D variation has been put into practice.

In comparison with other tomography, such as X-ray and WMS, electrical tomography has the lowest spatial resolution and hence represents the most challenging case in terms of reconstructing bubbles. This however implies that if bubble mapping works in the worst case, it could be adapted to become feasible for other techniques which produce better spatial resolution.

Despite its effectiveness, bubble mapping still has a few shortcomings which need to be addressed in the future. The first aspect worth further consideration is the threshold values because their determination depends on several parameters, such as physical properties of flow and hardware specification. Therefore, it is necessary to pay special attention to the determination, which may require both empirical and theoretical evidence. In addition, universal application of the values to every case in this study may not be the most suitable solution, in which case localised or case-specific ones may be considered to yield more accurate results.

In bubble mapping, bubbles are generated based on the mean concentration of the IC. For certain flow regimes where only small bubbles exist, i.e. bubbly flow, the procedure does not introduce any shift of mean concentration, whereas when large bubbles exist, the mean concentration is no longer retained due to the assumption that an IC is filled with gas when the corresponding concentration is higher than 40%, because of the introduction of considerable errors introduced by ERT in imaging large non-conductive objects. This could be improved by utilising advanced algorithms in both tomography and computer graphics, such as the one in the literature (Wang 2002) and (Anderson et al. 2010), respectively. However, the shift actually does not affect the identification and visualisation of flow regimes by comparing the results with images from a video logger.

When constructing an IC, the local velocity of the gas phase needs to be involved to reflect temporal information of electrical tomograms. However, it is assumed

to be equal to its superficial velocity, which introduces a certain amount of uncertainty. This could be improved by utilising the cross correlation method to the dataset gauged from a dual sensing plane with sufficient speed, such as the one in (Li et al. [2009a](#)).

It is also noted that the evaluation did not include all possible flow regimes, such as mist or finely dispersed bubbly flow. One reason is that the objectives of this study focuses on the aforementioned flow regimes, rather than covering all possible flow regimes. In addition, it is extremely challenging for the approach to be applicable to other uncovered flow regimes since they present little variation in either permittivity or conductivity, and thus are unable to be distinguished by electrical tomography.

CHAPTER 5

ENHANCEMENT OF SPATIAL AND TEMPORAL RESOLUTION OF ERT SYSTEMS

Highlights: Due to the inverse relationship between spatial and temporal resolution of ERT, spatial resolution needs to be sacrificed so that ERT is able to manage multiphase flow with high velocity when the cross-correlation method is applied. Two novel approaches are proposed, namely Asymmetrical Sensing and Imaging (ASI) and Regional Imaging with Limited Measurement (RILM), to retain high temporal resolution by conventional 8-electrode configured ERT while achieving the comparable spatial resolution by conventional 16-electrode configured ERT.

5.1 Introduction

Cross-correlation is a widely utilised approach to derive disperse phase velocity in ERT (Beck et al. 1987). As described in CHAPTER 2, the precision of the cross-correlation is determined by the sensing speed of ERT according to the discrimination error (Beck et al. 1987). On the other hand, multiphase flow with high speed is common in real industries, such as the one mentioned in CHAPTER 3, of which the gas speed is over 10m/s. In order to achieve 5% error, the sensing speed of over 2000 dual-frames per second is required, when other parameters are fixed. When characterising gas-liquid flow by ERT, there is always a trade-off between spatial and temporal resolution. If visualisation is a major objective, ERT with more electrodes, e.g. 16, is employed to offer higher spatial resolution, whereas if metering multiphase flow with a high velocity of disperse flow is a primary aim, ERT with less electrodes, e.g. 8, is usually considered for lower discrimination error. Therefore, the motivation behind the proposed approaches lies in taking advantage of the high temporal resolution associated with the ERT of 8 or fewer electrodes, while retaining the high spatial resolution

provided by the systems with 16 electrodes, by means of deploying fewer electrodes less than that in the conventional 16-electrode ERT configuration to derive partial tomograms, with minimal or even no modification of the hardware. In this chapter, two different strategies are investigated, namely Asymmetrical Sensing and Imaging (ASI) and Regional Imaging with Limited Measurement (RILM). Both approaches are evaluated using simulation/experiment, and the results are reported at the end of the chapter.

5.2 Asymmetrical Sensing and Imaging (ASI)

As its name indicates, ASI uses 8 asymmetrically-arranged electrodes (in a 16-electrode setup) to perform measurements. The primary goal of the experiments is to seek an appropriate arrangement of 8 asymmetrically-distributed electrodes which have an improved spatial resolution, in comparison with the conventional symmetrically arranged 8 electrodes system, for visualisation and measurement of upward vertical pipeline multiphase flows. In order to achieve the goal, the experiments are divided into 2 steps: the first is to determine the most suitable distribution of 8 asymmetrical electrodes which is capable of producing acceptable tomograms compared to the ones produced by a conventional ERT system with 8 and 16 electrodes; and the second step is to employ the selected ASI to gas-in-water vertical pipeline flow to evaluate the performance of the proposed ASI.

5.2.1 Determination of eligible distribution of ASI

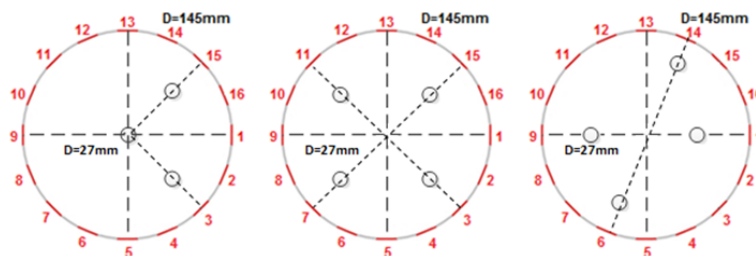


Figure 5.1: Physical positions of cylindrical objects in a small phantom of x -axial mirror, central quadric mirror, and π -repetition.

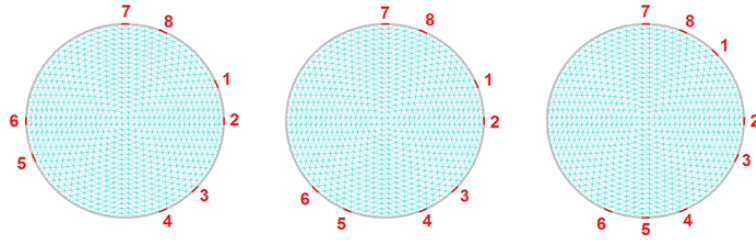


Figure 5.2: Mesh structures and electrode arrangements as ASI-A, ASI-B, and ASI-C

First of all, the most eligible arrangement of ASI has to be determined by experiment. The experiment was conducted on a small phantom with a few cylindrical objects with fixed position, as shown in Figure 5.1. The selected ASI arrangements are depicted in Figure 5.2. The data was collected using an ITS P2+ system (ITS 2009), and processed by SCG software with the parameters of 841-node mesh structure (Figure 5.2), reconstruction steps = 5, RMS = 0.0001, and the number of inverse iterations = 5. In order to evaluate the eligible ASI in Figure 5.2, another set of experiments was conducted employing a conventional 16-electrode configured ITS P2+ system, and the data was processed by SCG with the same parameters as for ASI.

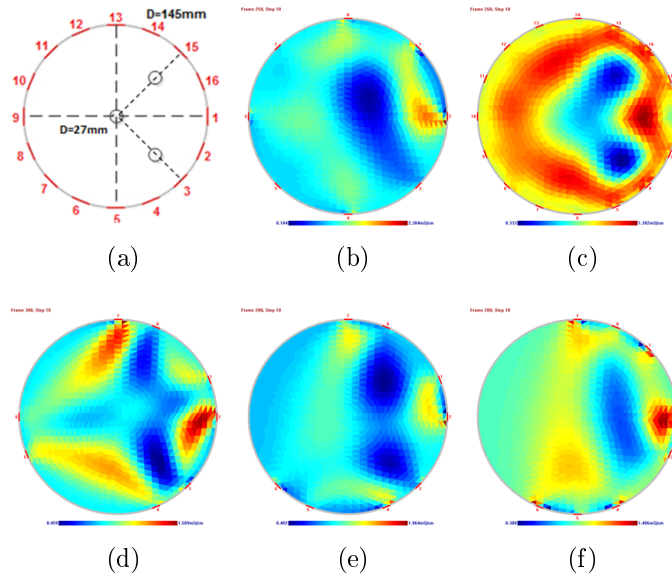


Figure 5.3: SCG-generated tomograms for the first positioning of cylindrical objects in a small phantom by (a) the conventional 8-electrode ERT, (b) the conventional 16-electrode ERT, (c) ASI-A, (d) ASI-B, and (e) ASI-C

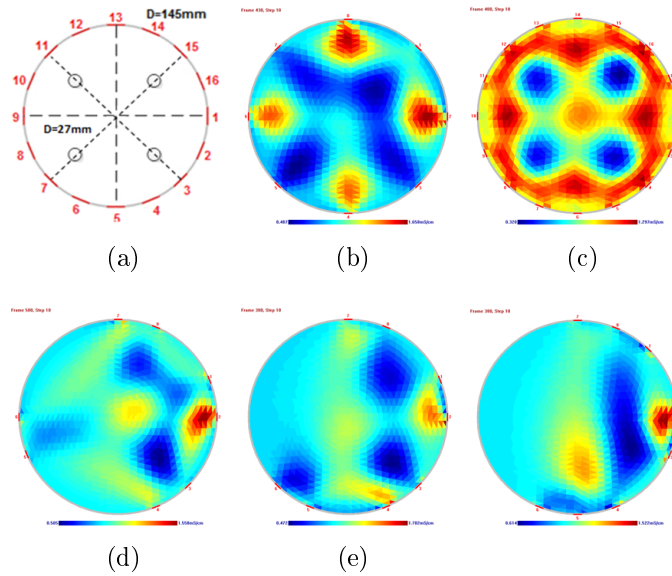


Figure 5.4: SCG-generated tomograms for the second positioning of cylindrical objects in a small phantom by (a) the conventional 8-electrode ERT, (b) the conventional 16-electrode ERT, (c) ASI-A, (d) ASI-B, and (e) ASI-C

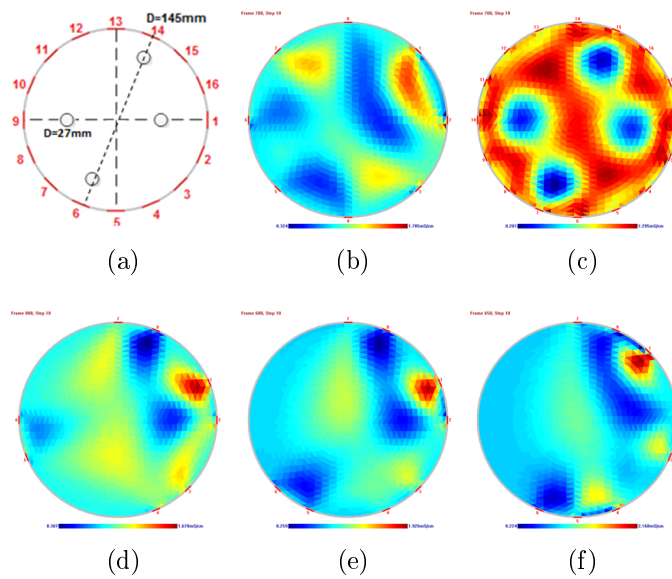


Figure 5.5: SCG-generated tomograms for the first positioning of cylindrical objects in a small phantom by (a) the conventional 8-electrode ERT, (b) the conventional 16-electrode ERT, (c) ASI-A, (d) ASI-B, and (e) ASI-C

Figure 5.3, Figure 5.4, and Figure 5.5 demonstrates the resulting tomograms from the first set of experiments. For each distribution of cylindrical objects, 5

tomograms were reconstructed with SCG with the same parameters, which were sensed by conventional 8 electrodes, conventional 16 electrodes, and the different ASIs (A, B, and C respectively). According to the arrangement of 8 electrodes in ASI, only the right half of the relating tomograms was considered. The figure shows that the conventional 16 electrodes produced the highest resolution tomograms, while the conventional 8 electrodes roughly identified the position of the static objects. Among the tomograms by 3 ASIs, the configuration B (the fourth tomogram for each distribution of cylindrical objects) outperformed the conventional 8 electrodes, while still being worse than conventional the 16 electrodes. Therefore, the ASI-B was chosen for further evaluation in gas-in-water vertical pipeline flow.

5.2.2 Evaluation of selected ASI on gas-water upwards flow

After the eligible ASI was selected, it was employed for measuring gas-water upwards flow in a vertical pipeline. In this step, two flow regimes were involved: bubbly flow and slug flow. The water flowrate was fixed at $7.4 \text{ m}^3/h$, and gas flowrate for bubbly flow and slug flow was at 10 l/min and 70 l/min . For each flow regime, three sets of data were collected by ASI, a conventional 8-electrode V5R system (Jia et al. 2010), and a conventional 16-electrode FICA (Wang et al. 2005). The sensors were placed in the flow rig as depicted in Figure 5.6.

All data were processed using SCG software with a mesh of 576 nodes. The reconstructed images were further processed by AIMFlow software to generate concentration and velocity maps. Since only half of the ASI-based tomograms are meaningful, the data inside the half was extracted and further averaged according to two different strategies, as indicated in Figure 5.7, to yield concentration and velocity profiles. Equation 5.1 explains the averaging strategies, where i is the index of the target profile element, j is the indices of the mesh defined in Table 1, N is the number of the mesh involved in the different averaging strategies, and $Z_{i,j}$ is the value of the concentration/velocity at mesh (i,j).

$$x_i = \frac{1}{N} \sum_{j=1}^N Z_{i,j} \quad i = [1, 12], \quad \text{and} \quad j = [1, N] \quad (5.1)$$

The results, generated based on the selected ASI-B, conventional 8-electrode and 16-electrode ERT, are illustrated in Figure 5.8. In Figure 5.8a and Figure 5.8b,

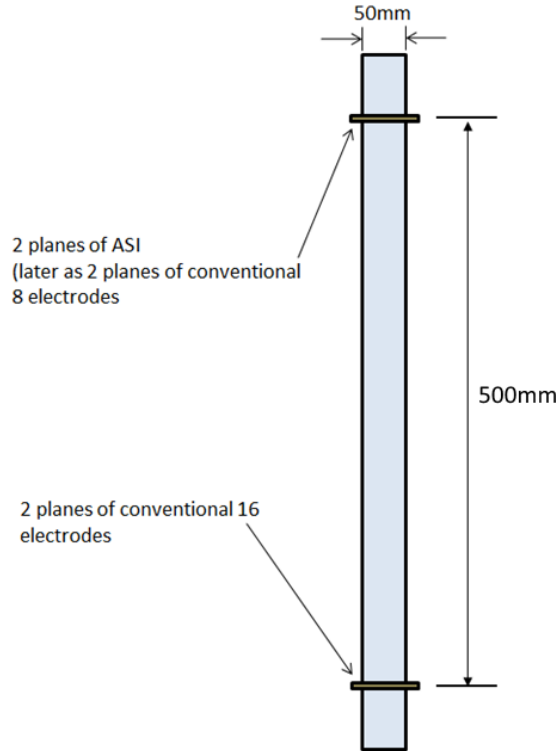


Figure 5.6: Physical position of 2 sets of sensor arrays in a vertical pipeline.

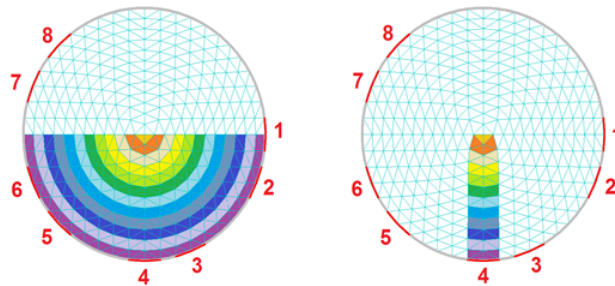


Figure 5.7: Two averaging strategies showing elements used to generate profiles.

the upper two charts are the velocity and concentration profiles averaged on the bottom half of AIMFlow-generated maps, and the bottom two charts are the profiles averaged on the bottom half of the vertical central area of the AIMFlow-generated maps. It can be concluded from Figure 5.8a that although the ASI-generated velocity profile are similar to the profile obtained from the conventional 8 electrodes, both were worse than the one using the conventional 16 electrodes, the ASI-generated concentration profiles are closer to the profiles of the conventional 16 electrodes compared to the one using the conventional 8 electrodes. As far as slug flow is concerned, as depicted in Figure 5.8b, the performance of selected

Table 5.1: Element indices used for averaging map to produce a profile.

Profile element No.	Profile by bottom half		Profile by bottom half of vertical central line	
	Mesh Indices	Total Number of Mesh	Mesh Indices	Total Number of Mesh
1 (purple)	1-46	46	22-25	4
2 (lavender)	93-134	42	112-115	4
3 (indigo)	177-214	38	194-197	4
4 (blue-grey)	253-286	34	268-271	4
5 (turquoise)	321-350	30	334-337	4
6 (light turquoise)	381-406	26	392-395	4
7 (green)	433-454	22	442-445	4
8 (lime)	477-494	18	484-487	4
9 (yellow)	513-526	14	518-521	4
10 (light yellow)	541-550	10	544-547	4
11 (orange)	561-566	6	562-565	4
12 (gold)	573-576	4	573-574	2

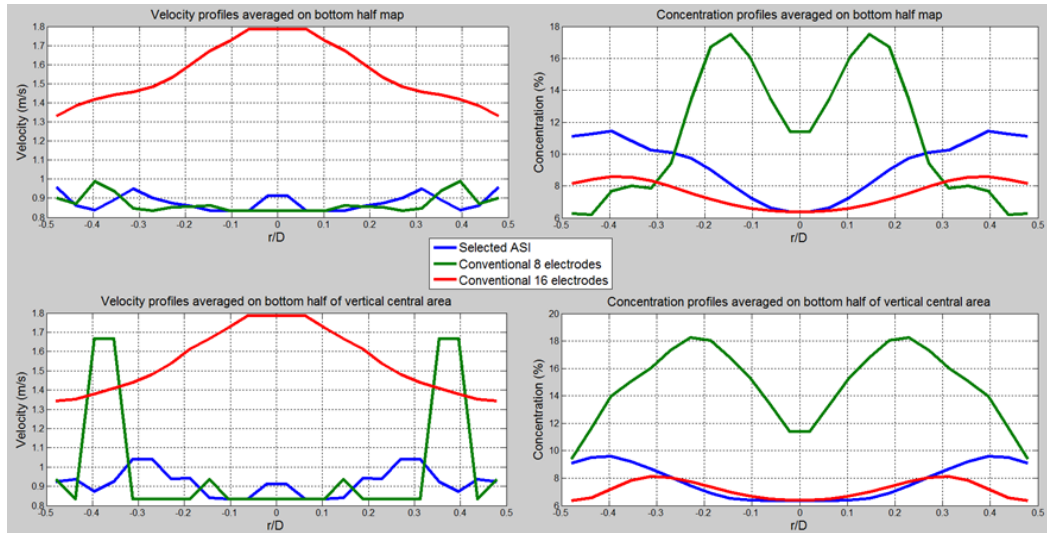
ASI is superior to that of conventional 8 electrodes, for both concentration and velocity profiles, although it is not better than the conventional 16 electrodes.

In order to quantify the performance of ASI, relative errors were applied, defined as Equation 5.2:

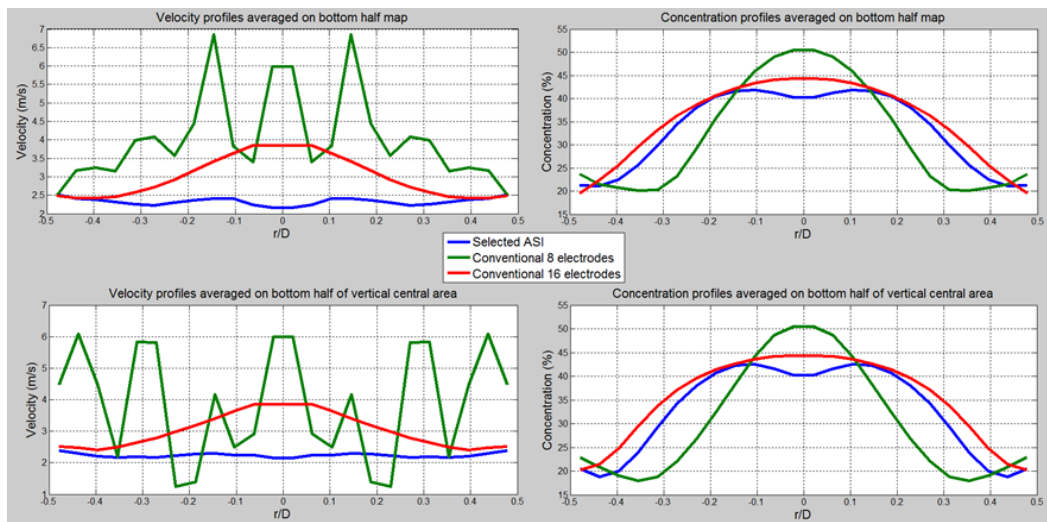
$$Error = \left| \frac{x_{t,i} - x_{16e,i}}{x_{16e,i}} \right| * 100 \quad i = [1, 12] \quad (5.2)$$

where t is either ASI or conventional 8 electrodes, $x_{t,i}$ is the value of either concentration or velocity at element i , and $x_{16e,i}$ is the value of either concentration or velocity at element i by 16 electrodes. The results are shown in Figure 5.9.

Figure 5.9a shows that ASI and conventional 8 electrodes produced very similar results with regard to the velocity profile of bubbly flow, and the averaged errors were even up to 43%. However, ASI outperformed conventional 8 electrodes in terms of the concentration profile of bubbly flow. As far as slug flow was concerned, ASI produced better results with respect to both velocity and concentration than the conventional 8 electrodes, and the improvement was significant, shown



(a)



(b)

Figure 5.8: Concentration and velocity profiles of bubbly flow by selected ASI, conventional 8 electrodes and 16 electrodes on (a) bubbly flow, and (b) slug flow.

in Figure 5.9b.

5.2.3 Conclusions

A new sensor configuration based on the asymmetrical distribution of 8-electrode ERT was investigated to derive the concentration and velocity of gas-water upward pipeline flow, and the results demonstrated the performance of the proposed

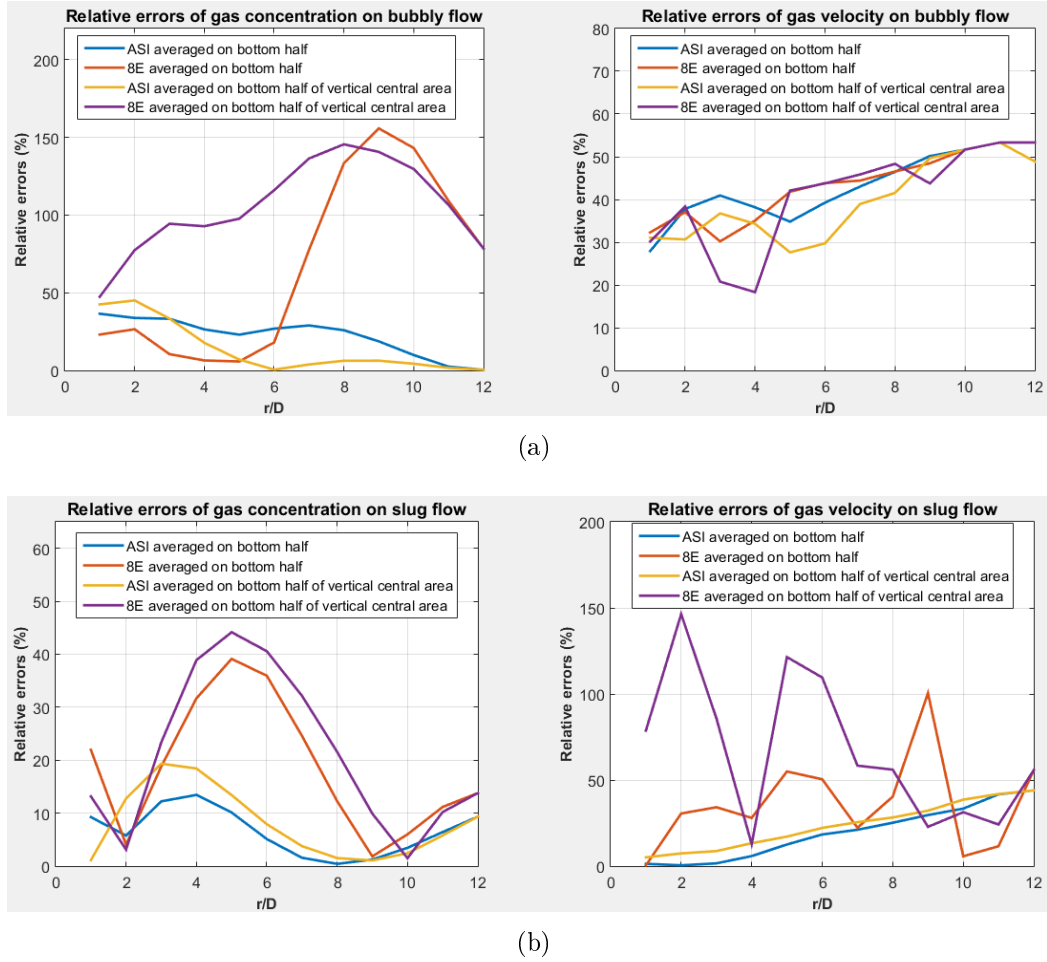


Figure 5.9: Relative errors of selected ASI, conventional 8 electrodes against 16 electrodes on (a) bubbly flow, and (b) slug flow.

method. The new approach produced a better resolution of tomograms, and thus concentration and velocity profiles, compared to the conventional 8-electrode ERT while the data acquisition speed was retained the same throughout. Unfortunately, it was noticed that there was still some discrepancy between the proposed method and the 16-electrode configured ERT. Although the experiments were only on a vertical pipeline, it should not be difficult to adapt the proposal to horizontal and inclined pipeline flow by means of properly positioning 8 asymmetrical sensors, with the common assumption of developed multiphase flows in horizontal and inclined pipelines to be symmetrical to the vertical diameter of pipeline.

5.3 Regional Imaging with Limited Measurement (RILM)

The investigation of ASI reveals that the approach was not able to derive promising images comparable to the ones produced by the conventional 16-electrode ERT, and further concentration and velocity profiles, even though the profiles are better than those obtained by a conventional ERT with 8 electrodes. Besides, the approach requires the modification of hardware since only 8 electrodes were applied to the 16-electrode based configuration. In order to overcome the disadvantages of ASI, regional imaging with limited measurement (RILM) is introduced. RILM requires no modification of hardware. Unlike conventional adjacent sensing strategy based, 16-electrode configured ERT, RILM chooses some of the measurements, which contribute to the imaging at the central area of full tomograms. As a result, the number of independent measurements decreases dramatically, and hence the data acquisition time declines considerably. In contrast to ASI which requires hardware modification, RILM does not need to modify the conventional 16-electrode configuration, which in consequence makes SBP still valid.

5.3.1 Methodology

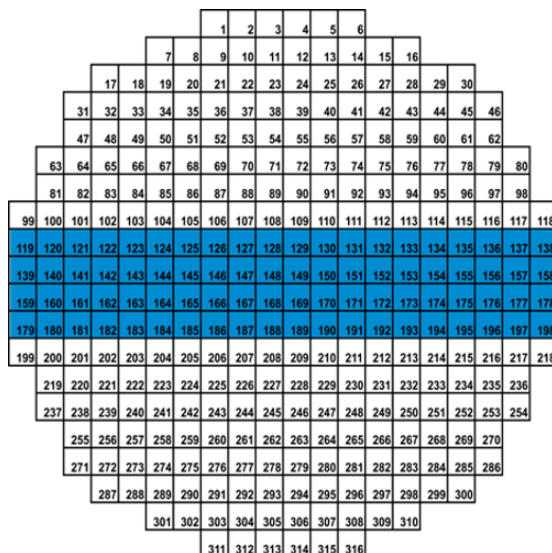


Figure 5.10: Arrangement of 316 tomogram elements by 20*20 grid (ITS 2009).

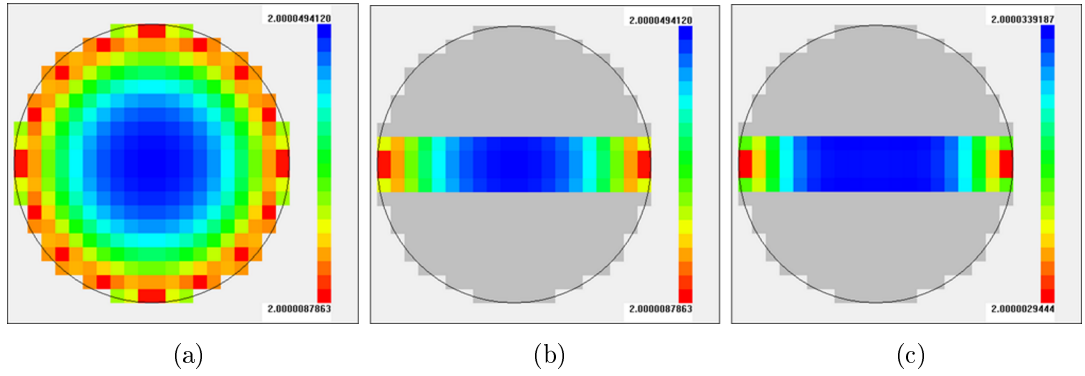


Figure 5.11: Sensitivity map: (a) full sensitivity map for adjacent measurement, (b) central axial sensitivity map for adjacent measurement, and (c) sensitivity map for RILM.

One assumption for the study is that the flow investigated is at steady state. Flow characteristics of multiphase flow such as disperse phase concentration and velocity distributions can be assumed as either radial symmetrical in a vertical pipeline or a central-vertical plane symmetrical in a horizontal pipeline. The necessary and minimum imaging area, which can represent the major features of pipeline flows when both cases are combined, is the row of pixels along the central-vertical plane, as indicated in Figure 5.10. Therefore, imaging only the central line or a few rows of a full tomogram requires less measurement thereby increasing the speed while keeping the spatial resolution to a comparable level. Figure 5.11 compares sensitivity maps using the conventional adjacent method and RILM. Since RILM only targets the central area, the full sensitivity map is masked to match the area of interest to RILM, shown as Figure 5.11b. Comparing Figure 5.11c with Figure 5.11b, it can be seen that RILM's sensitivity map is very close to the conventional one, and therefore is expected to produce comparable measurements during application.

In order to cover the regional area, three groups of excitation and measurement electrode pairs are selected and demonstrated in Figure 5.12, including the rotary band (Figure 5.12a), parallel band (Figure 5.12b), and complimentary band (Figure 5.12c). According to reciprocity theorem, no mutual projection for excitation and measurement is needed. Therefore, a total of 20 independent measurements are required, comprising 8 for the rotary band, 6 for the parallel band, and 6 for the complimentary band, for sensing the central area. The accumulated

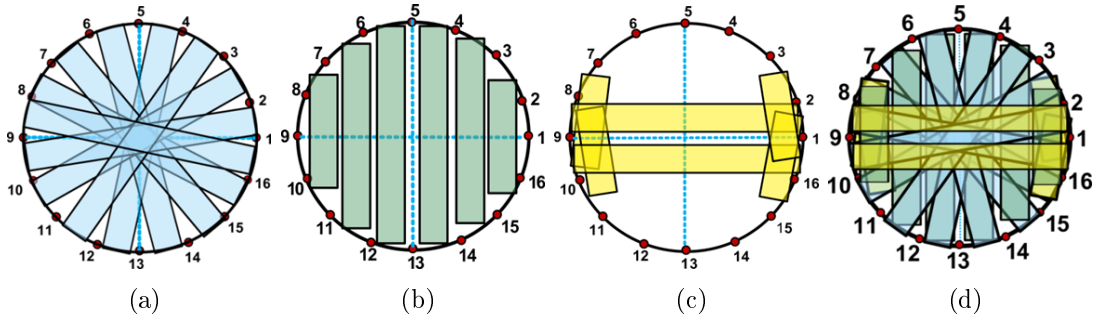


Figure 5.12: PILM sensing strategy, (a) Rotary band, (b) Parallel band, (c) Complementary band, and (d) Overall projections (Wang et al. 2016a).

projections are depicted in Figure 5.12d. Compared to the number of required measurements for a full tomogram, i.e. 256, RILM's requirement reduces to 20 per tomogram, which obviously results in a significant decrease in speed.

On the other hand, the widely applied single-step reconstruction algorithm is SBP (Kotre 1994), governed by Equation 5.3:

$$[\Delta\sigma]_{N \times 1} = 1 - [S]_{N \times M} \cdot [\Delta V]_{M \times 1} \quad (5.3)$$

where $[S]_{N \times M}$ is the pre-defined sensitivity matrix, $[\Delta\sigma]_{N \times 1}$ is the relative change of mixture conductivity, and $[\Delta V]_{M \times 1}$ is the relative change of measured voltages. In the case of the 16-electrode ERT with adjacent sensing strategy, Equation 5.3 is used for the generation of 316-pixel tomograms, and the arrangement of the pixels is in Figure 5.10. Then, the limited measurements required for RILM can be derived from the full set of measured voltages as:

$$[\Delta V']_{M \times 1} = [T]_{M \times M} \cdot [\Delta V]_{M \times 1} \quad (5.4)$$

where $[T]_{M \times M}$ is a diagonal matrix, whose diagonal elements are either 1 or 0. The diagonal matrix is able to transform the full measurement vector $[\Delta V]_{M \times 1}$ to the vector $[\Delta V']_{M \times 1}$ such that it has non-zero elements which correspond to the RILM's requirements. According to Figure 5.10, the target area contains the pixels from 119 to 198. The sensitivity matrix $[S]_{N \times M}$, therefore, can be modified to set all of its elements to zero except the ones in the blue-highlighted area in

Figure 5.10. Accordingly, Equation 5.3 becomes Equation 5.5:

$$\begin{aligned}
 [\Delta\sigma']_{N \times 1} &= 1 - [S]_{N \times M} \cdot [\Delta V']_{M \times 1} \\
 &= 1 - [S]_{N \times M} \cdot [T]_{M \times M} \cdot [\Delta V]_{M \times 1} \\
 &= 1 - \begin{bmatrix} 0 & \cdots & 0 \\ \vdots & \vdots & \vdots \\ 0 & \cdots & 0 \\ S_{119,1} & \cdots & S_{119,m} \\ \vdots & \vdots & \vdots \\ S_{198,1} & \cdots & S_{198,m} \\ 0 & \cdots & 0 \\ \vdots & \vdots & \vdots \\ 0 & \cdots & 0 \end{bmatrix} \cdot \begin{bmatrix} t_1 & & 0 \\ & \ddots & \\ 0 & & t_m \end{bmatrix} \cdot [\Delta V]_{M \times 1} \\
 &= 1 - \begin{bmatrix} 0 & \cdots & 0 \\ \vdots & \vdots & \vdots \\ 0 & \cdots & 0 \\ t_1 * S_{119,1} & \cdots & t_m * S_{119,m} \\ \vdots & \vdots & \vdots \\ t_1 * S_{198,1} & \cdots & t_m * S_{198,m} \\ 0 & \cdots & 0 \\ \vdots & \vdots & \vdots \\ 0 & \cdots & 0 \end{bmatrix} \cdot [\Delta V]_{M \times 1}
 \end{aligned} \tag{5.5}$$

Since t_i is either 0 or 1, some columns of the first matrix in Equation 5.5 are entirely zero. $[\Delta V]_{M \times 1}$ with $[\Delta V']_{M \times 1}$ in Equation 5.5 can be interchanged due to the presence of zero elements in the sensitivity matrix. By removing the zero filled columns and rows, in both the matrices, their dimensions can be decreased that will significantly reduce the time and resources required for the computation of matrix multiplication, and further relative conductivity. Taking the example given by the article, with 20 independent measurements and the 80 elements as demonstrated in Figure 5.11, the computation is reduced from $[316, 104] * [104]$ to $[80, 20] * [20]$. This computational reduction of more than one order promises to significantly enhance the overall performance of the proposed method.

5.3.2 Evaluation

Experiments were carried out to evaluate the performance of RILM in terms of visualisation and characterisation of multiphase flow. The experiments were fir-

stly on imaging static objects in a small phantom, and then on gas-water upward flow to extract concentration and velocity profiles.

5.3.2.1 Imaging of statically-positioned objects

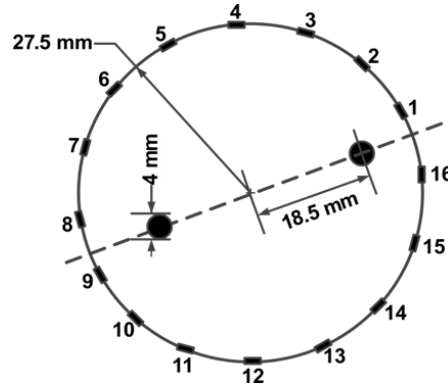


Figure 5.13: Distribution of non-conductive objects in a phantom.

Two non-conductive objects were positioned in a phantom as depicted in Figure 5.13. Sensors from the 16-electrode configuration were connected to the phantom. Measurement was performed using conventional adjacent sensing strategy. SBP was utilised for reconstructing cross-sectional conductivity tomograms. The targeting measurement for RILM was extracted from the full data set.

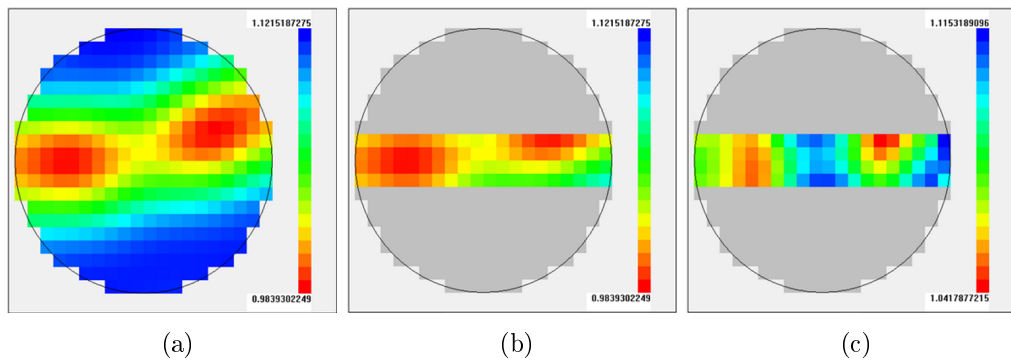


Figure 5.14: Conventional tomogram and PILM-generated tomogram of 2 static objects in a phantom: (a) original tomogram, (b) centre-visible original tomogram, and (c) tomogram from PILM (Wang et al. 2016a).

Figure 5.14 demonstrates the capability of RILM to visualise static objects in a phantom. As previously mentioned, RILM only concerns the central area of the

tomograms, and thus the region out of interest is masked. The full tomogram (Figure 5.14a) is also masked to only show the area of interest (Figure 5.14b) for the purpose of comparison. According to Figure 5.14c, the RILM-based approach is able to visually identify the objects, and the result is comparable to the masked tomogram by conventional configuration. Nevertheless, it is noticed that the two masked images are not identical since the measurement scales are different.

5.3.2.2 Evaluation of the gas-water pipeline flow

Further evaluation was performed at the University of Leeds on gas-water upward flow in a vertical pipeline with an inner diameter of 50 mm. Slug flow was chosen for this purpose, with the gas and water flowrate at 70 litre/min and 27 rpm, respectively. The FICA system (Wang et al. 2005) was applied for the experiment, at a speed of 1000 fps. The data for the RILM was retrieved from the full set of measured data by FICA. Similarly, concentration and velocity maps were generated using AIMFlow software based on the full measurement, and relevant data for RILM was also extracted from the full maps.

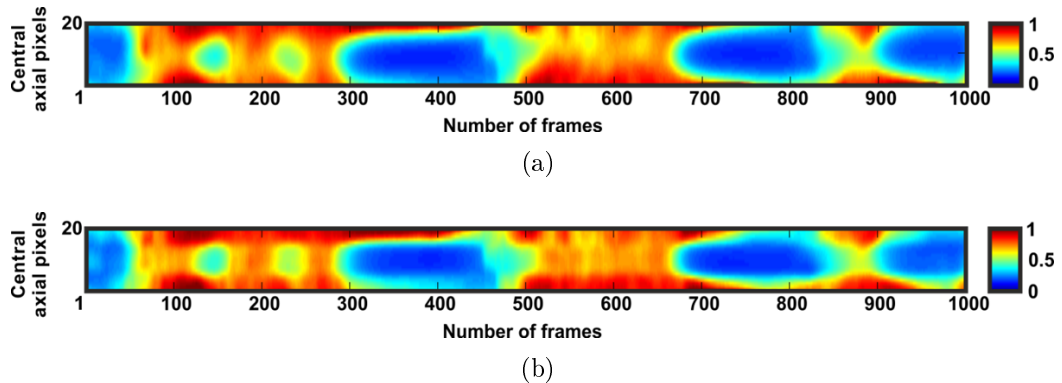


Figure 5.15: Stacked images of gas-water flow: (a) from full measurement and (b) from RILM (Wang et al. 2016a).

Figure 5.15 demonstrates the axial cross-sectional images extracted from 1000-frame stacked cross-sectional tomograms. Compared to the image obtained from the full tomograms (Figure 5.15a), the RILM-based image (Figure 5.15b) is able to deliver comparable visual information. In addition to visual evaluation, concentration and velocity profiles were also compared, and results are presented in Figure 5.16. As far as the concentration profile is concerned, the RILM-based one is very close to the original one, although slight underestimates existed, as

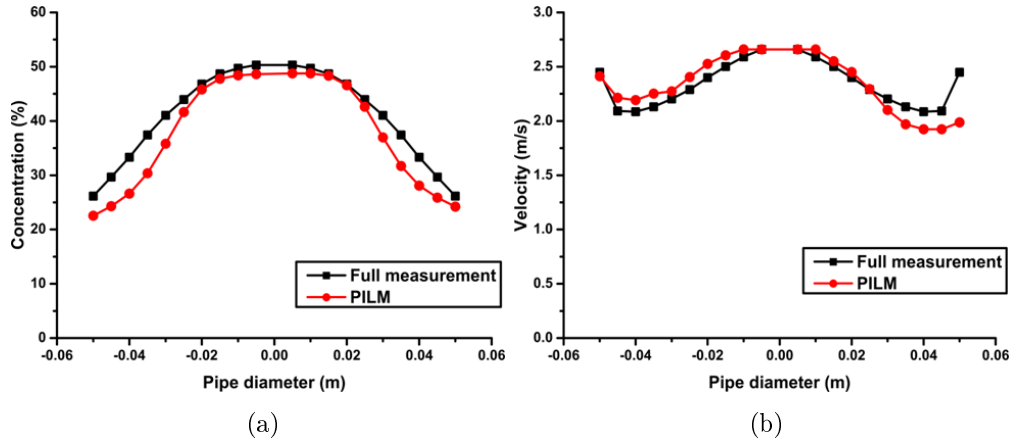


Figure 5.16: Comparison of (a) concentration profiles and (b) velocity profiles.

depicted in Figure 5.16a. As for the velocity profile, RILM is still able to produce a good result that is similar to the original one, as depicted in Figure 5.16b. The differences between both profiles are noticed to have a similar tendency, i.e. they become larger when closer to the pipe wall.

5.3.3 Conclusions

A novel approach was proposed to improve the spatial and temporal resolution of conventional ERT. The approach is on the basis of the conventional 16-electrode configuration therefore it requires no modification of the conventional hardware, but targets only a partial area produced by a lesser number of measurements. The evaluation on the visualisation of static objects in a phantom and characterisation of gas-water upward flow demonstrated the feasibility and capability of the proposal. From a visualisation point of view, the RILM-based approach was able to clearly identify both static objects in the phantom and slug bubbles in the pipeline flow. From a measurement perspective, it is also capable of extracting concentration and velocity profiles comparable to those of the original tomograms, although the discrepancy exists at the boundary area. It is mainly because of the weaker accumulation of the electrical field at boundary area by RILM, compared to the field generated by the conventional 16-electrode ERT.

Because of the dramatic decrease in the required number of measurements, and the considerable reduction of the computation involved in image reconstruction,

it is reasonable to expect that RILM would outperform conventional 16-electrode ERT in terms of measurement speed and data processing. The increase in the speed further contributes to the improvement of discrimination error, and thus velocity calculation.

5.4 Summary

High-speed multiphase flow in industrial sectors is very common, which challenges the performance of ERT systems in terms of the characterisation of such flow. In practice, it has to compromise either spatial resolution or temporal resolution to reach an acceptable outcome. For example, the ERT system in (Wang et al. 2015) has to be operated with an 8-electrode configuration so that it can produce 1250 fps to manage multiphase flow at high flowrate, whereas when visualisation is of high priority, e.g. in (Wang et al. 2017), the ERT system needs to work at the 16-electrode mode in order to provide better spatial resolution. This chapter addressed the problems. In principle, it tried to integrate the advantages of conventional a 8-electrode ERT systems, i.e. high temporal resolution, and a conventional 16-electrodes ERT systems, i.e. high spatial resolution, on the basis of the assumption that the flow under investigation is fully developed, whose cross-sectional tomograms are symmetrical to its diameter in a vertical pipeline or to its vertical diameter in a horizontal pipeline.

The first proposed approach, namely ASI, carefully selected 8 electrodes in a conventional 16-electrode configuration, and applied measurements through the selection to image half of full tomograms. In this case, DAS speed decreased significantly, while the tomograms yielded better spatial resolution than that by the conventional 8-electrode ERT. The experimental results demonstrated the feasibility of the approach. The temporal resolution of ASI is more than 6 times faster than that of the conventional 16-electrode ERT. It was expected that the spatial resolution of the images by ASI could be comparable with those by the conventional 16-electrode ERT. Unfortunately, it was not always true according to the results. Besides, the application of ASI required the modification of hardware.

Then the second approach was proposed, called RILM, to overcome the disadvantages of ASI. Essentially, RILM was fully compatible with the conventional

16-electrode system, and hence no modification of hardware was required. Unlike ASI, RILM chose several of the original measurements, which were crucial to image the central region of full tomograms. It is expected that the temporal improvement could be up to 7 times, while the spatial resolution is similar. There was also another factor contributing to the improvement of the overall performance of RILM, i.e. less computation was required in image reconstruction. The experimental outcomes explained the effectiveness of RILM in terms of visualising and characterising both static objects and gas-water upward flow. However, due to the unavailability of the hardware specifically designed for RILM to achieve maximum performance, the temporal improvement is not yet quantified.

CHAPTER 6

CONCLUSIONS AND SUGGESTIONS FOR FUTURE WORK

6.1 Conclusions

Electrical tomography, including ERT and ECT, has proved to be an effective, low-cost, non-intrusive/invasive technique for the measurement and visualisation of multiphase flow with relatively low spatial resolution but high temporal resolution (Crawford 2017; Wang et al. 2016b; Sun et al. 2015; Zhang et al. 2014; Wang 2015). However, considerable uncertainty may still exist when dealing with real-industrial cases with very high flow velocity. In addition, when the flow under investigation contains more than two phases, e.g. gas-oil-water three-phase flow, single-modality tomography is no longer suitable for extracting informative content of all phases, and therefore multi-modality systems are necessary to reveal the detailed distribution of each phase. With the practice of high speed and multiple modalities of tomographic systems, there is an apparent lack of systematic study in regard to thorough and explicit discussion, formalisation, and evaluation of critical aspects involved in data fusion and visualisation of three-phase flow, in spite of a number of pioneering dual-modality tomographic systems having been proposed (Qiu et al. 2007; Hjertaker et al. 2011; Santos et al. 2015; Sun et al. 2015; Zhang et al. 2015). Besides, due to the limitations of electrical tomography with respect to visualisation of multiphase flow, conventional colour mapping based imaging struggles to convey sufficient flow dynamics, e.g. flow regimes.

As far as dual-modality tomography is concerned, the majority of effort has made on hardware and/or reconstruction processes (Santos et al. 2015; Sun et al. 2015; Zhang et al. 2015), but few of them explicitly and methodically concern other aspects engaged in the data fusion and visualisation (Yue et al. 2013; Zhang et al. 2014; Puspanathan et al. 2014), as well as comprehensive evaluation of such systems. From a data fusion perspective, an enormous amount of algorithms have been proposed and put into practice, particularly those for the imaging fusion in

medical imaging (James et al. 2014), since similar tomographic techniques are used for medical purpose. It seems that data fusion in industrial multiphase flow is trivial as those algorithms in medical imaging and other domains could be applied to industrial multiphase flow imaging without much effort. On the contrary, data fusion for multiphase flow imaging is especially complex in terms of its implicit requirements to reveal flow dynamics, as well as quantification of phase distribution. In consequence, there is a wide gap between modern dual-modality tomography and data processing techniques. This research, therefore, tries to fill the gap.

The major objectives were successfully achieved during the study:

- **A general framework for the data fusion with dual-modality electrical tomography**

The framework described in CHAPTER 3 systematically explored some major technical challenges involved in the imaging of multiphase flow by ERT-ECT systems. It first discussed the data alignment techniques for ERT-ECT systems due to the different spatial and temporal resolution of ERT and ECT. It then addressed the issue of the integration of spatial and temporal information to let the fused results convey sufficient flow dynamics. Finally, the suitable rendering methods were presented based on conventional colour mapping. The framework was demonstrated using two different fusion algorithms, namely thresholding and fuzzy logic. The discussion of the framework was independent to the data fusion algorithms, and thus can conduct the pixel-level fusion for any specific algorithms. It can also easily be adapted for other imaging cases rather than electrical tomography

- **A threshold-based data fusion algorithm**

A new fusion algorithm was explicitly proposed based on conventional thresholding methods that are implicitly applied in the majority of modern dual-modality tomographic systems (CHAPTER 3). The procedure was described and the difference between traditional approach and this one was compared. The evaluation was performed by integrating the approach into the framework using the data gauged at industry-scale horizontal flow testing facilities, and the results proved the feasibility of the approach.

- **A fuzzy logic based data integration approach**

A fuzzy logic based fusion technique was implemented to overcome the difficulties in the determination of the critical threshold in the threshold-based approach (CHAPTER 3). The proposal utilised the characteristics of fuzzy logic, i.e. precise logic to handle imprecise data, to derive concentration distribution of each phase in gas-oil-water flow. The input dataset, i.e. two sets of concentration tomograms from the ERT and the ECT was fuzzified firstly by two membership functions, and the results were further interpreted by a number of pre-defined rules and aggregated for the defuzzification process, during which the aggregations were defuzzified to two single numbers. Those two numbers were eventually used for the decomposition of flow phases by a pre-defined decision tree. This advanced algorithm was verified by the incorporation of the framework using the same data from real-case industrial gas-oil-water flow in a horizontal pipe. The results were presented, in comparison with the ones from the threshold approach, and proved the feasibility and stability of the approach.

- **Experimental evaluation of the ERT-ECT systems on industry-scale flow facilities**

The performance of the dual-modality electrical tomography for gas-oil-water three-phase flow visualisation and measurement was thoroughly evaluated in CHAPTER 3, where the data was collected during the experiments with WLR 0% to 100% in parallel with GVF 0% to 100% on TUV-NEL's gas-oil-water flow testing facilities of a 4-inch horizontal pipe. The conditions were from oil-continuous gas-water-in-oil flow to water-continuous gas-oil-in-water flow, and hence produced typical disperse phase flow patterns. The fused images were compared with those by high-speed video logger, and good agreement was achieved. The performance results of the ERT-ECT as single-modality and dual-modality systems were presented, and their strength and weakness were also discussed. The capabilities of ERT-ECT dual-modality systems for three-phase flow measurement and visualisation were first time reported that they are an effective method when characterising gas-oil-water horizontal flow of WLR between 40% and 90%.

- **Bubble mapping based 3D visualisation of gas-liquid flow by electrical tomography**

A novel technique for 3D visualisation of gas-liquid flow using electrical

tomography was proposed in CHAPTER 4 to overcome the limits of conventional colour mapping based imaging. Instead of the colour-based lookup table, the proposal used a bubble-based lookup table to transfer re-scaled dataset based on the interrogation cell from scalar values in $[0.0, 1.0]$ to discrete number and size of bubbles. With the assistance of an enhanced iso-surface extraction algorithm, bubbles were rendered using modern technologies in computer graphics. The novel approach was evaluated with a high-speed video logger on a number of common flow regimes in different orientations of pipe, including horizontal and vertical, by different ERT systems, and the images implied the feasibility of the proposal, and its capability of independence from pipe orientation.

- **Improvement of spatial resolution of conventional ERT**

Two approaches were discussed in CHAPTER 5, namely ASI and RILM, to further improve the data acquisition speed of ERT to extend its capability for the flow with higher flow velocity. ASI takes the effect of applying a limited number of asymmetrically arranged electrodes on a conventional 16-electrode configuration of ERT to significantly reduce sensing time, whereas RILM works by carefully selecting a partial number of original independent measurements for conventional 16-electrode configured ERT, so that the number of required measurements and the computational efforts during reconstruction dramatically decrease, and hence the overall duration for sensing and processing is reduced. Both methods were evaluated with static objects and dynamic flow conditions, and their advantages and shortcomings were discussed.

In addition to the above contributions towards the theoretical studies on the multiphase flow visualisation and quantification, significant software engineering has been conducted to facilitate the experimentation and evaluation of ideas on-line and/or off-line, including:

- **A command-line system for off-line data fusion and visualisation of gas-oil-water flow by dual-modality electrical tomography**

This system was designated for the data fusion and displaying involved in the gas-oil-water three-phase flow visualisation by dual-modality electrical tomography. It implemented the concepts discussed in CHAPTER 3 with

modularised components to separate business logic, so that different fusion algorithms and rendering technologies can be seamlessly integrated into the system. Two aforementioned fusion algorithms have been settled in the system. The system has been evaluated by a large-scale set of experiments on gas-oil-water horizontal flow using the industry-scale multiphase flow testing facilities in TUV-NEL.

- **A command-line software for bubble mapping**

This software was implemented for the off-line 3D visualisation of gas-liquid flow on the basis of bubble mapping, as discussed in CHAPTER 4. With the assistance of the Visualization Toolkit (VTK, (Schroeder et al. 2006a)), a stack of input electrical concentration tomograms is transformed to bubble-based presentation of gas-liquid flow, regardless of pipe orientation. The software has been evaluated by different ERT systems under different flow conditions in both horizontal and vertical pipe.

- **A user-friendly online processing platform for ERT**

The platform was designed for on-line visualisation and measurement of multiphase flow by an ERT system, which enabled on-line presentation of cross-sectional and axially cross-sectional concentration tomograms, as well as quantitative monitoring of the flow under investigation. It has been successfully applied to various experiments, including gas-liquid two-phase flow and gas-oil-water three-phase flow in both horizontal and vertical pipe.

In this research, a few novel techniques were proposed for electrical tomography to visualise, interpret, and quantify multiphase flow. Feasible, experimental, multiphase flow visualisation and characterisation systems were developed, and the results demonstrated the feasibility of the techniques. The developed methods are significant tools for data analysing, fusion, and visualisation, and will be integrated together to form a platform which processes input tomographic data and generates process-relevant figures and/or images.

The qualitative (images) and quantitative (phase concentrations) results integrated from dual-modality ERT-ECT systems and 3D visualisation of gas-liquid flow using electrical tomography overcome current limits of single-modality electrical tomography on three-phase flow, in particular the transitional range from

oil-continuous to water-continuous flow, and hence provide prominent data regarding process performance. The techniques proposed in this study have been successfully applied for the investigation and verification of the visual flow pattern recognition and visualisation of gas-oil-water horizontal flow for conditions relevant to oil and gas production.

It is expected that this study would provide a fundamental understanding of the data fusion and visualisation of multiphase flow by electrical tomography, i.e. the advantages and challenges existing in state-of-the-art research in electrical process tomography. Although the effort was based on electrical tomography, it would be easy to applied to other tomographic systems since the data processing and visualisation in this study is purely on the basis of concentration tomograms. In addition, the approaches proposed in this research could be valuable information to evaluate simulation results, and hence to improve simulation parameters and models at design stage. They could also be helpful to develop process models when they may be unsuitable or unavailable due to a wide range of materials. Meanwhile, it would provide insightful information at operational stage for on-line monitoring and control, as well as off-line analysis, which is anticipated to offer integrated images with unambiguous flow dynamics, e.g. flow regimes.

6.2 Suggestions for Future Work

Despite the aforementioned achievements having been made in this study, there are still some aspects worthy of further investigation. Potential improvements are listed in the following sections.

6.2.1 Dual-modality electrical tomography

The generic framework has been evaluated by two different fusion algorithms to be feasible and fusion algorithm independent, but it will introduce extra uncertainty during data pre-processing. The primary source is artificial errors in the data interpolation due to non-alignment data along spatial and temporal dimensions, particularly linear interpolation was applied (Lehmann et al. 1999). Therefore, an advanced interpolation approach should be applied to reduce artificial error.

Essentially, the interpolation is mainly caused by different spatial and temporal resolution of ERT and ECT systems, i.e. different sampling speeds and grid definition. The issue of different sensing speeds can be overcome by synchronising the sensing of ERT and ECT systems, such as the one (Ji et al. 2016), in which case permittivity and conductivity are derived at the same time, and hence temporal registration is unnecessary.

A threshold-based fusion approach is conceptually simple and easy to be implemented, and therefore is eligible for on-line purposes. However, the threshold for ECT tomograms T_g was obtained by experience and may be case-specific, thereby needing further investigation to discover the best solution. Although the fuzzy logic based method overcame this limitation, it still has a few aspects requiring further attention. The employed membership functions have been evaluated to be superior to others in other fields, but if the result is still kept in DMTS it is worthwhile of more effort. In addition, an advanced reconstruction algorithm should be applied to yield better resolution of electrical concentration tomograms since the approach was sensitive to the quality of input images. For both methods, phase velocity was not included in the procedures, due to the primary objectives were not measurement but flow regime visualisation. Consequently, phase velocity information should be reflected in the future work to reveal the real distribution of each phase.

From a data fusion point of view, two fusion algorithms have been successfully applied. Those two algorithms were both performed at pixel level and directly on pixel concentration values, i.e. data fusion. However, there are some other pixel-level fusion techniques that have proved to be successful in other fields, such as the one in (James et al. 2014; Li et al. 2017). The principal barrier between those mature advanced algorithms and the data fusion in multiphase flow imaging by DMTS is that the one in DMTS is eager for not only qualitative images but also quantitative presentations of the phases in investigated flow. In other words, data fusion in DMTS needs to derive geometrical distributions of involved phases for visual perception by human and machines, as well as concentration distributions for measurement purposes. In addition to data-oriented fusion, image combination is also another set of technologies that may be helpful for fusion purposes in DMTS. For example, Zhang *et. al* proposed image-level fusion for oil-gas two-phase flow in (Zhang et al. 2014). But the applicability of image-level fusion to the imaging in three-phase flow is still unknown.

As far as the experimental evaluation of the ERT-ECT system is concerned, the experiments conducted in general covered a considerable amount of flow conditions. Unfortunately, it still lacks sufficient evidence for the determination of the lower bound of function range for an ERT system. Hence, more combination of WLR and GVF should be applied to dig out the precise working range for the ERT system. Another important aspect missed in the evaluation is the velocity information, which makes the quantitative comparison of the ERT-ECT system with the references more meaningful. In the meantime, an advanced fusion algorithm should be utilised to obtain improved results.

6.2.2 Bubble mapping

Bubble mapping is an effective way to deliver better visualisation results for gas-liquid flow imaging by electrical tomography than conventional methods. The investigation is still a preliminary trial and hence there are still a few aspects which need more attention. The determination of the upper threshold value T_g is the first aspect to be considered since it plays an essential role in final rendering, especially the size and shape of large bubbles. However, to pinpoint such value is non-trivial due to the limited spatial resolution of electrical tomography and the inhomogeneity of the electromagnetic field. Effort could be made on discovering the relationship between object size and corresponding tomograms so that the actual boundaries could be linked to concentration values in the tomograms, and hence the local threshold could be identified to fit different cases.

On the construction of the lookup table, averaged concentration is still retained during the reconstruction of small bubbles. This unfortunately is not valid for large bubbles since 40% instead of 100% was selected as the criterion for large bubble segmentation, although this had little visual impact from the viewpoint of flow regime visualisation. This situation could be improved using an appropriate threshold value, as well as utilise advanced algorithms in computer graphics, such as the one in (Anderson et al. 2010).

Another important aspect is the engagement of local velocity instead of superficial velocity of the gas phase when calculating the temporal dimension of the interrogation cell. Ideally, instantaneous velocity, i.e. velocity field, is the most eligible

candidate for the calculation since different bubbles have different velocities. Unfortunately, it is usually unavailable to tomography-based measurements. The most widely applied approach is statistical, e.g. cross-correlation, which reflects the averaged velocity of gas phase over a certain period and hence is still unable to distinguish the difference between individual bubbles. Nevertheless, this limitation could be relieved using iterative cross-correlation in (Li et al. 2009a) with a relatively small moving window with the assumption that bubbles have the same axial velocity within the window.

6.2.3 ASI and RILM

RILM has been proved to be theoretically feasible for multiphase flow quantification and qualification using static and dynamics conditions. However, due to the availability of the related hardware, the evaluation was not performed with dedicated hardware. Therefore, it needs to be further verified with dedicated hardware. In addition, more dynamic testing should be involved to fully evaluate the proposal.

6.2.4 GPU-accelerated on-line visualisation and measurement

On-line visualisation and measurement play an important role in the continuous understanding and monitoring of industrial processes, allowing instantaneous information for fault detection and system malfunction. It also provides an experimental methodology for the validation and optimisation of process design and engineering. Owing to the ever-increasing development of hardware for electrical tomography, contemporary electrical tomographic systems offer over 1000 frames per second, meaning a huge amount of data, over 10 Megabytes per second are gauged for further processing. In addition, time and resource consuming computation involved in the processing requires numerous amounts of computational power. All these barriers prevent modern electrical tomography from the application of modern electrical tomography to more industrial cases for on-line measurement and visualisation.

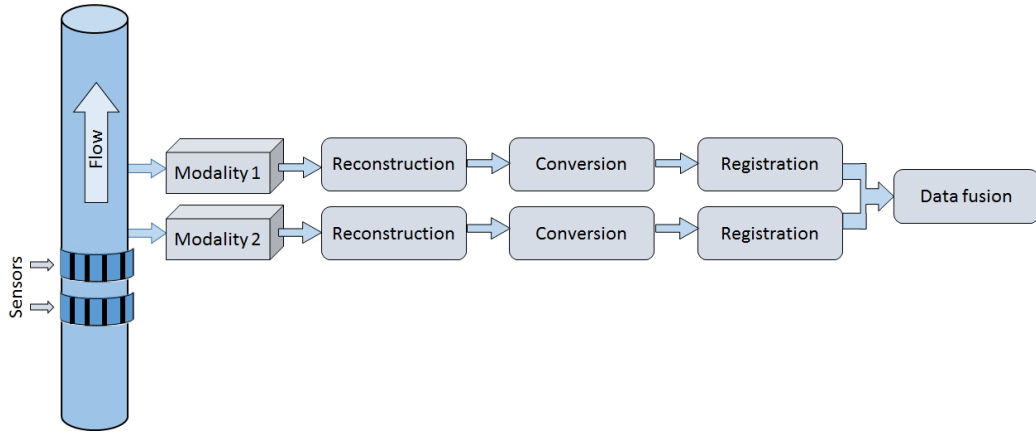


Figure 6.1: Data processing procedure in a DMTS to multiphase flow.

There are usually several steps which consume computational power in the processing of electrical tomography-based multiphase flow visualisation and measurement. Taking the example in Figure 6.1, the procedure mainly requires image reconstruction, data conversion, data registered, and data fusion. Image reconstruction is a computation-intensive process since it requires one or more matrix multiplication for LBP or iterative reconstruction algorithms. The conversion from electrical properties to concentration distribution is fairly simple by Maxwell equation, but considering the huge number of data to be converted, it requires some time for the performance. In data registration, the original tomograms are usually expanded to finer grids, i.e. the number of dimensions does not change but the resolution in each dimension is higher. The primary operation is linear interpolation in our case, and thus it consumes a certain amount of computing resource. The data fusion is no doubt a computationally-expensive process due to the tremendous amount of data to be fused and the fusion algorithm itself, even a simple threshold-based approach. Therefore, it is a great challenge to achieve on-line measurement and visualisation using the methodologies discussed in this study.

Graphics Processing Units (GPU) computing, on the other hand, has proved to be an effective and efficient way to boost scientific computing. In general, it utilises the power of modern GPU to serve complex computational process in other areas. With the introduction of programmable hardware in GPU, it became more flexible for programmers to perform general-purpose computation directly on GPU (Luebke et al. 2004). GPU computing has now entered a new era with the implementation of the unified graphics and computing GPU archi-

texture introduced in GeForce 8000 series GPU by NVidia in 2006 (Owens et al. 2007). With the unified processors capable of handling scalar instead of vector operations, the fully programmable graphics pipeline enables users to design and implement their computationally demanding problems using the Compute Unified Device Architecture (CUDA) by NVidia ¹ or the Open Computing Language (OpenCL) ². Comparing with multi-core processors in modern Central Processing Units (CPU), modern GPU vastly outnumbers it, in terms of three orders. By significantly improving the throughput of the pipeline in GPU, it dramatically reduces the overall computing time.

Pioneering research has been done on using GPU to accelerate the image reconstruction process and the results have proved that GPU performs exceptionally well in boosting the process to at least one order faster (Xu et al. 2007). Although this was for 3D image reconstruction in X-ray tomography, it still demonstrates the capability and potential of GPU computing in the application to electrical tomography. Later on, several reports have substantiated the applicability of GPU for improving the performance of image reconstruction in electrical tomography (Borsic et al. 2012; Gebhardt et al. 2013; Matusiak et al. 2013). Therefore, using GPU to eliminate this barrier seems promising, especially when single-step linear back-projection is applied.

In order to fully utilise the power of GPU, computation problems need to be paralleled, i.e. they can be split into independent sub-tasks so that each sub-task can be executed simultaneously on one or more processors. The conversion, on the other hand, involves the calculation of electrical properties to concentration by Maxwell equation, and is performed on a pixel basis. That is, the calculation for one pixel does not affect the others. As a result, this step could perfectly reside in GPU. In data registration, both sets of concentration tomograms are projected into a common coordinate system by interpolation. The operation is achieved by processing pixel by pixel, and then frame by frame. Therefore, parallel processing could be applied to the registration either on pixels, or frames, or both. In addition, since computer graphics heavily depend on interpolation operation during rendering and visualisation, modern GPU inherently supports interpolation with dedicated hardware (texture memory) to accelerate those calculations. As discussed previously, advanced interpolation, instead of a linear one, should be utilised

¹http://www.nvidia.com/object/cuda_home_new.html

²<https://www.khronos.org/opencl/>

to reduce artificial errors. There are some reports in medical imaging devoted to using GPU to improve the performance of advanced interpolation algorithms, or even on image registration directly (Shams et al. 2010; Eklund et al. 2013; Kubias et al. 2008). All these prove the potential of applying GPU to achieve an extremely high performance of data registration in our study.

In our study, data fusion is pixel-level, i.e. pixel by pixel. Combining two corresponding pixels from each registered tomogram into one fused pixel has no influence on other pixel fusion processes. Therefore, pixel-level fusion in our study can be paralleled. This potentially allows GPU to perform a number of pixel fusions simultaneously, and hence significantly reduce the processing time. Meanwhile, some research has been conducted on pixel-level image fusion, such as the ones in (Yoo et al. 2008; Li et al. 2013), which have proved the feasibility of employing GPU for pixel-by-pixel image integration with advanced fusion algorithms.

In short, the data processing procedure in our study contains a few steps that involve different types of computations/processing. According to the aforementioned discussion, GPU computing seems eligible for most of them as an effective and efficient approach to deal with computationally-intensive and expensive tasks. As a result, with careful design and implementation, the methodologies proposed in this study have great potential for on-line measurement and visualisation, with the assistance of GPU computing.

6.2.5 An integrated platform for on-line visualisation and measurement

As discussed in Section 1.2, this study focused on the development of different techniques suitable for the quantification and qualification of multiphase flow by electrical tomography. The second step of this study is to combine all proposed techniques together to build up an integrated platform. Therefore, a prominent task for future work is to perform the integration, besides the aforementioned suggestions.

References

- Ahmed, W H (2011). “Experimental investigation of air–oil slug flow using capacitance probes, hot-film anemometer, and image processing”. In: *International Journal of Multiphase Flow* 37.8, pp. 876 –887 (cit. on p. 6).
- Al-amri, Sm S, N V Kalyankar, and S D Khamitkar (2010). “Image Segmentation by Using Threshold Techniques”. In: *Journal of Computing* 2.5 (cit. on p. 26).
- Al-Wassai, F A, N V Kalyankar, and A A Al-Zuky (2011). “The IHS Transformations Based Image Fusion”. In: *CoRR* abs/1107.4396 (cit. on p. 51).
- Amolins, K, Y Zhang, and P Dare (2007). “Wavelet based image fusion techniques — An introduction, review and comparison”. In: *{ISPRS} Journal of Photogrammetry and Remote Sensing* 62.4, pp. 249 –263 (cit. on p. 52).
- Anderson, J C, C Garth, M A Duchaineau, and K I Joy (2010). “Smooth, Volume-Accurate Material Interface Reconstruction”. In: *IEEE Transactions on Visualization and Computer Graphics* 16.5, pp. 802–814 (cit. on pp. 148, 175).
- Anglart, H and M Z Podowski (2002). “Fluid mechanics of Taylor bubbles and slug flows in vertical channels”. In: *Nuclear science and engineering* 140.2, pp. 165–171 (cit. on p. 10).
- Banerjee, S (2013). *Numerical Methods for Multiphase Flow*. Zurich, Switzerland: The Energy Insitute, City College of New York (cit. on p. 10).
- Bankman, I (2008). *Handbook of medical image processing and analysis*. Academic Press (cit. on p. 26).
- Barra, V and J-Y Boire (2001). “A General Framework for the Fusion of Anatomical and Functional Medical Images”. In: *NeuroImage* 13.3, pp. 410 –424 (cit. on p. 76).
- Beck, M S and A Plaskowski (1987). *Cross Correlation Flowmeters, Their Design and Application*. Taylor & Francis (cit. on pp. 16, 19, 150).

- Bhardwaj, S and A Mittal (2012). “A Survey on Various Edge Detector Techniques”. In: *Procedia Technology* 4. 2nd International Conference on Computer, Communication, Control and Information Technology(C3IT-2012) on February 25 - 26, 2012, pp. 220 –226 (cit. on p. 24).
- Birchfield, S (2017). *Image Processing and Analysis*. CL Engineering (cit. on pp. 24, 26).
- Blum, R S and Z Liu (2005). *Multi-sensor image fusion and its applications*. CRC press (cit. on pp. 45, 76).
- Bolton, G T, C W Hooper, R Mann, and E H Stitt (2004). “Flow distribution and velocity measurement in a radial flow fixed bed reactor using electrical resistance tomography”. In: *Chemical Engineering Science* 59.10, pp. 1989 – 1997 (cit. on p. 17).
- Borsic, A, E A Attardo, and R J Halter (2012). “Multi-GPU Jacobian accelerated computing for soft-field tomography”. In: *Physiological measurement* 33.10, p. 1703 (cit. on p. 178).
- Boykov, Y Y and M P Jolly (2001). “Interactive graph cuts for optimal boundary and region segmentation of objects in N-D images”. In: *Proceedings Eighth IEEE International Conference on Computer Vision. ICCV 2001*. Vol. 1, 105–112 vol.1 (cit. on p. 26).
- Brennen, C E (2005). *Fundamentals of Multiphase Flows*. Cambridge University Press, p. 368 (cit. on pp. 5, 10, 30, 42, 130, 131).
- Brown, B H, D C Barber, and A D Seagar (1985). “Applied potential tomography: possible clinical applications”. In: *Clinical Physics and Physiological Measurement* 6.2, p. 109 (cit. on p. 12).
- Canny, J (1986). “A Computational Approach to Edge Detection”. In: *IEEE Transactions on Pattern Analysis and Machine Intelligence PAMI-8.6*, pp. 679–698 (cit. on p. 24).
- Carvalho, H, W Heinzelman, A Murphy, and C Coelho (2003). “A general data fusion architecture”. In: *Int. Conf. on Info. Fusion*, pp. 1465–1472 (cit. on p. 76).
- Chen, F and H Hagen (2011). “A Survey of Interface Tracking Methods in Multiphase Fluid Visualization”. In: *Visualization of Large and Unstructured Data Sets - Applications in Geospatial Planning, Modeling and Engineering (IRTG 1131 Workshop)*. Ed. by Ariane Middel, Inga Scheler, and Hans Hagen. Vol. 19.

- OpenAccess Series in Informatics (OASICs). Dagstuhl, Germany: Schloss Dagstuhl–Leibniz-Zentrum fuer Informatik, pp. 11–19 (cit. on p. 32).
- Chen, G and T T Pham (2000). *Introduction to fuzzy sets, fuzzy logic, and fuzzy control systems*. CRC press (cit. on p. 49).
- Corneliussen, S, J-P Couput, E Dahl, E Dykesteen, K-E Froysa, E Malde, H Moestue, P O Moksnes, L S, and H Tunheim (2005). *Handbook of Multiphase Flow Metering*. http://nfogm.no/wp-content/uploads/2014/02/MPFM_Handbook_Revision2_82-91341-89-3.pdf (cit. on pp. v, 5, 7, 11, 42, 106, 131, 132).
- Crawford, D (2017). *Multiphase flow reference metrology*. Tech. rep. Naitonal Engineering Laboratory (cit. on p. 168).
- Cui, Z, H Wang, Ziang Chen, Y Xu, and W Yang (2011). “A high-performance digital system for electrical capacitance tomography”. In: *Measurement Science and Technology* 22.5, p. 055503 (cit. on pp. 2, 36, 44).
- Deckwer, W-D (1992). *Bubble column reactors*. John Wiley and Sons Ltd (cit. on p. 136).
- Dong, F, Y B Xu, L J Xu, L Hua, and X T Qiao (2005). “Application of dual-plane {ERT} system and cross-correlation technique to measure gas–liquid flows in vertical upward pipe”. In: 16.2–3. Tomographic Techniques for Multiphase Flow Measurements 4th International Symposium on Measurement Techniques for Multiphase Flows, pp. 191 –197 (cit. on p. 17).
- Dudukovic, M P (2007). “Relevance of Multiphase Reaction Engineering to Modern Technological Challenges”. In: *Industrial & Engineering Chemistry Research* 46.25, pp. 8674–8686 (cit. on p. 21).
- Eklund, A, P Dufort, D Forsberg, and S M LaConte (2013). “Medical image processing on the {GPU} – Past, present and future”. In: *Medical Image Analysis* 17.8, pp. 1073 –1094 (cit. on p. 179).
- Fabre, J and B Figueroa-Espinoza (2014). “Taylor bubble rising in a vertical pipe against laminar or turbulent downward flow: symmetric to asymmetric shape transition”. In: *Journal of Fluid Mechanics* vol. 755, pp. 485–502 (cit. on p. 10).
- Faraj, Y, M Wang, J Jia, Q Wang, C Xie, G Oddie, K Primrose, and C Qiu (2015). “Measurement of vertical oil-in-water two-phase flow using dual-modality ERT–EMF system”. In: *Flow Measurement and Instrumentation* 46, Part B. Special issue on Tomography Measurement & Modeling of Multiphase Flows, pp. 255 –261 (cit. on p. 44).

- Felzenszwalb, P F and D P Huttenlocher (2004). “Efficient Graph-Based Image Segmentation”. In: *International Journal of Computer Vision* 59.2, pp. 167–181 (cit. on p. 26).
- Fischer, F, D Hoppe, E Schleicher, G Mattausch, H Flaske, R Bartel, and U Hampel (2008). “An ultra fast electron beam x-ray tomography scanner”. In: *Measurement Science and Technology* 19.9, p. 094002 (cit. on p. 35).
- Fischer, F and U Hampel (2010). “Ultra fast electron beam X-ray computed tomography for two-phase flow measurement”. In: *Nuclear Engineering and Design* 240.9. Experiments and {CFD} Code Applications to Nuclear Reactor Safety (XCFD4NRS), pp. 2254 –2259 (cit. on pp. 35, 53).
- Froystein, T, H Kvandal, and H Aakre (2005). “Dual energy gamma tomography system for high pressure multiphase flow”. In: *Flow Measurement and Instrumentation* 16.2–3. Tomographic Techniques for Multiphase Flow Measurements 4th International Symposium on Measurement Techniques for Multiphase Flows, pp. 99 –112 (cit. on p. 23).
- Gebhardt, P, M Gevers, and T Musch (2013). “GPU Accelerated 2.5D Solver for Fast and Accurate Modeling of EIT Forward Problem in Tube Geometries”. In: *7th World Congress on Industrial Process Tomography* (cit. on p. 178).
- Gehrke, S and K E Wirth (2005). “Application of conventional- and dual-energy X-ray tomography in process engineering”. In: *IEEE Sensors Journal* 5.2, pp. 183–187 (cit. on p. 23).
- Guet, S, G Ooms, and R V A Oliemans (2002). “Influence of bubble size on the transition from low-Re bubbly flow to slug flow in a vertical pipe”. In: *Experimental Thermal and Fluid Science* 26.6-7, pp. 635–641 (cit. on pp. 132, 134).
- Hansen, C D and C R Johnson (2011). *Visualization Handbook*. Elsevier Science (cit. on pp. 26, 27, 37, 39, 41, 65, 74).
- Heindel, T J (2011). “A Review of X-Ray Flow Visualization With Applications to Multiphase Flows”. In: *Journal of Fluids Engineering* 133 (7), pp. 074001–074001 (cit. on pp. 1, 11).
- Hjertaker, B T, R Maad, and G A Johansen (2011). “Dual-mode capacitance and gamma-ray tomography using the Landweber reconstruction algorithm”. In: *Measurement Science and Technology* 22.10, p. 104002 (cit. on pp. 1, 23, 44, 46, 47, 168).

- Hong, J-M, H-Y Lee, J-C Yoon, and C-H Kim (2008). “Bubbles Alive”. In: *ACM Trans. Graph.* 27.3, 48:1–48:4 (cit. on pp. 32, 33).
- Hoyle, B S (2016). “IPT in Industry – Application Need to Technology Design”. In: *8th World Congress on Industrial Process Tomography* (cit. on p. 22).
- Hoyle, B S, X Jia, F J W Podd, H I Schlaberg, H S Tan, M Wang, R A Williams R M West, and T A York (2001). “Design and application of a multi-modal process tomography system”. In: *Measurement Science and Technology* 12.8, p. 1157 (cit. on p. 23).
- Hoyle, B S and M Wang (2012). “Multi-dimensional opportunities and data fusion in Industrial Process Tomography”. In: *Instrumentation and Measurement Technology Conference (I2MTC), 2012 IEEE International*, pp. 916–920 (cit. on pp. 2, 45, 64).
- Hua, P (1987). “Effect of the measurement method on noise handling and image quality of EIT imaging”. In: *Proc. Annu. Int. Conf. Engng Med. and Biol. Soc.* Vol. 9, pp. 1429–1430 (cit. on p. 12).
- Issa, R I and M H W Kempf (2003). “Simulation of slug flow in horizontal and nearly horizontal pipes with the two-fluid model”. In: *International Journal of Multiphase Flow* 29.1, pp. 69 –95 (cit. on p. 6).
- Ito, D, H-M Prasser, H Kikura, and M Aritomi (2011). “Uncertainty and intrusiveness of three-layer wire-mesh sensor”. In: *Flow Measurement and Instrumentation* 22.4, pp. 249 –256 (cit. on p. 36).
- ITS (2009). *ITS System 2000 Version 7.0 p2+ Electrical Resistance Tomography System - User’s Manual*. Industrial Tomography Systems Plc. Speakers House, 39 Deansgate, Manchester M3 2BA (cit. on pp. 133, 139, 152, 159).
- James, A P and B V Dasarathy (2014). “Medical image fusion: A survey of the state of the art”. In: *Information Fusion* 19. Special Issue on Information Fusion in Medical Image Computing and Systems, pp. 4 –19 (cit. on pp. 43, 49, 169, 174).
- Jayanti, S and G F Hewitt (1992). “Prediction of the slug-to-churn flow transition in vertical two-phase flow”. In: *International Journal of Multiphase Flow* 18.6, pp. 847 –860 (cit. on p. 10).
- Ji, H, W Tan, Z Gui, B Wang, Z Huang, H Li, and G Wu (2016). “A New Dual-Modality ECT/ERT Technique Based on C4D Principle”. In: *IEEE Transactions on Instrumentation and Measurement* 65.5, pp. 1042–1050 (cit. on pp. 23, 104, 128, 174).

- Jia, J, M Wang, H Inaki Schlaberger, and H Li (2010). “A novel tomographic sensing system for high electrically conductive multiphase flow measurement”. In: *Flow Measurement and Instrumentation* 21.3. Special Issue: Validation and Data Fusion for Process Tomographic Flow Measurements Validation and Data Fusion for Process Tomographic Flow Measurements, pp. 184–190 (cit. on pp. [2](#), [36](#), [139](#), [154](#)).
- Jia, J, M Wang, and Y Faraj (2015). “Evaluation of EIT systems and algorithms for handling full void fraction range in two-phase flow measurement”. In: *Measurement Science and Technology* 26.1, p. 015305 (cit. on p. [37](#)).
- Jin, H, M Wang, and R A Williams (2007). “Analysis of bubble behaviors in bubble columns using electrical resistance tomography”. In: *Chemical Engineering Journal* 130.2–3. Special Issue for the 4th World Congress on Industrial Process Tomography Special Issue - Industrial Process Tomography, pp. 179–185 (cit. on pp. [132](#), [134](#)).
- Juneja, Mta and P S Sandhu (2009). “Performance Evaluation of Edge Detection Techniques for Images in Spatial Domain”. In: *International Journal of Computer Theory and Engineering* 1.5, pp. 614–621 (cit. on p. [24](#)).
- Kee, K E (2014). “A Study of Flow Patterns and Surface Wetting in Gas-Oil-Water Flow”. PhD thesis. Department of Mechanical, Systems Engineering Russ College of Engineering, and Technology Ohio University (cit. on p. [5](#)).
- Khaleghi, B, A Khamis, F O Karray, and S N Razavi (2013). “Multisensor data fusion: A review of the state-of-the-art”. In: *Information Fusion* 14.1, pp. 28–44 (cit. on pp. [45](#), [49](#)).
- Kim, B (2010). “Multi-phase Fluid Simulations Using Regional Level Sets”. In: *ACM Trans. Graph.* 29.6, 175:1–175:8 (cit. on pp. [32](#), [33](#)).
- Kim, B, Y Liu, I Llamas, X Jiao, and J Rossignac (2007). “Simulation of Bubbles in Foam with the Volume Control Method”. In: *ACM Trans. Graph.* 26.3 (cit. on pp. [32](#), [33](#)).
- Kim, D, O Song, and H-S Ko (2010). “A Practical Simulation of Dispersed Bubble Flow”. In: *ACM Trans. Graph.* 29.4, 70:1–70:5 (cit. on p. [32](#)).
- Kolev, N I (2007). *Multiphase flow dynamics 2: Thermal and mechanical interactions*. Vol. 2. Springer Science & Business Media (cit. on p. [8](#)).
- Kotre, C J (1994). “EIT image reconstruction using sensitivity weighted filtered backprojection”. In: *Physiological measurement* 15.2A, A125 (cit. on pp. [13](#), [127](#), [161](#)).

- Kubias, A, F Deinzer, T Feldmann, D Paulus, B Schreiber, and Th Brunner (2008). “2D/3D image registration on the GPU”. In: *Pattern Recognition and Image Analysis* 18.3, pp. 381–389 (cit. on p. 179).
- Lacroute, P and M Levoy (1994). “Fast volume rendering using a shear-warp factorization of the viewing transformation”. In: *Proceedings of the 21st annual conference on Computer graphics and interactive techniques*. ACM, pp. 451–458 (cit. on p. 29).
- Lehmann, T M, C Gonner, and K Spitzer (1999). “Survey: interpolation methods in medical image processing”. In: *IEEE Transactions on Medical Imaging* 18.11, pp. 1049–1075 (cit. on p. 173).
- Levy, O and D Stroud (1997). “Maxwell Garnett Theory for Mixtures of Anisotropic Inclusions: Application To Conducting Polymers”. In: *Physical Review B* 56.13, pp. 8035–8046 (cit. on p. 21).
- Li, H, M Wang, Y Wu, Y Ma, and R Williams (2005). “Measurement of oil volume fraction and velocity distributions in vertical oil-in-water flows using ERT and a local probe”. In: *Journal of Zhejiang University Science A* 6.12, pp. 1412–1415 (cit. on p. 17).
- Li, H, M Wang, Y-X Wu, and G Lucas (2009a). “Volume flow rate measurement in vertical oil-in-water pipe flow using electrical impedance tomography and a local probe”. In: *Multiphase Science and Technology* 21.1-2, pp. 81–93 (cit. on pp. 149, 176).
- Li, H, G-F Tang, F-X Wu, and C E Tan (2013). “Pixel-level Image Fusion Based on Programmable GPU”. In: *Applied Mechanics and Materials*. Vol. 347. Trans Tech Publ, pp. 3872–3876 (cit. on p. 179).
- Li, M, D Yu, C He, Q Liu, H Li, and H Wang (2010). “Multimodal medical image fusion based on IHS and PCA”. In: *Procedia Engineering* 7, pp. 280–285 (cit. on p. 51).
- Li, S, X Kang, L Fang, J Hu, and H Yin (2017). “Pixel-level image fusion: A survey of the state of the art”. In: *Information Fusion* 33, pp. 100–112 (cit. on pp. 48, 49, 52, 174).
- Li, Y and W Yang (2009b). “Measurement of multi-phase distribution using an integrated dual-modality sensor”. In: *Imaging Systems and Techniques, 2009. IST '09. IEEE International Workshop on*, pp. 335–339 (cit. on pp. 44, 46, 87, 104, 116, 123, 124).

- Livnat, Y and C Hansen (1998). “View dependent isosurface extraction”. In: *Visualization '98. Proceedings*, pp. 175–180 (cit. on p. 27).
- Lorensen, B (2013). *Marching Cubes Wiki*. online (cit. on p. 28).
- Lorensen, W E and H E Cline (1987). “Marching Cubes: A High Resolution 3D Surface Construction Algorithm”. In: *SIGGRAPH Comput. Graph.* 21.4, pp. 163–169 (cit. on pp. 27, 138).
- Lucas, G P, J Cory, R C Waterfall, W W Loh, and F J Dickin (1999). “Measurement of the solids volume fraction and velocity distributions in solids–liquid flows using dual-plane electrical resistance tomography”. In: *Flow Measurement and Instrumentation* 10.4, pp. 249 –258 (cit. on p. 17).
- Luebke, D, M Harris, J Krüger, T Purcell, N Govindaraju, I Buck, C Woolley, and A Lefohn (2004). “GPGPU: General Purpose Computation on Graphics Hardware”. In: *ACM SIGGRAPH 2004 Course Notes*. SIGGRAPH '04. Los Angeles, CA: ACM (cit. on p. 177).
- Ma, Y, N Holliday, Y Dai, M Wang, R A Williams, and G Lucas (2003). “A high performance online data processing EIT system”. In: *3rd World Congress on Industrial Process Tomography*. Banff, Canada (cit. on p. 17).
- Manera, A, H-M Prasser, D Lucas, and T H J J van der Hagen (2006). “Three-dimensional flow pattern visualization and bubble size distributions in stationary and transient upward flashing flow”. In: *International Journal of Multiphase Flow* 32.8, pp. 996 –1016 (cit. on pp. 5, 35, 40, 41, 53).
- Marashdeh, Q, W Warsito, L S Fan, and F L Teixeira (2007). “A Multimodal Tomography System Based on ECT Sensors”. In: *IEEE Sensors Journal* 7.3, pp. 426–433 (cit. on pp. 23, 128).
- Marashdeh, Q, L-S Fan, B Du, and W Warsito (2008). “Electrical Capacitance Tomography A Perspective”. In: *Industrial & Engineering Chemistry Research* 47.10, pp. 3708–3719 (cit. on p. 1).
- Marr, D and E Hildreth (1980). “Theory of edge detection”. In: *Proceedings of the Royal Society of London B: Biological Sciences* 207.1167, pp. 187–217 (cit. on p. 24).
- MathWorks (2016). *Fuzzy Logic Toolbox™*. URL: <http://uk.mathworks.com/products/fuzzy-logic/index.html> (cit. on pp. 49, 87).
- Matusiak, B, A Romanowski, D Sankowski, and K Grudziel (2013). “Forward problem solution acceleration with graphical processing units (GPU) for elec-

- trical tomography imaging”. In: *7th World Congress on Industrial Process Tomography* (cit. on p. 178).
- Maxwell, J C (1982). *A treatise on electricity and magnetism*. Ed. by J J Thomson. 3rd edition. Vol. 1. Oxford University Press (cit. on pp. 16, 62).
- Mitchell, H B (2012). *Data fusion: concepts and ideas*. Springer Science & Business Media (cit. on pp. 45, 65).
- Monaghan, J J (2005). “Smoothed particle hydrodynamics”. In: *Reports on Progress in Physics* 68.8, p. 1703 (cit. on p. 32).
- Monicka, J G, N G Sekhar, and K R Kumar (2011). “Performance evaluation of membership functions on fuzzy logic controlled ac voltage controller for speed control of induction motor drive”. In: *International Journal of Computer Applications* 13.5, pp. 8–12 (cit. on p. 89).
- Mosorov, V, D Sankowski, and T Dyakowski (2002). “The ‘best-correlated pixels’ method for solid mass flow measurements using electrical capacitance tomography”. In: *Measurement Science and Technology* 13.12, p. 1810 (cit. on p. 18).
- Nahvi, M and B S Hoyle (2008). “Wideband Electrical Impedance Tomography”. In: *Measurement Science and Technology* 19.9 (cit. on p. 23).
- Newman, T S and H Yi (2006). “A survey of the marching cubes algorithm”. In: *Computers & Graphics* 30.5, pp. 854–879 (cit. on p. 27).
- Nuryadin, S, M Ignaczak, D Lucas, and Deendarlianto (2015). “On the accuracy of wire-mesh sensors in dependence of bubble sizes and liquid flow rates”. In: *Experimental Thermal and Fluid Science* 65, pp. 73–81 (cit. on p. 36).
- Ohtake, Y and H Suzuki (2013). “Edge detection based multi-material interface extraction on industrial CT volumes”. In: *Science China Information Sciences* 56.9, pp. 1–9 (cit. on p. 24).
- Owens, J D, D Luebke, N Govindaraju, M Harris and J Krüger, A E Lefohn, and T J Purcell (2007). “A Survey of General-Purpose Computation on Graphics Hardware”. In: *Computer Graphics Forum* 26.1, pp. 80–113 (cit. on p. 178).
- Pajares, G and J M de la Cruz (2004). “A wavelet-based image fusion tutorial”. In: *Pattern Recognition* 37.9, pp. 1855–1872 (cit. on p. 52).
- Piella, G (2003). “A general framework for multiresolution image fusion: from pixels to regions”. In: *Information Fusion* 4.4, pp. 259–280 (cit. on pp. 45, 48, 76).

- Prasser, H-M, D Scholz, and C Zippe (2001). “Bubble size measurement using wire-mesh sensors”. In: *Flow Measurement and Instrumentation* 12.4, pp. 299–312 (cit. on pp. 1, 11, 34, 35, 43).
- Prasser, H-M, M Misawa, and I Tiseanu (2005). “Comparison between wire-mesh sensor and ultra-fast X-ray tomograph for an air–water flow in a vertical pipe”. In: *Flow Measurement and Instrumentation* 16.2–3. Tomographic Techniques for Multiphase Flow Measurements 4th International Symposium on Measurement Techniques for Multiphase Flows, pp. 73–83 (cit. on p. 35).
- Preim, B and D Bartz (2007). *Visualization in medicine: theory, algorithms, and applications*. Morgan Kaufmann (cit. on p. 30).
- Prosperetti, A and G Tryggvason (2009). *Computational methods for multiphase flow*. Cambridge University Press (cit. on pp. 10, 30).
- Pusppanathan, J, M Faramarzi, F R Yunus, N M N Ayobr, R A Rahim, F A Phang, M H F Rahiman, A Ahmad, L P Ling, and K H Abas (2014). “Image Fusion Using Fuzzy Logic Pixel Fusion for Dual Modality Tomography System”. In: *Jurnal Teknologi* 70.3 (cit. on pp. 48, 49, 51, 168).
- Qi, F S, G H Yeoh, S C P Cheung, J Y Tu, E Krepper, and D Lucas (2012). “Classification of bubbles in vertical gas–liquid flow: Part 1 – An analysis of experimental data”. In: *International Journal of Multiphase Flow* 39, pp. 121–134 (cit. on pp. 132, 134).
- Qiu, C, B S Hoyle, and F J W Podd (2007). “Engineering and application of a dual-modality process tomography system”. In: *Flow Measurement and Instrumentation* 18.5-6. Process Tomography and Flow Visualization, pp. 247–254 (cit. on pp. 1, 2, 20, 23, 44, 46, 78, 82, 87, 111, 136, 168).
- Ramskill, N P and M Wang (2011). “Boolean logic analysis for flow regime recognition of gas-liquid horizontal flow”. In: *Measurement Science and Technology* 22.10, p. 104016 (cit. on pp. 5, 148).
- Raol, J R (2015). *Data Fusion Mathematics: Theory and Practice*. CRC Press (cit. on p. 90).
- Ren, B, Y Jiang, C Li, and M C Lin (2015). “A simple approach for bubble modelling from multiphase fluid simulation”. In: *Computational Visual Media* 1 (2), pp. 171–181 (cit. on p. 33).
- Ross, T J (2009). *Fuzzy logic with engineering applications*. 3rd edition. John Wiley & Sons (cit. on pp. 89, 90).

- Roth, S D (1982). “Ray casting for modeling solids”. In: *Computer Graphics and Image Processing* 18.2, pp. 109–144 (cit. on p. 29).
- Santos, E N dos, T P Vendruscolo, R E M Morales, E Schleicher, U Hampel, and M J Da Silva (2015). “Dual-modality wire-mesh sensor for the visualization of three-phase flows”. In: *Measurement Science and Technology* 26.10, p. 105302 (cit. on pp. 1, 44, 46, 168).
- Schroeder, W, K Martin, and B Lorensen (2006a). *The Visualization Toolkit: An Object-oriented Approach to 3D Graphics*. Kitware (cit. on p. 172).
- (2006b). *Visualization Toolkit: An Object-Oriented Approach to 3D Graphics, 4th Edition*. Kitware (cit. on p. 39).
- Seagar, A D, D C Barber, and B H Brown (1987). “Theoretical limits to sensitivity and resolution in impedance imaging”. In: *Clinical Physics and Physiological Measurement* 8.4A, p. 13 (cit. on p. 14).
- Sean, R Sanders, M M Razzaque, J Schaan, K Nandakumar, J H Masliyah, A Afacan, and S Liu (2004). “Bubble Size Distributions for Dispersed Air-Water Flows in a 100 mm Horizontal Pipeline”. In: *The Canadian Journal of Chemical Engineering* 82.4, pp. 858–864 (cit. on pp. 132, 134).
- Senthilkumaran, N and R Rajesh (2009). “Edge detection techniques for image segmentation—a survey of soft computing approaches”. In: *International journal of recent trends in engineering* 1.2, pp. 250–254 (cit. on p. 26).
- Shams, R, P Sadeghi, R A Kennedy, and R I Hartley (2010). “A Survey of Medical Image Registration on Multicore and the GPU”. In: *IEEE Signal Processing Magazine* 27.2, pp. 50–60 (cit. on p. 179).
- Silva, M J Da, S Thiele, L Abdulkareem, B J Azzopardi, and U Hampel (2010). “High-resolution gas-oil two-phase flow visualization with a capacitance wire-mesh sensor”. In: *Flow Measurement and Instrumentation* 21.3. Special Issue: Validation and Data Fusion for Process Tomographic Flow Measurements—Validation and Data Fusion for Process Tomographic Flow Measurements, pp. 191–197 (cit. on p. 1).
- Sobel, I and G Feldman (1968). “A 3x3 isotropic gradient operator for image processing”. In: *a talk at the Stanford Artificial Project in*, pp. 271–272 (cit. on p. 24).
- Soleimani, M, C N Mitchell, R Banasiak, R Wajman, and A Adler (2009). “Four-dimensional electrical capacitance tomography imaging using experimental

- data”. In: *Progress In Electromagnetics Research* 90, pp. 171–186 (cit. on p. 11).
- Stathaki, T (2008). *Image Fusion: Algorithms and Applications*. Academic Press (cit. on pp. 48, 52).
- Sun, J and W Yang (2015). “A dual-modality electrical tomography sensor for measurement of gas–oil–water stratified flows”. In: *Measurement* 66, pp. 150–160 (cit. on pp. 23, 44, 45, 168).
- Tan, J and X-B Yang (2009). “Physically-based fluid animation: A survey”. In: *Science in China Series F: Information Sciences* 52.5, pp. 723–740 (cit. on pp. 32, 37).
- Teng, J, S Wang, J Zhang, and X Wang (2010). “Fusion algorithm of medical images based on fuzzy logic”. In: *Fuzzy Systems and Knowledge Discovery (FSKD), 2010 Seventh International Conference on*. Vol. 2. IEEE, pp. 546–550 (cit. on pp. 43, 49).
- Thorn, R, G A Johansen, and B T Hjertaker (2012). “Three-phase flow measurement in the petroleum industry”. In: *Measurement Science and Technology* 24.1, p. 012003 (cit. on p. 5).
- (2013). “Three-phase flow measurement in the petroleum industry”. In: *Measurement Science and Technology* 24.1, p. 012003 (cit. on p. 43).
- Tryggvason, G, R Scardovelli, and S Zaleski (2011). *Direct numerical simulations of gas-liquid multiphase flows*. 9. Recent Topics in Computational Fluid Dynamics. Cambridge University Press (cit. on p. 10).
- Tu, T-M, S-C Su, H-C Shyu, and P S Huang (2001). “A new look at IHS-like image fusion methods”. In: *Information Fusion* 2.3, pp. 177–186 (cit. on p. 51).
- Wang, M (2002). “Inverse solutions for electrical impedance tomography based on conjugate gradients methods”. In: *Measurement Science and Technology* 13.1, p. 101 (cit. on pp. 13, 68, 104, 127, 148).
- ed. (2015). *Industrial Tomography Systems and Applications*. Woodhead Publishing (cit. on pp. 1, 11, 52, 168).
- Wang, M, F J Dickin, and R Mann (1999). “Electrical Resistance Tomography Sensing Systems for Industrial Applications”. In: *Chemical Engineering Communications* 175.1, pp. 49–70 (cit. on pp. 1, 11, 14, 15, 36, 44, 53, 82, 87, 126, 134, 136).

- Wang, M, X Jia, M Bennett, and R A Williams (2001). “Flow regime identification and optimum interfacial area control of bubble columns using electrical impedance imaging”. In: *2nd World Congress on Industrial Process Tomography*, pp. 726–734 (cit. on p. 136).
- Wang, M and W Yin (2002). *Electrical impedance tomography*. US Patent 6,940,286 (cit. on p. 12).
- Wang, M, Y Ma, N Holliday, Y Dai, R A Williams, and G Lucas (2005). “A high-performance EIT system”. In: *Sensors Journal, IEEE* 5.2, pp. 289–299 (cit. on pp. 2, 36, 44, 139, 154, 164).
- Wang, M, J Jia, Y Faraj, Q Wang, C Xie, G Oddie, K Primrose, and C Qiu (2015). “A new visualisation and measurement technology for water continuous multiphase flows”. In: *Flow Measurement and Instrumentation* 46, Part B. Special issue on Tomography Measurement & Modeling of Multiphase Flows, pp. 204 –212 (cit. on pp. 17, 166).
- Wang, M, Q Wang, and B Karki (2016a). “Arts of electrical impedance tomographic sensing”. In: *Phil. Trans. R. Soc. A* 374.2070, p. 20150329 (cit. on pp. 12, 14, 36, 134, 161, 163, 164).
- Wang, Q, J Polansky, M Wang, K Wei, C Qiu, A Kenbar, and D Millington (2016b). “Experimental Evaluation of Dual-Modality Electrical Tomographic Systems on Gas-Oil-Water Flow in Horizontal Pipeline”. In: *8th World Congress on Industrial Process Tomography*. Iguassu Falls, Brazil (cit. on pp. 59, 61, 168).
- Wang, Q, M Wang, K Wei, and C Qiu (2017). “Visualisation of Gas-Oil-Water Flow in Horizontal pipeline using Dual-Modality Electrical Tomographic System”. In: *IEEE Sensors Journal* (cit. on pp. 44, 46, 65, 69, 72, 78, 80–83, 116, 166).
- Wei, K, C Qiu, M Soleimani, and K Primrose (2015). “ITS Reconstruction Tool-Suite: An inverse algorithm package for industrial process tomography”. In: *Flow Measurement and Instrumentation* 46, Part B. Special issue on Tomography Measurement & Modeling of Multiphase Flows, pp. 292 –302 (cit. on pp. 13, 39, 104).
- Wenger, R (2013). *Isosurfaces: Geometry, Topology, and Algorithms*. first edition. A K Peters/CRC Press (cit. on pp. 26, 27).
- Wikipedia (2013a). *Ray tracing (graphics)* — *Wikipedia, The Free Encyclopedia*. [Online; accessed May-2013] (cit. on p. 28).

- Wikipedia (2013b). *Volume ray casting* — *Wikipedia, The Free Encyclopedia*. [Online; accessed May-2013] (cit. on p. 29).
- (2015). *Kelvin–Helmholtz instability* — *Wikipedia, The Free Encyclopedia*. [Online; accessed June-2015] (cit. on p. 6).
- Wu, H, Y Yang, J Escudero, and J Jia (2016). “Feasibility Study of Frequency-difference Electrical Impedance Tomography on Industrial Applications”. In: *8th World Congress on Industrial Process Tomography* (cit. on p. 23).
- Wu, Y, H Li, M Wang, and R A Williams (2005). “Characterization of Air-Water Two-Phase Vertical Flow by Using Electrical Resistance Imaging”. In: *The Canadian Journal of Chemical Engineering* 83.1, pp. 37–41 (cit. on p. 17).
- Xu, F and K Mueller (2007). “Real-time 3D computed tomographic reconstruction using commodity graphics hardware”. In: *Physics in Medicine and Biology* 52.12, p. 3405 (cit. on p. 178).
- Y, G H and J Tu, eds. (2010). *Computational Techniques for Multiphase Flows*. Oxford: Butterworth-Heinemann, pp. iv – (cit. on pp. 8, 9, 30).
- Yang, W Q and L Peng (2003). “Image reconstruction algorithms for electrical capacitance tomography”. In: *Measurement Science and Technology* 14.1, R1 (cit. on pp. 36, 44, 127).
- Ye, L and W Yang (2012). “Real-time 3D visualisation in electrical capacitance tomography”. In: *Imaging Systems and Techniques (IST), 2012 IEEE International Conference on*, pp. 40–44 (cit. on pp. 41, 42).
- Yoo, S-H, S-U Jo, K-Y Choi, and C-S Jeong (2008). “A Framework for multisensor image fusion using graphics hardware”. In: *Information Fusion, 2008 11th International Conference on*. IEEE, pp. 1–5 (cit. on p. 179).
- York, T, H McCann, and K B Ozanyan (2011). “Agile Sensing Systems for Tomography”. In: *IEEE Sensors Journal* 11.12, pp. 3086–3105 (cit. on pp. 1, 11, 43).
- Yue, S, T Wu, J Pan, and H Wang (2013). “Fuzzy Clustering Based ET Image Fusion”. In: *Inf. Fusion* 14.4, pp. 487–497 (cit. on pp. 23, 44, 47, 128, 168).
- Zadeh, L A (1965). “Fuzzy sets”. In: *Information and control* 8.3, pp. 338–353 (cit. on p. 49).
- (2008). “Is there a need for fuzzy logic?” In: *Information Sciences* 178.13, pp. 2751–2779 (cit. on p. 49).
- Zhang, M, L Ma, and M Soleimani (2015). “Dual modality ECT-MIT multiphase flow imaging”. In: *Flow Measurement and Instrumentation* 46, Part B.

- Special issue on Tomography Measurement & Modeling of Multiphase Flows, pp. 240 –254 (cit. on pp. [44](#), [46](#), [168](#)).
- Zhang, R, Q Wang, H Wang, M Zhang, and H Li (2014). “Data fusion in dual-mode tomography for imaging oil-gas two-phase flow”. In: *Flow Measurement and Instrumentation* 37, pp. 1 –11 (cit. on pp. [43](#), [54](#), [168](#), [174](#)).
- Zhang, Z and R S Blum (1999). “A Categorization of Multiscale-decomposition-based Image Fusion Schemes with a Performance Study for a Digital Camera Application”. In: *Proceedings of the IEEE*, pp. 1315–1326 (cit. on p. [48](#)).
- Zhao, J and B K Bose (2002). “Evaluation of membership functions for fuzzy logic controlled induction motor drive”. In: *IECON 02 [Industrial Electronics Society, IEEE 2002 28th Annual Conference of the]*. Vol. 1, 229–234 vol.1 (cit. on pp. [48](#), [89](#), [104](#)).

List of Publications

1. Qiang Wang, Mi Wang, Kent Wei, and Changhua Qiu (2017). "Visualisation of Gas-Oil-Water Flow in Horizontal pipeline using Dual-Modality Electrical Tomographic System." In: *IEEE Sensors Journal*. Accepted.
2. Qiang Wang, Jiri Polansky, Bishal Karki, Mi Wang, Kent Wei, Changhua Qiu, Asaad Kenbar, and David Millington (2016). "Experimental tomographic methods for analysing flow dynamics of gas-oil-water flows in horizontal pipeline." *Journal of Hydrodynamics*, Ser. B, Volume 28, Issue 6, 2016, Pages 1018-1021, ISSN 1001-6058.
3. Mi Wang, Qiang Wang, and Bishal Karki. "Arts of electrical impedance tomographic sensing." In: *Phil. Trans. R. Soc. A* 374.2070 (2016): 20150329.
4. Qiang Wang, Jiri Polansky, Mi Wang, Kent Wei, Changhua Qiu, Asaad Kenbar, and David Millington (2016). "Experimental Evaluation of Dual-Modality Electrical Tomographic Systems on Gas-Oil-Water Flow in Horizontal Pipeline." In: *8th World Congress on Industrial Process Tomography*. Iguassu Falls, Brazil.
5. Jiabin Jia, Mi Wang, Yousef Faraj, Qiang Wang. "Online conductivity calibration methods for EIT gas/oil in water flow measurement." In: *Flow Measurement and Instrumentation*, Volume 46, 2015, Pages 213-217
6. Mi Wang, Jiabin Jia, Yousef Faraj, Qiang Wang, Cheng-gang Xie, Gary Oddie, Ken Primrose, Changhua Qiu. "A new visualisation and measurement technology for water continuous multiphase flows." In: *Flow Measurement and Instrumentation*, Volume 46, 2015, Pages 204-212
7. Yousef Faraj, Mi Wang, Jiabin Jia, Qiang Wang, Cheng-gang Xie, Gary Oddie, Ken Primrose, Changhua Qiu. "Measurement of vertical oil-in-water

- two-phase flow using dual-modality ERT-EMF system." In: *Flow Measurement and Instrumentation*, Volume 46, 2015, Pages 255-261
8. Qiang Wang, Bishal Karki, Yousef Faraj, Mi Wang (2015). "Improving Spatial and Temporal Resolution of Electrical Impedance Tomogram (EIT) by Partial Imaging with Limited Measurements (PILM)." in *7th International Symposium on Process Tomography*. Dresden, Germany.
 9. Wei Na, Jiabin Jia, Xin Yu, Yousef Faraj, Qiang Wang, Ying-feng Meng, Mi Wang, Wantong Sun. "Imaging of gas-liquid annular flows for underbalanced drilling using electrical resistance tomography." In: *Flow Measurement and Instrumentation*, Volume 46, 2015, Pages 319-326
 10. Qiang Wang, Yousef Faraj, Mi Wang (2014). "Effects of Asymmetrical Sensing and Imaging on Scalar and Vector Tomograms." In: *5th International Workshop on Process Tomography*. Jeju, South Korea.

List of Patents

1. Mi Wang, Jiabin Jia, Yousef FARAJ, Qiang Wang. "Tomography apparatus, multi-phase flow monitoring system, and corresponding methods". UK Patent PCT/GB2015/052672. 24th March 2016.
2. Mi Wang, Bishal Karki, Qiang Wang. "Tomography apparatus and method". UK Patent PCT/GB2015/052671. 24th March 2016.

Appendix A

Visualisation of Three-Phase Horizontal Flow

This appendix is to include some cross-sectional tomograms of gas-oil-water flow from electrical tomography, as a complement to the axially-stacked images presented in Section 3.6. The tomograms are from different WLR and GVF combinations, which are consistent with the flow conditions examined in Section 3.6. It is worth noting that the images are only for the conditions where dual-modality ERT-ECT systems are functional normally, i.e. with WLR from 40% to 90%.

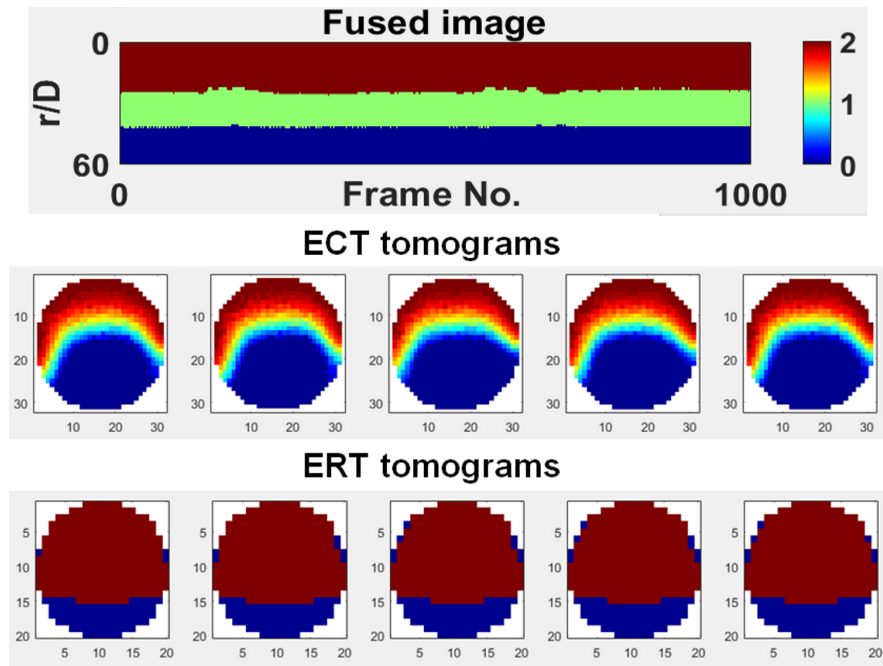


Figure A.1: Cross-sectional electrical tomograms for a stratified flow at WLR 50%. (See Figure 3.44a)

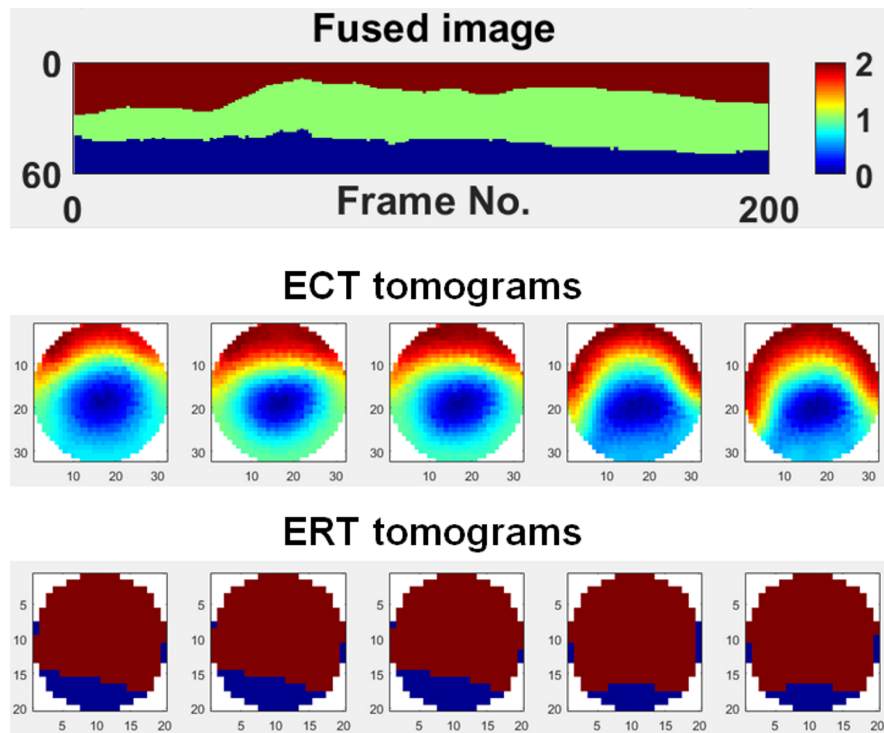


Figure A.2: Cross-sectional electrical tomograms for a slug flow at WLR 50%. (See Figure 3.44b)

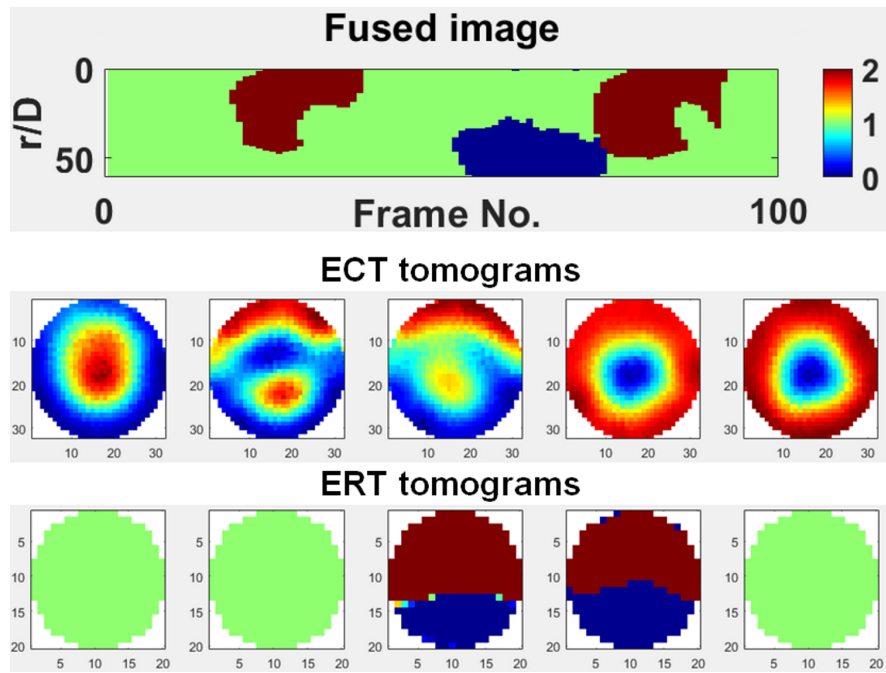


Figure A.3: Cross-sectional electrical tomograms for a plug flow at WLR 50%. (See Figure 3.44c)

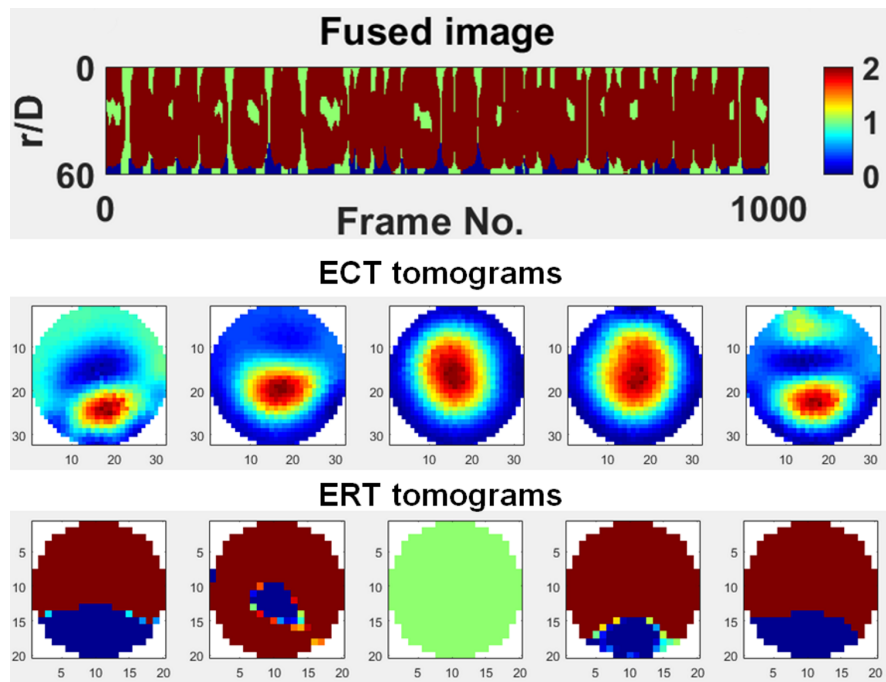


Figure A.4: Cross-sectional electrical tomograms for an annular flow at WLR 50%. (See Figure 3.44d)

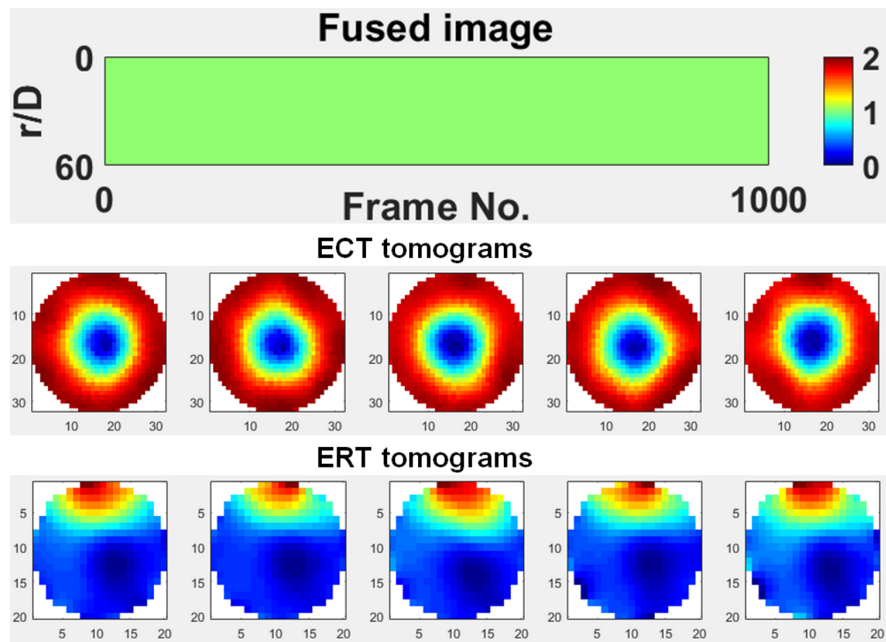


Figure A.5: Cross-sectional electrical tomograms for a bubbly flow at WLR 50%.
(See Figure 3.44e)

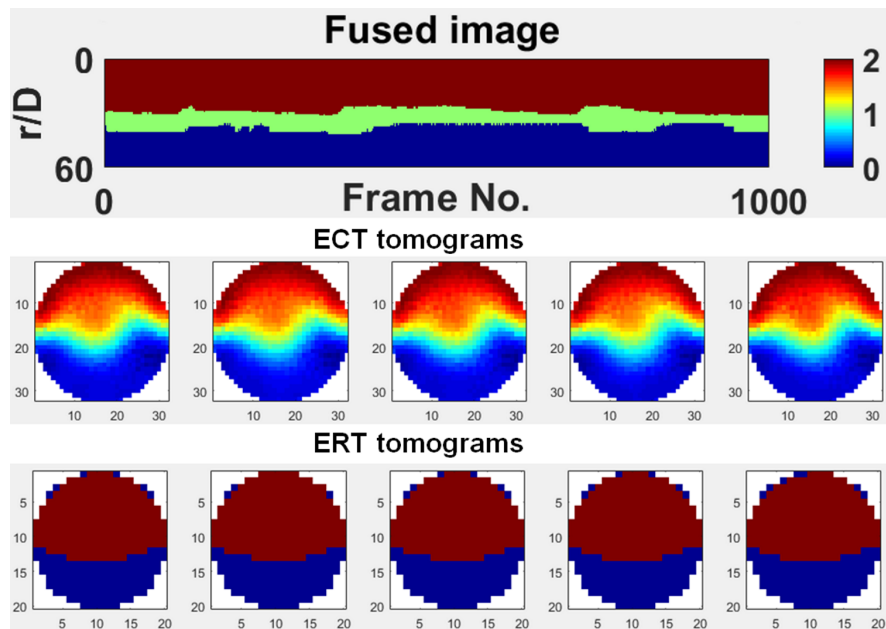


Figure A.6: Cross-sectional electrical tomograms for a stratified flow at WLR 75%. (See Figure 3.46a)

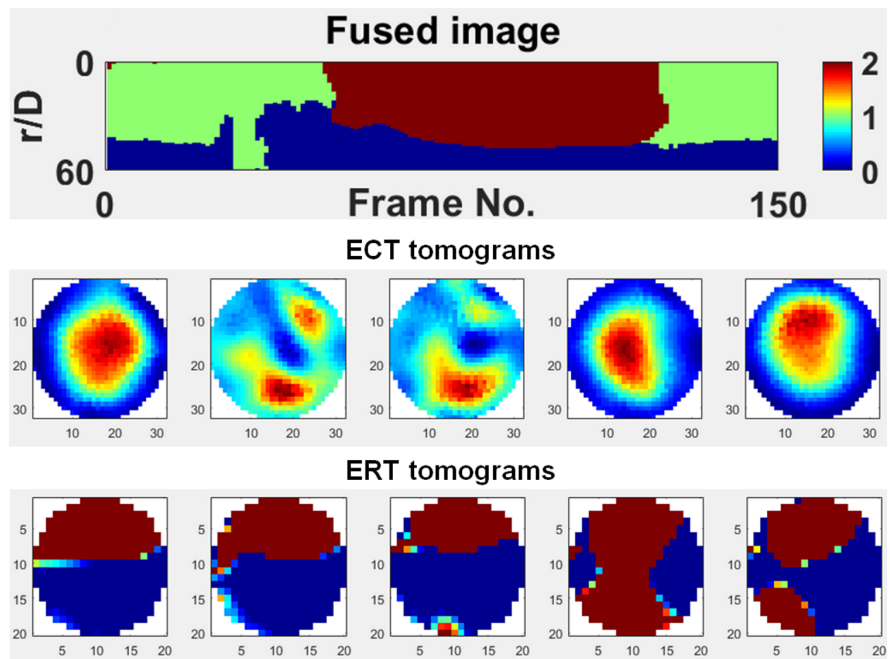


Figure A.7: Cross-sectional electrical tomograms for a slug flow at WLR 75%.
(See Figure 3.46b)

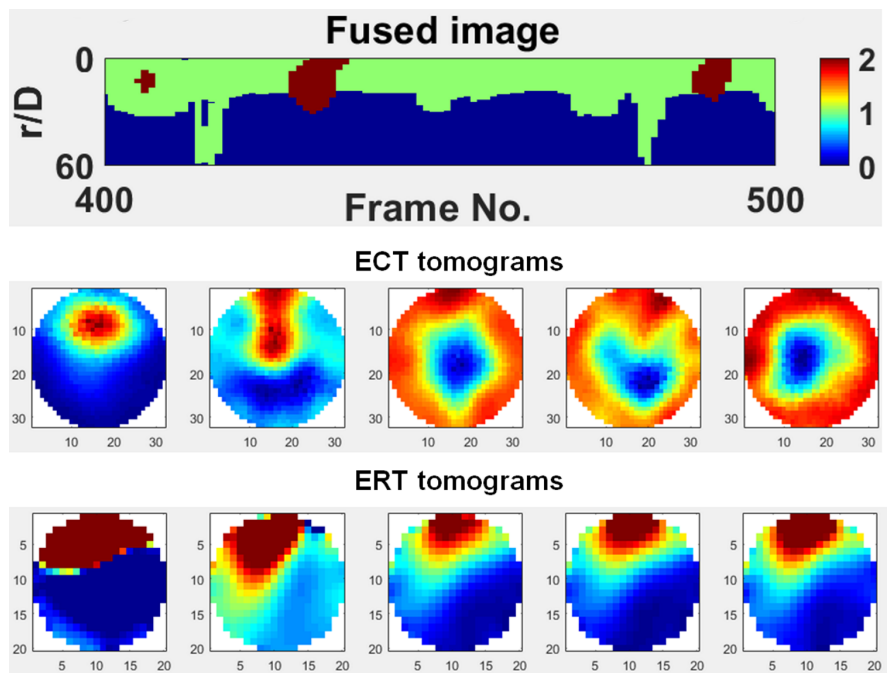


Figure A.8: Cross-sectional electrical tomograms for a plug flow at WLR 75%.
(See Figure 3.46c)

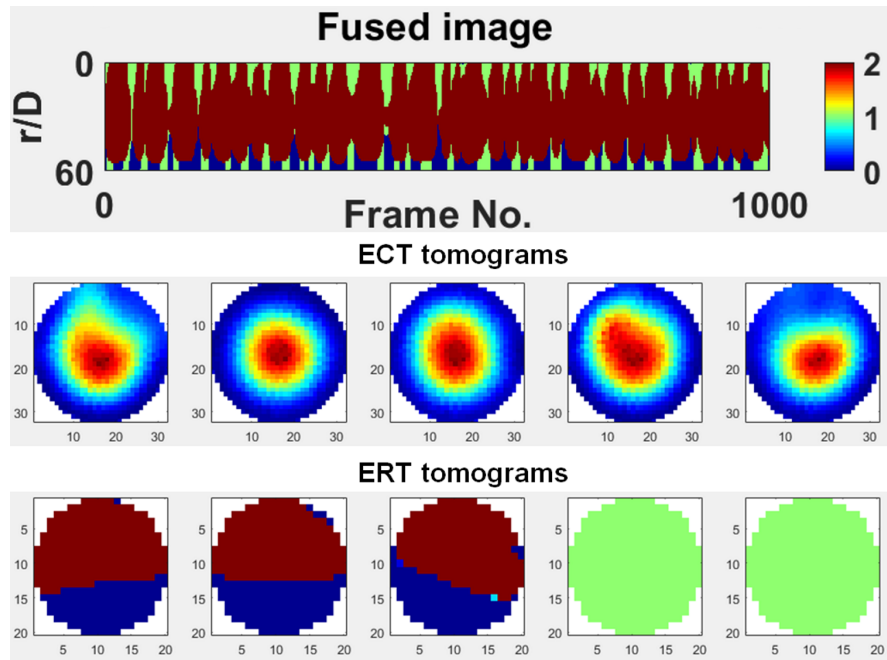


Figure A.9: Cross-sectional electrical tomograms for an annular flow at WLR 75%. (See Figure 3.46d)

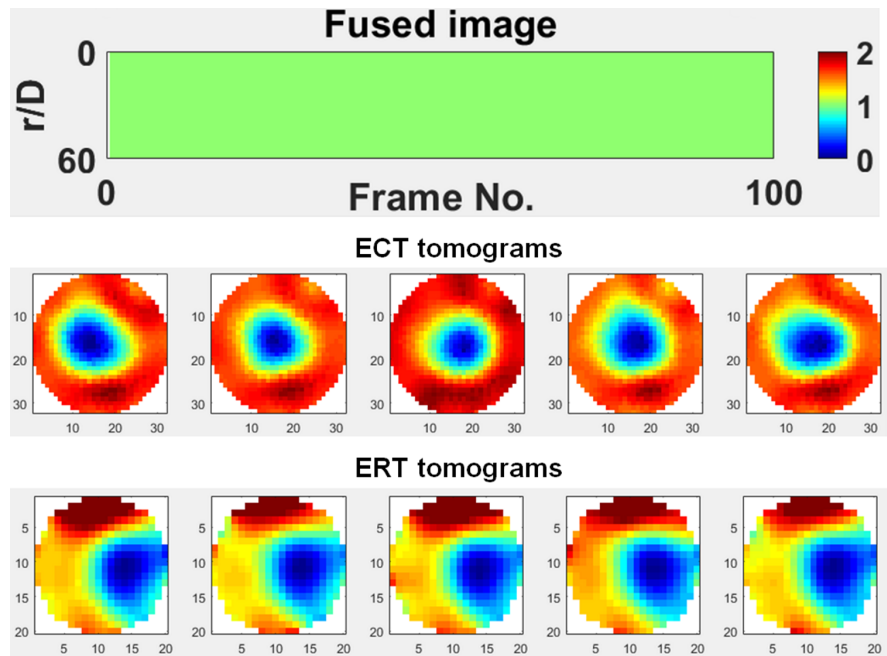


Figure A.10: Cross-sectional electrical tomograms for a bubbly flow at WLR 75%. (See Figure 3.46e)

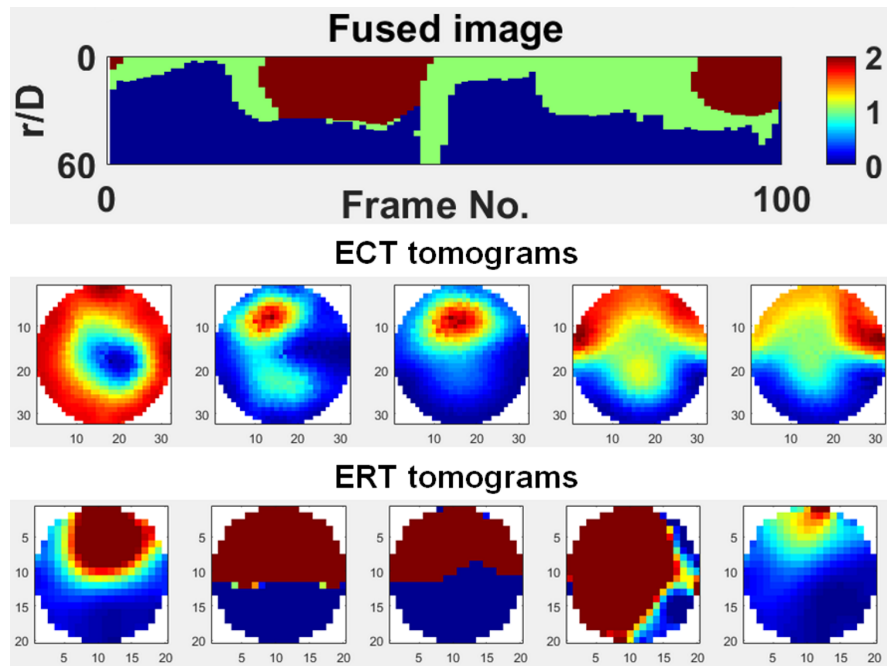


Figure A.11: Cross-sectional electrical tomograms for a slug flow at WLR 90%.
(See Figure 3.48a)

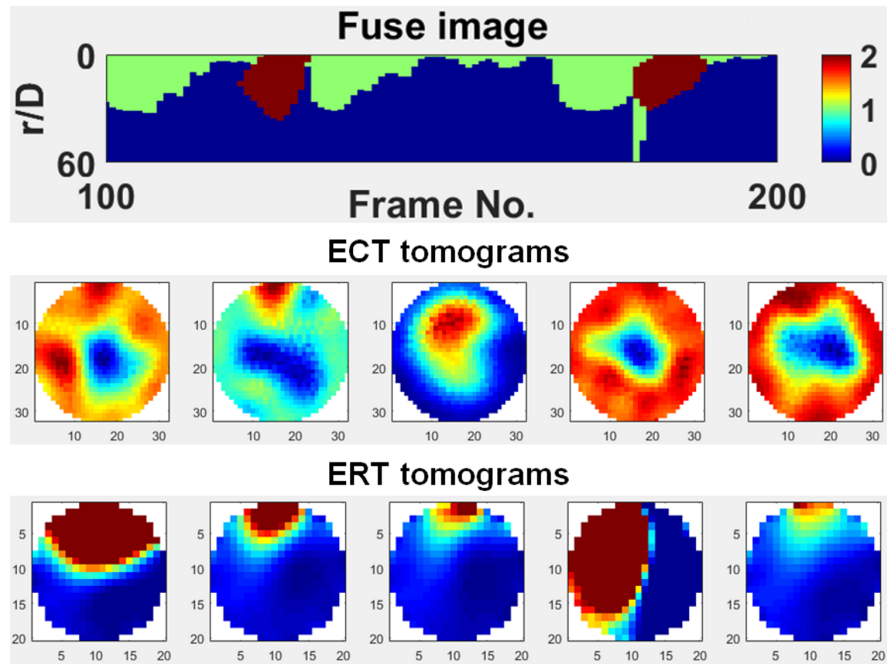


Figure A.12: Cross-sectional electrical tomograms for a plug flow at WLR 90%.
(See Figure 3.48b)

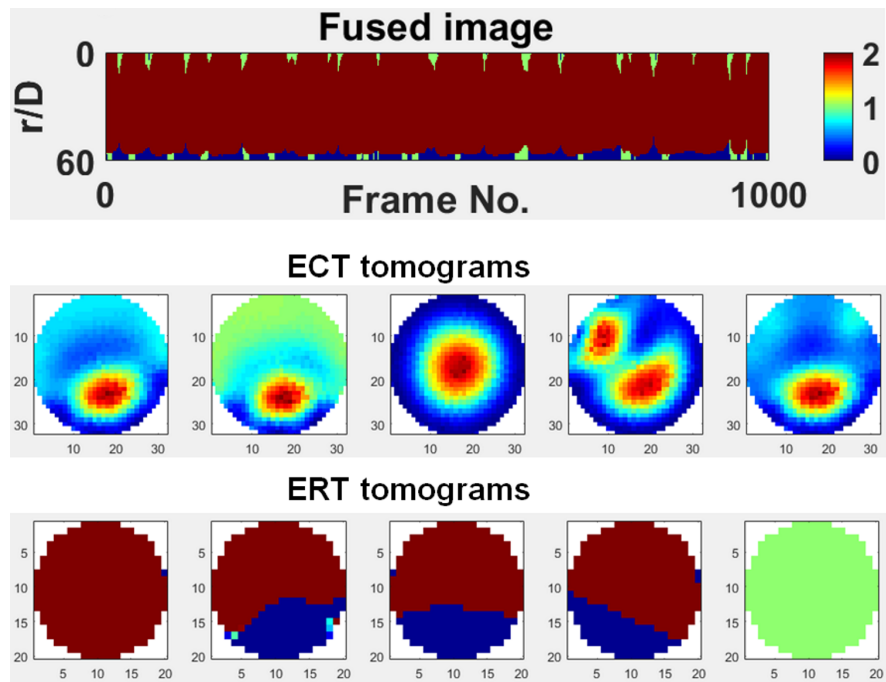


Figure A.13: Cross-sectional electrical tomograms for an annular flow at WLR 90%. (See Figure 3.48c)

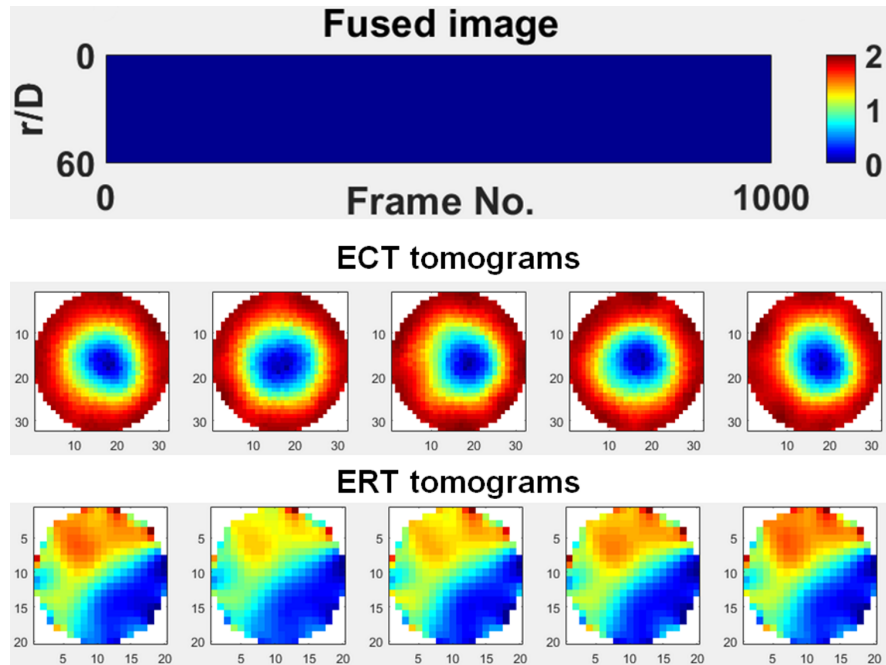


Figure A.14: Cross-sectional electrical tomograms for a bubbly flow at WLR 90%. (See Figure 3.48d)